Dissertation

WAVE BASED TECHNIQUE FOR THE NUMERICAL MID-FREQUENCY MODELLING OF COUPLED, UNBOUNDED VIBRO-ACOUSTIC PROBLEMS

zur Erlangung des akademischen Grades Doktor der Technischen Wissenschaften
eingereicht an der Fakultät für Maschinenbau und Wirtschaftswissenschaften der
Technischen Universität Graz

TU Graz

Graz University of Technology

vorgelegt von

Jan REJLEK

durchgeführt am
Kompetenzzentrum – Das Virtuelle Fahrzeug, Forschungsgesellschaft mbH

virtual vehicle

unter Begutachtung von

A.o.Univ.-Prof. Dipl.-Ing. Dr.techn. Hans-Herwig PRIEBSCH

Institut für Verbrennungskraftmaschinen und Thermodynamik
Technische Universität Graz

Dr.ir. Bert PLUYMERS

Afdeling Productietechnieken, Machinebouw en Automatisering (PMA)
Departement Werktuigkunde
Faculteit Ingenieurswetenschappen
Katholieke Universiteit Leuven, Belgium

Graz, März 2012

Dissertation

WAVE BASED TECHNIQUE FOR THE NUMERICAL MID-FREQUENCY MODELLING OF COUPLED, UNBOUNDED VIBRO-ACOUSTIC PROBLEMS

Fakultät für Maschinenbau und Wirtschaftswissenschaften
Technische Universität Graz

200 JAHRE TU GRAZ

Jan REJLEK

Matrikelnummer: 0531298

Neupauerweg 85
8052 Graz
Österreich

Begutachter:

A.o.Univ.-Prof. Dipl.-Ing. Dr.techn. Hans-Herwig PRIEBSCH

Institut für Verbrennungskraftmaschinen und Thermodynamik
Technische Universität Graz

Dr.ir. Bert PLUYMERS

Afdeling Productietechnieken, Machinebouw en Automatisering (PMA)
Departement Werktuigkunde
Faculteit Ingenieurswetenschappen
Katholieke Universiteit Leuven, Belgium

Graz, März 2012

Jan Rejlek
Neupauerweg 85
8052 Graz
Austria
jan.rejlek@gmail.com

264 pages with 148 illustrations

Typeset in LaTeX using the Times New Roman typeface

To my wife, Michaela

Eidesstattliche Erklärung

Ich erkläre an Eides statt, dass ich die vorliegende Arbeit selbstständig verfasst, andere als die angegebenen Quellen/Hilfsmittel nicht benutzt, und die den benutzten Quellen wörtlich und inhaltlich entnommenen Stellen als solche kenntlich gemacht habe.

Graz, am 21. März 2012   Unterschrift: . . . .

Preface

$\star \quad \star \quad \star$

"We choose to go to the Moon. We choose to go to the Moon in this decade and do the other things, not because they are easy, but because they are hard, because that goal will serve to organize and measure the best of our energies and skills, because that challenge is one that we are willing to accept, one we are unwilling to postpone, and one which we intend to win, and the others, too."[1]

John Fitzgerald Kennedy (1917–1963)

As considered in the classical (Newtonian) mechanics, time is supposed to be invariant with respect to the selection of a coordinate system. In practice this means the time is considered an absolute physical quantity, i.e. the time interval measured between any given pair of events is the same for all observers. Well, OK, this is what the theory tells us. Our daily life experience, however, often indicates rather different findings, which give credence to the speculations that time is relative, after all. After more than eight[2] years (!) in Austria, I can still vividly remember my first working day at ACC[3]. I arrived in Graz Hbf.[4] with no document[5] except my passport, exhausted after spending twelve hours on a night train slumbering in my sleeping bag. So I was standing in front of the *ACC's* main entrance and thinking about the duration of my traineeship before ringing the bell – perhaps three months will be fine... Well, and now, a few of years later, I am about to finish my Ph.D. That's what one calls a non-deterministic system!

Here, I would like to thank all the people who enabled me to write these words today. First and foremost, to my supervisor Prof. Hans-Herwig Priebsch for the inspiring discussions and many valuable hints and suggestions given during my research; to Dr. Josef Affenzeller, the former managing director of *ACC*, for proposing an interesting research topic to me and for creating the conditions that made it possible; Dr. Bert Pluymers *(Katholieke Universiteit Leuven)*, my co-referee, for the time invested in the revision of the manuscript and for useful comments and

---

[1] Speech addressed at the Rice University on the Nation's Space Effort, September 12, 1962.

[2] Including some discontinuities as one month trip to Cuba and a half year research fellowship at the *Katholieke Universiteit Leuven* within the Marie Curie Framework.

[3] As of June 17th, 2008, the *Acoustic Competence Centre Graz (ACC)* and the *Virtual Vehicle Competence Center (ViF)* were merged into one legal entity.

[4] Abbreviation of the German word *"Hauptbahnhof"* meaning the main railway station.

[5] All my documents including ID card, driving licence, credit/debit cards, health insurance card, etc. were stolen in a Prague night tram after celebrating the newly obtained M.Sc. degree.

advices. I express my deepest gratitude to Dr. Franz Diwoky *(AVL LIST GmbH)*, whose immense enthusiasm, phenomenal knowledge and readiness to answer my questions have been of tremendous assistance to me throughout my doctoral research. I am very grateful to Eugène Nijman, who has recently taken over the post of a scientific head of *ViF Area C*, for his constructive comments given in the final stage of my doctoral research. I really appreciate the opportunity to work together and I personally do like very much his genuine attitude to work and the inspiring way, how he approaches the problems. Finally, I would like to thank to Mike "ViF English all-star team lecturer" Phillips – the best English teacher ever, for the final proofreading of the manuscript. In addition, my special thank is addressed to all of my colleagues from the *ACC/ViF* for a unique working atmosphere and support. . . . Daniel, Duško, Martin, Gernot, Karoly, Michi, Thomas, Josef – you always have been at hand. Thank you for the many great moments we have spent together.

Furthermore, I highly acknowledge the opportunity to become a research fellow of the EU project SIMVIA2[6]. This fellowship allowed me to carry out part of my research at the Noise and Vibration Research Group of the *Katholieke Universiteit Leuven* for the period of six months and gave me the chance to meet the many new interesting people with whom I had the pleasure of working. In particular Prof. Wim Desmet and Dr. Bert Pluymers as my supervisors, whereby the latter one even became the co-referee of my Ph.D. thesis later on.

Also, I would like to thank the consortium of the EU project MID-MOD[7], and in particular the Dr. Carl Fredrik Hartung from *VOLVO Technology AB*, who has been in charge of coordinating this project. It has been the *VOLVO Technology AB* as an industrial partner within the MID-MOD collaborative network, who generously provided both the CAD data and the physical muffler for the experimental testing, and which were also used within the scope of this dissertation. I myself have been involved in the ongoing R&D activities of the MID-MOD as a project leader from the *ViF* side, and it has really been a great privilege for me to be a part of such a multifaceted community of NVH experts all across Europe.

Last but not least, I offer my deepest gratitude to my family, who have supported me over the years living abroad by giving me their love, unflagging support and gentle patience. My mother, Dagmar, had to make many sacrifices in her life so that I could pursue my studies. By supporting my higher education, she helped lay the ideal foundation that prepared me to carry out my Ph.D. studies in the latter years. Finally, there is someone to whom I owe a debt of gratitude. One extraordinary person who suddenly entered my life and showed me how to look at it from a different angle – my wife Michaela. And even though it was not always possible for her to physically stand by me, her love, sympathy and inspiration have pushed me steadily forward throughout the whole time we have spent together. Without her, it would never have been possible to finish this work.

But during these eight years in Austria, many non-work-related things have also happened – spending vast amounts of time on the roof of Hafnerriegel[8] enjoying the panorama of Graz with a couple of beers, hiking in the Alps (including stoking fireplaces to roast the Käsekrainers[9]), eating delicious kebaps[10] and having serious parties on the island Krk in Croatia. . . And all

---

[6]FP6 Marie Curie Host Fellowships for Early Stage Research Training (EST), EC grant agreement no. MEST-CT-2005-020263.

[7]FP7 Research & Technical Development (RTD) collaborative project, EC grant agreement no. SCP7-2008-218508.

[8]Legendary student dormitory in Graz.

[9]Boiled sausage containing up to 20 % of medium-hard cheese, Born in Graz!

[10]Euro Kebap-Pizza, Franziskanergasse 2, 8010 Graz owned by Kemal Göres – one of the best kebaps I ate ever!

these things and many more have I enjoyed together with the unique people whom I have had the pleasure of meeting in Graz. Daniel Rein – the booster of positive spirits and a never-ending source of fun, deserves special recognition! Thanks for all these things, which have made my life in Graz so exceptional.

Graz, March 2012

Jan Rejlek

Abstract

In several engineering areas, methodologies based on the Trefftz approach have received significant recognition over the last decades. The main reason for rediscovering the Trefftz methods consists in the fact that these techniques utilise the exact solutions of the governing differential equation for the field variables approximation. Especially when solving problems that exhibit a wave-like nature, such as acoustics, structural dynamics or electromagnetic problems, this represents a major advantage over the conventional element-based schemes, such as finite (FEM) or boundary element method (BEM).

In recent years, the wave based prediction technique (WBT) has been developed as an alternative method for solving steady-state vibro-acoustic problems in the mid-frequency gap. The method adopts an indirect Trefftz approach, in which it incorporates the a priori knowledge of the solved problem. Instead of simple polynomial shape functions, the exact solutions of the governing differential equation are used to approximate the dynamic field variables. As a result, fine element discretisation is no longer needed, which yields smaller numerical models that exhibit an enhanced computational efficiency. The WBT has proven to be a robust prediction tool for interior acoustics. A considerable class of real-life vibro-acoustic applications, however, involves the analysis of problems in unbounded spatial domains, such as sound scattering, transmission and radiation problems. Besides the methods based on the boundary integral formulation of governing differential equation, such as BEM, various strategies employing the standard finite element scheme have been developed to tackle unbounded problems. Infinite element method (I-FEM), perfectly matched layers (PML) and non-reflecting boundary conditions (NRBC) are the common extensions of the conventional FEM used to deal with the infinite extent of the acoustic domain. Although based on different approaches, all these concepts have the same basic idea in common, namely introducing an artificial truncation boundary that divides the infinite domain into a bounded region and an unbounded region. This dissertation explores the application of WBT for a three-dimensional analysis of problems involving both the free-field and semi-infinite acoustic domains.

Up to now, only a one-way vibro-acoustic coupling strategy has been employed in the wave based formulation for the analysis of three-dimensional problems involving unbounded acoustic domains. In real-life engineering practice, however, a significant group of problems involves the strong coupling effects between the structure and fluid. Unlike the uncoupled structural and acoustic problems, the mutual coupling interaction is no longer negligible in the coupled vibro-acoustic systems, which means that both parts of the problem have to be considered simultaneously. This dissertation reports on the concepts and applications of the WBT for the analysis of three-dimensional, fully coupled, unbounded vibro-acoustic problems. In this type of formulation, both the structural thin plate bending problem and the unbounded acoustic problem

are described by means of a coupled wave based model. The validation examples demonstrate the efficiency of this novel approach by comparing the WB results with those obtained by the state-of-the-art technologies based on the finite and boundary element method.

Kurzfassung

Berechnungsmethoden, die auf dem so genannten Trefftz-Verfahren basieren, haben im Verlauf der letzten Jahrzehnte zunehmende Anerkennung erhalten. Der Grund für die Wiederentdeckung dieser Methoden beruht auf der Tatsache, dass die Trefftz-Methoden die exakten Lösungen der Differenzialgleichung als Ansatzfunktionen für die Approximation der Feldgrößen nutzen. Besonders bei der Berechnung von Problemen, deren Lösungen Wellennatur aufweisen, wie zum Beispiel akustische, strukturdynamische oder elektromagnetische Probleme, stellen diese Methoden einen erheblichen Vorteil gegenüber der konventionell, elementebasierenden Methoden, wie die Finite Elemente Methode (FEM) oder die Randelementemethode (BEM), dar.

Die Wave Based Technik (WBT) wurde in den vergangenen Jahren als ein alternatives Verfahren zum Lösen von stationären Problemen der Vibroakustik im so genannten „*Mid-Frequency Gap*" Bereich entwickelt. Die Methode beruht auf dem indirekten Trefftz-Verfahren in dem sie die Vorkenntnisse des zu lösenden Problems umfasst. Zur Approximation der dynamischen Feldgrößen werden dabei die exakten Lösungen der Differenzialgleichung anstatt der einfachen polynomialen Ansatzfunktionen verwendet. Demzufolge erfordert die WBT keine feine Gebietsdiskretisierung mehr, was zu kleineren Berechnungsmodellen und erhöhter Recheneffizienz führt. Es hat sich gezeigt, dass die WBT im Bezug auf akustische Innenraumprobleme, ein robustes und recheneffizientes Tool darstellt. Ein bedeutendes Anwendungsgebiet in der Praxis besteht allerdings in der Analyse von Problemen in unendlichen akustischen Domänen, wie etwa Durchschallung, Schallstreuung und Schallabstrahlung. Außer Methoden, die auf der Integralformulierung der Differenzialgleichung basieren, wie zum Beispiel BEM, wurden unterschiedliche Strategien, in denen die klassische FEM zum Einsatz kommt, zum bewältigen von unendlichen Problemen entwickelt. Infinite Elemente Methode (I-FEM), Perfectly Matched Layers (PML) und Non-Reflecting Boundary Conditions (NRBC) sind die üblichen Ergänzungen der konventionellen FEM zum Lösen von Problemen, die die Analyse der Schallausbreitung in unendlichen Fluiddomänen ermöglichen. Obwohl die obengenannten Ansätze auf unterschiedlichen Konzepten basieren, ist allen drei dieselbe Grundidee gemein – nämlich, dass im Berechnungsmodell eine künstliche Abgrenzung eingeführt wird, welche die unendliche Domäne in ein Innen- und Außengebiet auftrennt. Diese Dissertation befasst sich mit der Anwendung der WBT zum Lösen von dreidimensionalen vibroakustischen Problemen in unendlichen und halbunendlichen Ausbreitungsgebieten.

Bislang wurde in der Formulierung der WBT zum Lösen von gekoppelten, dreidimensionalen, vibroakustischen Problemen in unendlichen Domänen nur die schwache einseitige Kopplungsstrategie eingesetzt. Eine wesentliche Gruppe von Problemenstellungen aus der technischen Praxis besteht allerdings im Lösen von Problemen, in denen die starke Kopplungsinteraktion zwischen Struktur und Fluid einen entscheidenden Einfluss auf das dynamische Verhalten des

Gesamtsystems hat. Im Gegensatz zu den ungekoppelten Strukturdynamik- bzw. Akustik-Problemen ist bei den stark gekoppelten vibroakustichen Systemen die wechselseitige Beeinflussung nicht mehr vernachlässigbar und demzufolge müssen die beide Bestandteile simultan betrachtet werden. Die vorgelegte Doktorarbeit berichtet über die Konzepte und Anwendungen der WBT zum Lösen von dreidimensionalen, vollgekoppelten vibroakustischen Problemen in unendlichen Ausbreitungsgebieten. In dieser Formulierung wird sowohl die Strutkurdynamik einer dünnen Platte als auch die Schallausbreitung in einem unendlichen Fluidgebiet mittels eines vollgekoppelten WBT Modells abgebildet. Die zahlreichen Validierungsbeispiele, die im Rahmen dieser Forschung mit sowohl der WBT als auch den Stand-der-Technik Methoden (FEM/BEM) analysiert wurden, demonstrieren die erhöhte Recheneffizienz von diesem neuartigen Berechnungsverfahren für unterschiedliche Anwendungsgebiete.

Nomenclature

Abbreviations

1D	one-dimensional
2D	two-dimensional
3D	three-dimensional
BC	boundary condition
BE	boundary element
BEM	boundary element method
CAD	computer-aided design
CAE	computer-aided engineering
CPU	central processing unit
dB	decibel
DML	distributed mode loudspeaker
DOF	degree of freedom
FE	finite element
FEM	finite element method
FRF	frequency response function
GP	Gauss point
IC	interface condition
I-FEM	infinite element method
MAC	modal assurance criterion
MLV	multi local velocities
NRBC	non-reflecting boundary conditions
PDE	partial differential equation
PML	perfectly matched layers
RAM	random access memory
RP	response point
SCR	selective catalytic reduction
SEA	statistical energy analysis
SPL	sound pressure level
WB	wave based
WBT	wave based technique
WF	wave function

Arabic symbols

a	edge length of a square	[m]
A	work	[J]
A	wave based system matrix	
a_n^e	structural finite element contribution factor	
b	barometric pressure	[Pa]
b	distributed body force $\{b_x \, b_y\}$	[N/m³]
b	wave based loading vector	
$\tilde{b}$	viscous damping coefficient accounting for viscous interaction forces	
c	speed of sound	[m/s]
c	set of corner points	
C	arbitrary constant	
c_w	set of corner points located at boundary with prescribed displacements $\Gamma_{w\theta} \cup \Gamma_{wM}$	
c_V	set of corner points located at boundary with prescribed generalised shear forces $\Gamma_{mV} \cup \Gamma_{\theta V}$	
C_p	specific heat at constant pressure	[J/K]
C_V	specific heat at constant volume	[J/K]
C$_a$	acoustic FE damping matrix	
C$_s$	structural FE damping matrix	
c̃	arbitrary weighting function	
D	plate bending stiffness	[Nm]
D	characteristic dimension of problem	[m]
D	elasticity matrix	
e	dilatational strain	
e	index of finite element	
E	Young's modulus	[N/m²]
f	frequency	[Hz]
F	point force	[N]
f$_a$	acoustic FE loading vector	
f$_s$	structural FE loading vector	
G	Green's kernel function	
G	transverse shear modulus	[N/m²]
G	matrix of transverse shear moduli	
He	dimensionless Helmholtz number	
$h_l^{(2)}(\bullet)$	spherical Hankel function of the second kind and argument $\bullet$	
h_{max}	maximum element edge size	[m]
$h_{max,a}$	maximum acoustic element edge size	[m]
$h_{max,s}$	maximum structural element edge size	[m]
$\mathrm{H}_0^{(2)}(\bullet)$	zero-order Hankel function of the second kind and argument $\bullet$	
i	index of wave function contribution factor	
i, j ,k	unit vectors in Cartesian coordinate system	
j	imaginary unit $= \sqrt{-1}$	
$j_n(\bullet)$	spherical Bessel function of order n and argument $\bullet$	
$\mathrm{J}_n(\bullet)$	Bessel function of order n and argument $\bullet$	
k	acoustic wave number	[m⁻¹]

k_b	structural bending wave number	$[\text{m}^{-1}]$
k_l	in-plane longitudinal wave number	$[\text{m}^{-1}]$
$k_{r\bullet}, k_{s\bullet}$	structural wave number components	
$k_{r\bullet}, k_{s\bullet}, k_{t\bullet}$	acoustic wave number components	
k_t	in-plane shear wave number	$[\text{m}^{-1}]$
K_b	bulk modulus of skeleton in vacuo	$[\text{Pa}]$
K_s	bulk modulus of the elastic solid the skeleton is made from	$[\text{Pa}]$
$\mathbf{K}_a$	acoustic FE stiffness matrix	
$\mathbf{K}_c$	FE–FE coupling matrix	
$\mathbf{K}_s$	structural FE stiffness matrix	
$\tilde{K}_f$	bulk modulus of fluid in pores	$[\text{Pa}]$
l	degree of spherical harmonics	
L	truncation number for the pressure expansion used in unbounded acoustic domain	
$\mathbf{L}$	strain differential operator	
L_x, L_y	dimensions of structural bounding box	$[\text{m}]$
L_x, L_y, L_z	dimensions of acoustic bounding box	$[\text{m}]$
$\mathbf{L}_c$	FE–BE coupling matrix	
m	order of spherical harmonics $m = \langle -l; l \rangle$	
M	molar mass	$[\text{kg/mol}]$
$\mathbf{M}$	vector of bending moments $\{M_x \, M_y \, M_{xy}\}$	$[\text{N}]$
M_a^{α}	acoustic degrees of freedom per subdomain α	
M_a^{si}	degrees of freedom of acoustic semi-infinite domain	
M_a^{u}	degrees of freedom of acoustic unbounded domain	
M_n	bending moment	$[\text{N}]$
M_{ns}	torsional moment	$[\text{N}]$
M_s^{α}	structural degrees of freedom per subdomain α	
$\mathbf{M}_a$	acoustic FE mass matrix	
$\mathbf{M}_s$	structural FE mass matrix	
n	index of node	
n	normal direction	
n	amount of substance	$[\text{mol}]$
N	number of nodal positions	
N	integer number	
$\mathbf{n}$	normal vector	
$\mathbf{N}$	in-plane stress resultant $\{N_x \, N_y \, N_{xy}\}$	$[\text{N/m}]$
n_a^e	number of acoustic finite elements	
$n_{a,n}$	total number of nodes in acoustic FE model	
$n_{a,n}^e$	number of constituting nodes per acoustic FE	
n_c	number of corner points	
n_{cw}	number of corner points located at boundary with prescribed displacements $\Gamma_{w\theta} \cup \Gamma_{wM}$	
n_{cV}	number of corner points located at boundary with prescribed generalised shear forces $\Gamma_{mV} \cup \Gamma_{\theta V}$	
n_{gp}	number of Gauss points per isoparametric coordinate	
$n_n(\bullet)$	spherical Neumann function of order n and argument $\bullet$	
n_r, n_s	truncation numbers for structural wave function set	
n_r, n_s, n_t	truncation numbers for acoustic wave function set	

n_s^e	number of structural finite elements	
$n_{s,n}$	total number of nodes in structural FE model	
$n_{s,n}^e$	number of constituting nodes per structural FE	
N_a	number of acoustic WB subdomains	
$N_{a,n}$	acoustic global shape function	
$N_{a,n}^e$	acoustic finite element shape function	
$\mathrm{N}_n(\bullet)$	Neumann function of order n and argument $\bullet$	
N_s	number of structural WB subdomains	
N_{si}	number of subdomains	
$N_{s,n}$	structural global shape function	
$N_{s,n}^e$	structural finite element shape function	
N_x, N_y	in-plane longitudinal forces	[N/m]
N_{xy}	in-plane shear force	[N/m]
$\mathbf{N}_a$	vector of acoustic FE shape functions	
$\mathbf{N}_s$	vector of structural FE shape functions	
p	pressure	[Pa]
P	complex sound pressure magnitude	[Pa]
$\mathbf{p}$	vector of nodal acoustic pressure	
$\mathbf{p}$	vector of acoustic wave function contribution factors	
p_i	pressure contribution factor	[Pa]
p_n	acoustic FE contribution function	
p_n^e	acoustic finite element contribution factor	
p_{sc}	scattered acoustic wave	[Pa]
p_I	incoming acoustic wave	[Pa]
$\mathrm{P}_n(\bullet)$	Legendre polynomial of order n and argument $\bullet$	
$\mathrm{P}_l^m(\bullet)$	associated Legendre polynomial of argument $\bullet$	
$\hat{p}_q(\mathbf{r})$	particular pressure solution function	[Pa]
q	strength amplitude of acoustic volume velocity point source	
	per unit volume	[s^{-1}]
Q	heat	[J]
$\mathbf{Q}$	transverse shear forces $\{Q_x\,Q_y\}$	[N/m]
Q_n	shear force	[N/m]
$\tilde{Q}$	potential coupling coefficient between the dilatation and	
	stress of the two phases	[Pa]
r, s	subsets of structural wave function set	
r, s, t	subsets of acoustic wave function set	
r, φ, ϑ	radial, azimuthal and zenithal spherical coordinates	[m],[rad],[rad]
R	radius	[m]
R	universal gas constant (8.3144621)	[J mol^{-1}K^{-1}]
$R_\bullet$	residual error associated with quantity $\bullet$	
$\mathbf{r}$	position vector	[m]
$\mathbf{r}_q$	position vector of a point source	[m]
$\mathbf{r}_F$	position vector of a point force	[m]
$\hat{\mathbf{r}}, \hat{\boldsymbol{\varphi}}, \hat{\boldsymbol{\vartheta}}$	unit vectors in spherical coordinate system	
$\tilde{R}$	bulk modulus of fluid occupying a fraction ϕ of a unit volume	
	of aggregate	[Pa]
S	surface	[m^2]
$\mathbf{s}$	tangential vector	

t	plate thickness	[m]
t	time	[s]
T	truncation parameter	
$\mathbf{T}$	FE–BE transformation matrix	
T_a	truncation parameter for bounded acoustic wave function set	
T_s	truncation parameter for structural wave function set	
T_u	truncation parameter for unbounded acoustic wave function set	
U	internal energy of a system	[J]
$\mathbf{u}_f$	displacement of the intersticial fluid	[m]
$\mathbf{u}_s$	displacement of skeleton	[m]
V	volume	[m^3]
$\mathbf{v}$	velocity vector $\{v_x\, v_y\, v_z\}$	[m/s]
v_n	normal velocity	[m/s]
V_n	generalised shear force	[N/m]
w	out-of-plane bending displacement	[m]
$\mathbf{w}$	vector of structural FE translational and rotational DOF	
$\mathbf{w}$	vector of translational displacements $\{w_x\, w_y\, w_z\}$	[m]
$\mathbf{w}$	vector of structural wave function contribution factors	
w_i	out-of-plane displacement contribution factor	[m]
w_n	structural FE contribution function	
$\hat{w}_F(\mathbf{r})$	particular displacement solution function	[m]
x, y, z	Cartesian coordinates	[m]
$\mathrm{Y}_l^m(\bullet)$	spherical harmonics of degree l, order m and argument $\bullet$	
Z	normal impedance	[kg m^{-2}s^{-1}]
$\bar{Z}_{int}$	the impedance coupling factor	[kg m^{-2}s^{-1}]

Greek symbols

α	internal angle	[rad]
α	ID of a corresponding WB subdomain	
γ	shear strain angles	[rad]
$\boldsymbol{\gamma}$	vector of transverse shear strains $\{\gamma_{xz}\, \gamma_{yz}\}$	
Γ	boundary of domain Ω	
Γ_a	physical boundary of acoustic domain	
Γ_i	interface between two WB subdomains	
Γ_s	physical boundary of structural domain	
Γ_{sa}	structural-acoustic interface	
Γ_p	acoustic boundary with prescribed pressure boundary condition	
Γ_v	acoustic boundary with prescribed normal velocity boundary condition	
$\Gamma_{w\theta}$	structural boundary with prescribed kinematic boundary conditions	
Γ_{wM}	structural boundary with prescribed mixed boundary conditions of type 1	
Γ_{MV}	structural boundary with prescribed mechanical boundary conditions	
Γ_T	truncation boundary dividing infinite domain into bounded and unbounded parts	
Γ_Z	acoustic boundary with prescribed normal impedance boundary condition	
$\Gamma_{\theta V}$	structural boundary with prescribed mixed boundary conditions of type 2	

Γ_∞	acoustic boundary at the infinity, where the Sommerfeld radiation condition is applied	
δ	phase angle	[rad]
δ	Dirac delta function	2D: $[\mathrm{m}^{-2}]$
		3D: $[\mathrm{m}^{-3}]$
Δf	frequency step	[Hz]
ε	relative prediction error	
$\boldsymbol{\varepsilon}$	strain vector $\{\varepsilon_x\,\varepsilon_y\,\varepsilon_{xy}\}$	
ζ	argument of (spherical) Bessel/Neumann function	
η	material loss factor	
η	argument of Legendre polynomial	
Θ	thermodynamic temperature	[K]
$\boldsymbol{\theta}$	vector of rotations $\{\theta_x\,\theta_y\}$	[rad]
θ_n	normal rotation	[rad]
θ_s	tangential rotation	[rad]
κ	shear correction coefficient	
κ	adiabatic index	
μ	double layer potential	
ν	Poisson's ratio	
ξ	distance	[m]
$\boldsymbol{\xi}$	position vector	[m]
ρ	mass density	$[\mathrm{kg/m}^3]$
ρ_{11}	mass coefficient of solid $\rho_{11} = (1-\phi)\rho_s - \rho_{12}$	$[\mathrm{kg/m}^3]$
ρ_{12}	coefficient for the interaction between the inertia forces of the solid and fluid phases	$[\mathrm{kg/m}^3]$
ρ_{22}	mass coefficient of fluid $\rho_{22} = \phi\rho_f - \rho_{12}$	$[\mathrm{kg/m}^3]$
ρ_a	ambient fluid density	$[\mathrm{kg/m}^3]$
ρ_s	structural density	$[\mathrm{kg/m}^3]$
ρ_f	mass density of the interstitial fluid	$[\mathrm{kg/m}^3]$
ρ_s	mass density of the solid the skeleton is made from	$[\mathrm{kg/m}^3]$
$\rho\mathbf{v}$	mass flux	$[\mathrm{kg\,m^{-2}s^{-1}}]$
$\tilde{\rho}_{11}, \tilde{\rho}_{22}, \tilde{\rho}_{12}$	effective densities	$[\mathrm{kg/m}^3]$
ϱ	distance in radial direction	[m]
σ	single layer potential	
$\boldsymbol{\sigma}$	vector of stresses $\{\sigma_x, \sigma_y\,\tau_{xy}\}$	$[\mathrm{N/m}^2]$
$\hat{\boldsymbol{\sigma}}_s$	stress of the skeleton in vacuo	$[\mathrm{N/m}^2]$
ϕ	polar angle	[rad]
ϕ	irrotational potential	$[\mathrm{m}^2]$
ϕ	porosity	
Φ	acoustic wave function	
$\boldsymbol{\Phi}$	vector of acoustic wave functions	
$\boldsymbol{\chi}$	vector of bending curvatures $\{\chi_x\,\chi_y\,\chi_{xy}\}$	$[\mathrm{m}^{-1}]$
ψ	solenoidal potential	$[\mathrm{m}^2]$
Ψ	structural wave function	
$\boldsymbol{\Psi}$	vector of structural wave functions	
ω	circular frequency	[rad/s]
Ω	rotational strain	
Ω	domain	

Ω_a	acoustic domain
Ω_a^e	acoustic finite element
Ω_b	bounded acoustic domain
Ω_u	unbounded acoustic domain
Ω_p	poroelastic domain
Ω_s	structural domain
Ω_s^e	structural finite element
Ω_{si}	semi-infinite acoustic domain

Miscellaneous symbols

$\mathbf{a}$	vector
$\mathbf{A}$	matrix
$\bullet^b$	out-of-plane bending quantity
$\bullet^b$	quantity related to bounded spatial domain
$\bullet^m$	in-plane membrane quantity
$\bullet^u$	quantity related to unbounded spatial domain
$\bullet^{si}$	quantity related to semi-infinite spatial domain
$\bullet^\alpha$	quantity related to WB subdomain α
$\hat{\bullet}$	approximation of $\bullet$
$\tilde{\bullet}$	weighting function
$\tilde{\bullet}$	complex and frequency-dependent quantity
$\bar{\bullet}$	predefined value of $\bullet$
$\bullet'$	quantity related to structural part of coupled vibro-acoustic problem
$\bullet'$	perturbation of $\bullet$
$\bullet_0$	ambient value of $\bullet$
$\bullet^{\mathsf{T}}$	transpose operator
$\lvert \bullet \rvert$	absolute value of $\bullet$
$\lVert \bullet \rVert$	norm of $\bullet$
$[\![\bullet]\!]$	jump operator
$\lceil \bullet \rceil$	ceiling function applied on $\bullet$
$\mathrm{d}\bullet$	total (exact) differential of $\bullet$
$\delta\bullet$	inexact differential of $\bullet$
$\partial\bullet$	partial derivative of $\bullet$
$\dfrac{\partial}{\partial n}\bullet$	normal derivative of $\bullet$
$\partial\Omega$	boundary of domain Ω
$\nabla\bullet$	gradient operator applied on $\bullet$
$\nabla^2\bullet$	Laplace operator applied on $\bullet$
$\nabla \cdot \bullet$	divergence operator applied on $\bullet$
$\nabla \times \bullet$	curl operator applied on $\bullet$
$\Re\{\bullet\}$	real part of $\bullet$
$\Im\{\bullet\}$	imaginary part of $\bullet$
$\mathcal{L}_\bullet$	differential operator
$\mathcal{L}_\theta(\bullet)$	normal rotation differential operator applied on $\bullet$

$\mathcal{L}_M(\bullet)$	bending moment differential operator applied on $\bullet$
$\mathcal{L}_{Ms}(\bullet)$	torsional moment differential operator applied on $\bullet$
$\mathcal{L}_Q(\bullet)$	shear force differential operator applied on $\bullet$
$\mathcal{L}_v(\bullet)$	normal velocity differential operator applied on $\bullet$
$\mathcal{L}_V(\bullet)$	generalised shear force differential operator applied on $\bullet$
$\mathcal{L}_Z(\bullet)$	normal impedance differential operator applied on $\bullet$
$\max\{\bullet\}$	maximum of $\bullet$
$\mathbb{Z}$	set of integers
∞	infinity
$\emptyset$	empty set

Table of contents

Part I

INTRODUCTION AND STATE-OF-THE-ART

Chapter 1

Introduction

*"Noise consists of all unwanted sound – sound that is loud, unpleasant or unex-
pected. It has been increasing in urban areas to the point where it has become a
matter of public concern. According to one estimate, around 20 % of the popula-
tion of Western Europe (some 80 million people) suffer from noise levels that experts
consider unacceptable. This noise is caused by traffic, industrial and recreational
activities."* [1]

The above-mentioned passage, excerpted from the *European Commission's Green Paper of 4
November 1996 on Future Noise Policy*, clearly states the importance of noise as an environ-
mental factor in the globalised world. Many Europeans consider environmental noise caused
by traffic, industrial and recreational activities as their main local environmental problem, es-
pecially in urban areas. Exposure to high noise levels has been proven to contribute to the
development of hearing impairment, insomnia and various health disorders related to the car-
diovascular system (e.g. high blood pressure). The increasing number of complaints from
the public about noise is evidence of the growing concern of citizens (European Commission,
1996). The latest publication of the World Health Organization (WHO) and the Joint Research
Centre of the Commission even shows that at least one million healthy life years are lost every
year from traffic-related noise in the western part of Europe (World Health Organization, 2011).

The European Community measures for addressing environmental noise problems have been in
existence for over three decades and have essentially consisted of legislation that sets maximum
sound levels for individual sectors, such as vehicles, aeroplanes and machines. As such, they
have not been conceived as part of an overall environmental noise reduction programme. The
Member States have enacted a multitude of supplementary regulations and other measures aim-
ing to reduce environmental noise problems, and although there is some evidence to show that
noise levels in the noisiest areas ("blackspots") have been reduced, recent data show that the
overall noise problem is worsening, and the numbers of people living in so-called "grey areas"
has increased. In particular, the continuing growth in traffic volume in all modes coupled with
suburban development have caused high levels of noise exposure to be spread ever wider over
both space and time and are part of the reason for this general worsening of the noise problem.
In addition, over the past two decades, leisure activities and tourism have created new spots and
new sources of noise. As a result of these developments, the impacts of the policy measures
implemented to date to address the noise problem are being offset.

---

[1]/* COM/96/540 FINAL */.

Generally, action by the European Community and the Member States on environmental noise has had a lower priority than those actions taken to solve other pollution problems (e.g. air and water pollution), despite the fact that opinion polls show that noise is considered one of the main causes of declining quality of life. Some of the reasons may be that decision makers are not aware of the problems or are unfamiliar with the effects of noise, which are subtle: noise is insidious, not catastrophic. As far as the European Community is concerned, the lower priority accorded to noise has in part been due to the fact that noise is very much a local problem with very diverse perceptions in different parts of the European Community as to the acceptability of the problem. However, the sources of many of the causes of environmental noise are not of local origin. In addition, despite the local dimension to environmental noise problems, there is a general international consensus on the levels of unacceptable noise to which the public should not be exposed in order to protect health and quality of life.

In this context, the EU noise expert group recently presented an updated Strategy Paper for future research to reduce environmental noise in Europe (CALM network, 2004). The expert group concludes that research is a key element in reducing the effects of high sound levels. Research should cover aspects such as the assessment of noise exposure and perception, the health impacts of exposure to noise, noise abatement (including cost-benefit aspects), new technologies and system approaches for improved noise control at the source, and the further development of legislative standards.

1.1 CAE in the product design process

Driven by both increasingly restrictive legal regulations and growing customers expectations, the functional performance and quality of the product have gained significant importance over the last decades. At the same time, the product development phase and costs have been reduced in order to comply with the competitive nature of market. Companies must develop innovative designs and bring them to market before their competitor. Better products must be launched on a shorter time frame and at lower cost. Physical prototype phases must be reduced, and product decisions must be taken earlier in the design process (Donders, 2008). To cope with these often conflicting design targets, computer-aided engineering (CAE) tools have become an essential part of the product design process. The extensive development of information technology in the second half of the 20th century has made it possible to embed the CAE tools in the early stage of a product development cycle and establish them as an inherent part of it.

The first main breakthrough was achieved by the massive development of the finite element schemes for structural analysis in the early 1950s (Clough and Wilson, 1999). The majority of the research conducted was motivated by the need to solve practical problems in the aerospace engineering. The pioneering work of Turner et al. (1956) conducted at *Boeing* is generally accepted to be the first practical application of the finite element method ever (Zienkiewicz et al., 2005). By employing the finite element method to a structural analysis of a swept wing, the designers obtained new insight into its functional performance, which led to a detailed design of lightweight supersonic aircraft structures.

Despite this, the crucial factor that boosted the spread of the CAE even further was the space race between the great powers during the Cold War. Inspired by President Kennedy's ambitious and challenging plan formulated in the early 1960s[2] to land a man on the Moon and return

---

[2]A part of J.F.K's memorable speech addressed to a joint session of Congress on May 25th , 1961.

(a)

(b)

(c)

(d)
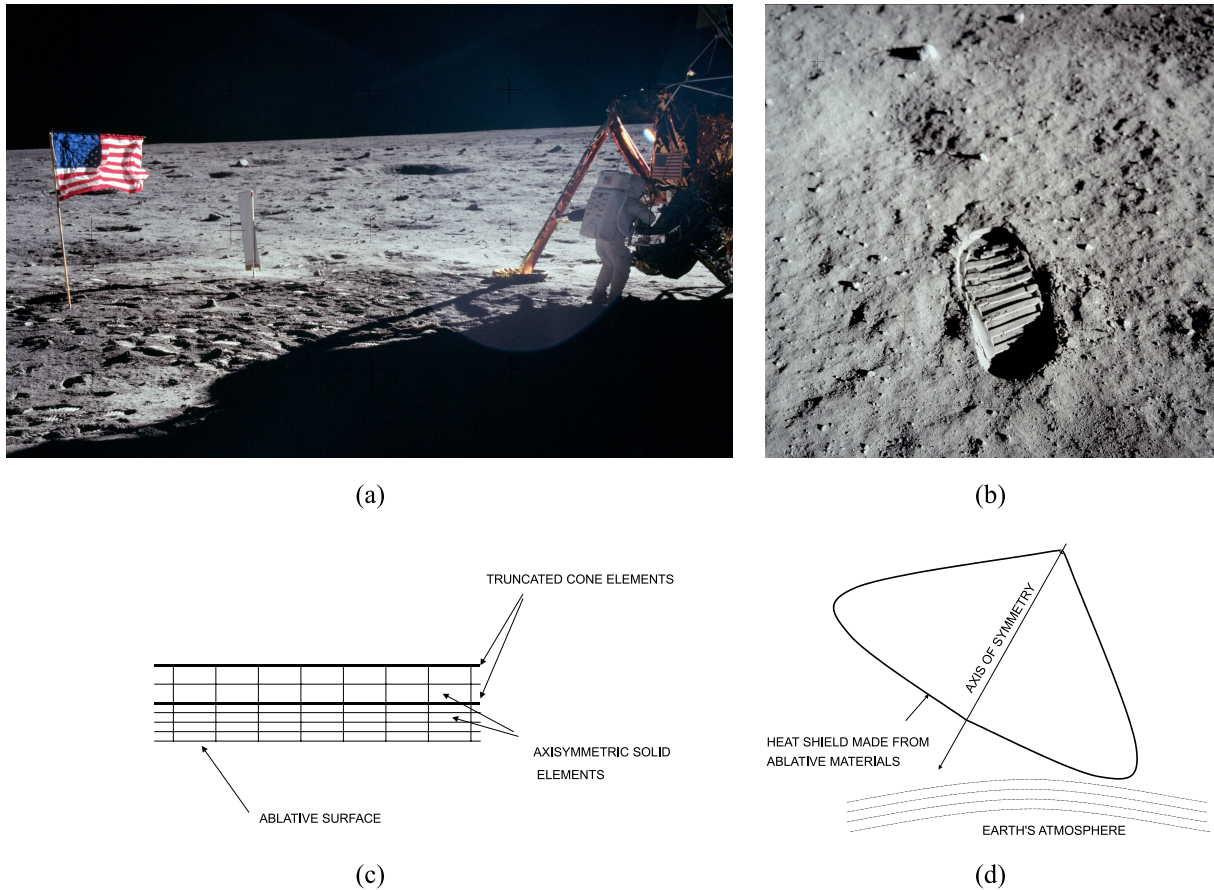
Figure 1.1: History was written – an unprecedented landmark in the history of mankind and still one of the most outstanding technical achievements the man has ever made: (a) "Houston, Tranquility Base here. The Eagle has landed." – July 20th, 1969, (b) "That's one small step for a man, one giant leap for mankind." – figuratively as well, thanks to the emerging CAE technologies – (c) the finite element model of the (d) Apollo Command Module heat shield developed by *AEROJET* and utilised in the early design stage of the Apollo programme (images courtesy of *NASA* and *AEROJET*)

him safely to the Earth before the decade was out, *NASA*[3] realised that a large-scale FE program was the missing technology link for designing spacecraft for lunar exploration. In the early days, every aerospace company was separately developing its own proprietary FE code. The 1964 annual review of *NASA's* structural dynamics research program revealed that those software packages did not fit NASA's requirements and recommended that a single generic software program should be used instead. In response, a committee was formed which established a cooperative project to develop this software and created a specification that outlined its capabilities. A contract was awarded to *Computer Sciences Corporation (CSC)* to develop the software named *NASTRAN* (acronym formed from NAsa STRuctural ANalysis). Parallel to this, NASA awarded several subcontracts for the development of the Apollo manned moon landing mission to a number of aerospace companies during the 1960s. In particular, the design of an ablative heat shield for the Apollo Command Module (CM) during re-entry to the Earth's atmosphere was based on a thermal stress analysis carried out by *Aerojet*, see figure 1.1(c). After years of extensive development *NASTRAN* was released to NASA in 1968, and in the late

---

[3]National Aeronautics and Space Administration.

1960s, the *MacNeal-Schwendler Corporation (MSC)*, one of the principal and original developers, started to market and support its own version of *NASTRAN*. Stimulated by the great success of *NASA* after Neil Armstrong and Buzz Aldrin imprinted their footsteps in the Mare Tranquillitatis, other industries, including the automotive, chemical, electronics and civil engineering industries, quickly recognised the huge potential of this novel engineering discipline, and there was nothing that would obstruct its further expansion. Besides *NASTRAN*, other large FE-based packages, such as *ANSYS* and *ABAQUS*, became commercial products and claimed their share of the market. During a relatively short period of time, the initial finite element scheme originally developed for structural analysis was further adapted to solve both linear and nonlinear problems, such as heat transfer, fluid dynamics and electromagnetic problems. These include new explicit formulations for tackling highly non-linear effects, such as the large elastic-plastic deformations that occur during a crash event.

The second major catalyst which enabled a seamless integration of the CAE technology into a product design process has been the immense progress in the field of high-performance computing over the last 60 years. In 1965, Gordon Moore, co-founder of *Intel*, made a statement which today is interpreted to mean that any computer-performance-related quantity (e.g. number of transistors on a chip, computing power, number of finite elements in a model), doubles every 18 (optimistic guess) to 24 months (pessimistic guess) at about the same cost, see figure 1.2.

Figure 1.2: Moore's law (baseline image courtesy of W. G. Simon)

How does this "law" apply to a real-life industrial problem? To prove his prophesy, the "biggest ever" jobs at different dates have been examined. As crash analysis is broadly accepted to be the pioneering area of an early employment of computer-aided engineering tools, the example of a passenger car crash simulation is taken. The frontal crash simulation of a *Volkswagen Polo* performed in 1986 on a *CRAY1* supercomputer using the *PAM-CRASH* simulation package, see figure 1.3, is generally recognised as the first full-scale crash simulation of a passenger car ever (Haug et al., 1986). The finite element model consisted of 5 555 thin shells, and the run went over about 40 000 time steps of 1.5 microseconds for a crash event duration of 60 milliseconds in about 4 CPU hours. In 2004, 18 years after the *Polo* simulation, "The biggest *PAM-CRASH* job at that time" was presented at the *EUROPAM 2004* Conference. The *NEON-04 US-NCAP* car-to-car offset frontal crash event utilised a computational model consisting of more than 9 million thin shell finite elements, i.e. an equivalent of about 1620 *Polos*. The 300 000 time steps of the whole crash event took 16 hours and 12 minutes wall clock time to be performed on 128 *Itanium* 1.5 GHz *HP-UX* CPUs at the HP Böblingen RX2600 *InfiniBand* cluster (Haug, 1981, 2005). Nevertheless, it has to be noted that it is not only the steadily growing computational power, which allows faster and more efficient computation. Including some a priori knowledge about the solved problem into the numerical scheme may also result in high computational efficiency, while the convergence rate can be substantially increased.
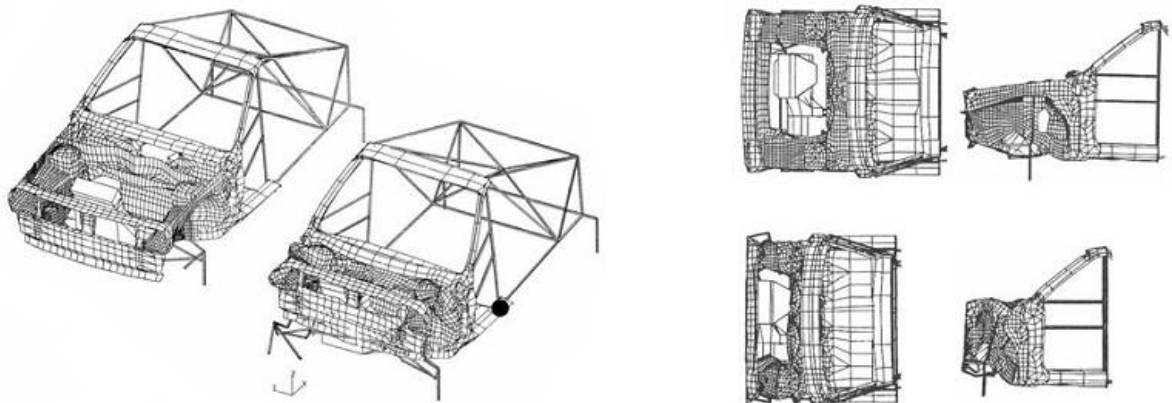
Figure 1.3: The first full-scale frontal car crash simulation performed in 1986: a *Volkswagen Polo* collided with a rigid concrete barrier at 50 km/h (Haug et al., 1986), (images courtesy of *Volkswagen Group*)

Probably no other industries have incorporated more extensive application of CAE tools than aerospace and automotive in the past 30 years. In order to accelerate time-to-market while coping with legal limits that have become increasingly restrictive over the last decades, CAE has become an indispensable tool covering all major fields in a modern aerospace/automotive product design process. Crashworthiness, occupant safety, aerodynamics, NVH[4] and electromagnetic compatibility are the main fields that are nowadays seamlessly integrated into the product design process by utilising virtual prototyping techniques, see figure 1.4. Moreover, the overall trend in the automotive industry is currently moving towards the use of lightweight designs and downsizing measures to meet demands to reduce both fuel consumption and exhaust emissions. Modern vehicle bodies have to be lightweight yet stiff enough to comply with the requirements for both crashworthiness and NVH performance. The large V engines needs

---

[4]Noise, vibration and harshness.

to be downsized to more compact four-cylinder inline engines, which are often supplemented with an exhaust turbo charger, in order to achieve high fuel efficiency, while keeping the NVH comfort attributes customers expect to get for their money. Thus, CAE analysts are often facing even more demanding challenges to allow for a system-level analysis and synthesis of different, often conflicting design targets.

| (a) | (b) |
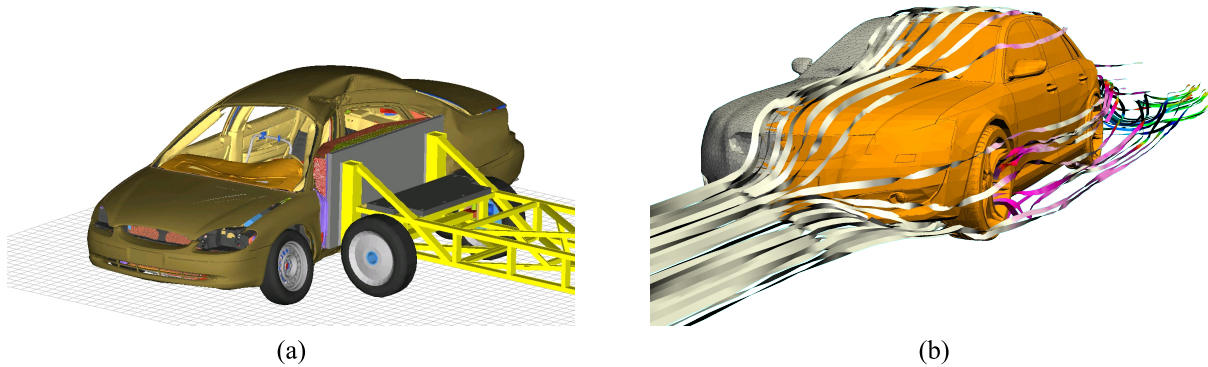
Figure 1.4: Utilisation of CAE in the early design stage of a modern vehicle: (a) side impact assessment in accordance with the *Euro NCAP* standard – mobile deformable barrier impacts the driver's door at 50 km/h, (b) CFD analysis of exterior aerodynamics – streamlines visualise the air flow around the passenger car cruising at 50 km/h (images courtesy of *ViF*)

1.2 State-of-the-art in numerical vibro-acoustic modelling

In an ideal case, there would be one generic modelling tool used in numerical vibro-acoustics that would be able to cover the whole frequency range of interest that is usually considered within the audible frequency range spanning from approximately 16 Hz up to 20 kHz. However, due to the multi-scale nature of vibro-acoustics, different prediction techniques have to be used in the specific frequency regions instead (Lalor and Priebsch, 2007). In this dissertation, the terms *"low/high-frequency"* will refer to regions of low/high frequencies and/or small/large characteristic dimensions of the problem. In the literature, however, a rather misleading definition is often used, which considers the frequency only. As vibro-acoustics relates the spatial and temporal (frequency) scales to each other, both scales must be considered when speaking of the (vibro-acoustic) complexity of the problem. Hence, a dimensionless Helmholtz number $\mathrm{He} = kD$ [-] that relates both the frequency and characteristic dimension provides a more adequate estimate for the vibro-acoustic complexity of the solved problem. A classic example is an airliner being analysed at 50 Hz. Imagine an *A380* having a wingspan of some 80 m – huge dimensions that are big enough to become a high-frequency problem even at 50 Hz. An ultrasonic transducer submerged in water and radiating sound at 40 kHz, on the other hand, can be treated as a low-frequency problem, namely due to its tiny dimensions (i.e. typically on the order of centimeters), which become comparable with the acoustic wavelength.

In the low frequency range, the steady-state dynamic behaviour of a system is predominantly driven by its modal properties. The dynamic behaviour is robust for small perturbations in the material and geometrical properties (Van Hal, 2004). Deterministic element-based techniques, such as finite element method (FEM) (Zienkiewicz et al., 2005; Harari, 2006; Thompson, 2006)

Deterministic techniques
→ element-based methods
→ simple polynomial shape functions
→ fine discretisation

no efficient tool available

Statistical techniques
→ energy-based methods
→ high modal overlap
→ spatially averaged results

MIND THE GAP

WBT

FEM/BEM   gap   SEA

"low-frequency problems"   *"high-frequency problems"*

1   10   100 $\log(kD)$
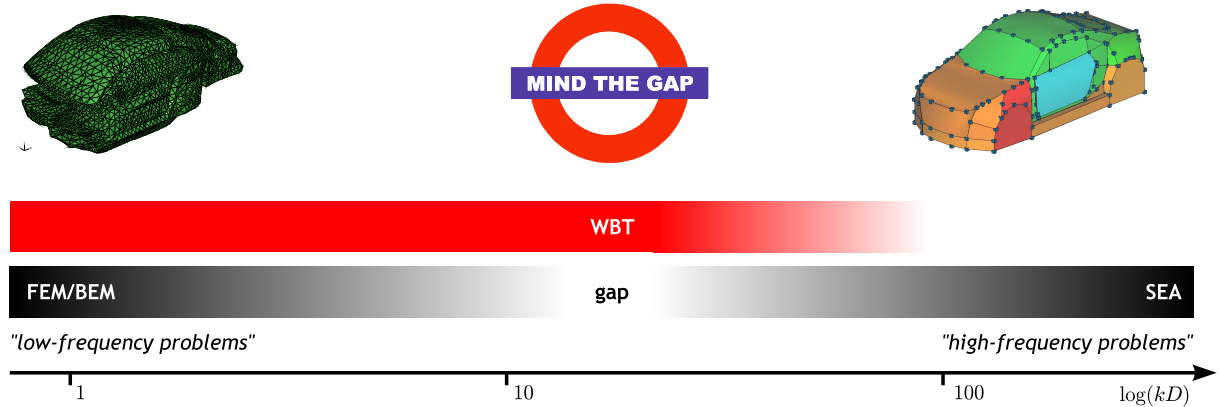
Figure 1.5: The "mid-frequency gap" (Rejlek, 2008)

and boundary element method (BEM) (Juhl, 1993; Greengard and Rokhlin, 1987; Kirkup, 1998; Von Estorff, 2000; Fischer et al., 2004) are well established in this region and present an adequate tool for predicting the vibro-acoustic characteristics of the problem being solved. As these methods require either the solution domain or its boundary to be discretised into a large number of small elements, they provide spatially and frequency resolved results. Within these elements, the dynamic response variables are described in terms of simple, polynomial shape functions. However, as the frequency increases, the wave length becomes shorter, which implies that the computational mesh has to be refined in order to maintain the prediction accuracy. At a certain frequency, the size of the corresponding element-based model increases rapidly, which leads to prohibitive computational costs (Babuška et al., 1995; Marburg, 2002). As a result, the practical use of the element-based methods is essentially restricted to low-frequency applications.

At higher frequencies, the modal overlap increases so that the individual modes can no longer be distinguished. The dynamic behaviour of a system becomes more sensitive for small perturbations in the material and geometrical properties, which means that the description in terms of modal characteristics becomes less appropriate. Instead of using discrete, locally defined dynamic quantities, it is more suitable to consider spatially and frequency averaged variables and so statistical approaches come to the fore. Statistical energy analysis (SEA) (Lyon and DeJong, 1995; Shorter and Langley, 2005) is a classic method used for the analysis of high-frequency problems. The whole system is subdivided into a number of large subsystems, each of which contain a sufficient number of modes to ensure that statistical assumptions are correctly accounted for. The dynamic behaviour of a vibro-acoustic problem is then represented as energy flow between the interconnected subsystems. In order to comply with the vital requirement that SEA must have a sufficient number of modes accumulated within each subsystem, both the frequency and characteristic dimension have to be correspondingly high. As the size of the problem is given, there is, however, an inherent frequency limit below which the modal density becomes too low for the statistical assumptions to be still valid. Violating this essential principle of SEA implies that the prediction is no longer reliable, which automatically restricts the application of statistical methods for the high-frequency range only.

For specific applications, a twilight zone may still exist between the range of low- and high-frequency techniques – the so-called *"mid-frequency gap"*, where no robust and efficient CAE tool is currently available, see figure 1.5. The range of the mid-frequency gap is indeed problem-dependent, but speaking in terms of automotive applications, it typically spans from about 200 Hz up to several kilohertz (Van Hal, 2004). Unfortunately, this corresponds exactly to the range of the highest sensitivity of human perception to noise, which is typically located around 3 kilohertz, and this puts even more emphasis on the need to bridge or at least narrow this transition region. Recently, a vast amount of effort has been spent to develop alternative mid-frequency techniques that aim to relax the mid-frequency gap. In general, three main research approaches can be recognised:

- extending the computational limitation of deterministic techniques towards higher frequencies

- shifting the range of validity of statistical methods towards lower frequencies

- utilising hybrid schemes that combine "the best of both worlds", namely the deterministic and statistical methods.

Chapter 3 provides an overview of the state-of-the-use deterministic modelling techniques commonly applied in computational vibro-acoustics. The wave based technique (Pluymers et al., 2007) upon which this dissertation focuses on, falls into the first class of methods. The basic principles of this novel methodology are outlined in section 1.3.

1.3   Wave Based Technique

Desmet (1998) has proposed an alternative computational scheme for tackling steady-state vibro-acoustic problems. The wave based technique (WBT) adopts an indirect Trefftz approach (Trefftz, 1926), in which it incorporates the a priori knowledge of the solved problem. The key feature of WBT is the approximation of the dynamic field variables. Instead of using simple polynomial basis functions, which are commonly applied in the concepts of finite or boundary element method, the WBT expresses the field variables in terms of globally defined basis functions. These are the exact solutions of the homogeneous governing differential equation, which represent the propagating and evanescent plane waves. As a result, fine element discretisation is no longer needed, which yields smaller numerical models that exhibit an enhanced computational efficiency.

1.3.1   Characteristic properties of WBT

($+$) **Model size** – As the underlying physics of the problem is fully incorporated into the approximation functions of the method, only a small number of subdomains is needed for the spatial subdivision of the problem to meet the accuracy requirements. This yields a substantial reduction of the number of degrees of freedom.

($+$) **Computational efficiency** – Due to the smaller size of WB models, the solution of the system of equations can be performed very efficiently. This is even more pronounced for problems of moderate complexity. Moreover, the WBT exhibits a higher convergence

rate compared to conventional deterministic schemes, which allows the problems to be tackled up to higher frequencies.

$(+)$ **Accuracy of derived variables** – Due to the inherent nature of the approximation functions used, which are the exact solutions of the governing differential equation, the WB solution scheme does not induce numerical pollution errors. Moreover, the derived field variables, such as the particle velocity or stress, can be derived without any additional loss in accuracy.

$(+)$ **Model refinement** – In contrast to element-based methods, the refinement of a wave model relies on increasing the order of the approximation functions (p-refinement scheme) rather than refining its spatial discretisation (h-refinement scheme). This can be done in a very straightforward way, which also allows the adaptive solution scheme (increasing the order of functions over frequency) to be adopted.

(0) **System matrix properties** – The WBT yields fully populated matrices with complex, frequency-dependent coefficients. As with any other Trefftz-based method, the WBT system matrices suffer from ill-conditioning. The resulting system of equations is typically much smaller than that of FEM or BEM. Moreover, due to the inherent complex and frequency-dependent nature of the matrices, inclusion of damping or poroelastic materials does not jeopardise the performance of WBT.

$(-)$ **Geometrical flexibility** – The favourable size of the wave models also implies the main drawback of this methodology, which is its limited ability to tackle problems involving geometrically complex boundaries. To analyse such problems, the corresponding WB models would become prohibitively large, which would result into a decrease of the computational efficiency. Since the WB formulation is only admissible for problems for which an analytical solution of the governing differential equation is available, the application of this method is further restricted to the analysis of flat plates.

$(-)$ **Construction of the system matrices** – The assembly of the WB system matrices involves numerical integration. The frequency-dependent integrands, however, exhibit a highly oscillatory behaviour, which may also become very spatially localised. In addition, due to the global nature of the solution expansion, these integrals need to be evaluated over large boundaries. Given the inherently poor conditioning of the WBT system matrix, special care must be taken during the numerical integration in order to calculate the matrix coefficients with sufficient accuracy.

1.3.2 Development status of WBT

Over the past years, the WBT has evolved into an efficient prediction tool for tackling coupled and uncoupled vibro-acoustic problems. Desmet (1998) provided a theoretical basis for the WBT and proved the ability of this new approach to provide reliable predictions in the mid-frequency range. He proposed the formulations for interior acoustics, thin plate bending problems and coupled, interior vibro-acoustic problems and demonstrated the convergence of WBT when selecting complete sets of functions. In his work, Desmet also proposed a WB solution scheme for tackling poroelastic materials based on Biot equations, see section 2.6, which was further developed by Lanoye (2007) and Deckers et al. (2010).

The work of Desmet was further extended by Van Hal (2004), who incorporated new multi-physical coupling effects and laid down the fundamental principles for a hybrid finite element – wave based coupling approach. Van Hal's early developments in 2D were in turn extended towards three-dimensional problems by Pluymers (2006) and Silar (2007). Pluymers also proposed the first implementation of WBT for the analysis of two-dimensional unbounded and semi-infinite acoustic problems, which was then extended into 3D by Jegorovs (2007) and Diwoky et al. (2008).

Vanmaele (2007) further extended Desmet's original WBT formulation for structural problems by applying the WBT to membrane problems and the structural analysis of flat plate assemblies. In her work, she also extended the hybrid FE–WB scheme to structural problems and investigated the inclusion of suitable enrichment functions to improve the convergence when solving problems that have a singularity in the solution field.

Hepberger et al. (2004) showed how to weakly couple a structural finite element model with an acoustic wave based counterpart in a very efficient way by adopting a geometrical mapping strategy. Van Genechten (2010) then proposed a direct hybrid finite element – wave based modelling technique for coupled vibro-acoustic analysis. He further extended this framework by applying a modal reduction technique for the FE part, which was later applied to the hybrid FE–WB approach for 3D acoustics developed by Pluymers and Silar. Bergen (2011) proposed a multi-level WBT framework, which allows an efficient solution of complex multiple-scatterer problems. Recently, Vergote et al. (2011) demonstrated how to couple WBT and SEA in a hybrid deterministic-statistical approach for a mid-frequency analysis of vibro-acoustic systems.

Figure 1.6 shows the historical overview of WBT development in the context of existing finite element schemes. It also shows the contributions and achievements of this doctoral research to the further development of this methodology, which are discussed in more detail in sections 1.4 and 1.6.
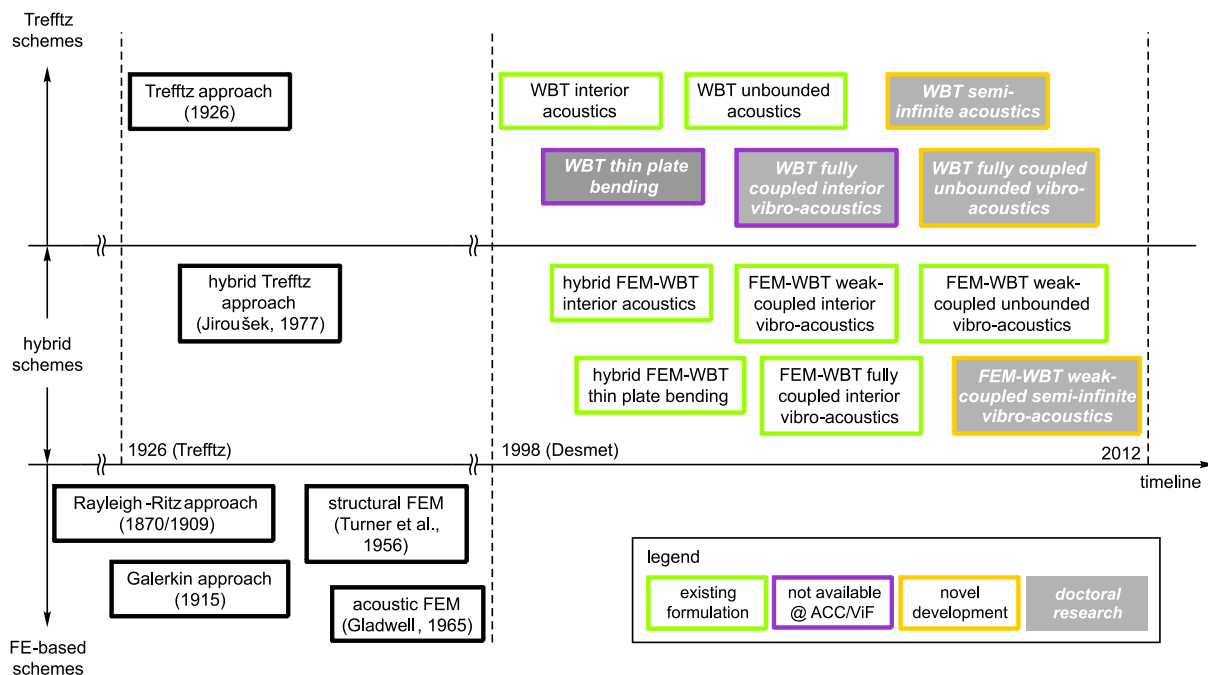
Figure 1.6: The WBT development road map – a historical overview: development status at the start of the presented doctoral research project and the main contributions of this dissertation to the further extension of WBT towards coupled, unbounded vibro-acoustics

In the course of more than ten years of collaboration between ACC/ViF and KU Leuven in the field of WBT, both institutions have actively participated in consortiums of several EU projects focused on mid-frequency wave based modelling, of which three have been coordinated by either ACC/ViF (SIMVIA2, GRESIMO[5]) or KU Leuven (MID-FREQUENCY[6]). Although the WBT has proven to be computationally more efficient than the conventional deterministic schemes, two aspects need to be further investigated in order for the methodology to become a generally applicable CAE tool for mid-frequency modelling. These two aspects, which comprise the main objectives of this doctoral research project, are introduced in section 1.4.

1.4   Research project objectives

A broad class of engineering vibro-acoustic problems involves the mutual coupling interaction between the structure and fluid. In this type of problem, the back-coupling effects are no longer negligible, and the problem has to be considered as a fully coupled system. The conventional state-of-the-art techniques adopt the element-based schemes, such as the finite (FEM) (Zienkiewicz et al., 2005) and boundary element methods (BEM) (Von Estorff, 2000). The inherent non-symmetric nature of a coupled system, however, compromises the computational efficiency of the uncoupled sparse solvers, mainly due to the high bandwidth of the system matrices. As a result, the practical applicability of these methods is restricted to a limited frequency range. The application of these techniques above the problem-specific frequency limit yields prohibitively large numerical models, which involve a huge amount of computational resources and are thus less efficient.

Moreover, a considerable class of real-life acoustic applications involves the analysis of problems in unbounded spatial domains, such as sound scattering or sound radiation problems. Besides the methods based on the boundary integral formulation of the governing differential equation, such as BEM, various strategies that employ the standard finite element scheme have been developed in order to tackle unbounded problems. Infinite element method (Bettess, 1992; Astley et al., 1994; Astley, 2000; Gerdes, 1998b,a), perfectly matched layers (Berenger, 1994, 1996; Collino and Monk, 1998) and non-reflecting boundary conditions (Harari et al., 1998; Thompson and Huan, 1999; Grote and Kirsch, 2007; Givoli and Cohen, 1995; Givoli et al., 2003) are the common modifications of the conventional FE scheme used to deal with the infinite extent of the acoustic domain.

First research goal

The first objective consists in the *further development of a deterministic prediction technique for a steady-state analysis of fully coupled, unbounded vibro-acoustic problems*. The first part of the doctoral research presented discusses the concept and application of the wave based technique for the steady-state analysis of three-dimensional, fully coupled vibro-acoustic problems involving unbounded acoustic domains. In this type of formulation, both the structural thin plate bending problem and the unbounded acoustic problem are described by means of a coupled, wave based model. Both parts of the coupled problem are solved simultaneously, in order to account for the strong coupling interaction. As such, the first research goal is divided into three main parts, which cover the following fields:

---

[5]FP7 Marie Curie Initial Training Network (ITN), EC grant agreement no. 290050.
[6]FP7 Marie Curie Initial Training Network (ITN), EC grant agreement no. 214909.

- First, the WBT is applied to solve the uncoupled thin plate bending problems. These problems form the basis for the later extension of the wave based formulation towards fully coupled problems. In this context, only flat thin plates are considered throughout this dissertation.

- Next, the formulation of WBT for tackling the unbounded three-dimensional acoustic problems is developed, which represents a complementary part to thin plate problems. The WBT is successively applied for the analysis of both the free-field and semi-infinite acoustic problems. The latter represents a special subset of general unbounded acoustic problems.

- Finally, by synthesising the formulations of the thin plate bending and unbounded acoustic problems, a general, fully coupled vibro-acoustic wave model is introduced.

Second research goal

For a variety of industrial problems the structural-acoustic coupling interaction can be considered weak, and both subsystems can therefore be analysed in a one-way-coupled manner. In this class of problems, the vibrating structure can be regarded as independent of external pressure loading arising from the surrounding acoustic domain. This holds true for many real-life engineering problems, where, for instance, a stiff structure is surrounded by low-density fluid. To tackle the one-way-coupled vibro-acoustic problems, a concept for coupling the structural FE model with an unbounded acoustic wave model based on a geometrical mapping technique has recently been developed. Therefore, the second goal of the research work carried out within the framework of this dissertation addresses *the extension of the geometrical mapping strategy towards unbounded, one-way-coupled vibro-acoustic problems and the application of the wave based technique for real-life industrial cases*.

1.5   Outline of the dissertation

The remainder of this Ph.D. thesis, which consists of four parts, eight chapters and seven appendices, is organised as follows.

Part I: INTRODUCTION AND STATE-OF-THE-ART

Chapter 1 gives a historical overview of the emergence and evolution of the CAE technologies over the last fifty years. It demonstrates their diffusion from the original application field in structural dynamic analysis towards an integrated product design process. Next, the state-of-the-art in the numerical vibro-acoustic modelling is presented, and the classification into deterministic and statistical schemes is introduced. In view of this classification, this chapter further reports on the current development trends and open challenges, whereby the objectives of the research work presented are defined. The basic concepts and distinctive characteristics of the wave based technique are briefly presented. Finally, the main achievements of this doctoral research are summarised.

Chapter 2 provides a general classification of the vibro-acoustic problems and reviews the formulation of the mathematical models used in the practical implementation of the various

computational methods. These formulations form the basis for the subsequent application of WBT for the analysis of the vibro-acoustic problems considered.

Chapter 3 presents the state-of-the-use in the deterministic modelling of vibro-acoustic problems. The conventional numerical methods are discussed in terms of their basic principles, ranges of validity and inherent limitations.

Part II: WBT FOR THREE-DIMENSIONAL PROBLEMS

Part II considers the application of the WBT to different types of three-dimensional vibro-acoustic problems. All of the chapters in this part adopt a unified structure. First, a general problem is defined and the basic concepts of the wave based approach for tackling the type of problem considered are explained. These theoretical concepts are further extended towards a practical numerical implementation. Finally, the applicability and computational efficiency of the wave based technique are demonstrated by various validation examples.

In **chapter 4**, the application of the WBT for the solution of uncoupled thin plate bending problems is discussed. Since only bending motion of flat structures radiates sound efficiently, the out-of-plane vibrations are of vital importance. As such, the proposed formulation hence becomes basis for a further extension of WBT towards a fully coupled analysis of unbounded vibro-acoustic problems.

Chapter 5 introduces the formulation of WBT for solving uncoupled, unbounded acoustic problems. It shows the additional modifications of the original solution scheme for interior acoustics that are needed in order to tackle problems involving unbounded spatial domains. First, an implementation for the analysis of free-field acoustic problems is proposed. In the next step, the solution scheme for problems involving semi-infinite acoustic domains is derived from the general free-field case.

Chapter 6 provides the missing link between chapters 4 and 5 by incorporating the effect of a strong fluid-structure interaction between the two uncoupled models. It presents a generic WBT approach for tackling fully coupled, unbounded vibro-acoustic problems. In this type of formulation, both the structural thin plate bending problem and the unbounded acoustic problem are described by means of a coupled wave based model. A simultaneous solution of such a coupled system accounts for the strong coupling interaction between the structure and fluid.

While chapter 6 presents an approach for strong coupling of the structural and acoustic problems, **chapter 7** considers only the one-way coupling between the two subsystems. It shows how a geometrical mapping strategy can be employed to couple structural FE and acoustic WB models in a weak manner. In this respect, a conventional FE modelling strategy can still be used to describe the structural part of the problem, whereas the WBT is applied for tackling the unbounded acoustic part of the coupled problem.

Part III: CONCLUSIONS

Chapter 8 summarises the conclusions of this doctoral thesis and provides recommendations for further research on this topic. After the general conclusions, the bibliography is provided.

Part IV: ADDENDA

Part IV provides some appended information. In **appendix A**, the mathematical model governing the thin plate bending motion is derived from a general three-dimensional theory of elasticity. **Appendix B** shows the derivation of the steady-state wave equation, which governs the propagation of small disturbances through homogeneous, compressible, inviscid fluid. **Appendix C** presents the formulation of the wave based method for solving the two-dimensional uncoupled acoustic problems and forms a theoretical background for the next chapter. The formulation of both the interior and unbounded acoustic problems is considered. **Appendix D** reports on performance investigations concerning the enrichment of the set of basis functions in the particular case where a discontinuous boundary condition occurs in the wave model. Since this study considers only two-dimensional acoustic problems, it is not incorporated into part II, which addresses three-dimensional vibro-acoustic problems. **Appendix E** lists the analytical form of the orthonormalised spherical harmonics up to degree $l = 10$, which are adopted for a pressure expansion in the unbounded part of an acoustic wave model. Finally, the author's curriculum vitae is presented in **appendix F**, and **appendix G** lists the publications which the author published in the framework of this doctoral research.

1.6   Main conclusions and achievements

This dissertation addresses the current industrial needs to narrow the gap between low-frequency deterministic techniques the high-frequency probabilistic methods. The main focus is thus a further development and extension of the application field of the wave based technique, which is a promising mid-frequency CAE tool that offers an alternative to conventional deterministic schemes. In view of the existing development status of the wave based technique, a dual goal strategy was pursued in this doctoral research.

- A novel formulation and development of the WBT for a steady-state analysis of fully coupled, three-dimensional, unbounded vibro-acoustic problems including problems involving semi-infinite acoustic domains.

- Utilising a geometrical mapping strategy to couple the structural FE and acoustic WB model, thereby extending the application field of WBT towards industrial, one-way-coupled, three-dimensional, unbounded vibro-acoustic problems.

1.6.1   Formulation and implementation of WBT for fully coupled, unbounded vibro-acoustic problems

In view of the first objective of the presented doctoral research, first the WBT is implemented to analyse both uncoupled problems. Based on the Kirchhoff thin plate theory, the WBT is applied for the steady-state analysis of the out-of-plane bending motion of flat plates. Two validation examples are considered throughout the validation study, in which plates of convex and non-convex shape are analysed by means of WBT and standard FEM. In addition to FE validation, experimental measurements are carried out for selected configurations of boundary conditions. Both validation examples prove the feasibility of WBT for solving steady-state plate bending problems. For the convex plate, the WBT outperforms the FEM in terms of accuracy and

computational load. The prediction accuracy achieved by WBT is comparable to conventional FEM, however, the computational effort is substantially lower. In general, calculations can be accelerated by a factor of 2–4. Nonetheless, in the second validation example, which considers a non-convex plate, a deterioration of the prediction accuracy is observed, due to the existence of the corner stress singularities. Compared with FE predictions, the WBT is still able to capture the physics of the problem fairly accurately and with lower computational load. Since only convex structures are considered in the later formulation of the wave based technique for the analysis of fully coupled, vibro-acoustic problems, the problem of the corner stress singularities is not further addressed in the framework of this dissertation.

Following the application to structural plate bending problems, the formulation of WBT for tackling the uncoupled, unbounded acoustic problems is developed and implemented. The application field is further extended towards problems involving semi-infinite acoustic domains. The methodology is validated by means of four validation examples. The first validation case is the application to sound scattering problems, in which it is used for the analysis of plane wave scattering by a rigid sphere. This choice was motivated by the existence of a closed-form analytical solution. Due to the simple geometry of the scatterer, an analytical solution may be derived, which is used as a reference for the convergence study. The convergence analysis proves that the convergence rate of WBT is substantially higher than that of BEM. Since an emphasis is put on the semi-infinite acoustic problems, the remaining validation examples involve this type of acoustic problem. The WBT is applied to three semi-infinite problems, ranging from a simple academic problem up to an industry-sized case. Adopting both the baffled and non-planar structures, the methodology is thoroughly tested. All validation examples demonstrate the feasibility of WBT for tackling the steady-state, unbounded acoustic problems. Depending on the problem being analysed, the calculations are six times faster than with the conventional BE approach.

Finally, both uncoupled systems are synthesised, and the WBT is formulated for a steady-state analysis of three-dimensional, fully coupled, unbounded vibro-acoustic problems. An extensive numerical validation study is carried out by considering three validation examples. The first test case presents the application of WBT to an academic example involving a free-field acoustic domain. As such, this validation example is divided into two stages. The purpose of the first pretesting phase is merely the verification of the coupled, structural-acoustic formulation, which is applied to an interior acoustic problem and compared to a reference coupled FE–FE analysis. Encouraged by the promising results, the formulation for the strong structural-acoustic coupling is further extended to unbounded vibro-acoustic problems. The next validation example considers the application of WBT to an industry-sized problem consisting of a simplified car-like structure involving a semi-infinite acoustic domain. In this particular case, the computational efforts involved in solving the reference coupled FE–BE model on the computer platform used to perform the numerical analyses are prohibitive. While the WBT provides an efficient prediction on a standard laptop PC, the FE–BE calculation is done on a high-performance multi-core workstation in order to obtain the same level of accuracy. In the final validation example, the WBT is applied for a coupled analysis of the so-called distributed mode loudspeaker (DML), which involves both the free-field and semi-infinite acoustic domains. In addition to the numerical validation work, a study on the directivity characteristics of this novel loudspeaker design is carried out by adopting the computationally efficient wave based model. Although still restricted to problems involving flat structures of moderate geometrical complexity, the variety of validation examples demonstrates the application versatility and the computational efficiency of this novel approach.

1.6.2 Extension of the WBT applicability to industrial, one-way-coupled, unbounded vibro-acoustic problems

To attain the second research goal of this dissertation, the concept of geometrical mapping between the structural FE and acoustic WB models is first developed further. From the initially proposed weak-coupled analysis of interior vibro-acoustic problems, this concept is extended towards problems involving unbounded acoustic domains. As a next step, the WBT is applied to two industry-sized problems, which demonstrates its suitability for tackling real-life engineering problems. It adopts a geometrical mapping strategy (MLV) to weakly couple the structural finite element model with an unbounded acoustic wave based counterpart.

The first validation example considers a free-field noise radiation analysis of a car engine block–gearbox assembly. The structural velocity field calculated by a commercial FE code is coupled to an acoustic unbounded wave model. A BE model utilising the same structural results is used as a reference baseline approach. A comparison between the BEM and WBT shows the increased computational efficiency of the proposed wave based approach.

The second example consists of a study on the structure-borne noise radiation of a truck exhaust muffler involving a semi-infinite acoustic domain. A truck exhaust muffler is selected as a representative test case to assess the performance of the wave based approach in the mid-frequency range. Extensive experimental measurement campaigns complement the numerical validation work based on BEM. The structural response is analysed by means of an FE model, which is correlated by the experimental testing data. The predicted structural FE results are then projected onto the WB model and compared with the measurements carried out in a semi-anechoic chamber. The applied baseline BE model already involves a huge computational burden in the considered frequency range. The WBT, on the contrary, achieves comparable prediction accuracy as BEM. In this way, it shows its practical applicability to cope with industrial problem and demonstrates its enhanced computational efficiency compared to state-of-the-art techniques.

1.6.3 Main recommendations for future work

Although both research goals defined in section 1.4 have been accomplished, some recommendations for further developments of the proposed wave based technique beyond the scope of this doctoral thesis can be given.

Different plate bending models – Thus far, only the Kirchhoff thin plate theory has been considered within the scope of this research work. The more general Reissner-Mindlin thick plate model includes the effects of both the shear stresses and the rotatory inertia. Furthermore, an implementation of WBT for the single and double curved shells and general 3D solid problems would further extend the application field of this method. However, since WBT, as any other indirect Trefftz approach, relies on exact solutions of the differential equation, the future research should focus on definition of complete function sets, which allow a fast convergence of the method.

High-performance coding – As for the current software development status, the methodology is not yet available in a commercial software. Except for the one-way-coupled FE–WB scheme, which is coded in *Fortran*, the novel formulations presented in this dissertation are implemented in *MATLAB*. WBT is an R&D code, for which *MATLAB* offers an open platform for a continuous development of this technique. Since *MATLAB* cannot

be considered as a high-performance programming language, the superior computational efficiency of WBT has not been fully exploited yet. Implementation of the code in a high-performance programming language, such as *Fortran* or *C++*, can further increase the computational efficiency of WBT.

Preprocessing of wave models – Currently, the preprocessing of wave models is still mainly done manually and relies on the user's knowledge of the problem being solved. However, to reach an industrial level of maturity, a semi- or fully automated preprocessing has to be developed.

Poroelastic materials – In view of the application of WBT on real-life engineering problems, inclusion of poroelastic materials into WB models is an industrial must have. The first formulations of WBT for tackling the poroelastic domains based on Biot material model have shown the potential of this solution scheme. Research on this topic is currently ongoing (Deckers et al., 2012).

A priori error estimation – Thus far, the dynamic selection of the appropriate number of basis functions has been based on a frequency-dependent rule of thumb. However, a more sophisticated a priori estimator, which might adopt a residual-error-controlled adaptive strategy, for example, would provide a more robust and efficient self-adaptive wave based scheme.

Automation of the MLV mapping strategy – Future research will also address the automation of the MLV approach. The robustness of the proposed technique has to be further investigated for the particular case of strongly incompatible computational meshes.

Non-deterministic modeling – Future research should also address accurate acoustic source modelling and possibly account for the effects of uncertainty and variability in the numerical vibro-acoustic analysis. By including non-determinism into the wave models in either parametric or non-parametric way, the WB prediction can be enhanced for the analysis of physical phenomena that are not completely known in a deterministic sense. This would allow a numerical analysis of uncertain and variable processes, which provides information on ranges of possible system behaviour rather than unique predictions.

Chapter 2

Formulation of vibro-acoustic problems

This chapter provides an overview of the underlying mathematical formulations behind the vibro-acoustic problems considered within the scope of this dissertation. First, section 2.1 presents a general classification of the vibro-acoustic problems based on different aspects. Second, sections 2.2 and 2.3 introduce the uncoupled structural and acoustic problems, respectively. Third, sections 2.4 and 2.5 describe the coupled and uncoupled unbounded vibro-acoustic problems, respectively. Finally, section 2.6 discusses vibro-acoustic problems that involve poroelastic materials. In these sections, a unified structure is adopted, in which (i) the generalised mathematical models are derived by introducing some initial assumptions, and (ii) the vibro-acoustic problems are subsequently described in terms of the governing differential equations and the corresponding boundary conditions. These formulations form the basis for the further application of the wave based technique for the analysis of the various vibro-acoustic problems. Section 2.7 concludes the chapter with a summary.

2.1   General classification

Vibro-acoustic problems can be classified based on the following criteria.

Structural versus acoustic problems

Structural problems consider the vibrational behaviour of solid-phase mechanical systems, such as beams, plates or general three-dimensional assemblies. Acoustic problems refer to the propagation of mechanical disturbances within fluid regions such as air or water.

Bounded versus unbounded problems

Acoustic problems that consider confined regions are called bounded problems, while those that involve infinite solution domains are referred to as unbounded problems. Sound radiation,

scattering and transmission are typical examples of unbounded acoustic problems. In practical applications, the structural problems are usually regarded as bounded.

Closed versus open problems

Problems in which the boundary of an acoustic problem consists of a closed body are referred to as closed. If the boundary does not enclose fluid of a finite volume (e.g. if there are openings present at the boundary), the problem is considered open. However, an open problem can be regarded as a special case of an exterior problem with closed boundary (KU Leuven, 2007), in which both sides of the boundary surface are composed of two separate parts. These two sides correspond to a positive and negative orientation of the normal vector. In addition to common boundary conditions prescribed on the boundary, the acoustic pressure must be continuous along the free edges between the positive and negative sides of the boundary surface. According to this definition, a loudspeaker equipped with a conventional sealed enclosure would be a closed problem, while a bass-reflex speaker with a ported cabinet would be an open problem.

Interior versus exterior problems

First, an acoustic problem featuring a closed boundary is considered. If the solution domain is entirely enclosed inside the problem boundary, the acoustic problem is referred to as an interior acoustic problem. An exterior acoustic problem, in contrast, restricts its solution domain to an outer region located outside the problem boundary. A special case is the combined interior/exterior problem, which combines two separate fluid domains divided by the closed boundary. An example of a combined problem would be the analysis of an aircraft fuselage by considering both the pressurised air inside the cabin and the surrounding fluid.

Coupled versus uncoupled problems

Whenever a structure is surrounded by fluid, the mutual coupling interaction between the structure and the fluid influences the vibro-acoustic behaviour of the system (Desmet, 1998). This phenomena can occur, for instance, when an elastic structure is submerged in high-density fluid, or when a thin lightweight structure is coupled to a fluid. An example of the first case is the coupled analysis of a sonar submerged in water, while the latter case is represented by a coupled simulation of a loudspeaker diaphragm. This type of problem is referred to as fully coupled vibro-acoustic problem. However, one specific class of problems allows the strong mutual coupling to be omitted and both subsystems to be considered weakly coupled. Therefore, if the mutual coupling interaction between the structure and fluid can be considered to be very weak, only the one-way coupling effects must be taken into account. These problems are referred to as one-way-coupled vibro-acoustic problems. In this respect, a distinction has to be drawn between two types of one-way-coupled problems. The first type only accounts for the one-way structural loading effects on fluid, while the second type only considers the acoustic pressure loading onto a structure. An example of the first case is the uncoupled vibro-acoustic analysis of an elastic high-stiffness structure surrounded by low-density fluid, such as engine noise radiation into a surrounding air domain. The latter case is represented by the analysis of an uncoupled vibro-acoustic system, in which the fluid acts as an independent excitation for the structural part – the vibrations of window panes induced by traffic noise, for instance, would be a classic example. If the problem can be considered weakly coupled, it can be decomposed into

two independent parts, which are then solved sequentially. It is crucial to distinguish between coupled and uncoupled vibro-acoustic problems, particularly from the computational performance point of view.

Transient versus steady-state problems

Transient analysis is a time-domain type of solution, in which one investigates a time-dependent response of a system to change from its equilibrium due to the excitation. In a steady-state analysis, the inherent time dependency of the governing dynamic equations is implicitly omitted by assuming a time-harmonic $\mathrm{e}^{\mathrm{j}\omega t}$ nature of the excitation. Therefore, the original problem is transformed from a time domain into a frequency domain. The reformulation of the original problem into a steady-state type of solution usually implies a huge reduction of computational costs. As one normally considers only a limited frequency range, a steady-state analysis can be performed in a more efficient way than an expensive numerical solution of an equivalent problem in the time domain.

Dimensionality

A distinction is made based on the dimensionality of the problem being solved. In engineering practise, all three types (i.e. one, two and three-dimensional problems) are common depending on the complexity and merit of the corresponding model. One special class of two-dimensional problems consists of axisymmetric problems, which make use of some problem-specific geometrical features. The choice of the dimensionality of the problem being solved has a vital effect on the computational efficiency of the resulting numerical model. With a 3D model the dynamic field variables must be resolved in all three spatial directions, which implies higher number of degrees of freedom than a comparable 2D model. Thus, if this problem includes a special geometrical feature (e.g. a symmetry plane or axis of revolution), it is advisable to reduce the dimension of the model, which leads to a significant reduction in its size.

This dissertation considers the common types of steady-state vibro-acoustic problems present in the current NVH product design process (i.e. uncoupled structural thin-plate bending problems, uncoupled unbounded acoustic problems and coupled vibro-acoustic problems) in both 2D and 3D.

2.2   Uncoupled, structural thin plate problems

Consider a general structural plate bending problem, as shown in figure 2.1. The underlying differential equation and the corresponding boundary conditions presented in section A.2 are restated here for the reader's convenience. The problem consists of a plate Ω characterised by its density ρ^{1}, Young's modulus E, material loss factor η, the Poisson's ratio ν and the thickness t. The dynamic field variables are expressed in terms of a local coordinate system (x', y', z'). The plate is subjected to a point force F acting at position $\mathbf{r}_F$ directed in the out-of-plane direction z'. The dynamic excitation has a time-harmonic behaviour with a circular frequency ω. The inherent steady-state nature of the out-of-plane displacement $w = w_z(\mathbf{r})\mathrm{e}^{\mathrm{j}\omega t}$

---

[1]When considering only uncoupled structural or acoustic problems, the indices $\bullet_s$ and $\bullet_a$, which refer to the corresponding mass density, are omitted for the sake of brevity, and the symbol ρ is used instead.

is not explicitly written out in full for the sake of brevity. According to the Kirchhoff thin plate theory discussed in section A.2.1, the bending motion of a plate is described by the out-of-plane displacement field of the middle plane

$$\mathbf{w}(\mathbf{r}) = w_z(\mathbf{r}), \tag{2.1}$$

which is governed by the following dynamic equation

$$\nabla^4 w_z(\mathbf{r}) - k_b^4 w_z(\mathbf{r}) = \frac{F}{D}\delta(\mathbf{r}_F), \quad \forall \mathbf{r} \in \Omega \tag{2.2}$$

with

$$\nabla^4 = \frac{\partial^4}{\partial x^4} + 2\frac{\partial^4}{\partial x^2 \partial y^2} + \frac{\partial^4}{\partial y^4} \tag{2.3}$$

and the bending wave number k_b and bending stiffness D defined as follows

$$k_b = \sqrt[4]{\frac{\rho t \omega^2}{D}}, \tag{2.4}$$

$$D = \frac{Et^3(1 + \mathrm{j}\eta)}{12(1 - \nu^2)}. \tag{2.5}$$
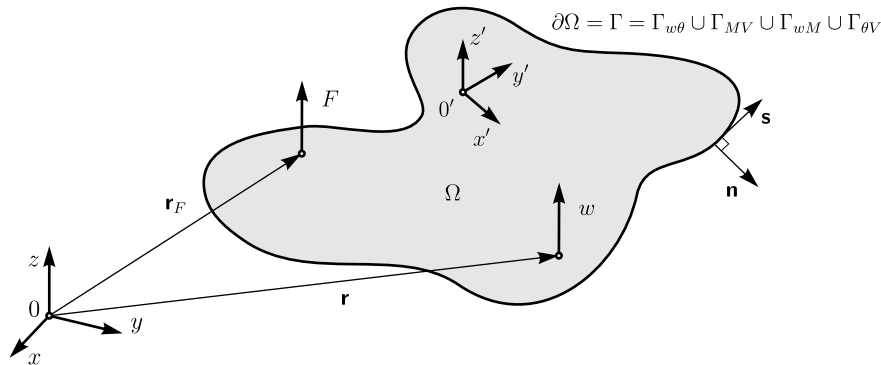
Figure 2.1: Thin plate bending problem

In order for the problem to be well-posed, the following boundary conditions forming a non-overlapping set $\Gamma = \Gamma_{w\theta} \cup \Gamma_{MV} \cup \Gamma_{wM} \cup \Gamma_{\theta V}$ have to be prescribed at the boundary of the problem:

- kinematic boundary conditions $\forall \mathbf{r}' \in \Gamma_{w\theta}$:

$$w_z(\mathbf{r}') = \bar{w}(\mathbf{r}), \tag{2.6a}$$

$$\mathcal{L}_\theta(w_z(\mathbf{r}')) = \bar{\theta}_n(\mathbf{r}), \tag{2.6b}$$

- mechanical boundary conditions $\forall \mathbf{r}' \in \Gamma_{MV}$:

$$\mathcal{L}_M(w_z(\mathbf{r}')) = \bar{M}_n(\mathbf{r}), \tag{2.6c}$$

$$\mathcal{L}_V(w_z(\mathbf{r}')) = \bar{V}_n(\mathbf{r}), \tag{2.6d}$$

- mixed boundary conditions type 1 $\forall \mathbf{r}' \in \Gamma_{wM}$:

$$w_z(\mathbf{r}') = \bar{w}(\mathbf{r}), \tag{2.6e}$$

$$\mathcal{L}_M(w_z(\mathbf{r}')) = \bar{M}_n(\mathbf{r}), \tag{2.6f}$$

- mixed boundary conditions type 2 $\forall \mathbf{r}' \in \Gamma_{\theta V}$:

$$\mathcal{L}_\theta(w_z(\mathbf{r}')) = \bar{\theta}_n, \tag{2.6g}$$

$$\mathcal{L}_V(w_z(\mathbf{r}')) = \bar{V}_n \tag{2.6h}$$

with $\bar{M}_n(\mathbf{r})$, $\bar{V}_n(\mathbf{r})$, $\bar{w}(\mathbf{r})$ and $\bar{\theta}_n(\mathbf{r})$ the prescribed values of the bending moment, generalised shear force, transverse out-of-plane displacement and the normal rotation, respectively. The differential operators $\mathcal{L}_\bullet(w_z(\mathbf{r}))$ are defined in (A.28).

2.3 Uncoupled, unbounded acoustic problems

Consider an unbounded three-dimensional acoustic problem, as shown in figure 5.1(a). For the full derivation of the fundamental differential equation governing the pressure perturbation fields in fluids and the corresponding boundary conditions, please see appendix B. The problem consists of a closed boundary surrounded by fluid characterised by its speed of sound c and the density ρ. Assuming that the system is linear, the fluid is inviscid and the process is adiabatic, the steady-state pressure response $p(\mathbf{r}, t) = p(\mathbf{r})\mathrm{e}^{\mathrm{j}\omega t}$ at an arbitrary position $\mathbf{r}$ within the solution domain Ω is governed by the Helmholtz equation

$$\nabla^2 p(\mathbf{r}) + k^2 p(\mathbf{r}) = -\mathrm{j}\rho\omega q \delta(\mathbf{r}, \mathbf{r}_q), \quad \forall \mathbf{r} \in \Omega, \tag{2.7}$$

where $\nabla^2 \equiv \triangle \equiv \frac{\partial^2}{\partial x^2} + \frac{\partial^2}{\partial y^2} + \frac{\partial^2}{\partial z^2}$ represents the Laplace operator in Cartesian coordinates, $\mathbf{r}$ the position vector, $\mathrm{j} = \sqrt{-1}$ the imaginary unit, ω the circular frequency, $k = \omega/c$ the wave number, q the strength amplitude of the acoustic volume velocity point source located at position $\mathbf{r}_q$ and δ the Dirac delta function.

Since the Helmholtz equation (2.7) is a second-order partial differential equation, one boundary condition has to be specified at each point of the boundary in order for the problem to be well-posed. At the problem boundary $\partial\Omega = \Gamma$, the following three types of boundary condition forming a non-overlapping set $\Gamma = \Gamma_p \cup \Gamma_v \cup \Gamma_Z$ may be imposed:

- pressure boundary condition (Dirichlet/essential) $\forall \mathbf{r} \in \Gamma_p$:

$$p(\mathbf{r}) = \bar{p}(\mathbf{r}), \tag{2.8a}$$

- normal velocity boundary condition (Neumann/natural) $\forall \mathbf{r} \in \Gamma_v$:

$$\mathcal{L}_v(p(\mathbf{r})) = \frac{\mathrm{j}}{\rho\omega}\frac{\partial p(\mathbf{r})}{\partial n} = \bar{v}_n(\mathbf{r}), \tag{2.8b}$$

- normal impedance boundary condition (Robin/mixed) $\forall \mathbf{r} \in \Gamma_Z$:

$$\mathcal{L}_Z(p(\mathbf{r})) = \mathcal{L}_v(p(\mathbf{r})) - \frac{p(\mathbf{r})}{\bar{Z}_n(\mathbf{r})} = 0 \tag{2.8c}$$

with $\frac{\partial}{\partial n}$ the normal derivative and $\bar{p}(\mathbf{r})$, $\bar{v}_n(\mathbf{r})$ and $\bar{Z}_n(\mathbf{r})$ the prescribed values of the acoustic pressure, normal velocity and normal impedance, respectively. Moreover, as the solution domain Ω is unbounded, an additional Sommerfeld radiation condition has to be imposed at Γ_∞ in order to ensure, that no acoustic energy reflections occur at infinity

$$\lim_{|\mathbf{r}|\to\infty}\left[|\mathbf{r}|\left(\frac{\partial p(\mathbf{r})}{\partial|\mathbf{r}|} + \mathrm{j}kp(\mathbf{r})\right)\right] = 0. \tag{2.9}$$
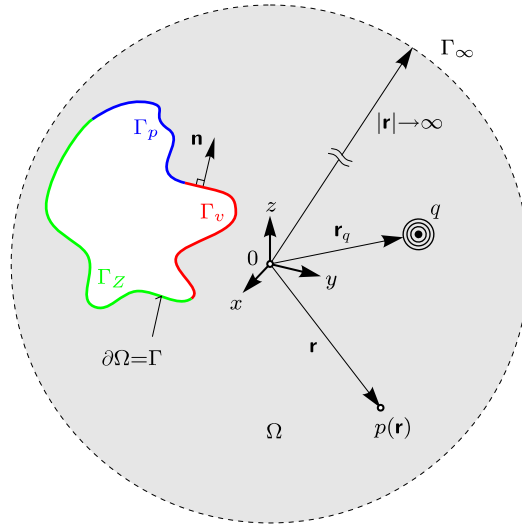
Figure 2.2: A three-dimensional unbounded acoustic problem (Rejlek et al., 2008b)

2.4   **Fully coupled, unbounded vibro-acoustic problems**

Synthetising the uncoupled structural plate bending and unbounded acoustic problem yields a three-dimensional fully coupled, unbounded vibro-acoustic problem, see figure 2.3. Both uncoupled problems have already been discussed in sections 2.2 and 2.3. The structural part Ω_s consists of a thin flat plate subjected to (i) boundary conditions imposed at the physical boundary Γ_s, (ii) a point force F acting in the out-of-plane, and (iii) the acoustic pressure loading p arising from the coupling to an acoustic domain. In the structural problem, these coupling effects caused by the acoustic pressure loading along the structural-acoustic interface Γ_{sa} are incorporated as a distributed transverse force by extending the particular solution of the governing differential equation.

The acoustic part Ω_a consists of a closed physical boundary Γ_a surrounded by fluid, which forms an unbounded acoustic domain. The acoustic part is subjected to (i) boundary conditions defined at Γ_a, (ii) the point source having an acoustic volume velocity strength amplitude q, and (iii) the normal velocity distributed at the structural-acoustic interface Γ_{sa}, which accounts for the coupling effects caused by the plate dynamics. An additional normal velocity boundary condition applied at Γ_{sa} allows for these acoustic-structural coupling effects.

The dynamic excitations exhibit a time-harmonic behaviour $\mathrm{e}^{\mathrm{j}\omega t}$, which causes a corresponding time-harmonic response of the structural-acoustic system described in terms of both the steady-state out-of-plane displacement w_z and the acoustic pressure p field.
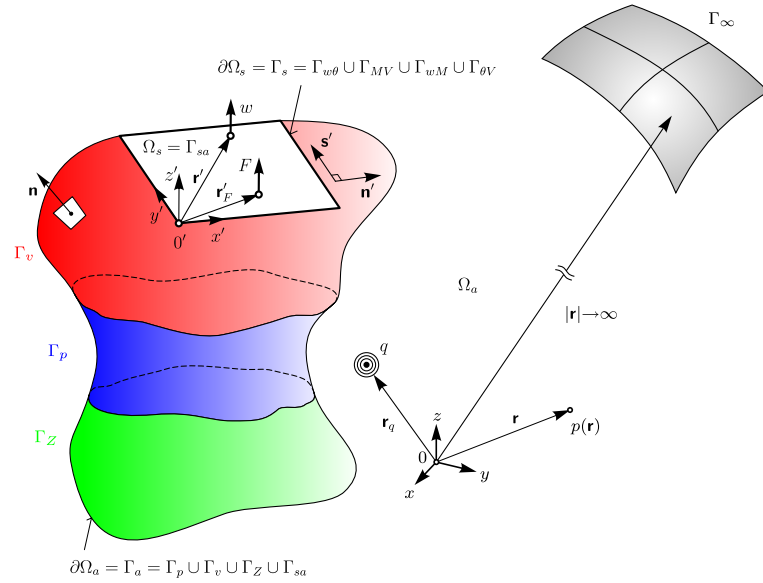
Figure 2.3: A general fully coupled, unbounded vibro-acoustic problem (Rejlek and Priebsch, 2010)

2.4.1 Structural part

The structural displacement field is governed by the steady-state dynamic equation

$$\nabla^4 w_z(\mathbf{r}') - k_b^4 w_z(\mathbf{r}') = \frac{p}{D} + \frac{F}{D}\delta(\mathbf{r}'_F), \quad \forall \mathbf{r} \in \Omega_s \tag{2.10}$$

based on Kirchhoff thin plate theory for the out-of-plane bending motion (Leissa, 1993). All quantities in (2.10) are defined in a plate local coordinate system (x', y', z'), see figure 2.3. At the physical boundary a non-overlapping set of boundary conditions is prescribed $\partial\Omega_s = \Gamma_s = \Gamma_{w\theta} \cup \Gamma_{MV} \cup \Gamma_{wM} \cup \Gamma_{\theta V}$ in order for the problem to be well-posed. The possible boundary conditions are as follows:

- kinematic boundary conditions $\forall \mathbf{r}' \in \Gamma_{w\theta}$:

$$w_z(\mathbf{r}') = \bar{w}(\mathbf{r}), \tag{2.11a}$$

$$\mathcal{L}_\theta(w_z(\mathbf{r}')) = \bar{\theta}_n(\mathbf{r}), \tag{2.11b}$$

- mechanical boundary conditions $\forall \mathbf{r}' \in \Gamma_{MV}$:

$$\mathcal{L}_M(w_z(\mathbf{r}')) = \bar{M}_n(\mathbf{r}), \tag{2.11c}$$

$$\mathcal{L}_V(w_z(\mathbf{r}')) = \bar{V}_n(\mathbf{r}), \tag{2.11d}$$

- mixed boundary conditions type 1 $\forall \mathbf{r}' \in \Gamma_{wM}$:

$$w_z(\mathbf{r}') = \bar{w}(\mathbf{r}), \tag{2.11e}$$

$$\mathcal{L}_M(w_z(\mathbf{r}')) = \bar{M}_n(\mathbf{r}), \tag{2.11f}$$

- mixed boundary conditions type 2 $\forall \mathbf{r}' \in \Gamma_{\theta V}$:

$$\mathcal{L}_\theta(w_z(\mathbf{r}')) = \bar{\theta}_n(\mathbf{r}), \tag{2.11g}$$

$$\mathcal{L}_V(w_z(\mathbf{r}')) = \bar{V}_n(\mathbf{r}), \tag{2.11h}$$

where $\mathcal{L}_\bullet(w_z(\mathbf{r}'))$ are the differential operators as defined in (A.28) in terms of a generalised plate coordinate system (n, s) with $\mathbf{n}'$ and $\mathbf{s}'$ the direction tangential and normal to the plate boundary, see figure 2.3.

2.4.2 Acoustic part

The Helmholtz equation governing the steady-state acoustic pressure perturbation field in the fluid domain

$$\nabla^2 p(\mathbf{r}) + k^2 p(\mathbf{r}) = -\mathrm{j}\rho_a \omega q \delta(\mathbf{r}, \mathbf{r}_q), \quad \forall \mathbf{r} \in \Omega_a \tag{2.12}$$

forms the acoustic part of the problem. Again, the appropriate boundary conditions have to be imposed in order for the problem to be well-posed. The following boundary condition types forming a non-overlapping set $\partial \Omega_a = \Gamma_a = \Gamma_p \cup \Gamma_v \cup \Gamma_Z \cup \Gamma_{sa}$ are defined at the physical boundary:

- pressure boundary condition (Dirichlet/essential) $\forall \mathbf{r} \in \Gamma_p$:

$$p(\mathbf{r}) = \bar{p}(\mathbf{r}), \tag{2.13a}$$

- normal velocity boundary condition (Neumann/natural) $\forall \mathbf{r} \in \Gamma_v$:

$$\mathcal{L}_v(p(\mathbf{r})) = \bar{v}_n(\mathbf{r}), \tag{2.13b}$$

- normal impedance boundary condition (Robin/mixed) $\forall \mathbf{r} \in \Gamma_Z$:

$$\mathcal{L}_v(p(\mathbf{r})) = \frac{p(\mathbf{r})}{\bar{Z}_n(\mathbf{r})}, \tag{2.13c}$$

- normal displacement continuity condition at the fluid-structure interface (Neumann/natural) $\forall \mathbf{r} \in \Gamma_{sa}$:

$$\mathcal{L}_v(p(\mathbf{r})) = \mathrm{j}\omega w_z(\mathbf{r}) \tag{2.13d}$$

with the differential operator $\mathcal{L}_v(p(\mathbf{r}))$ as defined in (B.36b). As the acoustic domain Ω_a is unbounded, an additional Sommerfeld radiation condition has to be imposed $\forall \mathbf{r} \in \Gamma_\infty$:

$$\lim_{|\mathbf{r}|\to\infty} \left[|\mathbf{r}| \left(\frac{\partial p(\mathbf{r})}{\partial |\mathbf{r}|} + \mathrm{j}kp(\mathbf{r}) \right) \right] = 0. \tag{2.14}$$

2.5   One-way-coupled, unbounded vibro-acoustic problems

The weakly coupled vibro-acoustic problems form a special subset of the general fully coupled systems, in which one considers only the one-way coupling phenomena. Figure 2.4 shows a general three-dimensional, one-way-coupled, unbounded vibro-acoustic problem. Since the mutual coupling interaction between the structure and fluid is considered to be very weak, in this particular case, only the one-way structural excitation effects on fluid are taken into account. This allows the problem to be decomposed into two parts, which can be solved successively. The structural part consists of a closed boundary, which constitutes the wetted surface Γ_{sa}. The system is excited by a harmonic point force F applied in a normal direction to the boundary at the position $\mathbf{r}_F$, see figure 2.4(a).

(a)   (b)
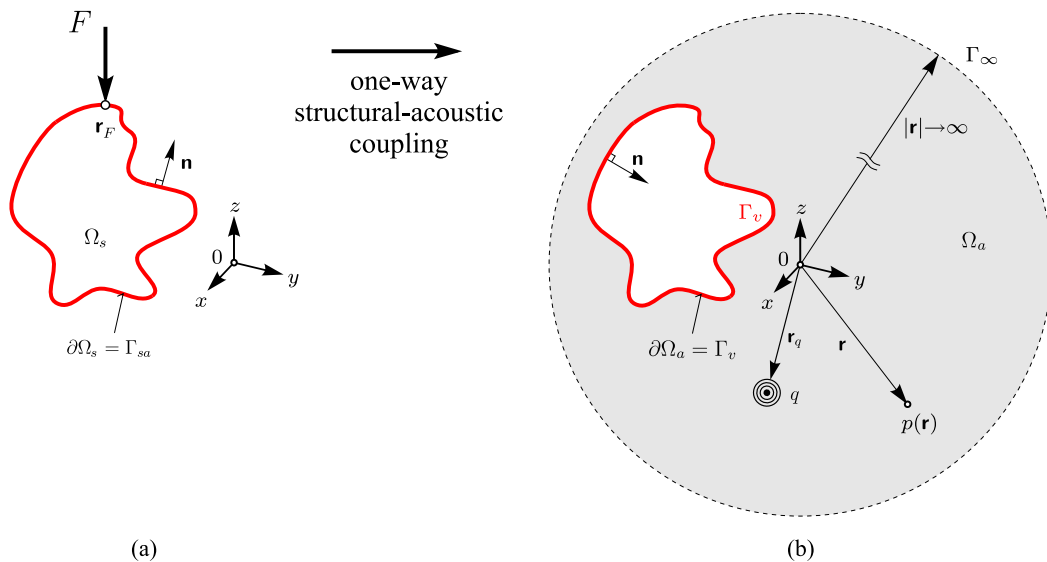
Figure 2.4: A one-way-coupled, unbounded vibro-acoustic problem: (a) the structural and (b) acoustic parts of the problem (Rejlek et al., 2009)

The acoustic part consists of a closed boundary surrounded by fluid, which forms an unbounded acoustic domain Ω_a, see figure 2.4(b). Assuming the system is linear, the fluid is inviscid, and

the process is adiabatic, the steady-state pressure response $p(\mathbf{r}, t) = p(\mathbf{r})\mathrm{e}^{\mathrm{j}\omega t}$ at an arbitrary position $\mathbf{r}$ within the solution domain Ω_a is governed by the Helmholtz equation

$$\nabla^2 p(\mathbf{r}) + k^2 p(\mathbf{r}) = -\mathrm{j}\rho_a \omega q \delta(\mathbf{r}, \mathbf{r}_q), \quad \forall \mathbf{r} \in \Omega_a. \tag{2.15}$$

At the boundary of the problem $\partial\Omega_a = \Gamma_v$, the normal velocity boundary condition is imposed $\forall \mathbf{r} \in \Gamma_v$:

$$\mathcal{L}_v(p(\mathbf{r})) = \frac{\mathrm{j}}{\rho_a \omega} \frac{\partial p(\mathbf{r})}{\partial n} = \bar{v}_n(\mathbf{r}) \tag{2.16}$$

with $\frac{\partial}{\partial n}$ the normal derivative and $\bar{v}_n(\mathbf{r})$ the prescribed normal velocity given by the structural part of the problem. Once again, as the solution domain Ω_a is unbounded, an additional Sommerfeld radiation condition has to be imposed at Γ_∞ in order to ensure that no acoustic energy reflections occur at infinity $\forall \mathbf{r} \in \Gamma_\infty$:

$$\lim_{|\mathbf{r}| \to \infty} \left[|\mathbf{r}| \left(\frac{\partial p(\mathbf{r})}{\partial |\mathbf{r}|} + \mathrm{j} k p(\mathbf{r}) \right) \right] = 0. \tag{2.17}$$

2.6   Vibro-acoustic problems involving poroelastic materials

Thus far, this dissertation has only considered problems in which the structural and acoustic domains are directly coupled (i.e. with no intervening layer). However, in industrial engineering, the application of poroelastic insulation materials[2] on the structural-acoustic coupling interface is a commonly used measure for controlling the interior vehicle noise, see figure 2.5. Nevertheless, those treatments represent an additional mass applied in the vehicle, which often conflicts with the current development trends striving for a lightweight design and space-saving packaging. Hence, an efficient application of the sound insulation materials, which would result in higher acoustic comfort while keeping the weight and costs of the developed product at a reasonable level, is an important task in current vehicle engineering. Clearly, an early insight into the vibro-acoustic performance attributes of these materials and their effect on the global dynamic behaviour of the full system is the key element, in which the employment of the CAE tools plays an indisputable role. However, the computational modelling of the poroelastic materials is quite challenging.

Fluid-saturated poroelastic materials, see figure 2.6, consist of two phases – the solid one, which forms the skeleton or frame, and the interstitial fluid phase, which is contained within the pores formed by the solid phase. The skeleton can be continuous, such as in plastic foams or porous ceramics, or non-continuous, such as in fibrous or granular materials (Lanoye, 2007). Since both the transversal and longitudinal wave can exist in an isotropic solid, and since a longitudinal waves occurs in a fluid, three types of waves can propagate through a poroelastic domain. As the solid frame and the fluid interact with each other, various dissipation mechanisms take place.

Over the last decades, various poroelastic models have been developed, which range from simple concepts to sophisticated methods (Allard and Atalla, 2009). The most straightforward way

---

[2]Also referred to as trim or sound package.
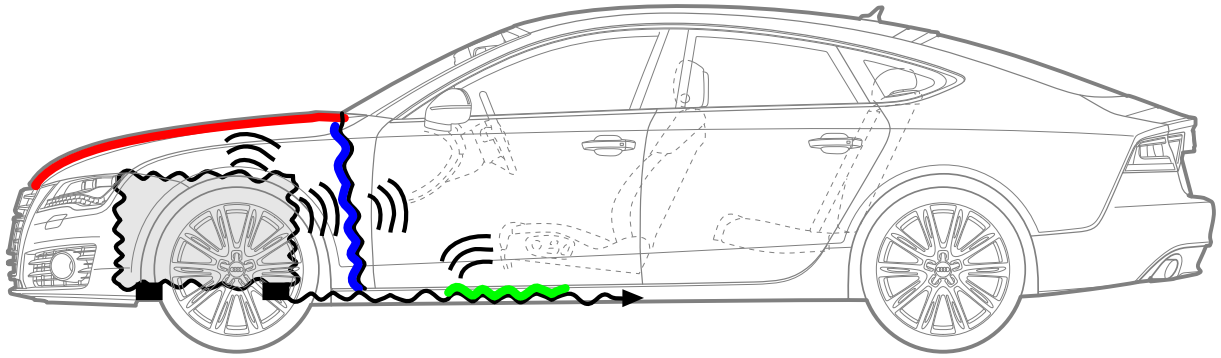
Figure 2.5: Typical noise control strategies based on application of a sound package in vehicle – reduction of the reverberant sound field by an increased absorption (red), reduction of the airborne transmission by increasing the sound insulation (blue) and reduction of the structure-borne transmission by adding a structural damping (green) (baseline drawing courtesy of Audi AG)

to account for the effect of a poroelastic damping layer is to impose a frequency-dependent, but spatially invariant normal impedance boundary condition for the cavity pressure field. A more advanced technique is equivalent fluid modelling, in which the poroelastic material is represented as a homogeneous fluid medium having equivalent physical properties. This assumption is valid, for example, for materials that have a stiff frame, in which only one longitudinal wave will propagate through a porous medium. If the frame can no longer be considered stiff, the Biot theory, which was developed for general fluid-saturated porous materials involving an elastic frame, must be applied (Biot, 1956). According to this theory, the pores are assumed to be distributed homogeneously, and the microstructural dynamic motion in both phases can be described on a macroscopic scale by applying modelling principles commonly used in isotropic continuum mechanics (Desmet, 1998). In the classical Biot theory, the macroscopic time-harmonic displacement of a poroelastic material is described by means of two vector fields $(\mathbf{u}_s, \mathbf{u}_f)$. Recently, Atalla et al. (1998) have developed a mixed displacement-pressure formu-
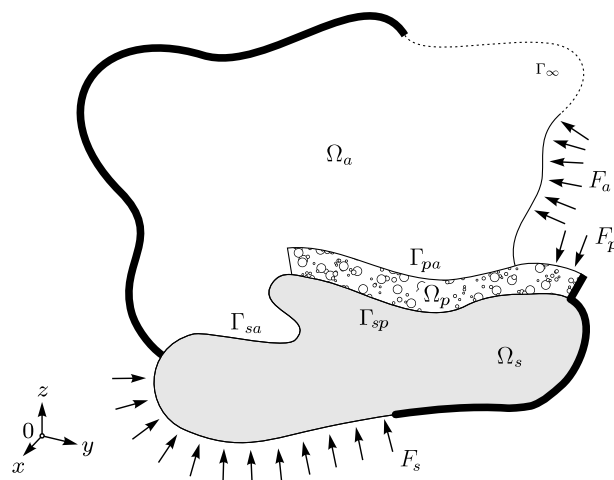
Figure 2.6: A coupled vibro-poroelastic-acoustic problem – Ω_s structural part, Ω_p poroelastic material, Ω_a acoustic fluid domain, $\Gamma_\bullet$ the corresponding interfaces and $F_\bullet$ the loads

lation $(\mathbf{u}_s, p)$ based on the displacement field in the solid phase and the macroscopic pressure of the interstitial fluid, which has proven to be numerically more efficient than the classical formulation

$$\nabla \cdot \hat{\boldsymbol{\sigma}}_s(\mathbf{u}_s) + \tilde{\rho}\omega^2 \mathbf{u}_s + \tilde{\gamma}\nabla p = 0 \tag{2.18a}$$

$$\triangle p + \frac{\tilde{\rho}_{22}}{\tilde{R}}\omega^2 p + \frac{\tilde{\rho}_{22}}{\phi^2}\tilde{\gamma}\omega^2\nabla \cdot \mathbf{u}_s = 0 \tag{2.18b}$$

with

$$\tilde{\gamma} = \phi\left(\frac{\tilde{\rho}_{12}}{\tilde{\rho}_{22}} - \frac{\tilde{Q}}{\tilde{R}}\right). \tag{2.19}$$

In equations (2.18) and (2.19) $\tilde{\bullet}$ denotes a complex and frequency-dependent quantity, $\hat{\boldsymbol{\sigma}}_s$ is the stress of the skeleton in vacuo, ϕ is porosity, $\tilde{Q}$ is the potential coupling coefficient between the dilatation and stress of the two phases, $\tilde{R}$ is the bulk modulus of fluid occupying a fraction ϕ of a unit volume of aggregate, and $\tilde{\rho}_{11}$, $\tilde{\rho}_{22}$ and $\tilde{\rho}_{12}$ are the effective densities defined as follows

$$\tilde{\rho}_{11} = \rho_{11} + \frac{\tilde{b}}{\mathrm{j}\omega} \tag{2.20a}$$

$$\tilde{\rho}_{22} = \rho_{22} + \frac{\tilde{b}}{\mathrm{j}\omega} \tag{2.20b}$$

$$\tilde{\rho}_{12} = \rho_{12} - \frac{\tilde{b}}{\mathrm{j}\omega} \tag{2.20c}$$

with $\rho_{11} = (1 - \phi)\rho_s - \rho_{12}$ the mass coefficient of solid, $\rho_{22} = \phi\rho_f - \rho_{12}$ the mass coefficient of fluid, ρ_{12} the coefficient for the interaction between the inertia forces of the solid and fluid phases, ρ_f the mass density of the interstitial fluid, ρ_s the mass density of the solid the skeleton is made from, and $\tilde{b}$ the viscous damping coefficient accounting for viscous interaction forces. The elastic coefficients $\tilde{Q}$ and $\tilde{R}$ are given by

$$\tilde{Q} = \frac{\left(1 - \phi - \dfrac{K_b}{K_s}\right)\phi K_s}{1 - \phi - \dfrac{K_b}{K_s} + \phi\dfrac{K_s}{\tilde{K}_f}} \tag{2.21}$$

$$\tilde{R} = \frac{\phi^2 K_s}{1 - \phi - \dfrac{K_b}{K_s} + \phi\dfrac{K_s}{\tilde{K}_f}} \tag{2.22}$$

with K_b the bulk modulus of skeleton in vacuo, K_s the bulk modulus of the elastic solid the skeleton is made from, and $\tilde{K}_f$ the bulk modulus of fluid in pores. In the Biot poroelasticity

equations (2.18), the first two terms of the structural equation represent the dynamic behaviour of the material in vacuo, while the first two terms of the fluid equation represent the dynamic behaviour of the fluid when the frame is at rest. The third terms in both equations couple the dynamics of the two phases (Atalla et al., 1998).

Currently, the two most widely used numerical methods for the analysis of sound package components are the transfer matrix method and the finite element modelling of poroelastic materials, both of which adopt the Biot model. In the concept of the transfer matrix method, the sound propagation through a stratified media containing porous layers is represented in terms of transfer matrices. This semi-analytical model is based on a matrix representation of plane wave propagation in different laterally infinite media (Tournour et al., 2007). The latter method uses an integral formulation of the modified Biot equations (2.18), in which the poroelastic material is represented in terms of an FE model (Duval et al., 2008; d'Udekem et al., 2011; Guj et al., 2011).

Since this topic is beyond the scope of this dissertation, the poroelastic materials are not further considered in the context of the newly developed wave based approach for the analysis of vibro-acoustic problems. Desmet (1998) and Lanoye (2007) describe how the wave based prediction technique can be used for the prediction of the steady-state dynamic response of fluid-saturated poroelastic materials.

2.7 Summary

This chapter presents the mathematical models of the different types of vibro-acoustic problems considered within the scope of this dissertation. These models are used for the subsequent formulation of the wave based technique for the analysis of thin plate bending problems, unbounded acoustic problems and the one-way and fully coupled vibro-acoustic problems, see chapters 4, 5, 7 and 6, respectively. For each type of problem, the governing differential equation and the corresponding boundary conditions are defined, while the full derivation of the mathematical models from the general continuum mechanics is described in appendices A and B.

Chapter 3

State-of-the-use in the deterministic modelling of vibro-acoustic problems

This chapter provides an overview of the state-of-the-use deterministic modelling tools commonly applied for a steady-state analysis of vibro-acoustic problems. Section 3.1 introduces the concepts of the finite element method for the analysis of both structural and acoustic problems. The basic principle and the application fields of the direct and indirect formulation of the boundary element method are discussed in section 3.2, and section 3.3 summarises this chapter.

3.1 Finite Element Method

The finite element method (FEM) is generally recognised to be one of the most versatile CAE tools used for solving real-life engineering problems in different industrial fields. Provided that the governing differential equation with the corresponding boundary conditions is given, the problem can be tackled with FEM. In the concept of FEM, the original problem of determining the spatial and temporal distribution of the field variables in a continuous medium is approximately transformed into a problem of finding field variables at some discrete nodal positions within each element of the computational mesh (Zienkiewicz et al., 2005). This transformation results in a set of algebraic equations. Hence, the FEM is an appropriate tool for a steady-state analysis of structural and acoustic problems. Moreover, the FEM is also capable of tackling problems involving multi-physical effects, such as fully coupled vibro-acoustic systems. The FEM modelling strategy consists of the discretisation of the entire solution domain into a large number of small subdomains, i.e. the finite elements. Within each of these elements, linear combination of simple polynomial basis functions is used to approximate the exact solution. The nodal values of the field variables considered form the unknown degrees of freedom of an FE model. Sections 3.1.1, 3.1.2 and 3.1.3 discuss the application of the FEM for the analysis of the uncoupled thin plate bending problem, the interior acoustic problem and the coupled vibro-acoustic problem, respectively.
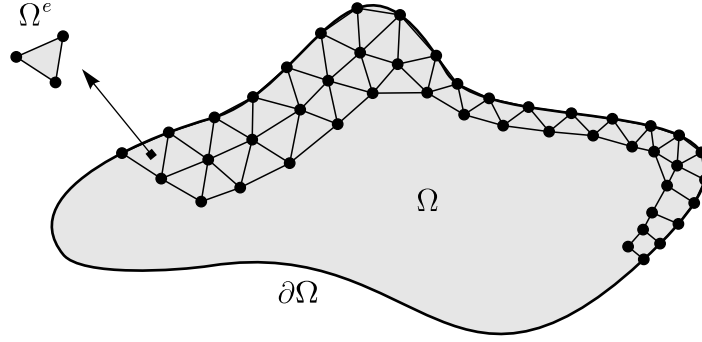
Figure 3.1: The concept of finite element method

3.1.1 Uncoupled thin plate bending problems

In order to apply the FEM for an uncoupled structural thin plate bending problem, the structural domain Ω_s is first subdivided into n_s^e non-overlapping finite elements Ω_s^e

$$\Omega_s = \bigcup_{e=1}^{n_s^e} \Omega_s^e \quad \text{with} \quad \Omega_s^i \cap \Omega_s^j = \emptyset, \quad \forall i \neq j, \tag{3.1}$$

see figure 3.1. Depending on the mesh topology, each element is constituted by $n_{s,n}^e$ nodes defined at some discrete particular positions within the element. This yields a total number of nodes $n_{s,n}$, which constitute the whole computational mesh. Within each element, the distribution of the field variable, which is the out-of-plane displacement w_z, is approximated as an expansion $\hat{w}_z$ in terms of the prescribed shape functions

$$w_z(\mathbf{r}) \approx \hat{w}_z(\mathbf{r}) = \sum_{n=1}^{3n_{s,n}^e} N_{s,n}^e(\mathbf{r})a_n^e, \quad \forall \mathbf{r} \in \Omega_s^e. \tag{3.2}$$

The contribution factors a_n^e form the unknown element degrees of freedom, which are the out-of-plane displacement w_z and the normal rotations θ_x and θ_y. Each element shape function $N_{s,n}^e$ is defined such that it has a value of unity at node n of the element and equals zero at all remaining nodes of the element. Based on the element shape functions $N_{s,n}^e$ defined in one element Ω_s^e, some global shape functions $N_{s,n}$ can be assembled, which are defined in the entire structural domain Ω_s. In each element Ω_s^e to which the node n belongs, the global shape function $N_{s,n}$ is identical to the corresponding element shape function $N_{s,n}^e$, while it has a zero value in the all other elements

$$w_z(\mathbf{r}) \approx \hat{w}_z(\mathbf{r}) = \sum_{n=1}^{n_{s,n}} N_{s,n}(\mathbf{r})w_n = \mathbf{N}_s(\mathbf{r})\mathbf{w}, \quad \forall \mathbf{r} \in \Omega_s \tag{3.3}$$

with $\mathbf{w}$ the vector of unknown nodal translational and rotational degrees of freedom. Next, the original problem is transformed into an equivalent integral formulation, such as the weighted residual approach, variational formulation or principle of virtual work. By adopting the Galerkin

approach to this integral formulation, the continuous mathematical model is transformed into a set of algebraic equations

$$\left(\mathbf{K}_s + \mathrm{j}\omega \mathbf{C}_s - \omega^2 \mathbf{M}_s \right) \mathbf{w} = \mathbf{f}_s, \tag{3.4}$$

which forms the global FE model. In the square matrix system (3.4), $\mathbf{K}_s$ is the structural stiffness matrix, $\mathbf{C}_s$ is the structural damping matrix and $\mathbf{M}_s$ is the structural mass matrix. The right hand side loading vector $\mathbf{f}_s$ contains the terms in the a priori assigned nodal degrees of freedom and the contributions from the external pressure, force and moment loading acting on the plate. Solution of the matrix system (3.4) yields the solution vector $\mathbf{w}$, which consists of the unknown nodal translational and rotational degrees of freedom. Once the nodal DOFs have been determined, the dynamic out-of-plane displacement field at an arbitrary position inside the finite element model can be postprocessed by applying the element basis functions (3.3).

3.1.2 Uncoupled acoustic problems

Similar to the structural problem discussed above, the acoustic domain Ω_a is first subdivided into n_a^e non-overlapping finite elements Ω_a^e in order to apply the FEM for an uncoupled interior acoustic problem

$$\Omega_a = \bigcup_{e=1}^{n_a^e} \Omega_a^e \quad \text{with} \quad \Omega_a^i \cap \Omega_a^j = \emptyset, \quad \forall i \neq j, \tag{3.5}$$

see figure 3.1. Depending on the mesh topology, each element is constituted by $n_{a,n}^e$ nodes defined at some discrete particular positions within the element. This yields a total number of nodes $n_{a,n}$, which constitute the whole computational mesh. Within each element, a linear combination of simple polynomial basis functions approximates the exact pressure solution given by the governing differential equation (2.7)

$$p(\mathbf{r}) \approx \hat{p}(\mathbf{r}) = \sum_{n=1}^{n_{a,n}^e} N_{a,n}^e(\mathbf{r}) p_n^e, \quad \forall \mathbf{r} \in \Omega_a^e. \tag{3.6}$$

Each element shape function $N_{a,n}^e$ is defined such that it has a value of unity at node n of the element and equals zero at all remaining nodes of the element. Based on the element shape functions $N_{a,n}^e$ defined in one element Ω_a^e, some global shape functions $N_{a,n}$ can be assembled, which are defined in the entire acoustic domain Ω_a. In each element Ω_a^e, to which the node n belongs, the global shape function $N_{a,n}$ is identical to the corresponding element shape function $N_{a,n}^e$, while it has a zero value in the all other elements

$$p(\mathbf{r}) \approx \hat{p}(\mathbf{r}) = \sum_{n=1}^{n_{a,n}} N_{a,n}(\mathbf{r}) p_n = \mathbf{N}_a(\mathbf{r}) \mathbf{p}, \quad \forall \mathbf{r} \in \Omega_a. \tag{3.7}$$

In (3.7), the contribution factors $\mathbf{p}$ are the unknown nodal degrees of freedom, which are in general the nodal acoustic pressures, and $\mathbf{N}_a$, which are the corresponding shape functions. In a next step, the original problem is transformed into an equivalent integral formulation, such as the weighted residual approach, variational formulation or principle of virtual work. By

adopting the Galerkin approach to this integral formulation, the continuous mathematical model is transformed into a set of algebraic equation

$$\left(\mathbf{K}_a + \mathrm{j}\omega\mathbf{C}_a - \omega^2\mathbf{M}_a\right)\mathbf{p} = \mathbf{f}_a, \tag{3.8}$$

which forms the global FE model. In the square matrix system (3.8), $\mathbf{K}_a$ is the acoustic stiffness matrix, $\mathbf{C}_a$ is the acoustic damping matrix, $\mathbf{M}_a$ the acoustic mass matrix, and $\mathbf{f}_a$ is the loading vector, which accounts for the effects of the acoustic source loading and the normal velocity boundary condition. The prescribed pressure boundary condition (2.8a) does not appear explicitly in the FE model (3.8). This type of boundary condition is accounted for by a priori assigning the prescribed values directly to the nodal degrees of freedom and by eliminating these nodal pressures from the vector of unknowns $\mathbf{p}$. Solution of the matrix system (3.8) yields the solution vector $\mathbf{p}$, which contains the unknown nodal pressure values. Once the nodal pressures have been determined, the dynamic pressure field at an arbitrary position inside the finite element model can be postprocessed by employing the element basis functions (3.7).

3.1.3   Coupled vibro-acoustic problems

Fully coupled vibro-acoustic problems, which involve strong coupling interaction between the structure and fluid, can be tackled by the coupled FE–FE formulation. Synthesising the two uncoupled problems (3.4) and (3.8) yields the coupled system

$$\left(\begin{bmatrix}\mathbf{K}_s & \mathbf{K}_c \\ 0 & \mathbf{K}_a\end{bmatrix} + \mathrm{j}\omega\begin{bmatrix}\mathbf{C}_s & 0 \\ 0 & \mathbf{C}_a\end{bmatrix} - \omega^2\begin{bmatrix}\mathbf{M}_s & 0 \\ -\rho_a\mathbf{K}_c^{\mathsf{T}} & \mathbf{M}_a\end{bmatrix}\right)\begin{Bmatrix}\mathbf{w} \\ \mathbf{p}\end{Bmatrix} = \begin{Bmatrix}\mathbf{f}_s \\ \mathbf{f}_a\end{Bmatrix}, \tag{3.9}$$

where $\mathbf{K}_c$ represents the fluid-structure coupling interaction. The coefficients in the coupled stiffness matrix and coupled mass matrix are still frequency independent but, in contrast to an uncoupled structural or uncoupled acoustic finite element model, these coupled matrices are no longer symmetric. This is due to the fact that the force loading of the fluid on the structure is proportional to the pressure, which results in a cross-coupling matrix $\mathbf{K}_c$ in the coupled stiffness matrix, while the force loading of the structure on the fluid is proportional to the acceleration, which results in a cross-coupling matrix $-\rho_a\mathbf{K}_c^{\mathsf{T}}$ in the coupled mass matrix (Desmet, 1998).

Equation (3.9) represents the so-called Eulerian formulation, in which the acoustic response is described in terms of a single scalar function, such as pressure, while the structural response is represented by a displacement vector (KU Leuven, 2007). In contrast to a Langrangian approach, which expresses both the structural and acoustic responses by a displacement vector, the Euler formulation benefits from a smaller model size and does not suffer from the existence of spurious rotational modes.

3.1.4   Characteristic properties of FEM

$(+)$ **Geometrical flexibility** – Since it relies on a fine spatial discretisation of the solved problem, the FEM is unrestricted with respect to geometrical features of the boundary of the problem considered.

$(+)$ **Sparsely populated and symmetric matrices** – Since the shape functions are only locally defined within an element, $\mathbf{K}$, $\mathbf{C}$ and $\mathbf{M}$ are sparsely populated, banded matrices. Moreover, for uncoupled structural and uncoupled acoustic problems, which can be cast into a variational formulation, the resulting matrices are symmetric. Due to these matrix properties, the solution vector of unknown nodal values can be obtained from efficient matrix solvers. This, however, does not apply for a coupled model, in which the matrices are no longer symmetric, and the bandwidth of the matrices is substantially larger.

$(+)$ **Real-valued matrix coefficients** – Since the shape functions have real values, the coefficients of the stiffness matrix $\mathbf{K}$ and the mass matrix $\mathbf{M}$ are real.

(0) **Frequency-independent submatrices** – Since the shape functions are independent of frequency, the stiffness matrix $\mathbf{K}$ and the mass matrix $\mathbf{M}$ have frequency-independent coefficients. This allows the use of standard eigenvalue solvers for the calculation of the undamped natural frequencies and mode shapes of structural and acoustic system. Hence, for uncoupled problems, the modal superposition technique can be adopted, in which the dynamic field variables are expanded in terms of the modes of the system considered. This leads to a substantial reduction of the model size. However, if the problem includes damping or poroelastic materials, which have in general frequency-dependent properties, the frequency-independent nature of the FE submatrices is compromised and does no longer represent a computational asset.

$(-)$ **Model size** – The size of an FE model is usually very large, which is even more pronounced for three-dimensional coupled problems.

$(-)$ **Unbounded problems** – Since the FEM requires a discretisation of the whole computational domain, this method is inherently restricted to the analysis of bounded vibro-acoustic problems.

3.2 Boundary Element Method

Unlike the FEM, the basic principle of BEM relies on boundary integral formulation (Von Estorff, 2000). As a consequence, the key advantage of BEM is its ability to relate the field variables at an arbitrary position in the solution domain Ω to the boundary variables at $\partial\Omega$. Due to this inherent feature of BEM, this numerical method has become very popular for tackling unbounded acoustic problems over the last decades. In view of the practical implementation, the BEM solution procedure as such is divided into two steps. First, the boundary of the problem is discretised into a large number of elements. Similar to FEM strategy, the acoustic boundary variables are expressed in terms of simple polynomial shape functions within these elements. Once the nodal unknown values have been determined, the field variables inside the solution domain are recovered by applying the boundary integral formulation in the subsequent postprocessing step. Depending on the type of integral formulation applied, two classes of boundary element method are distinguished. Section 3.2.1 reports on the concepts of the direct collocational BEM, while the indirect variational formulation of BEM is introduced in section 3.2.2.
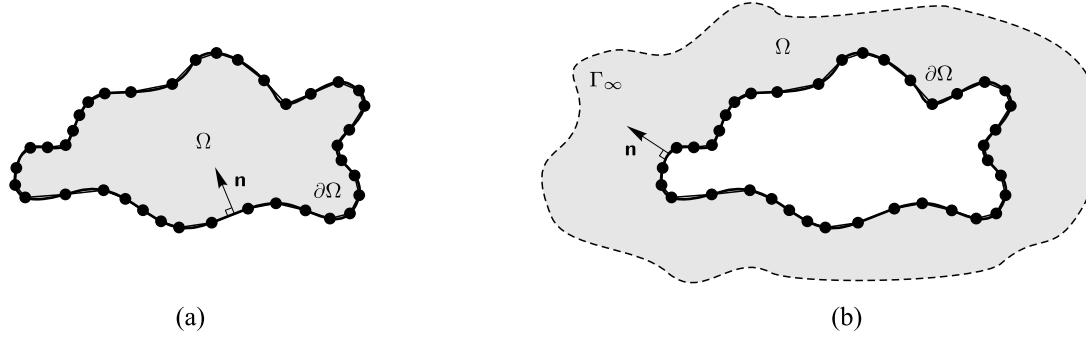
Figure 3.2: The direct boundary element method – (a) interior and (b) exterior formulation

3.2.1 Direct collocational scheme

The direct BEM adopts a direct boundary integral formulation for interior or exterior problems, see figure 3.2, in which it relates the pressure p at an arbitrary position $\mathbf{r}$ in a domain Ω_a to the pressure and normal velocity distribution at position $\boldsymbol{\xi}$ on a closed boundary $\Gamma_a = \partial\Omega_a$

$$p(\mathbf{r}) = \int_{\Gamma_a} \left(p(\boldsymbol{\xi})\frac{\partial G(\mathbf{r},\boldsymbol{\xi})}{\partial n} + \mathrm{j}\rho_a\omega v_n(\boldsymbol{\xi})G(\mathbf{r},\boldsymbol{\xi}) \right) \mathrm{d}\Gamma_a(\boldsymbol{\xi}) \tag{3.10}$$

with $G(\mathbf{r},\boldsymbol{\xi})$ the Green's kernel function. For a three-dimensional problem, the $G(\mathbf{r},\boldsymbol{\xi})$ represents a free-field pressure field at $\mathbf{r}$ caused by an acoustic point source located at $\boldsymbol{\xi}$

$$G(\mathbf{r},\boldsymbol{\xi}) = \frac{\mathrm{e}^{\mathrm{j}k\|\mathbf{r}-\boldsymbol{\xi}\|}}{4\pi\|\mathbf{r}-\boldsymbol{\xi}\|}. \tag{3.11}$$

The application of the collocational scheme results in the following numerical model

$$\mathbf{A}\mathbf{p} = \mathrm{j}\rho_a\omega\mathbf{B}\mathbf{v}_n \tag{3.12}$$

with $\mathbf{A}$ and $\mathbf{B}$ the matrices relating the nodal pressure values to the nodal normal velocity vales. In a practical implementation, the direct BEM follows a two-step procedure. First, by solving equation (3.12), a distribution of the pressure and normal velocity on the boundary is determined. By applying the integral formulation (3.10) in the subsequent step, these primary quantities are postprocessed at an arbitrary position in the solution domain, which yields the unknown pressure.

The direct BEM can also be applied in a framework of a coupled FEM–BEM scheme. In this type of coupled model, the FEM is used for the structural part of the problem, while the acoustics is tackled by BEM, which yields a non-symmetric matrix system

$$\begin{bmatrix} \mathbf{K}_s + \mathrm{j}\omega\mathbf{C}_s - \omega^2\mathbf{M}_s & \mathbf{L}_c \\ \rho_a\omega^2\mathbf{B}(\omega)\mathbf{T} & \mathbf{A}(\omega) \end{bmatrix} \begin{Bmatrix} \mathbf{w} \\ \mathbf{p} \end{Bmatrix} = \begin{Bmatrix} \mathbf{f}_s \\ \mathbf{f}_a \end{Bmatrix}. \tag{3.13}$$

In (3.13), $\mathbf{T}$ is the transformation matrix which relates the fluid normal velocity to the structural displacement at the structural-acoustic interface, and $\mathbf{L}_c$ results from the acoustic pressure loading on the structure.

3.2.2 Indirect variational scheme

(a)   (b)
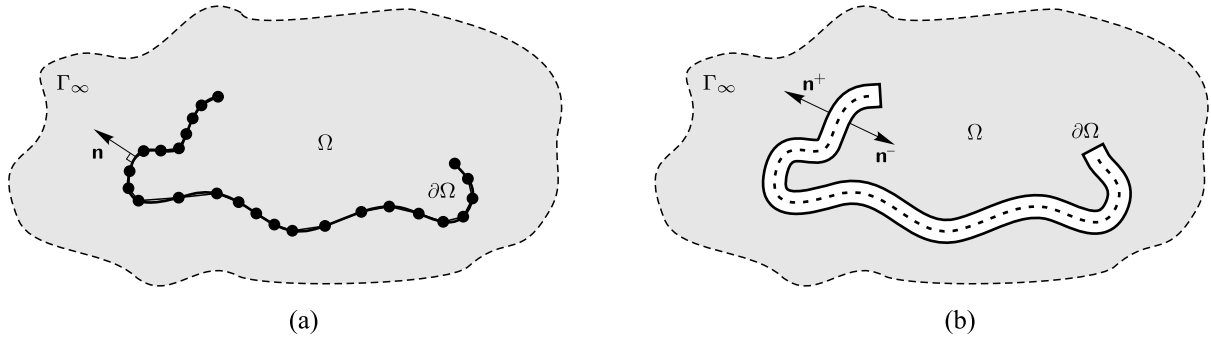
Figure 3.3: The indirect boundary element method – (a) the combined interior/exterior problem and (b) definition of the positive and negative sides of the boundary surface

In contrast to the direct solution scheme, the indirect approach is applicable to combined interior/exterior problems, which may feature an open boundary, see figure 3.3(a). In such systems, both sides of the problem boundary are in contact with the acoustic fluid. The indirect boundary element approach is based on an indirect boundary integral formulation, which relates the pressure field in the acoustic domain Ω_a to a distribution of so-called single $\sigma(\boldsymbol{\xi})$ and double layer potentials $\mu(\boldsymbol{\xi})$ on its boundary surface

$$p(\mathbf{r}) = \int_{\Gamma_a} \left(\mu(\boldsymbol{\xi}) \frac{\partial G(\mathbf{r}, \boldsymbol{\xi})}{\partial n} + \sigma(\boldsymbol{\xi}) G(\mathbf{r}, \boldsymbol{\xi}) \right) \mathrm{d}\Gamma_a(\boldsymbol{\xi}) \tag{3.14}$$

with the double layer potential representing the pressure difference between the two sides of the boundary surface

$$\mu(\boldsymbol{\xi}) = p(\mathbf{r}^+) - p(\mathbf{r}^-) \tag{3.15}$$

and the single layer potential representing the difference in the normal pressure between the two sides of the boundary surface

$$\sigma(\boldsymbol{\xi}) = \frac{\partial p(\mathbf{r}^+)}{\partial n} - \frac{\partial p(\mathbf{r}^-)}{\partial n} \tag{3.16}$$

with $\mathbf{r}^+$ and $\mathbf{r}^-$ indicating the positive and negative sides of the boundary surface with respect to the definition of a normal vector n as denoted in figure 3.3(b). A weighted residual formulation of the indirect boundary integral formulation (3.14) and the associated boundary conditions (2.8) results in a symmetric system of algebraic equations, which governs the nodal single and double layer potential values (Van Genechten, 2010)

$$\begin{bmatrix} \mathbf{E} & \mathbf{D} \\ \mathbf{D}^\mathsf{T} & \mathbf{F} \end{bmatrix} \begin{Bmatrix} \sigma \\ \mu \end{Bmatrix} = \begin{Bmatrix} \tilde{\mathbf{f}}_\sigma \\ \tilde{\mathbf{f}}_\mu \end{Bmatrix}. \tag{3.17}$$

Similar to the direct solution scheme, the indirect BEM can also be coupled with a structural FE model, which yields a symmetric model

$$
\begin{bmatrix} \mathbf{K}_s + \mathrm{j}\omega\mathbf{C}_s - \omega^2\mathbf{M}_s & \mathbf{L}_c \\ \mathbf{L}_c^\mathsf{T} & \dfrac{\mathbf{F}(\omega)}{\rho_a\omega^2} \end{bmatrix} \begin{Bmatrix} \mathbf{w} \\ \boldsymbol{\mu} \end{Bmatrix} = \begin{Bmatrix} \mathbf{f}_s \\ \mathbf{f}_a \end{Bmatrix}.
\tag{3.18}
$$

3.2.3 Characteristic properties of BEM

(+) **Geometrical flexibility** – Similar to FEM, the BEM offers a high geometrical flexibility with regard to the geometry of the problem being solved.

(+) **Model size** – Since only the boundary of the problem being considered needs to be discretised, the resulting BE model is substantially smaller than its FEM counterpart. This feature becomes even more distinctive when tackling three-dimensional problems.

(+) **Unbounded problems** – Since the integral boundary formulation inherently satisfies the Sommerfeld radiation conditions, the BEM is very well suited for solving unbounded problems.

(+) **Accuracy** – Unlike with FEM, the BEM does not involve a loss in accuracy for the derived variables, such as velocity field, since the derivation can be carried out analytically.

(−) **Fully populated system** – Due to the global nature of the boundary integral formulation, the BE system matrices are fully populated.

(−) **Frequency-dependent matrices** – Since the Green's kernel function implicitly depends on wave number, the matrix coefficients are frequency-dependent. This precludes an application of the efficient modal superposition technique, since a standard eigenvalue problem cannot be formulated.

(−) **Complex matrix coefficients** – Moreover, since the Green's kernel function is a complex function, the resulting BE matrices are also complex.

(−) **Numerical integration** – Since the Green's kernel function and its derivative become singular when the distance between $\mathbf{r}$ and $\boldsymbol{\xi}$ reaches zero, the numerical evaluation involves some special attention.

(−) **Non-uniqueness problem** – If the physical boundary of the acoustic problem constitutes a closed body, the so-called non-uniqueness problem may occur (Juhl, 1993). This phenomenon is purely related to the mathematical formulation of BEM, which may result in a non-uniqueness of the solution at certain critical frequencies. Schenck (1968) proved that for an exterior Neumann problem, these critical frequencies correspond to an eigenfrequency of the associated interior Neumann problem. As a consequence, the solution becomes numerically polluted at these critical frequencies. In the direct formulation of BEM the so-called **C**ombined **H**elmholtz **I**ntegral **E**quation **F**ormulation (CHIEF) is a commonly used measure for circumventing the non-uniqueness of the solution. In this approach, some additional equations related to points located inside the closed boundary are introduced to the original problem, and the overdetermined system is then solved. In the indirect BEM, one of the strategies for mitigating the effect of this phenomenon is

to apply an impedance boundary condition at the inner side of the acoustic boundary, in order to damp those fictitious resonances.

3.3 Summary

This chapter introduced the basic concepts of the state-of-the-use deterministic modelling tools commonly utilised for the analysis of vibro-acoustic problems. For each method considered, the inherent features, including the pros/cons, were discussed in view of the application fields of the newly developed wave based prediction technique. A more comprehensive overview on the concepts and applications of these deterministic methods for the steady-state analysis of vibro-acoustic problems can be found in (Van Hal, 2004) and (Pluymers, 2006).

Part II

METHODOLOGY AND APPLICATION OF THE WAVE BASED TECHNIQUE FOR THREE-DIMENSIONAL, VIBRO-ACOUSTIC PROBLEMS

Chapter 4

The Wave Based Technique for uncoupled, thin plate bending problems

This chapter addresses the application of the wave based technique for steady-state dynamic analysis of thin flat plate bending problems. First, section 4.1 restates the problem. Section 4.2 then discusses the methodology of the WBT for plate bending problems. The out-of-plane vibrations are of great importance, since only the bending motion of those components radiates sound efficiently. The proposed formulation thus becomes a basis for further extension towards a fully coupled, unbounded vibro-acoustic model, as discussed in chapter 6. The applicability of WBT is illustrated by means of two validation examples. Section 4.3 considers a set of single-domain problems consisting of a polygonal convex domain. Three different combinations of boundary conditions are successively applied to the same geometrical problem, see sections 4.3.1, 4.3.2 and 4.3.3, respectively. The comparison of the wave based predictions with both the results of reference FE model and the experimental measurement data demonstrates the accuracy of the proposed approach. Section 4.4 reviews the analysis of problems that involve non-convex domain, for which domain decomposition strategy comes into play. Once again, a validation study is carried out in order to assess the achieved prediction accuracy. Finally, section 4.5 summarises the main conclusions of this chapter.

4.1   Problem definition

The steady-state dynamic out-of-plane displacement field $w_z(\mathbf{r})$ in a thin plate is governed by the Kirchhoff equation

$$\nabla^4 w_z(\mathbf{r}) - k_b^4 w_z(\mathbf{r}) = \frac{F}{D}\delta(\mathbf{r}_F), \quad \forall \mathbf{r} \in \Omega \tag{4.1}$$

with the following boundary conditions

- kinematic boundary conditions $\forall \mathbf{r}' \in \Gamma_{w\theta}$:

$$w_z(\mathbf{r}') = \bar{w}(\mathbf{r}), \tag{4.2a}$$

$$\mathcal{L}_\theta(w_z(\mathbf{r}')) = \bar{\theta}_n(\mathbf{r}), \tag{4.2b}$$

- mechanical boundary conditions $\forall \mathbf{r}' \in \Gamma_{MV}$:

$$\mathcal{L}_M(w_z(\mathbf{r}')) = \bar{M}_n(\mathbf{r}), \tag{4.2c}$$

$$\mathcal{L}_V(w_z(\mathbf{r}')) = \bar{V}_n(\mathbf{r}), \tag{4.2d}$$

- mixed boundary conditions type 1 $\forall \mathbf{r}' \in \Gamma_{wM}$:

$$w_z(\mathbf{r}') = \bar{w}(\mathbf{r}), \tag{4.2e}$$

$$\mathcal{L}_M(w_z(\mathbf{r}')) = \bar{M}_n(\mathbf{r}), \tag{4.2f}$$

- mixed boundary conditions type 2 $\forall \mathbf{r}' \in \Gamma_{\theta V}$:

$$\mathcal{L}_\theta(w_z(\mathbf{r}')) = \bar{\theta}_n, \tag{4.2g}$$

$$\mathcal{L}_V(w_z(\mathbf{r}')) = \bar{V}_n. \tag{4.2h}$$

4.2 Basic concepts of the Wave Based Technique

The wave based technique adopts an indirect Trefftz approach (Trefftz, 1926; Jiroušek and Wroblewski, 1995; Jiroušek and Zielinski, 1997), in which it incorporates the a priori knowledge of the solved problem. The field variables are expressed in terms of globally defined basis functions, which are the exact solutions of the homogeneous governing differential equation. Given that the basis function expansion forms a complete set of Trefftz functions, the convergence of the method is ensured, provided that the solution domain is convex. The only approximation error is introduced in the definition of boundary conditions. Using a weighted residual scheme, the residual errors arising at the boundary are enforced to zero in an integral sense. The resulting system matrix is fully populated and suffers from ill-conditioning, which is, however, an inherent feature of all indirect Trefftz methods (Van Hal, 2004). Solving the system of algebraic equations yields the contribution factors of the wave functions, which are the degrees of freedom. The wave based models are substantially smaller than their finite element counterparts and exhibit an increased computational efficiency. The concepts presented in the following sections are based on the work of Van Hal et al. (2000) and Vanmaele (2007).

4.2.1 Domain decomposition

Desmet (1998) has proven that the WBT converges towards an exact solution, provided that the solution domain is convex. If the considered problem consists of a non-convex domain, partitioning into non-overlapping convex subdomains is required

$$\Omega = \bigcup_{\alpha}^{N_s} \Omega^\alpha \quad \text{with} \quad \bigcap_{\alpha}^{N_s} \Omega^\alpha = \emptyset, \tag{4.3}$$

see figure 4.1. In addition to the boundary conditions (4.2) imposed at the physical boundary of the problem, the following coupling conditions have to be prescribed at the interface Γ_i between the subdomains to ensure the continuity of the dynamic field variables:

- kinematic coupling conditions $\forall \mathbf{r} \in \Gamma_{i_{w\theta}}^{(\alpha,\beta)}$:

$$w^\alpha = w^\beta, \tag{4.4a}$$

$$\mathcal{L}_\theta^\alpha(w^\alpha) = -\mathcal{L}_\theta^\beta(w^\beta), \tag{4.4b}$$

- mechanical coupling conditions $\forall \mathbf{r} \in \Gamma_{i_{MV}}^{(\alpha,\beta)}$:

$$\mathcal{L}_M^\alpha(w^\alpha) = -\mathcal{L}_M^\beta(w^\beta), \tag{4.5a}$$

$$\mathcal{L}_V^\alpha(w^\alpha) = \mathcal{L}_V^\beta(w^\beta). \tag{4.5b}$$

The WBT adopts a direct coupling approach, in which the interface conditions (4.4)–(4.5) are directly enforced as boundary conditions to a corresponding subdomain. For the problem to be well-posed, two continuity conditions are imposed on each subdomain. In practical implementation, the displacement compatibility conditions (4.4) are imposed as a boundary condition on subdomain Ω^α, while the force equilibrium conditions (4.5) are applied to subdomain Ω^β.

4.2.2 Field variable expansion

Within each subdomain Ω^α, the following field variable expansion approximates the exact solution of the steady-state out-of-plane displacement

$$w^\alpha(\mathbf{r}) \approx \hat{w}^\alpha(\mathbf{r}) = \sum_{i=1}^{M_s^\alpha} w_i^\alpha \Psi_i^\alpha(\mathbf{r}) + \hat{w}_F^\alpha(\mathbf{r}) = \mathbf{\Psi}^\alpha(\mathbf{r})\,\mathbf{w}^\alpha + \hat{w}_F^\alpha(\mathbf{r}) \tag{4.6}$$

with Ψ the basis functions, which will be referred to as *wave functions* throughout this dissertation. In (4.6) each wave function $\mathbf{\Psi}^\alpha$ satisfies the homogenous part of the differential equation (4.1) and the wave function contribution factors $\mathbf{w}^\alpha$ form the degrees of freedom of the structural wave model. The linear combination of the wave functions is further extended by the particular
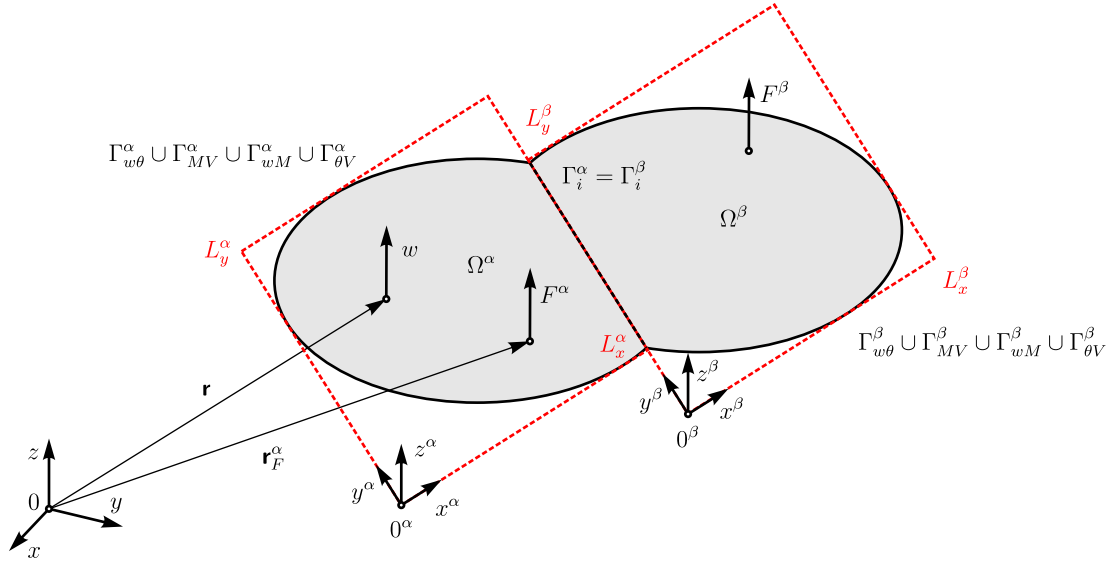
Figure 4.1: Partitioning of a non-convex structural domain – the bounding box of the corresponding subdomain indicated in red

solution function that accounts for the external loading term of (4.1) due to the applied point force F^α at position $\mathbf{r}_F^\alpha$

$$\hat{w}_F^\alpha(\mathbf{r}) = -\frac{\mathrm{j}F^\alpha}{8k_b^2 D}\left[\mathrm{H}_0^{(2)}(k_b\|\mathbf{r}-\mathbf{r_F^\alpha}\|) - \mathrm{H}_0^{(2)}(-\mathrm{j}k_b\|\mathbf{r}-\mathbf{r_F^\alpha}\|)\right] \tag{4.7}$$

with $\mathrm{H}_0^{(2)}(\bullet)$ the zero-order Hankel function of the second kind. Two subsets (r,s) form the set of wave functions which are defined as follows

$$\boldsymbol{\Psi}^\alpha(\mathbf{r}) = \begin{cases} \Psi_{r1}^\alpha(x,y) = \cos(k_{rx}^\alpha x)\,\mathrm{e}^{-\mathrm{j}k_{r1y}^\alpha y} \\[2mm] \Psi_{r2}^\alpha(x,y) = \cos(k_{rx}^\alpha x)\,\mathrm{e}^{-\mathrm{j}k_{r2y}^\alpha y} \\[2mm] \Phi_{s1}^\alpha(x,y) = \mathrm{e}^{-\mathrm{j}k_{s1x}^\alpha x}\,\cos(k_{sy}^\alpha y) \\[2mm] \Phi_{s2}^\alpha(x,y) = \mathrm{e}^{-\mathrm{j}k_{s2x}^\alpha x}\,\cos(k_{sy}^\alpha y). \end{cases} \tag{4.8}$$

Since the only requirement for the wave number components in (4.8) is that

$$\left((k_{r\bullet}^\alpha)^2 + (k_{s\bullet}^\alpha)^2\right)^2 = k_b^4, \tag{4.9}$$

an infinite number of wave functions (4.8) can be defined for the expansion (4.6). The structural wave number components are selected as follows (Desmet, 1998)

$$k_{r\bullet}^\alpha = \begin{cases} k_{rx}^\alpha = \dfrac{r^\alpha \pi}{L_x^\alpha}, \quad r^\alpha = 0,1,2,\ldots,n_r^\alpha \\[3mm] k_{r1y}^\alpha = \pm\sqrt{k_b^2 - (k_{rx}^\alpha)^2} \\[3mm] k_{r2y}^\alpha = \pm\mathrm{j}\sqrt{k_b^2 + (k_{rx}^\alpha)^2}, \end{cases} \tag{4.10a}$$

$$
k_{s\bullet}^{\alpha} = \begin{cases} k_{sy}^{\alpha} = \dfrac{s^{\alpha}\pi}{L_y^{\alpha}}, \quad s^{\alpha} = 0, 1, 2, \dots, n_s^{\alpha} \\[2ex] k_{s1x}^{\alpha} = \pm\sqrt{k_b^2 - (k_{sy}^{\alpha})^2} \\[2ex] k_{s2x}^{\alpha} = \pm\mathrm{j}\sqrt{k_b^2 + (k_{sy}^{\alpha})^2} \end{cases} \tag{4.10b}
$$

with L_x^{α} and L_y^{α} the dimensions of the smallest rectangular box enclosing the corresponding subdomain Ω^{α}, see figure 4.1, which is referred to as the *bounding box*. For the practical implementation of WBT the wave function set (4.8) needs to be truncated, since only a finite number of wave number components (4.10) is admissible for analysis on a digital computer. Therefore, the integer sets r^{α} and s^{α} are truncated from above by the truncation numbers n_r^{α} and n_s^{α}, which yields the M_s^{α} degrees of freedom of the α-th subdomain

$$
M_s^{\alpha} = \dim \boldsymbol{\Psi}^{\alpha} = 4(n_r^{\alpha} + 1) + 4(n_s^{\alpha} + 1). \tag{4.11}
$$

Two truncation strategies are considered throughout this dissertation. While the first uses fixed truncation numbers $n_\bullet^{\alpha}$ to control the size of the considered problem, the latter one employs a frequency-dependent selection scheme based on the following formula

$$
n_r^{\alpha} \geq \left\lceil T\frac{k_b L_x^{\alpha}}{\pi} \right\rceil, \tag{4.12a}
$$

$$
n_s^{\alpha} \geq \left\lceil T\frac{k_b L_y^{\alpha}}{\pi} \right\rceil \tag{4.12b}
$$

with T a user-defined truncation parameter and $\lceil \bullet \rceil$ the ceiling function.

The wave functions comprised in the wave function set (4.8) represent two different wave types – propagating and evanescent waves. The distinction depends on the value of the corresponding wave number component (4.10). In the propagating type of wave, both wave number components $k_{\bullet x}^{\alpha}$ and $k_{\bullet y}^{\alpha}$ are real numbers, which implies that the amplitudes of the associated wave function are restricted to the interval $\langle -1, 1 \rangle$. However, for low frequencies and/or higher values of the integer numbers r^{α} and s^{α}, the wave number component in one direction remains a real number, while the other one becomes a complex number. As a consequence, the amplitudes of the resulting wave function may become substantially larger than 1. In this evanescent type of wave, the amplitudes show a harmonic behaviour in one spatial direction, while an exponential decay is observed in the other direction. However, for the numerical conditioning of the resulting wave model it is essential that the amplitudes of all wave functions must not be larger than one within their definition domain. In order to control the amplitudes of the evanescent wave functions, some scaling factors are introduced in the definition of the wave functions. These scaling factors are defined with respect to the dimensions of a bounding box of the corresponding subdomain. More details on this topic are given in (Desmet, 1998) and (Pluymers, 2006).

4.2.3 Evaluation of boundary and interface conditions

The out-of-plane displacement approximation (4.6) satisfies the governing differential equation (4.1), but violates the boundary conditions (4.2) and the interface conditions (4.4) and (4.5). The unknown contribution functions w_i are determined by minimising the approximation errors of the boundary and interface conditions in an integral sense by applying the weighed residual formulation (Vanmaele, 2007). The residuals errors arising at the boundaries and interfaces of the corresponding subdomain are defined as follows

$$\mathbf{r} \in \Gamma_{w\theta}^{\alpha} \cup \Gamma_{wM}^{\alpha} \ : \ R_w^{\alpha}(\mathbf{r}) \quad = \hat{w}^{\alpha}(\mathbf{r}) - \bar{w}(\mathbf{r}), \tag{4.13a}$$

$$\mathbf{r} \in \Gamma_{w\theta}^{\alpha} \cup \Gamma_{\theta V}^{\alpha} \ : \ R_{\theta}^{\alpha}(\mathbf{r}) \quad = \mathcal{L}_{\theta}^{\alpha}(\hat{w}^{\alpha}(\mathbf{r})) - \bar{\theta}_n, \tag{4.13b}$$

$$\mathbf{r} \in \Gamma_{wM}^{\alpha} \cup \Gamma_{MV}^{\alpha}: \ R_M^{\alpha}(\mathbf{r}) \quad = \mathcal{L}_M^{\alpha}(\hat{w}^{\alpha}(\mathbf{r})) - \bar{M}_n(\mathbf{r}), \tag{4.13c}$$

$$\mathbf{r} \in \Gamma_{mV}^{\alpha} \cup \Gamma_{\theta V}^{\alpha} \ : \ R_V^{\alpha}(\mathbf{r}) \quad = \mathcal{L}_V^{\alpha}(\hat{w}^{\alpha}(\mathbf{r})) - \bar{V}_n(\mathbf{r}), \tag{4.13d}$$

$$\mathbf{r} \in c_w^{\alpha} \qquad\qquad : \ R_{c_w}^{\alpha}(\mathbf{r}) \quad = \hat{w}^{\alpha}(\mathbf{r}) - \bar{w}(\mathbf{r}), \tag{4.13e}$$

$$\mathbf{r} \in c_V^{\alpha} \qquad\qquad : \ R_{c_V}^{\alpha}(\mathbf{r}) \quad = \llbracket \mathcal{L}_{Ms}^{\alpha}(\hat{w}(\mathbf{r})) - \bar{M}_{ns}(\mathbf{r}) \rrbracket, \tag{4.13f}$$

$$\mathbf{r} \in \Gamma_{i_{w\theta}}^{(\alpha,\beta)} \qquad\quad : \ R_{i_{w\theta}}^{(\alpha,\beta)}(\mathbf{r}) = \left\{ \begin{array}{c} \hat{w}^{\alpha} = \hat{w}^{\beta} \\ \mathcal{L}_{\theta}^{\alpha}(\hat{w}^{\alpha}) = -\mathcal{L}_{\theta}^{\beta}(\hat{w}^{\beta}) \end{array} \right\}, \tag{4.13g}$$

$$\mathbf{r} \in \Gamma_{i_{MV}}^{(\alpha,\beta)} \qquad\quad : \ R_{i_{MV}}^{(\alpha,\beta)}(\mathbf{r}) = \left\{ \begin{array}{c} \mathcal{L}_M^{\alpha}(\hat{w}^{\alpha}) = -\mathcal{L}_M^{\beta}(\hat{w}^{\beta}) \\ \mathcal{L}_V^{\alpha}(\hat{w}^{\alpha}) = \mathcal{L}_V^{\beta}(\hat{w}^{\beta}) \end{array} \right\}. \tag{4.13h}$$

Note that not only continuous residual error functions are incorporated in (4.13), but some additional discrete residual errors also arise at the corner points of structural subdomain Ω^{α}, see figure 4.2. The set of corner points $c = [1, n_c]$ is subdivided into two non-overlapping sets, the set $c_w = [1, n_{cw}]$ of corner points located at the part of the boundary with prescribed displacements $\Gamma_{w\theta}^{\alpha} \cup \Gamma_{wM}^{\alpha}$ and the set $c_V = [1, n_{cV}]$ of corner points located at the part of the boundary with imposed generalised shear forces $\Gamma_{mV}^{\alpha} \cup \Gamma_{\theta V}^{\alpha}$. While the first one (4.13e) represents the approximation error for the out-of-plane displacement w, the later one (4.13f) accounts for the concentrated corner point force related to the discontinuity of the torsion moment. In (4.13f) the $\llbracket \bullet \rrbracket_c$ denotes the discontinuity operator providing measure for the discontinuity in the quantity $\bullet$ at the corner point c due to the non-uniquely defined normal $\mathbf{n}$ or tangential $\mathbf{s}$ vector.

$$\llbracket \bullet \rrbracket_c = \bullet(\mathbf{r}_c^+) - \bullet(\mathbf{r}_c^-). \tag{4.14}$$

Besides the corner residuals introduced in the weighted residual formulation of the boundary and interface conditions (4.13), bending moments can become singular in the corner points for a polygonal plate domain. These singularities are induced either by concentrated loads or by discontinuous boundary conditions. Vanmaele (2007) carried out an extensive survey on this topic and proposed a strategy for including special-purpose functions in the expansion set in order to preserve the favourable convergence rate of the wave based approach. More details about the existence of this phenomenon can be found in section 4.4.
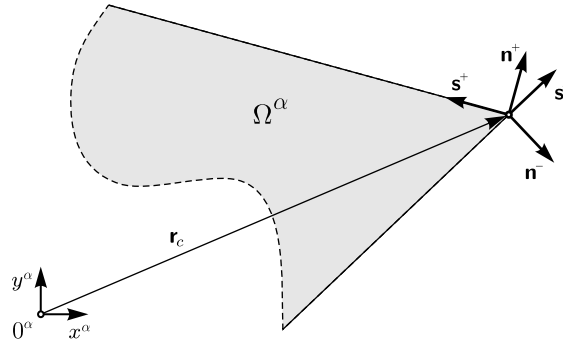
Figure 4.2: Definition of corner residuals

For each subdomain Ω^α, the residual error functions involved (4.13) are orthogonalised with respect to some weighting functions, which are obtained by applying the differential operators (A.28) on a weighting function $\tilde{w}$ (Desmet, 1998)

$$
\begin{aligned}
0 = & \int_{\Gamma^\alpha_{w\theta} \cup \Gamma^\alpha_{wM}} \mathcal{L}^\alpha_V(\tilde{w}^\alpha)(\hat{w}^\alpha - \bar{w})\,\mathrm{d}s + \sum_{c_w=1}^{n_{cw}} [\![\mathcal{L}^\alpha_{Ms}(\tilde{w}^\alpha)]\!]_{c_w} (\hat{w}^\alpha - \bar{w})|_{c_w} \\
& + \int_{\Gamma^\alpha_{w\theta} \cup \Gamma^\alpha_{\theta V}} \mathcal{L}^\alpha_M(\tilde{w}^\alpha)(\mathcal{L}^\alpha_\theta(\hat{w}^\alpha) - \bar{\theta}_n)\,\mathrm{d}s - \int_{\Gamma^\alpha_{wM} \cup \Gamma^\alpha_{MV}} \mathcal{L}^\alpha_\theta(\tilde{w}^\alpha)(\mathcal{L}^\alpha_M(\hat{w}^\alpha) - \bar{M}_n)\,\mathrm{d}s \\
& - \int_{\Gamma^\alpha_{mV} \cup \Gamma^\alpha_{\theta V}} \tilde{w}^\alpha(\mathcal{L}^\alpha_V(\hat{w}^\alpha) - \bar{V}_n)\,\mathrm{d}s - \sum_{c_V=1}^{n_{cV}} \tilde{w}^\alpha|_{c_V} [\![\mathcal{L}^\alpha_{Ms}(\hat{w}^\alpha) - \bar{M}_{ns}]\!]_{c_V} \\
& + \sum_{\beta=1,\beta\neq\alpha}^{N_s} \left[\int_{\Gamma^{(\alpha,\beta)}_{i_{w\theta}}} \mathcal{L}^\alpha_V(\tilde{w}^\alpha)(\hat{w}^\alpha - \hat{w}^\beta)\,\mathrm{d}s + \int_{\Gamma^{(\alpha,\beta)}_{i_{w\theta}}} \mathcal{L}^\alpha_M(\tilde{w}^\alpha)(\mathcal{L}^\alpha_\theta(\hat{w}^\alpha) + \mathcal{L}^\beta_\theta(\hat{w}^\beta))\,\mathrm{d}s \right] \\
& - \sum_{\beta=1,\beta\neq\alpha}^{N_s} \left[\int_{\Gamma^{(\alpha,\beta)}_{i_{MV}}} \mathcal{L}^\beta_\theta(\tilde{w}^\beta)(\mathcal{L}^\beta_M(w^\beta) + \mathcal{L}^\alpha_M(w^\alpha))\,\mathrm{d}s + \int_{\Gamma^{(\alpha,\beta)}_{i_{MV}}} \tilde{w}^\beta(\mathcal{L}^\beta_V(\hat{w}^\beta) - \mathcal{L}^\alpha_V(\hat{w}^\alpha))\,\mathrm{d}s \right].
\end{aligned}
\tag{4.15}
$$

Using the Galerkin approach, the weighting functions are expanded in terms of the same basis functions $\boldsymbol{\Psi}$ as that used for the out-of-plane approximation $\hat{w}$ (4.6)

$$
\tilde{w}^\alpha(\mathbf{r}) = \sum_{i=1}^{M^\alpha_s} \tilde{c}^\alpha_i \Psi^\alpha_i(\mathbf{r}) = \boldsymbol{\Psi}^\alpha(\mathbf{r})\,\tilde{\mathbf{c}}^\alpha,
\tag{4.16}
$$

where $\tilde{\mathbf{c}}$ represents an arbitrary weighting function contribution factor. Substituting the out-of-plane displacement approximation (4.6) and the weighting function (4.16) in the weighted residual formulation (4.15), together with the requirement that this relation should hold for any set of contribution factors $\tilde{\mathbf{c}}$, yields the structural WB model

$$
\begin{bmatrix} (\mathbf{A}^\alpha + \mathbf{C}^\alpha_b) & \mathbf{C}^{\alpha\beta} \\ \mathbf{C}^{\beta\alpha} & (\mathbf{A}^\beta + \mathbf{C}^\beta_b) \end{bmatrix} \begin{Bmatrix} \mathbf{w}^\alpha \\ \mathbf{w}^\beta \end{Bmatrix} = \begin{Bmatrix} \mathbf{b}^\alpha + \mathbf{c}^\alpha_b + \mathbf{c}^{\alpha\beta} \\ \mathbf{b}^\beta + \mathbf{c}^\beta_b + \mathbf{c}^{\beta\alpha} \end{Bmatrix}.
\tag{4.17}
$$

The model contributions $\mathbf{A}^\alpha$ and $\mathbf{b}^\alpha$ represent the uncoupled matrices and vectors defined as follows

$$\mathbf{A}^\alpha = \mathbf{A}^\alpha_w + \mathbf{A}^\alpha_\theta + \mathbf{A}^\alpha_M + \mathbf{A}^\alpha_V \qquad \text{with} \tag{4.18a}$$

$$\mathbf{A}^\alpha_w = \int_{\Gamma^\alpha_{w\theta} \cup \Gamma^\alpha_{wM}} \mathcal{L}^\alpha_V(\mathbf{\Psi}^{\alpha\mathsf{T}})\mathbf{\Psi}^\alpha \,\mathrm{d}s + \sum_{c_w=1}^{n_{cw}} \left[\!\left[\mathcal{L}^\alpha_{Ms}(\mathbf{\Psi}^{\alpha\mathsf{T}}) \right]\!\right]_{c_w} \mathbf{\Psi}^\alpha|_{c_w}, \tag{4.18b}$$

$$\mathbf{A}^\alpha_\theta = \int_{\Gamma^\alpha_{w\theta} \cup \Gamma^\alpha_{\theta V}} \mathcal{L}^\alpha_M(\mathbf{\Psi}^{\alpha\mathsf{T}})\mathcal{L}^\alpha_\theta(\mathbf{\Psi}^\alpha) \,\mathrm{d}s, \tag{4.18c}$$

$$\mathbf{A}^\alpha_M = -\int_{\Gamma^\alpha_{wM} \cup \Gamma^\alpha_{MV}} \mathcal{L}^\alpha_\theta(\mathbf{\Psi}^{\alpha\mathsf{T}})\mathcal{L}^\alpha_M(\mathbf{\Psi}^\alpha) \,\mathrm{d}s, \tag{4.18d}$$

$$\mathbf{A}^\alpha_V = -\int_{\Gamma^\alpha_{mV} \cup \Gamma^\alpha_{\theta V}} \mathbf{\Psi}^{\alpha\mathsf{T}}\mathcal{L}^\alpha_V(\mathbf{\Psi}^\alpha) \,\mathrm{d}s - \sum_{c_V=1}^{n_{cV}} \mathbf{\Psi}^{\alpha\mathsf{T}}|_{c_V} \left[\!\left[\mathcal{L}^\alpha_{Ms}(\mathbf{\Psi}^\alpha) \right]\!\right]_{c_V} \tag{4.18e}$$

and

$$\mathbf{b}^\alpha = \mathbf{b}^\alpha_w + \mathbf{b}^\alpha_\theta + \mathbf{b}^\alpha_M + \mathbf{b}^\alpha_V \qquad \text{with} \tag{4.19a}$$

$$\mathbf{b}^\alpha_w = \int_{\Gamma_{w\theta} \cup \Gamma_{wM}} \mathcal{L}^\alpha_V(\mathbf{\Psi}^{\alpha\mathsf{T}})(\bar{w} - \hat{w}^\alpha_F) \,\mathrm{d}s + \sum_{c_w=1}^{n_{cw}} \left[\!\left[\mathcal{L}_{Ms}(\mathbf{\Psi}^{\alpha\mathsf{T}}) \right]\!\right]_{c_w} (\bar{w} - \hat{w}^\alpha_F)|_{c_w}, \tag{4.19b}$$

$$\mathbf{b}^\alpha_\theta = \int_{\Gamma_{w\theta} \cup \Gamma_{\theta V}} \mathcal{L}^\alpha_M(\mathbf{\Psi}^{\alpha\mathsf{T}}) \left(\bar{\theta}_n - \mathcal{L}_\theta(\hat{w}^\alpha_F) \right) \,\mathrm{d}s, \tag{4.19c}$$

$$\mathbf{b}^\alpha_M = -\int_{\Gamma_{wM} \cup \Gamma_{MV}} \mathcal{L}^\alpha_\theta(\mathbf{\Psi}^{\alpha\mathsf{T}}) \left(\bar{M} - \mathcal{L}_M(\hat{w}_F) \right) \,\mathrm{d}s, \tag{4.19d}$$

$$\mathbf{b}^\alpha_V = -\int_{\Gamma_{mV} \cup \Gamma_{\theta V}} \mathbf{\Psi}^{\alpha\mathsf{T}} \left(\bar{V} - \mathcal{L}^\alpha_V(\hat{w}^\alpha_F) \right) \,\mathrm{d}s - \sum_{c_V=1}^{n_{cV}} \mathbf{\Psi}^{\alpha\mathsf{T}}|_{c_V} \left[\!\left[\bar{M}_s - \mathcal{L}_{Ms}(\hat{w}^\alpha_F) \right]\!\right]_{c_V} \tag{4.19e}$$

with $\bullet^\mathsf{T}$ the transpose operator. The terms $\mathbf{C}^\alpha_b$, $\mathbf{C}^\beta_b$, $\mathbf{c}^\alpha_b$ and $\mathbf{c}^\beta_b$ represent the back-coupling

matrices and vectors given by

$$
\mathbf{C}_b^\alpha = \int_{\Gamma_{i_{w\theta}}^{(\alpha,\beta)}} \mathcal{L}_V^\alpha(\mathbf{\Psi}^{\alpha\mathsf{T}})\mathbf{\Psi}^\alpha \, \mathrm{d}s \qquad + \int_{\Gamma_{i_{w\theta}}^{(\alpha,\beta)}} \mathcal{L}_M^\alpha(\mathbf{\Psi}^{\alpha\mathsf{T}})\mathcal{L}_\theta^\alpha(\mathbf{\Psi}^\alpha) \, \mathrm{d}s, \tag{4.20a}
$$

$$
\mathbf{C}_b^\beta = -\int_{\Gamma_{i_{MV}}^{(\alpha,\beta)}} \mathcal{L}_\theta^v(\mathbf{\Psi}^{\alpha\mathsf{T}})\mathcal{L}_M^\alpha(\mathbf{\Psi}^\alpha) \, \mathrm{d}s - \int_{\Gamma_{i_{MV}}^{(\alpha,\beta)}} \mathbf{\Psi}^{\alpha\mathsf{T}}\mathcal{L}_V^\alpha(\mathbf{\Psi}^\alpha) \, \mathrm{d}s, \tag{4.20b}
$$

$$
\mathbf{c}_b^\alpha = -\int_{\Gamma_{i_{w\theta}}^{(\alpha,\beta)}} \mathcal{L}_V^\alpha(\mathbf{\Psi}^{\alpha\mathsf{T}})\hat{w}_F^\alpha \, \mathrm{d}s \qquad - \int_{\Gamma_{i_{w\theta}}^{(\alpha,\beta)}} \mathcal{L}_M^\alpha(\mathbf{\Psi}^{\alpha\mathsf{T}})\mathcal{L}_\theta^\alpha(\hat{w}_F^\alpha) \, \mathrm{d}s, \tag{4.20c}
$$

$$
\mathbf{c}_b^\beta = \int_{\Gamma_{i_{MV}}^{(\alpha,\beta)}} \mathcal{L}_\theta^\alpha(\mathbf{\Psi}^{\alpha\mathsf{T}})\mathcal{L}_M^\alpha(\hat{w}_F^\alpha) \, \mathrm{d}s + \int_{\Gamma_{i_{MV}}^{(\alpha,\beta)}} \mathbf{\Psi}^{\alpha\mathsf{T}}\mathcal{L}_V^\alpha(\hat{w}_F^\alpha) \, \mathrm{d}s. \tag{4.20d}
$$

The model contributions $\mathbf{C}^{\alpha\beta}$, $\mathbf{C}^{\beta\alpha}$, $\mathbf{c}^{\alpha\beta}$ and $\mathbf{c}^{\beta\alpha}$ represent the coupling matrices and vectors given by

$$
\mathbf{C}^{\alpha\beta} = -\int_{\Gamma_{i_{w\theta}}^{(\alpha,\beta)}} \mathcal{L}_V^\alpha(\mathbf{\Psi}^{\alpha\mathsf{T}})\mathbf{\Psi}^\beta \, \mathrm{d}s \qquad + \int_{\Gamma_{i_{w\theta}}^{(\alpha,\beta)}} \mathcal{L}_M^\alpha(\mathbf{\Psi}^{\alpha\mathsf{T}})\mathcal{L}_\theta^\beta(\mathbf{\Psi}^\beta) \, \mathrm{d}s, \tag{4.21a}
$$

$$
\mathbf{C}^{\beta\alpha} = -\int_{\Gamma_{i_{MV}}^{(\alpha,\beta)}} \mathcal{L}_\theta^\beta(\mathbf{\Psi}^{\beta\mathsf{T}})\mathcal{L}_M^\alpha(\mathbf{\Psi}^\alpha) \, \mathrm{d}s + \int_{\Gamma_{i_{MV}}^{(\alpha,\beta)}} \mathbf{\Psi}^{\beta\mathsf{T}}\mathcal{L}_V^\alpha(\mathbf{\Psi}^\alpha) \, \mathrm{d}s = -\mathbf{C}^{\alpha\beta\mathsf{T}}, \tag{4.21b}
$$

$$
\mathbf{c}^{\alpha\beta} = \int_{\Gamma_{i_{w\theta}}^{(\alpha,\beta)}} \mathcal{L}_V^\alpha(\mathbf{\Psi}^{\alpha\mathsf{T}})\hat{w}_{F_\beta}^\beta \, \mathrm{d}s \qquad - \int_{\Gamma_{i_{w\theta}}^{(\alpha,\beta)}} \mathcal{L}_M^\alpha(\mathbf{\Psi}^{\alpha\mathsf{T}})\mathcal{L}_\theta^\beta(\hat{w}_{F_\beta}^\beta) \, \mathrm{d}s, \tag{4.21c}
$$

$$
\mathbf{c}^{\beta\alpha} = \int_{\Gamma_{i_{MV}}^{(\alpha,\beta)}} \mathcal{L}_\theta^\beta(\mathbf{\Psi}^{\beta\mathsf{T}})\mathcal{L}_M^\alpha(\hat{w}_{F_\alpha}^\alpha) \, \mathrm{d}s - \int_{\Gamma_{i_{MV}}^{(\alpha,\beta)}} \mathbf{\Psi}^{\beta\mathsf{T}}\mathcal{L}_V^\alpha(\hat{w}_{F_\alpha}^\alpha) \, \mathrm{d}s. \tag{4.21d}
$$

The model is assembled by minimising the approximation errors (4.13) at boundary and interface conditions in an integral sense. Hence, construction of the matrix system (4.17) requires the integration of the residual errors over the edges of different subdomains. In the practical implementation, the terms (4.18), (4.19), (4.20) and (4.21), which involve the line integrals, are evaluated in a numerical manner using the Gauss-Legendre quadrature rule. For the selection of the number of Gauss points used along one boundary segment, the following strategy is adopted

$$
n_{gp} \geq 2\max\left(\|k_{\bullet x}^\alpha\|, \|k_{\bullet y}^\alpha\|\right) \tag{4.22}
$$

with n_{gp} the number of Gauss points used per isoparametric coordinate. The resulting number of integration points applied for the actual boundary segment is then obtained by multiplying n_{gp} with the length of the corresponding boundary edge. This rule ensures that at least twelve Gauss points are applied per shortest wavelength included in the truncated wave function set (Van Hal et al., 2000).

4.3 Validation example: convex plate

The first set of validation examples considers problems related to convexly shaped domains. The problems consist of a polygonal plate of main dimensions 0.69×0.45 m, see figure 4.3. The plate is made of aluminium having a mass density of $\rho = 2\,650$ kg/m^3, the Young's modulus $E = 69 \cdot 10^9$ Pa and the Poisson's ratio $\nu = 0.3$. The plate has a thickness of $t = 0.0029$ m and is excited by a point force $F = 1$ N applied at the position $\mathbf{r}_F = (0.51, 0.03)$ m. The following response points are used to evaluate the frequency response functions RP1 = $(0.37, 0.34)$ m, RP2 = $(0.28, 0.12)$ m and RP3 = $(0.025, 0.025)$ m. In sections 4.3.1, 4.3.2 and 4.3.3, respectively, three cases with different boundary conditions are considered.
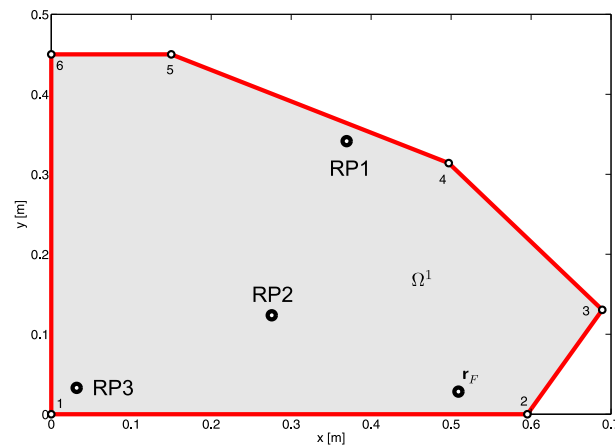
Figure 4.3: Convex plate

The FE calculations utilise the *MSC.Nastran* solver (MSC Software Corporation, 2008) and are performed using the direct solution method, while the WBT code is implemented in *MATLAB* (MathWorks, Inc., 2007). All calculations presented in this section are performed on a 2.26 GHz dual-core *Intel*-based computer using 4 Gbyte RAM and running the *Windows Vista 64-bit* operating system.

4.3.1 Clamped plate

In the first case, all boundary segments are clamped, and both the response fields and the frequency response functions are considered for the validation. The reference FE model consists of $34\,061$ nodes yielding $199\,584$ degrees of freedom. The nodes constitute a quad4 dominant mesh containing $33\,758$ linear quad4 and tria3 elements with a maximum element edge size of $h_{max} = 0.0025$ m. As the plate has a convex shape, the WB model consists of only one subdomain. Figures 4.4 and 4.5 show the predicted fields at 940 Hz and 1 580 Hz, respectively. The displacement fields calculated at the selected frequencies are mainly driven by the shapes of mode number 15 at 857.4 Hz and mode number 29 at 1542 Hz, respectively. The WB predictions are carried out by employing the frequency-dependent truncation strategy with $T = 4$ yielding, respectively, 220 and 284 degrees of freedom. Both prediction results demonstrate the accuracy of the wave approach. In particular, it is evident that the clamped boundary conditions have been taken into account correctly.

Figure 4.6(a) compares the predicted structural frequency response functions (w/F) evaluated at response point RP1. The reference FE model, see table 4.1, requires approximately 7 307 s to
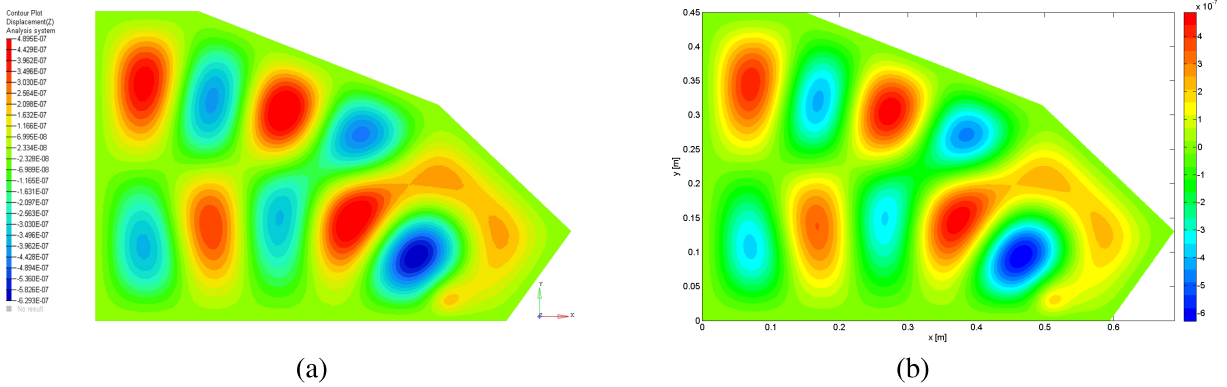
Figure 4.4: Clamped plate: the real part of the out-of-plane displacement at 940 Hz: (a) FEM, (b) WBT
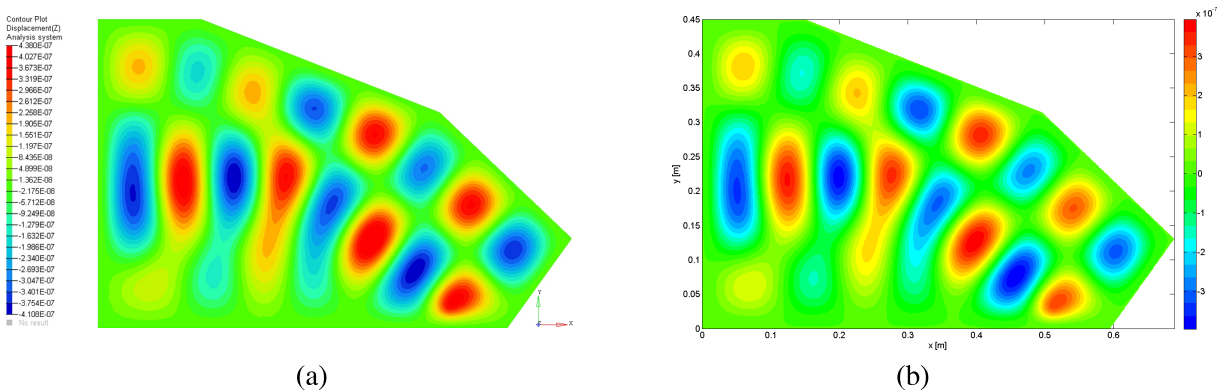
Figure 4.5: Clamped plate: the real part of the out-of-plane displacement at 1 580 Hz: (a) FEM, (b) WBT

attribute	denotation	value
solution scheme		FEM direct
number of nodes	#nod	34 061
number of elements	#ele	33 758
mesh topology	topo	quad4 dominant
maximum element edge size	h_{max}	0.0025 m
degrees of freedom	DOF	199 584
FRF range	f_{min}, f_{max}	1–2 000 Hz
FRF step	Δf	1 Hz
number of modes up to f_{max}	#mod	40
CPU time needed for FRF	t_{FRF}	7 307 s

Table 4.1: Clamped plate: attributes of FE model

perform the direct frequency response analysis from 1 to 2 000 Hz with a frequency resolution of 1 Hz. The first WB model employs the frequency-dependent truncation strategy with $T = 2$ and requires roughly 2 208 s to calculate the same response, see table 4.2. The indicated CPU time for the wave model consists of both assembling the system of algebraic equations and its solution. Both the FE and WB predictions correspond well except for the lower frequency

attribute	denotation	value
number of subdomains	N_s	1
truncation strategy		frequency-dependent
truncation parameter	T	2
degrees of freedom	$\dim\mathbf{\Psi}$	16–160
FRF range	f_{min}, f_{max}	1–2 000 Hz
FRF step	Δf	1 Hz
CPU time needed for FRF	t_{FRF}	2 208 s

Table 4.2: Clamped plate: attributes of WB model
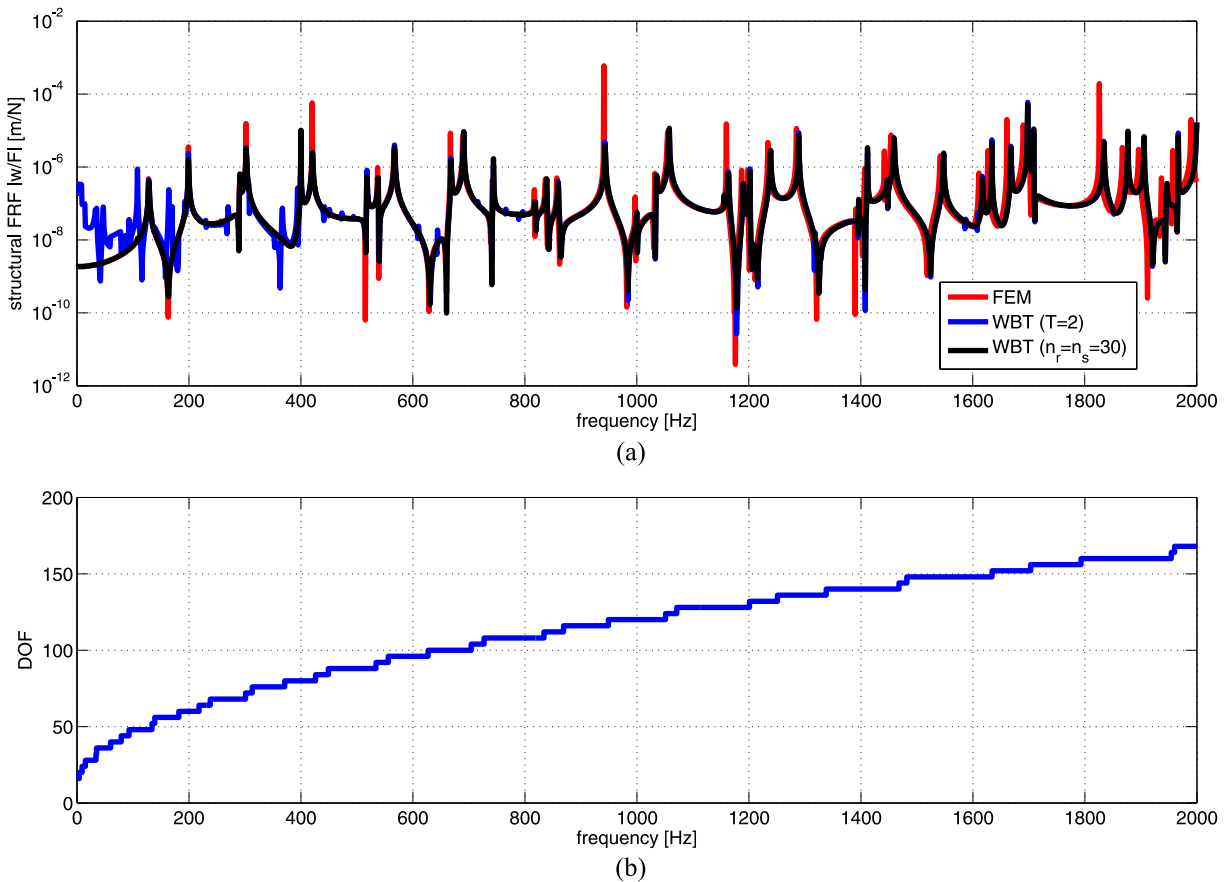
Figure 4.6: Clamped plate: (a) frequency response functions at point RP1 and (b) the number of wave functions for $T = 2$

range up to approximately 700 Hz, where a slight deterioration of the WB prediction can be observed. This error is caused by the relatively low number of wave functions resulting from the frequency-dependent truncation rule (4.12). Figure 4.6(b) plots the evolution of the number of wave functions over the frequency. In the critical range the number of wave functions only varies between 16 and 100. Hence, increasing the number of wave functions in the lower frequency range resolves the problem, as can be seen in the prediction obtained by the wave model using a constant wave function set truncation over the frequency (black curve). This wave model uses $n_r = n_s = 30$ truncation numbers yielding 248 degrees of freedom and requires 12 223 s to carry out the frequency response. At higher frequencies both wave models perform

equally, although a slight variation in the FRF compared to FE can be observed. The small frequency shift in FRF corresponds to the different underlying plate theories. While the standard structural dynamics FE packages (e.g. *MSC.Nastran*) adopt the Reissner-Mindlin thick plate model, the WBT is formulated in terms of the Kirchhoff thin plate theory, see sections A.2.1 and A.2.2. Due to the absence of the effect of shear stress, in general the Kirchhoff thin plate theory tends to overestimate the resonance frequencies. Vanmaele (2007) carried out a qualitative analysis of both theories with respect to their application for the plate bending problems.

4.3.2   Clamped-free plate

In the second example, only one edge is clamped, while the remaining part of the boundary is kept free. Once again, the validation of the wave based approach is carried out in terms of both the predicted response fields and the frequency response functions. Besides the FE analysis, a comparison with an experimentally acquired data is also considered (Rejlek and Priebsch, 2011). Figure 4.9(a) illustrates the experimental set-up – the plate is clamped in a vice and excited by a shaker equipped with the force cell, while the deflection shape is scanned by the laser vibrometer. A scanning mesh is used for the laser vibrometry as shown in figure 4.8(a). The measurements are carried out in a frequency range 1–2 048 Hz with a resolution of $\Delta f = 0.125$ Hz, and the resulting experimental data is obtained by averaging a set of four measurement samples.

attribute	denotation	value
solution scheme		FEM direct
number of nodes	#nod	34 061
number of elements	#ele	33 758
mesh topology	topo	quad4 dominant
maximum element edge size	h_{max}	0.0025 m
degrees of freedom	DOF	203 976
FRF range	f_{min}, f_{max}	1–500 Hz
FRF step	Δf	1 Hz
number of modes up to f_{max}	#mod	20
CPU time needed for FRF	t_{FRF}	2 703 s

Table 4.3: Clamped-free plate: attributes of FE model

Figure 4.7 plots the real part of the out-of-plane displacement at the frequency 77 Hz and 425 Hz, respectively. The displacement fields calculated at the selected frequencies are mainly driven by the corresponding shapes of mode number 5 at 82.5 Hz and mode number 18 at 402 Hz, respectively. For the FE analyses, the same mesh as was applied in section 4.3.1 is utilised, while the WB predictions use the $T = 4$ model. Once again, the contour plots prove the accurate representation of the boundary conditions.

Figure 4.10 displays the structural frequency response functions (w/F) up to 500 Hz evaluated at position RP2 corresponding to a laser scanning point 30, see figure 4.8. A fairly good agreement between both the measurement and simulation results is achieved in the whole frequency range of interest. While the reference FE model requires 2 703 s to carry out the direct response analysis, the $n_r = n_s = 20$ WB model consisting of merely 168 degrees of freedom requires

(a) measurement 77 Hz

(d) measurement 425 Hz

(b) FEM 77 Hz

(e) FEM 425 Hz

(c) WBT 77 Hz

(f) WBT 425 Hz
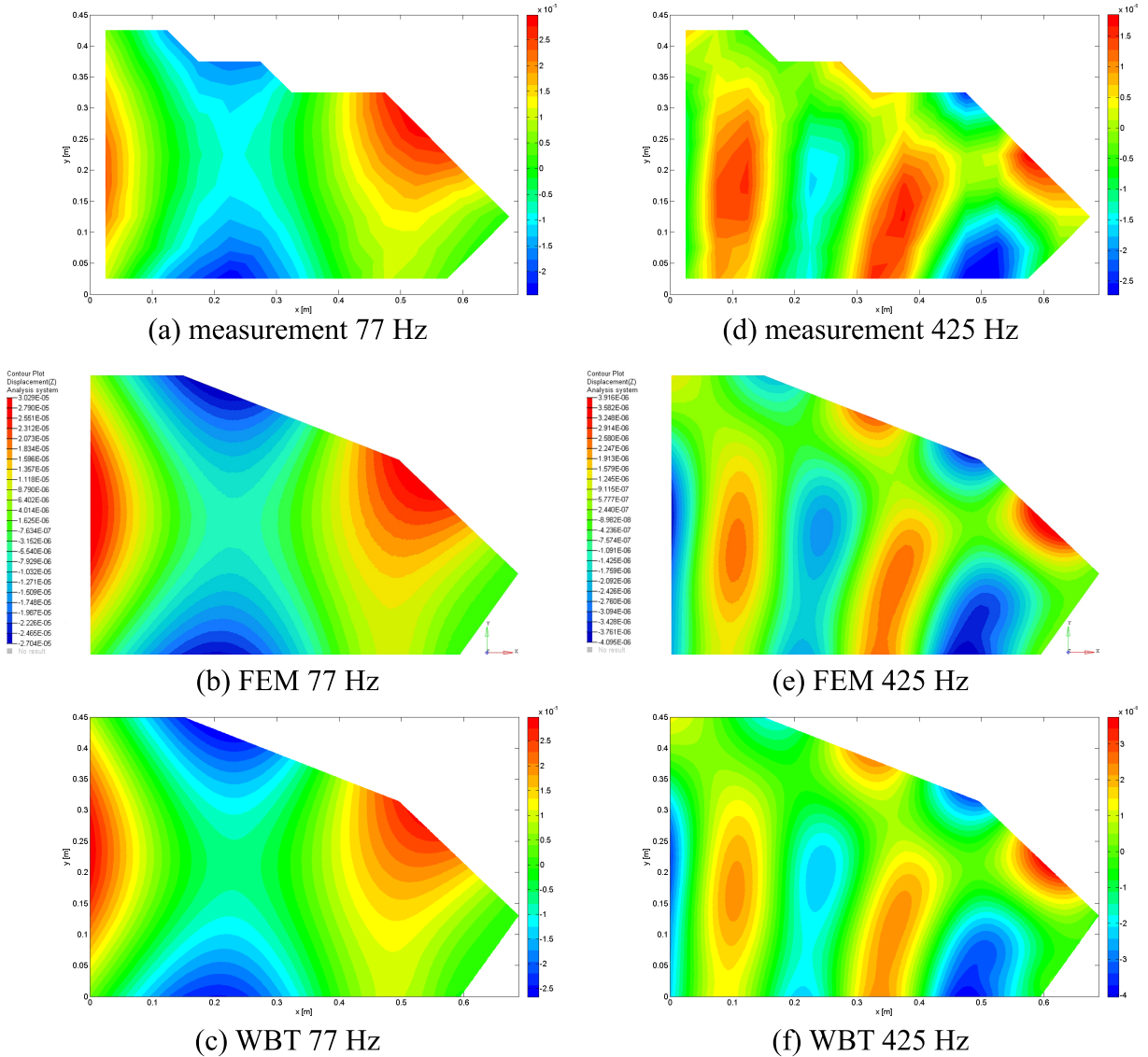
Figure 4.7: Clamped-free plate: the real part of the out-of-plane displacement at (a)–(c) 77 Hz and (d)–(f) 425 Hz (Rejlek and Priebsch, 2011)

attribute	denotation	value
number of subdomains	N_s	1
truncation strategy		constant
truncation parameters	n_r, n_s	20
degrees of freedom	$\dim \mathbf{\Psi}$	168
FRF range	f_{min}, f_{max}	1–500 Hz
FRF step	Δf	1 Hz
CPU time needed for FRF	t_{FRF}	1 465 s

Table 4.4: Clamped-free plate: attributes of WB model

1 465 s for the same calculation. The attributes of both the FE and WB model are summarised in table 4.3 and 4.4, respectively.

(a)

(b)
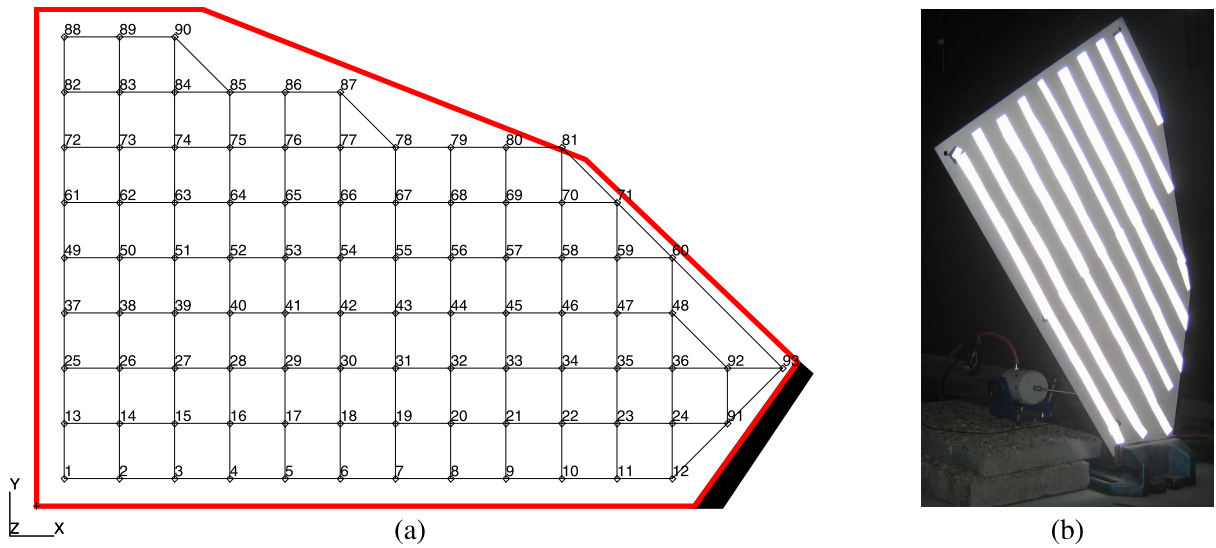
Figure 4.8: The laser vibrometry: (a) definition of scanning mesh – the physical boundary is indicated in read; the black quadrangle on the right hand side indicates the segment of the boundary clamped in a vice during the measurements and (b) the stripes made of reflexive material used to improve the signal-noise ratio

(a)

(b)
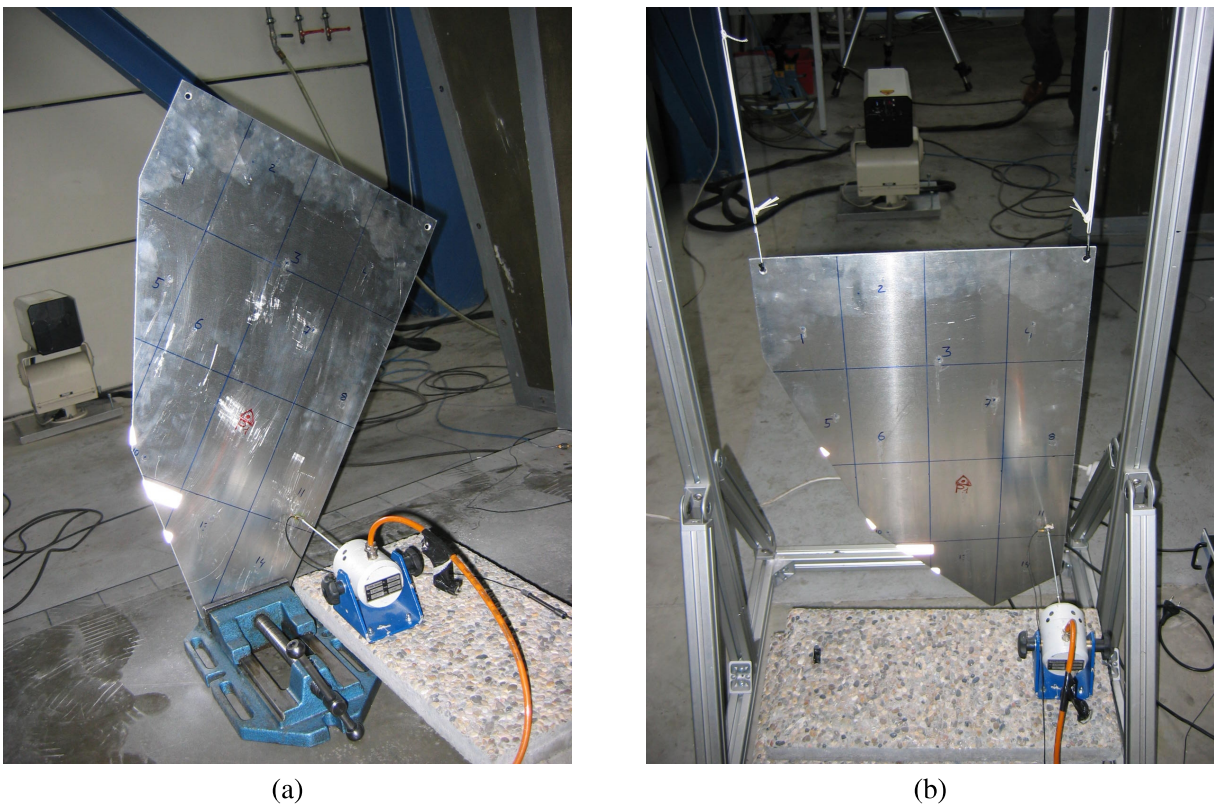
Figure 4.9: The experimental measurement set-up: (a) the clamped-free plate and (b) free-free plate (Rejlek and Priebsch, 2011)
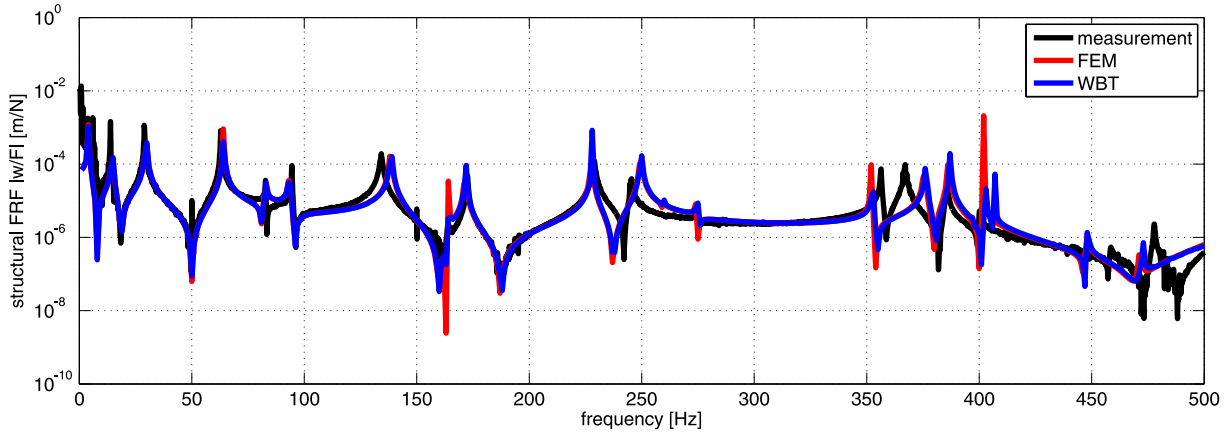
Figure 4.10: Clamped-free plate: frequency response functions at point RP2 (Rejlek and Priebsch, 2011)

4.3.3 Free plate

The last case consists of a free plate. Similar to the previous example discussed in section 4.3.2, both the measurement and the fine reference FE model are considered for the validation study. During the measurement campaigns the plate is suspended from an auxiliary frame by two flexible lightweight cords, see figure 4.9(b). Once again, the plate is excited by a shaker, and the resulting dynamic velocity field is scanned by the laser vibrometer. Figure 4.11 shows the real part of the out-of-plane displacement field at the frequencies of 44 Hz and 372 Hz. The displacement fields calculated at the selected frequencies are mainly driven by the corresponding shapes of mode number 2 at 46.5 Hz and mode number 14 at 365.5 Hz. The FE predictions utilise the reference FE model based on the computational mesh introduced in section 4.3.1. The WB model obeys the $T = 4$ truncation rule. The contour plots confirm that the plate dynamics are captured correctly.

attribute	denotation	value
solution scheme		FEM direct
number of nodes	#nod	34 061
number of elements	#ele	33 758
mesh topology	topo	quad4 dominant
maximum element edge size	h_{max}	0.0025 m
degrees of freedom	DOF	204 366
FRF range	f_{min}, f_{max}	1–1 000 Hz
FRF step	Δf	1 Hz
number of modes up to f_{max}	#mod	35[1]
CPU time needed for FRF	t_{FRF}	4 073 s

Table 4.5: Free plate: attributes of FE model

Figure 4.12(a) compares the structural frequency response functions (w/F) at point RP3 predicted up to $1\,000$ Hz by FEM and WBT, see table 4.5 and 4.6, with the one being measured

---

[1]Non-rigid body modes.

(a) measurement 44 Hz

(d) measurement 372 Hz

(b) FEM 44 Hz

(e) FEM 372 Hz

(c) WBT 44 Hz

(f) WBT 372 Hz
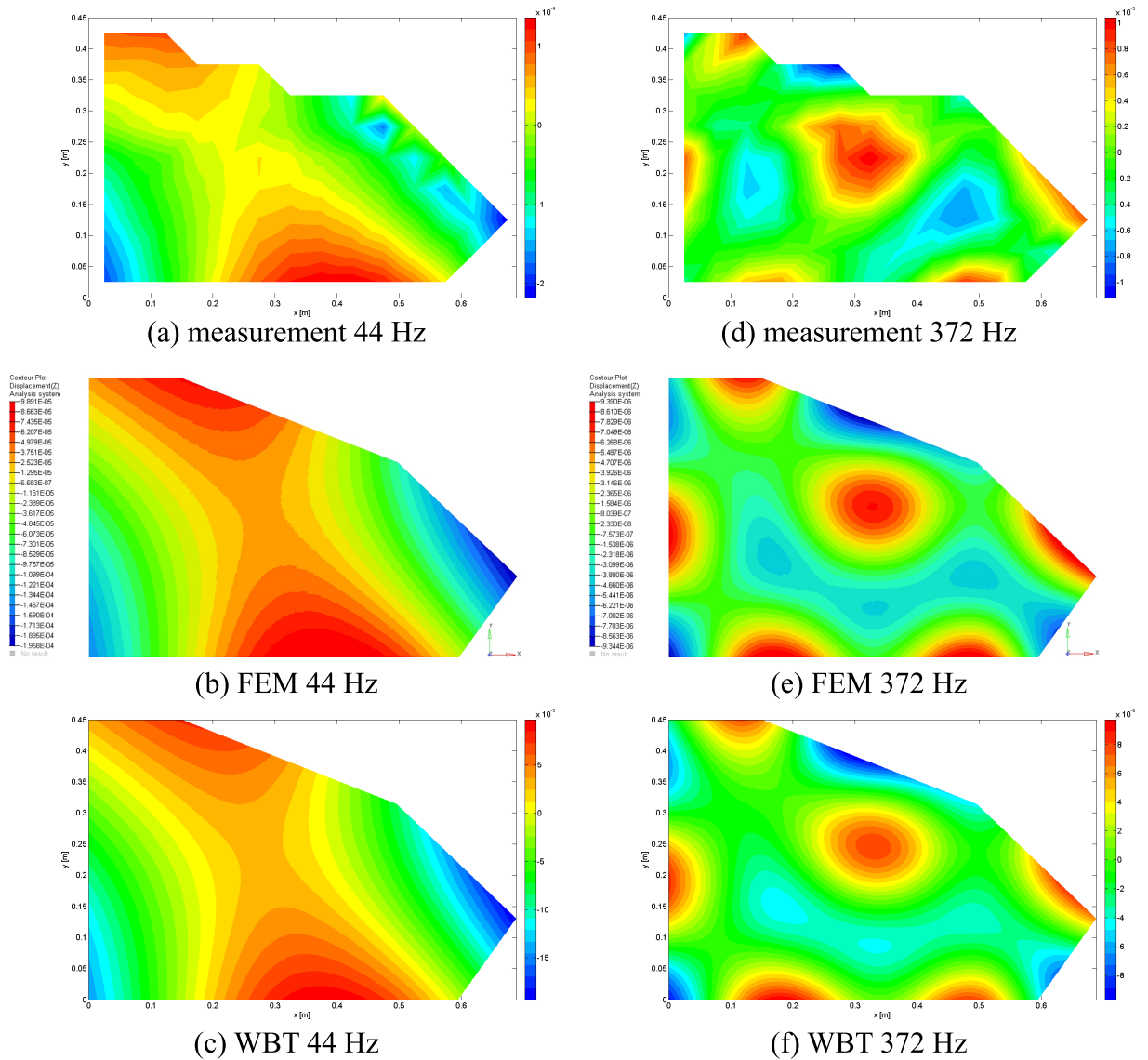
Figure 4.11: Free plate: the real part of the out-of-plane displacement at (a)–(c) 44 Hz and (d)–(f) 425 Hz

attribute	denotation	value
number of subdomains	N_s	1
truncation strategy		frequency-dependent
truncation parameter	T	2
degrees of freedom	$\dim \boldsymbol{\Psi}$	16–120
FRF range	f_{min}, f_{max}	1–1 000 Hz
FRF step	Δf	1 Hz
CPU time needed for FRF	t_{FRF}	1 129 s

Table 4.6: Free plate: attributes of WB model

in laser scanning point 1. The computational load involved in performing the direct response analysis with the reference FE model reaches 4 073 s, while the $T = 2$ wave models requires

about 1 129 seconds. Figure 4.12(b) plots the WB model degrees of freedom against frequency. An almost perfect match between both predictions can be observed across the entire frequency range, while some difference compared to the measured data can be seen. The deterioration of the experimental results can be observed from 250 Hz up to 500 Hz mainly in the range between two modes, which can be related to bad coherence of the measurement data. Nevertheless, the global modal characteristics of the system are captured accurately up to 250 Hz. Once again, at the higher frequencies, slight discrepancies arise due to the different plate theories involved in the formulation of FEM and WBT, see section 4.3.1.

(a)

(b)
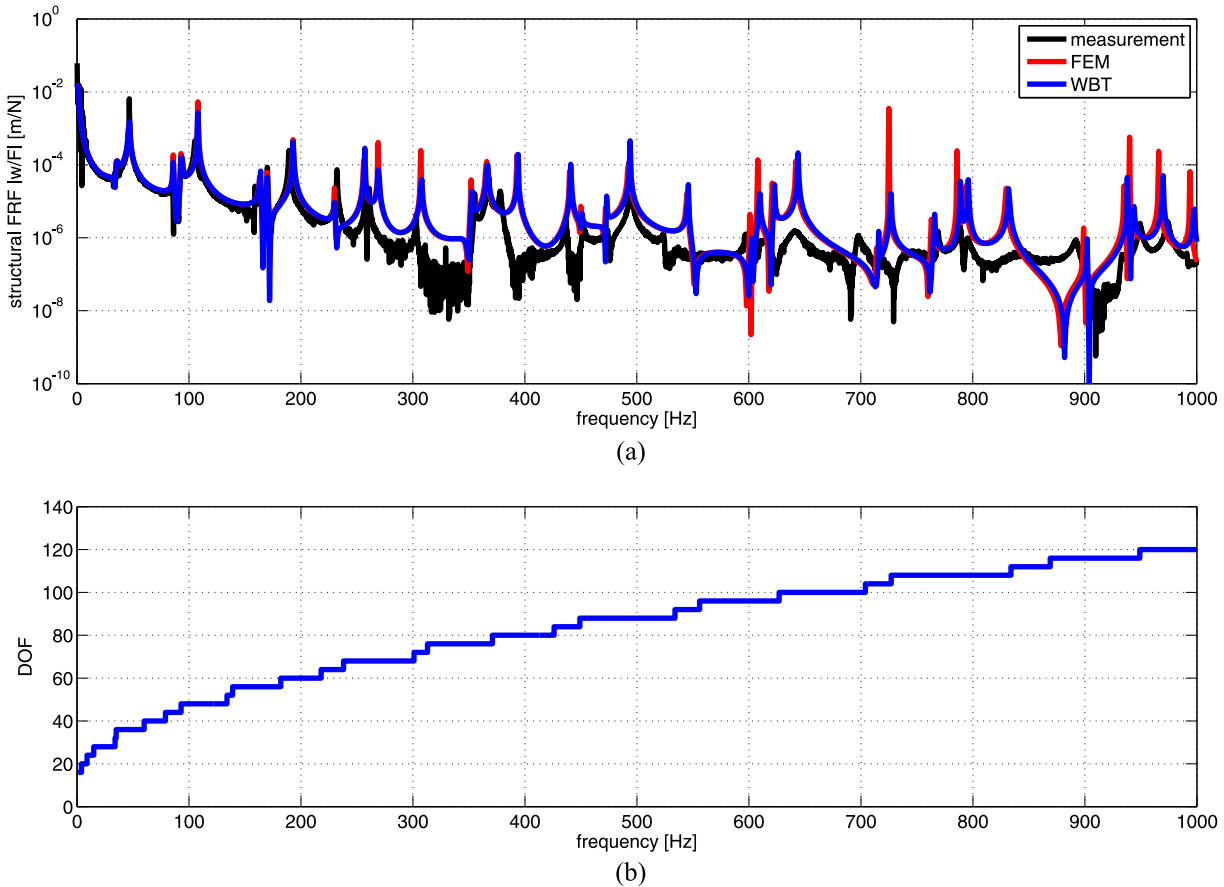
Figure 4.12: Free plate: (a) frequency response functions at point RP3 and (b) the number of wave functions for $T = 2$

4.4   Validation example: non-convex plate

The second validation example consists of a non-convex plate of the main dimensions 2.2×1 m, see figure 4.13. The plate is made of steel with a mass density of $\rho = 7\,800$ kg/m^3, the Young's modulus $E = 2 \cdot 10^{11}$ Pa and the Poisson's ratio $\nu = 0.25$. The plate has a thickness of $t = 0.003$ m and is subjected to a point force $F = 1$ N applied at the position $\mathbf{r}_F = (0.2, 0.5)$ m. For the evaluation of frequency response functions, the following response point RP1 $= (1.66, 0.56)$ m is selected.

A fine FE model consisting of $17\,649$ nodes, which yields $102\,396$ degrees of freedom, is used as a reference. The resulting quad4 dominant mesh consists of $17\,372$ linear quad4 and tria3
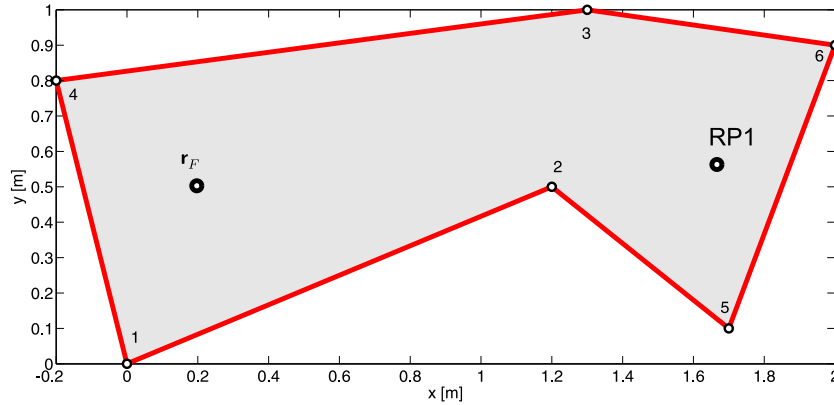
Figure 4.13: Non-convex plate

elements with a maximum element edge size of $h_{max} = 0.01$ m. Since the problem is no longer convex, domain decomposition strategy has to be employed. Figure 4.14 illustrates a possible domain subdivision resulting in two non-overlapping subdomains Ω^1 and Ω^2 coupled via common interface $\Gamma_i^1 = \Gamma_i^2$. Moreover, the bounding boxes are depicted in conjunction with the corresponding local coordinate system $(x^\bullet, y^\bullet)$.
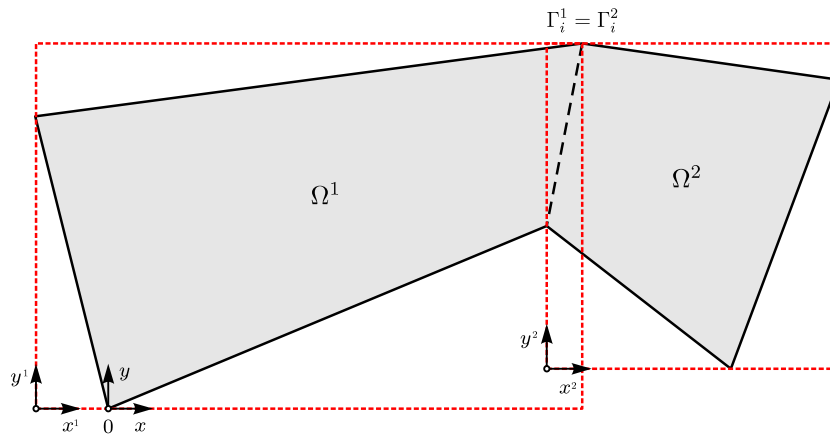
Figure 4.14: Subdivision of the WB model into two convex subdomains – the corresponding bounding boxes with the designated local coordinate systems $(x^\bullet, y^\bullet)$ are indicated in red

For the validation study, both the predicted response fields and the frequency response functions are considered. The calculations are performed on the same computer platform as described in the previous section 4.3. Figures 4.15 and 4.16 compare the calculated out-of-plane displacement fields at 100 and 501 Hz, respectively. The WB predictions are carried out by employing the frequency-dependent truncation rule with $T = 4$ yielding 272 and 584 degrees of freedom, respectively. Figures 4.15 and 4.16 prove that both the boundary and interface conditions have been correctly accounted for.

Two wave models are considered for the prediction of structural frequency response functions (w/F) from 1 to 500 Hz with a resolution of 1 Hz. The first one employs the frequency-depended truncation scheme with $T = 2$, which results in a model with a total number of degrees of freedom that varyies between 36 and 304, see figure 4.17(b). This model, see table 4.8, requires about 662 s to perform the calculation. The second wave model uses a fixed truncation

(a)   (b)
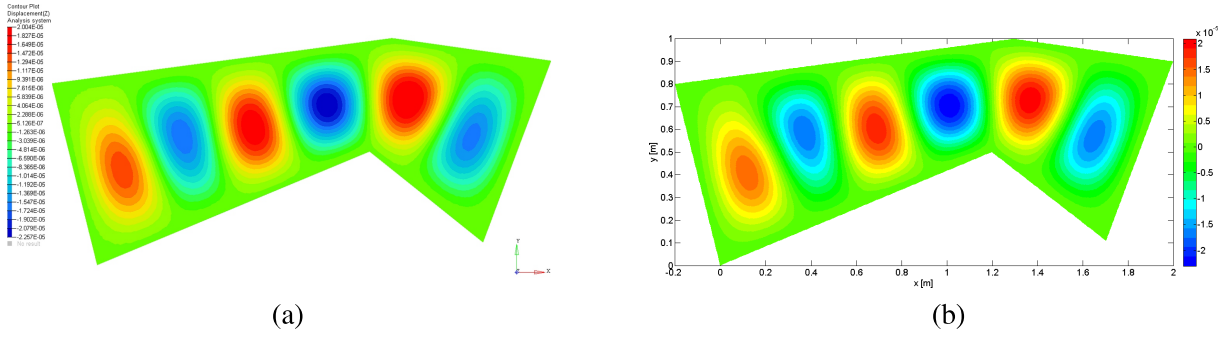
Figure 4.15: Non-convex plate: the real part of the out-of-plane displacement at 100 Hz: (a) FEM, (b) WBT

(a)   (b)
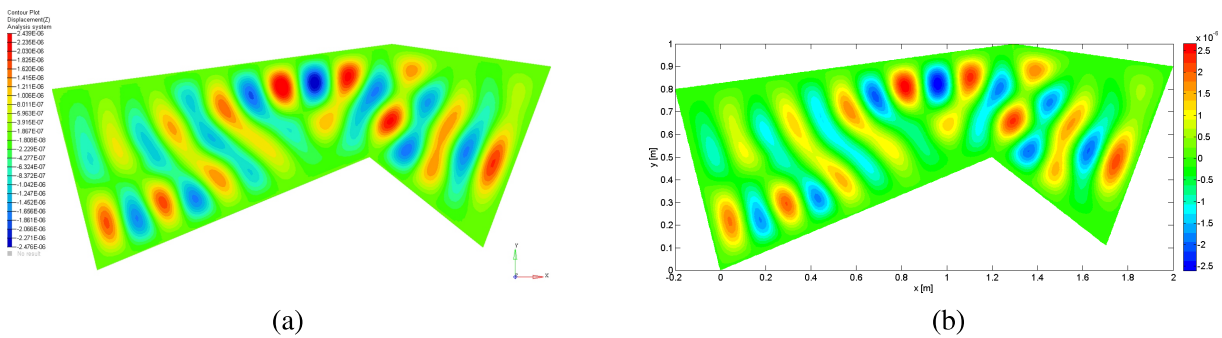
Figure 4.16: Non-convex plate: the real part of the out-of-plane displacement at 501 Hz: (a) FEM, (b) WBT

of the wave function set with $n_r = n_s = 30$, which yields 496 degrees of freedom over the whole frequency range and requires $3\,095$ s. For the reference FE model it takes approximately 772 seconds to perform the analysis of 500 frequency steps, see table 4.8. Figure 4.17(a) plots the resulting frequency response functions up to 500 Hz at position RP1. Even though the WB predictions vary slightly from those of the FE model, the main resonance frequencies are captured fairly well in the frequency range considered.

attribute	denotation	value
solution scheme		FEM direct
number of nodes	#nod	17 649
number of elements	#ele	17 372
mesh topology	topo	quad4 dominant
maximum element edge size	h_{max}	0.01 m
degrees of freedom	DOF	102 396
FRF range	f_{min}, f_{max}	1–500 Hz
FRF step	Δf	1 Hz
number of modes up to f_{max}	#mod	53
CPU time needed for FRF	t_{FRF}	772 s

Table 4.7: Non-convex plate: attributes of FE model

attribute	denotation	value
number of subdomains	N_s	2
truncation strategy		frequency-dependent
truncation parameter	T	2
degrees of freedom	$\dim\mathbf{\Psi}$	36–304
FRF range	f_{min}, f_{max}	1–500 Hz
FRF step	Δf	1 Hz
CPU time needed for FRF	t_{FRF}	662 s

Table 4.8: Non-convex plate: attributes of WB model
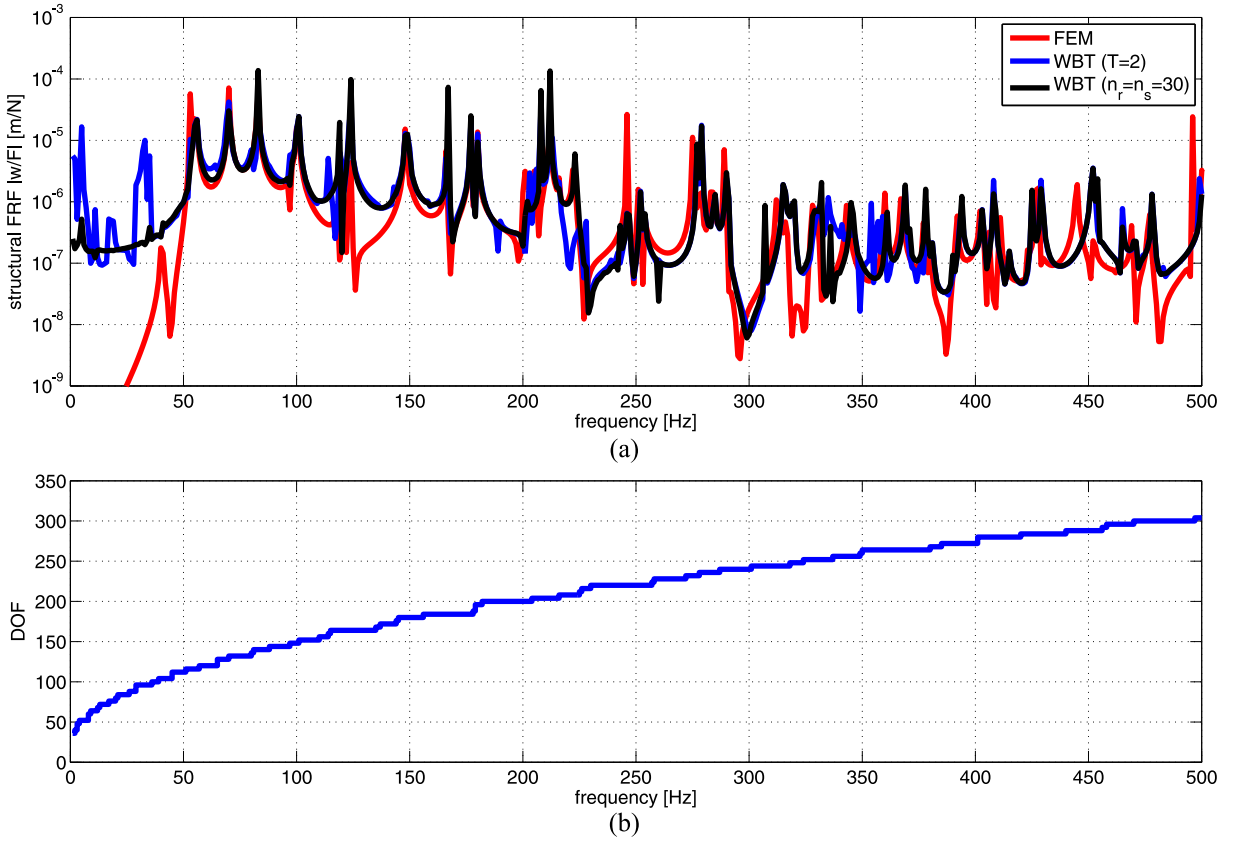
Figure 4.17: Non-convex plate: (a) frequency response functions at point RP1 and (b) the number of wave functions for $T = 2$

The deterioration of the prediction accuracy is related to the existence of the corner stress singularities. Vanmaele et al. (2007) proved, that the bending moment singularities occur if the internal angle α formed by the two adjacent edges exceeds a certain critical value. For the clamped-clamped corner these singularities can only arise for $\alpha > \pi$, which is, however, the case with corner 2, see figure 4.13. Obviously, this can only happen in a non-convex problem, which is also the reason, why the convex clamped plate problem discussed in section 4.3.1 does not suffer from the existence of such phenomena. Since only convex structures are considered in the later formulation of the wave based technique for the analysis of fully coupled vibro-acoustic problems, the problem of the corner stress singularities is not further addressed within the framework of this dissertation.

4.5 Summary

This chapter presented the methodology and application of the WBT for the thin, flat plate bending problems. The plate bending problems represent the first WBT developments made in the framework of this doctoral research project. Two validation examples were considered, namely a single-domain and a multi-domain problem. The latter also involves the domain subdivision strategy, since its solution domain has a non-convex shape. For validation purposes, a reference FE model consisting of very fine mesh was utilised. In order to get the most accurate reference results possible, the direct frequency response analysis is preferred to the modal superposition technique. The FE predictions were carried out by using *MSC.Nastran* – a standard FE package, whose plate bending elements adopt the Reissner-Mindlin theory. The formulation of WBT, in contrast, uses the Kirchhoff thin plate theory, which omits the effects of both the shear deformations and the rotatory inertia. As a result, a slight frequency shift is introduced in the frequency responses calculated by FEM and WBT. Furthermore, experimentally acquired data was also considered during the validation study of the single-domain problem for specific boundary condition cases.

Both validation examples proven the feasibility of WBT for solving steady-state plate bending problems. For all cases considered, WBT performs faster than FEM while achieving a comparable prediction accuracy. However, a deterioration of the prediction accuracy can be observed in the case of the non-convex problem. This is mainly due to the presence of the so-called stress singularities, which can arise at corner points under certain conditions. The existence of these phenomena can compromise the favourable computational efficiency of WBT. Nevertheless, the addition of some special-purpose functions into the set of basis functions to mitigate this problem preserves the computational efficiency of the method (Vanmaele, 2007).

Future work should address further efficiency improvements, which can be achieved by revising the WBT implementation. In the current doctoral research project, the FE analyses were carried out by *MSC.Nastran* – a high-performance CAE tool which has undergone more than 40 years of continuous evolution. The *Nastran* solver is implemented in *Fortran*, whereas WBT implementation relies on *MATLAB*. Moreover, the existing WBT code predominately uses loop-based statements instead of vectorisation techniques. Rebuilding the code with respect to the vectorisation of loops can improve the performance significantly by fully exploiting the multi-core layout of the modern CPU architectures. In this way, the computational efficiency of WBT can be further enhanced.

In view of scope of this doctoral research project only the classical thin plate theory has been applied for the description of the out-of-plate bending motion. As a result, only flat plates are considered throughout this dissertation. This decision was mainly motivated by the simplicity of the involved mathematical model and the further extension the WB methodology towards fully coupled vibro-acoustic problems, in which only plane structural-acoustic interfaces are considered.

Chapter 5

The Wave Based Technique for uncoupled, unbounded acoustic problems

---

This chapter outlines the methodology of the wave based approach and its application for a steady-state analysis of three-dimensional uncoupled, unbounded acoustic problems. Section 5.1 restates the problem definition. Section 5.2 presents the basic concepts of WBT for unbounded acoustic problems. In particular, the concept of the domain truncation is introduced therein. The computational efficiency of WBT is demonstrated on several validation examples. Section 5.3 reports on the application to wave scattering problems. Due to the simple geometry of the scatterer, it is possible to derive an analytical solution, which is then used as a reference for the convergence study. The remaining validation examples involve semi-infinite solution domains. In section 5.4, the WBT is applied for the sound radiation analysis of a baffled piston radiator. Again, it is possible to obtain an analytical solution in this particular case, which becomes the reference for the subsequent convergence analysis. The next validation example presents a more complex problem, in which the domain decomposition strategy is applied in the bounded part of the wave model, see section 5.5. The final validation example considers an application to an industry-sized problem, see section 5.6, which demonstrates the practical applicability of the wave based approach. Section 5.7 closes the chapter with a summary.

5.1   Problem definition

The steady-state acoustic pressure perturbation field in an inviscid fluid is governed by the Helmholtz equation

$$\nabla^2 p(\mathbf{r}) + k^2 p(\mathbf{r}) = -\mathrm{j}\rho\omega q \delta(\mathbf{r}, \mathbf{r}_q), \quad \forall \mathbf{r} \in \Omega \tag{5.1}$$

with the corresponding boundary conditions defined as follows

- pressure boundary condition (Dirichlet/essential) $\forall \mathbf{r} \in \Gamma_p$:

$$p(\mathbf{r}) = \bar{p}(\mathbf{r}), \tag{5.2a}$$

- normal velocity boundary condition (Neumann/natural) $\forall \mathbf{r} \in \Gamma_v$:

$$\mathcal{L}_v(p(\mathbf{r})) = \frac{\mathrm{j}}{\rho\omega}\frac{\partial p(\mathbf{r})}{\partial n} = \bar{v}_n(\mathbf{r}), \tag{5.2b}$$

- normal impedance boundary condition (Robin/mixed) $\forall \mathbf{r} \in \Gamma_Z$:

$$\mathcal{L}_Z(p(\mathbf{r})) = \mathcal{L}_v(p(\mathbf{r})) - \frac{p(\mathbf{r})}{\bar{Z}_n(\mathbf{r})} = 0. \tag{5.2c}$$

As the solution domain Ω is unbounded, the Sommerfeld radiation condition must also be imposed at Γ_∞ in order to ensure, that no acoustic energy reflections occur at the infinity

$$\lim_{|\mathbf{r}|\to\infty}\left[|\mathbf{r}|\left(\frac{\partial p(\mathbf{r})}{\partial|\mathbf{r}|} + \mathrm{j}kp(\mathbf{r})\right)\right] = 0. \tag{5.3}$$

5.2   Basic concepts of the Wave Based Technique

The wave based prediction technique has been developed as an alternative method for solving steady-state acoustic problems in the mid-frequency range. Based on an indirect Trefftz approach, the WBT has proven to be a robust prediction tool for interior acoustics. However, a considerable class of real-life acoustic applications involves the analysis of problems in unbounded spatial domains, such as sound scattering and sound radiation problems. Besides the boundary element method, which is based on boundary integral formulation of the governing differential equation, various strategies employing the standard finite element schemes have been developed in order to tackle unbounded problems, such as non-reflecting boundary condition, infinite elements or perfectly matched layers. Although based on different approaches, all these concepts share the same basic idea, namely introducing an artificial truncation boundary that divides the infinite domain into the bounded and unbounded part.

As WBT inherently consists in discretisation of an entire solution domain, an additional treatment of the interior WB formulation is required (Pluymers et al., 2005) in order to tackle the problems involving unbounded spatial domains. By adopting a similar strategy, as discussed in the previous paragraph (i.e. by introducing an artificial truncation boundary Γ_T, see figure 5.1), the solution domain Ω is divided into a bounded and unbounded part $\Omega = \Omega^b + \Omega^u$. While the conventional interior formulation is used in the bounded part, some novel functions, which also satisfy the Sommerfeld radiation condition (5.3), are adopted in the unbounded part of the WB model. The bounded part is further subdivided into convex subdomains. A distinction is made between two types of unbounded problems – the free-field problems, which involve an unbounded spatial domain and the semi-infinite ones, which introduce a rigid baffle plane. The concepts introduced in sections 5.2.1, 5.2.2 and 5.2.3 are based on the work of Pluymers (2006) and Diwoky et al. (2008).
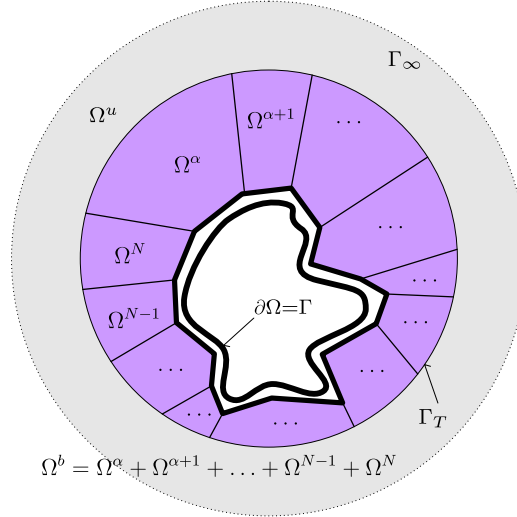
Figure 5.1: The concept of the truncation boundary Γ_T (Rejlek et al., 2008b)

5.2.1 Domain decomposition

Similar to the structural plate plate bending problem discussed in section 4.2.1, partitioning into non-overlapping convex subdomains is required within the bounded part of the wave model in order to ensure the convergence of WBT

$$\Omega = \bigcup_{\alpha}^{N_a} \Omega^\alpha \quad \text{with} \quad \bigcap_{\alpha}^{N_a} \Omega^\alpha = \emptyset, \tag{5.4}$$

see figure 5.2. In addition to boundary conditions (5.2) imposed at the physical boundary of the problem, the following coupling conditions have to be prescribed at the common interface Γ_i between the subdomains:

- coupling condition type 1 $\forall \mathbf{r} \in \Gamma_i^{(\alpha,\beta)}$:

$$\mathcal{L}_v^\alpha(p^\alpha(\mathbf{r})) - \frac{p^\alpha(\mathbf{r})}{\bar{Z}_{int}} = -\mathcal{L}_v^\beta(p^\beta(\mathbf{r})) - \frac{p^\beta(\mathbf{r})}{\bar{Z}_{int}}, \tag{5.5a}$$

- coupling condition type 2 $\forall \mathbf{r} \in \Gamma_i^{(\beta,\alpha)}$:

$$\mathcal{L}_v^\beta(p^\beta(\mathbf{r})) - \frac{p^\beta(\mathbf{r})}{\bar{Z}_{int}} = -\mathcal{L}_v^\alpha(p^\alpha(\mathbf{r})) - \frac{p^\alpha(\mathbf{r})}{\bar{Z}_{int}} \tag{5.5b}$$

with $\mathcal{L}_v^\beta(p^\beta(\mathbf{r}))$ denoting the normal velocity differential operator (5.2b) and $\bar{Z}_{int} = 0.1\rho c$ the impedance coupling factor, which is assumed to be one tenth of the characteristic impedance throughout the dissertation. This coupling strategy is referred to as an impedance one (Pluymers, 2006). In order for the problem to be well-posed, one continuity condition is imposed on each subdomain. While the first compatibility condition (5.5a) is prescribed at the common interface $\Gamma_i^{(\alpha,\beta)}$ on the subdomain Ω^α, the second coupling condition (5.5b) is applied to the latter subdomain Ω^β along $\Gamma_i^{(\beta,\alpha)}$. As the same physical quantity is applied on both sides of a common interface (i.e. the normal velocity), the relations (5.5) represent an equivalent way of expressing the continuity conditions.
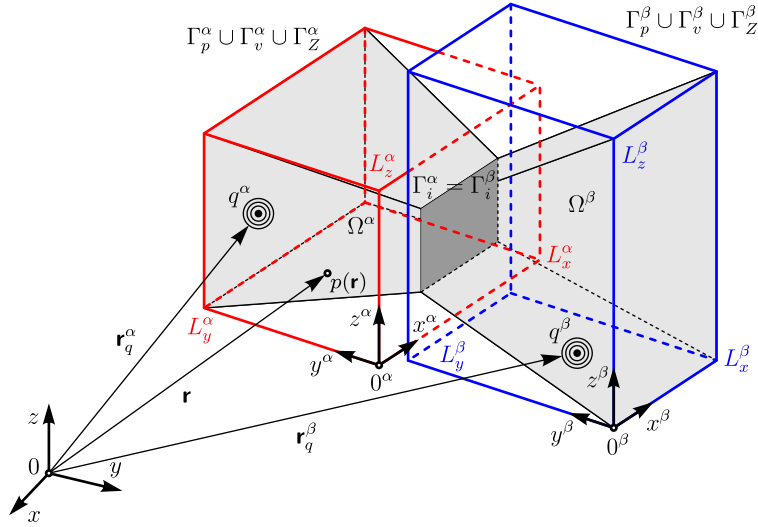
Figure 5.2: Partitioning of a non-convex acoustic domain – the red and blue lines represent the bounding box of a corresponding subdomain

5.2.2 Field variable expansion

Following the concept of domain truncation introduced in section 5.2, different solution expansions are applied depending on the region of the wave model. In the bounded part, a linear combination of basis functions extended by a particular solution function approximates the exact pressure solution. Similar to plate bending problems, these basis functions take the form of the exact solutions of the homogeneous governing differential equation in Cartesian coordinates. For the explicit modelling of the unbounded domain, however, an appropriate solution expansion must be chosen, which additionally accounts for the Sommerfeld radiation condition (5.3). In order to tackle problems involving semi-infinite domains, the solution expansion used in the unbounded region is further truncated to comply with the presence of a rigid baffle plane.

5.2.2.1 Bounded domain

Within each subdomain Ω^α, the following solution expansion approximates the steady-state acoustic pressure field

$$p^\alpha(\mathbf{r}) \approx \hat{p}^\alpha(\mathbf{r}) = \sum_{i=1}^{M_a^\alpha} p_i^\alpha \Phi_i^\alpha(\mathbf{r}) + \hat{p}_q^\alpha(\mathbf{r}) = \mathbf{\Phi}^\alpha(\mathbf{r})\, \mathbf{p}^\alpha + \hat{p}_q^\alpha(\mathbf{r}). \tag{5.6}$$

In (5.6) each wave function $\mathbf{\Phi}^\alpha$ satisfies the homogenous part of the differential equation (5.1) and the wave function contribution factors $\mathbf{p}^\alpha$ form the degrees of freedom of the acoustic wave model. The linear combination of wave functions is further extended by the particular solution function resulting from the acoustic source term in the right hand side of the inhomogeneous Helmholtz equation (5.1)

$$\hat{p}_q^\alpha(\mathbf{r}) = \frac{\mathrm{j}\rho\omega q^\alpha}{4\pi} \frac{\mathrm{e}^{-\mathrm{j}k\|\mathbf{r}-\mathbf{r}_q^\alpha\|}}{\|\mathbf{r}-\mathbf{r}_q^\alpha\|} \tag{5.7}$$

with q^α being the acoustic volume velocity strength and $\mathbf{r}_q^\alpha$ being the position of the point source. The wave function set consists of three subsets (r, s, t) and is defined as follows

$$\mathbf{\Phi}^\alpha(\mathbf{r}) = \begin{cases} \Phi_r^\alpha(x, y, z) = \cos(k_{rx}^\alpha x) \, \cos(k_{ry}^\alpha y) \, \mathrm{e}^{-\mathrm{j}k_{rz}^\alpha z} \\[2mm] \Phi_s^\alpha(x, y, z) = \cos(k_{sx}^\alpha x) \, \mathrm{e}^{-\mathrm{j}k_{sy}^\alpha y} \, \cos(k_{sz}^\alpha z) \\[2mm] \Phi_t^\alpha(x, y, z) = \mathrm{e}^{-\mathrm{j}k_{tx}^\alpha x} \, \cos(k_{ty}^\alpha y) \, \cos(k_{tz}^\alpha z). \end{cases} \tag{5.8}$$

Since the only requirement for the wave number components in (5.8) is that

$$(k_{rx}^\alpha)^2 + (k_{ry}^\alpha)^2 + (k_{rz}^\alpha)^2 = (k_{sx}^\alpha)^2 + (k_{sy}^\alpha)^2 + (k_{sz}^\alpha)^2 = (k_{tx}^\alpha)^2 + (k_{ty}^\alpha)^2 + (k_{tz}^\alpha)^2 = k^2 \tag{5.9}$$

an infinite number of wave functions (5.8) can be defined for the expansion (5.6). Desmet (1998) proposed selecting the following acoustic wave number components

$$k_{r\bullet}^\alpha = \begin{cases} k_{rx}^\alpha = \dfrac{r^\alpha \pi}{L_x^\alpha}, \quad r_1^\alpha = 0, 1, 2, \ldots, n_{r1}^\alpha \\[3mm] k_{ry}^\alpha = \dfrac{r^\alpha \pi}{L_y^\alpha}, \quad r_2^\alpha = 0, 1, 2, \ldots, n_{r2}^\alpha \\[3mm] k_{rz}^\alpha = \pm\sqrt{k^2 - (k_{rx}^\alpha)^2 - (k_{ry}^\alpha)^2}, \end{cases} \tag{5.10a}$$

$$k_{s\bullet}^\alpha = \begin{cases} k_{sx}^\alpha = \dfrac{s^\alpha \pi}{L_x^\alpha}, \quad s_1^\alpha = 0, 1, 2, \ldots, n_{s1}^\alpha \\[3mm] k_{sy}^\alpha = \pm\sqrt{k^2 - (k_{sx}^\alpha)^2 - (k_{sz}^\alpha)^2} \\[3mm] k_{sz}^\alpha = \dfrac{s^\alpha \pi}{L_z^\alpha}, \quad s_2^\alpha = 0, 1, 2, \ldots, n_{s2}^\alpha, \end{cases} \tag{5.10b}$$

$$k_{t\bullet}^\alpha = \begin{cases} k_{tx}^\alpha = \pm\sqrt{k^2 - (k_{ty}^\alpha)^2 - (k_{tz}^\alpha)^2} \\[3mm] k_{ty}^\alpha = \dfrac{t^\alpha \pi}{L_y^\alpha}, \quad t_1^\alpha = 0, 1, 2, \ldots, n_{t1}^\alpha \\[3mm] k_{tz}^\alpha = \dfrac{t^\alpha \pi}{L_z^\alpha}, \quad t_2^\alpha = 0, 1, 2, \ldots, n_{t2}^\alpha \end{cases} \tag{5.10c}$$

with L_x^α, L_y^α and L_z^α the dimensions of the bounding box, which is preferably the smallest rectangular box enclosing the corresponding physical subdomain Ω^α, see figure 5.2. The integer sets $r_\bullet^\alpha$, $s_\bullet^\alpha$ and $t_\bullet^\alpha$ truncated from above by the truncation numbers $n_{r\bullet}^\alpha$, $n_{s\bullet}^\alpha$ and $n_{t\bullet}^\alpha$ yield the M_a^α degrees of freedom of the α-th acoustic subdomain

$$M_a^\alpha = \dim \mathbf{\Phi}^\alpha = 2(n_{r1}^\alpha + 1)(n_{r2}^\alpha + 1) + 2(n_{s1}^\alpha + 1)(n_{s2}^\alpha + 1) + 2(n_{t1}^\alpha + 1)(n_{t2}^\alpha + 1). \tag{5.11}$$

Analogous to the formulation of WBT for structural plate bending problems, see section 4.2.1, two wave function set truncation strategies are considered. The first uses a fixed truncation numbers $n_\bullet^\alpha$, while the second employs a frequency dependent selection rule

$$n_{r1}^\alpha = n_{s1}^\alpha \geq \left\lceil T \frac{kL_x^\alpha}{\pi} \right\rceil, \tag{5.12a}$$

$$n_{r2}^\alpha = n_{t1}^\alpha \geq \left\lceil T\frac{kL_y^\alpha}{\pi} \right\rceil , \tag{5.12b}$$

$$n_{s2}^\alpha = n_{t2}^\alpha \geq \left\lceil T\frac{kL_z^\alpha}{\pi} \right\rceil \tag{5.12c}$$

with T a user-defined truncation parameter and $\lceil \bullet \rceil$ the ceiling function.

Similar to the formulation of WBT for thin plate bending problems, the concept of wave function scaling is also applied for acoustic problems. Once again, the proposed wave function set (5.8) contains two different physical types of waves – propagating and evanescent plane waves. The distinction depends on the value of the corresponding acoustic wave number component (5.10). In the propagating type of wave, all three wave number components $k_{\bullet x}^\alpha$, $k_{\bullet y}^\alpha$ and $k_{\bullet z}^\alpha$ are real numbers, which implies that the amplitudes of the associated wave function are restricted to the interval $\langle -1, 1 \rangle$. For low frequencies and/or higher values of the integer numbers $r_\bullet^\alpha$, $s_\bullet^\alpha$ and $t_\bullet^\alpha$, the wave number components in two spatial direction still remain real numbers, while the third one becomes a complex number. As a consequence, the amplitudes of the resulting wave function may become substantially larger than 1. In this evanescent type of wave, the amplitudes show a harmonic behaviour in two spatial directions, while an exponential decay is observed in the third direction. However, a vital requirement for the numerical conditioning of the resulting wave model is that all wave functions must have amplitudes of one or less within their definition domain. In order to control the amplitudes of the evanescent wave functions, some scaling factors are introduced in the definition of the wave functions. These scaling factors are defined with respect to the dimensions of a bounding box of the corresponding subdomain. More details are available in (Desmet, 1998) and (Pluymers, 2006).

5.2.2.2 Unbounded domain

Besides the Helmholtz equation (5.1), the pressure approximation in the unbounded domain has to satisfy the Sommerfeld radiation condition (5.3). The following pressure solution expansion complies with these requirements and converges for $L \to \infty$

$$p(r, \vartheta, \varphi) \approx \sum_{l=0}^{L} \sum_{m=-l}^{l} p_{lm}^u \, h_l^{(2)}(kr) Y_l^m(\vartheta, \varphi) \tag{5.13}$$

with r, φ and ϑ the radial, azimuthal and zenithal spherical coordinates, which are defined according to figure 5.3(a) and can be obtained from the Cartesian coordinates (x, y, z) by following transformation relations

$$r = \sqrt{x^2 + y^2 + z^2}, \tag{5.14a}$$

$$\vartheta = \arccos \frac{z}{\sqrt{x^2 + y^2 + z^2}}, \tag{5.14b}$$

$$\varphi = \text{atan2}(y, x) \tag{5.14c}$$

with $\mathrm{atan2}(y, x)$ the four-quadrant inverse tangent. In figure 5.3(a), $\hat{\mathbf{r}}$, $\hat{\boldsymbol{\varphi}}$ and $\hat{\boldsymbol{\vartheta}}$ are the unit vectors in the spherical coordinates. In solution expansion (5.13), $h_l^{(2)}(kr)$ is the spherical Hankel function of the second kind

$$h_l^{(2)}(kr) = \sqrt{\frac{\pi}{2kr}} \mathrm{H}_{l+\frac{1}{2}}^{(2)}(kr), \tag{5.15}$$

which represents the radial decay function and $\mathrm{Y}_l^m(\vartheta, \varphi)$ are the spherical harmonics

$$\mathrm{Y}_l^m(\vartheta, \varphi) = \sqrt{\frac{2l+1}{4\pi} \frac{(l-m)!}{(l+m)!}} \, \mathrm{P}_l^m(\cos\vartheta) \mathrm{e}^{\mathrm{j}m\varphi}, \tag{5.16}$$

which stand for an angular portion of the solution of the differential equation. Appendix E lists the spherical harmonics up to degree $l = 10$. In (5.15), $\mathrm{H}_{l+\frac{1}{2}}^{(2)}(\bullet)$ denotes the Hankel function of half-integer order and the second kind. In the spherical harmonics (5.16), $\mathrm{P}_l^m(\cos\vartheta)$ is the associated Legendre polynomial. In the following equation, the identity

$$\mathrm{Y}_l^{-m}(\vartheta, \varphi) = (-1)^m \overline{\mathrm{Y}}_l^m(\vartheta, \varphi) \tag{5.17}$$

is used for $m < 0$. Rewriting (5.13) and adding the particular solution function $\hat{p}_q^u(\mathbf{r})$ yields the solution expansion which approximates the exact steady-state acoustic pressure field in the unbounded domain

$$p^u(\mathbf{r}) \approx \hat{p}^u(\mathbf{r}) = \sum_{i=1}^{M_a^u} p_i^u \Phi_i^u(\mathbf{r}) + \hat{p}_q^u(\mathbf{r}) = \mathbf{\Phi}^u(\mathbf{r})\,\mathbf{p}^u + \hat{p}_q^u(\mathbf{r}) \tag{5.18}$$

with $\mathbf{\Phi}^u(\mathbf{r})$ the wave function set

$$\mathbf{\Phi}^u(\mathbf{r}) = \mathbf{\Phi}^u(r, \vartheta, \varphi) = \sum_{l=0}^{L} \sum_{m=-l}^{l} h_l^{(2)}(kr) \mathrm{Y}_l^m(\vartheta, \varphi) \tag{5.19}$$

and $\mathbf{p}^u$ the unknown contribution factors yielding the unbounded degrees of freedom

$$M_a^u = \dim\mathbf{\Phi}^u = (L+1)^2. \tag{5.20}$$

The frequency-dependent truncation of the wave function set used in the acoustic unbounded domain is based on the following selection rule

$$L = \max\left\{ L_{min}, \left\lceil T_u \frac{2\pi R}{\lambda} \right\rceil \right\}, \tag{5.21}$$

where L_{min} is a user-defined threshold for the order of the solution expansion (5.19) controlling the smallest size of the set, R is the radius of truncation sphere Γ_T, λ is the physical acoustic wavelength, and T_u is a user-defined truncation parameter. This truncation strategy represents the number of acoustic wavelengths λ circumscribed in the truncation sphere of radius R. Since the dynamic truncation rule used in the bounded acoustic domains (5.12) is inherently related to frequency, the equation (5.21) represents a compatible type of wave function truncation strategy applied in the unbounded acoustic domain.
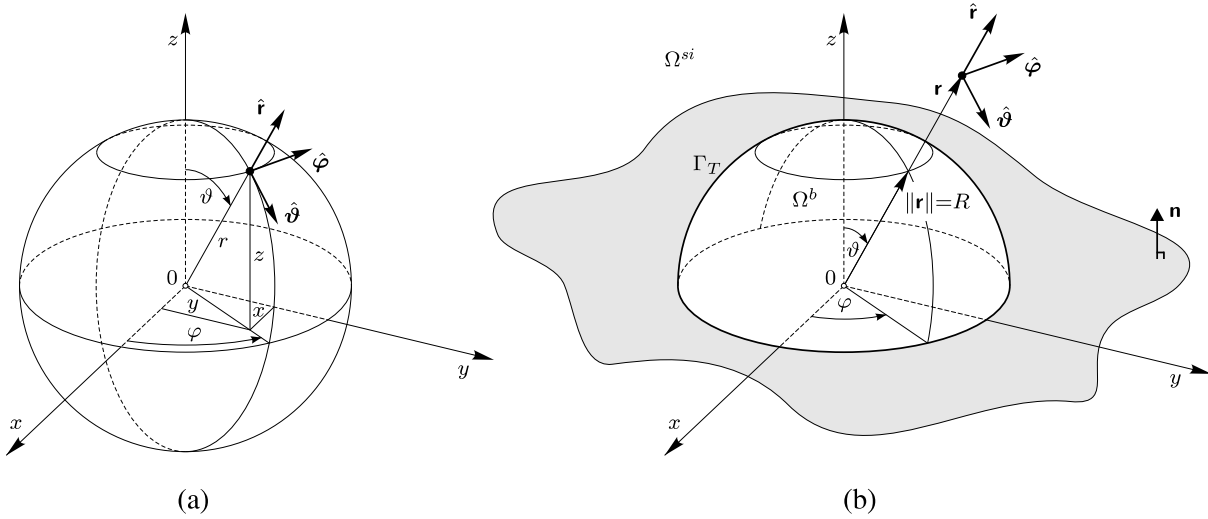
Figure 5.3: (a) Spherical coordinate system and (b) definition of a rigid baffle plane (Rejlek et al., 2008b)

5.2.2.3 Semi-infinite domain

Thusfar, this dissertation has considered an unbounded acoustic domain, as defined in section 5.2.2.2. Once a rigid baffle is introduced in an unbounded acoustic problem, see figure 5.3(b), the original free-field problem becomes subdivided into two semi-infinite regions with a rigid boundary condition imposed along the baffle plane $z = 0$

$$\left.\frac{\partial p(\mathbf{r})}{\partial n}\right|_{\vartheta=\frac{\pi}{2}, r\geq 0} = 0. \tag{5.22}$$

To account for the semi-infinite domain, wave functions used in the solution expansion inherently need to incorporate the rigid boundary condition (5.22) (Rejlek et al., 2008b). Since the problem becomes symmetric with respect to the baffle plane, it is sufficient to restrict the expansion in spherical harmonics (5.16) to indices for which $(l + m)$ is even. To prove this, the selection of appropriate functions starts from the original free-field wave function set (5.19). Expressing the solution expansion (5.13) for the particular case, where a response point coincides with the baffle, yields

$$\left.\frac{\partial p(\mathbf{r})}{\partial \vartheta}\right|_{\vartheta=\frac{\pi}{2}, r\geq R} = \sum_{l=0}^{L}\sum_{m=-l}^{m=l} p_{lm}^{u}\, h_{l}^{(2)}(kr) \underbrace{\sqrt{\frac{2l+1}{2\pi}\frac{(l-|m|)!}{(l+|m|)!}}e^{jm\varphi}}_{\neq f(\vartheta)} \underbrace{P_{l}^{'|m|}(\cos\vartheta)}_{\stackrel{!}{=}0} = 0. \tag{5.23}$$

Clustering of all ϑ-independent terms in (5.23) allows to separate the part of the expression that depends on zenithal coordinate ϑ and which is solely the derivative of an associated Legendre polynomial with respect to ϑ. Obviously, only the derivative of the associated Legendre polynomial $P_{l}^{'m}(0)$ must equal zero in order for the condition (5.22) to be fulfilled. From the properties

of the associated Legendre polynomials (Thompson and Huan, 1999)

$$P_l'^m(0) = \begin{cases} 0, & \text{for} \quad l+m = 2N; \, \forall N \in \mathbb{Z} \\ (-1)^{\left(\frac{l+m-1}{2}\right)} \dfrac{1 \cdot 3 \cdot 5 \ldots (l+m)}{2 \cdot 4 \cdot 6 \ldots (l-m-1)}, & \text{for} \quad l+m = 2N+1; \, \forall N \in \mathbb{Z}, \end{cases} \quad (5.24)$$

where N is an integer number.

$Y_l^m(\vartheta, \varphi)$	-3	-2	-1	$m=0$	1	2	3
$l=0$							
1							
2							
3							

Legend:
- $\Re\{Y_l^m\} \geq 0$
- $\Re\{Y_l^m\} \leq 0$
- $\Im\{Y_l^m\} \geq 0$
- $\Im\{Y_l^m\} \leq 0$

Table 5.1: Spherical harmonics $Y_l^m(\vartheta, \varphi)$ up to degree $l = 3$ (Rejlek et al., 2008b)

only the spherical harmonics for which $l + m = 2N$ satisfy the baffle condition (5.22). As a result, the even configurations are retained in the wave function set, while those with an odd shape are removed. As a consequence, the size of the original free-field wave function set (5.19) becomes smaller due to the omission off the odd $Y_l^m(\vartheta, \varphi)$ components. Table 5.1 captures the spherical harmonics up to degree $l = 3$ and the corresponding orders $m = -l, -l+1, \ldots, l-1, +l$ plotted as directional characteristics for various azimuths φ and zeniths ϑ. In the diagrams red and blue denote the positive and negative values of the real part of Y_l^m, while green and yellow represent positive and negative values of the imaginary part of Y_l^m. Functions with an even configuration forming the semi-infinite wave function set $\boldsymbol{\Phi}^{si}$ are depicted in colour, while the odd ones rendered in greyscale are removed, thereby yielding a reduced size of the wave function set (cf. (5.20))

$$M_a^{si} = \dim\boldsymbol{\Phi}^{si} = \frac{(L+1)(L+2)}{2}. \quad (5.25)$$

Thus, the following solution expansion approximates the exact steady-state acoustic pressure field in a semi-infinite domain

$$p^{si}(\mathbf{r}) \approx \hat{p}^{si}(\mathbf{r}) = \sum_{i=1}^{M_a^{si}} p_i^{si} \Phi_i^{si}(\mathbf{r}) + \hat{p}_q^{si}(\mathbf{r}) = \mathbf{\Phi}^{si}(\mathbf{r}) \, \mathbf{p}^{si} + \hat{p}_q^{si}(\mathbf{r}) \tag{5.26}$$

with $\mathbf{p}^{si}$ the $(M_a^{si} \times 1)$ vector of unknown contribution factors and $\mathbf{\Phi}^{si}(\mathbf{r})$ the semi-infinite wave function set

$$\mathbf{\Phi}^{si}(\mathbf{r}) = \mathbf{\Phi}^{si}(r, \vartheta, \varphi) = \sum_{l=0}^{L} \sum_{m=0}^{l} h_l^{(2)}(kr) \mathrm{Y}_l^{2m-l}(\vartheta, \varphi). \tag{5.27}$$

5.2.3 Evaluation of boundary and interface conditions

The pressure approximations in both the bounded (5.6) and unbounded part (5.13) of an acoustic wave model satisfy the governing differential equation (5.1), but violate the boundary (5.2) and interface conditions (5.5). The unknown contribution functions $\mathbf{p}^\alpha$, $\mathbf{p}^u$ and $\mathbf{p}^{si}$ are determined by minimising the approximation errors of the boundary and interface conditions in an integral sense by applying the weighed residual formulation. The residual errors arising at the boundaries and interfaces of the corresponding subdomain are defined as follows

$$\mathbf{r} \in \Gamma_p^\alpha \quad : \quad R_p^\alpha(\mathbf{r}) \quad = \hat{p}^\alpha(\mathbf{r}) - \bar{p}(\mathbf{r}), \tag{5.28a}$$

$$\mathbf{r} \in \Gamma_v^\alpha \quad : \quad R_v^\alpha(\mathbf{r}) \quad = \mathcal{L}_v^\alpha(\hat{p}^\alpha(\mathbf{r})) - \bar{v}_n, \tag{5.28b}$$

$$\mathbf{r} \in \Gamma_Z^\alpha \quad : \quad R_Z^\alpha(\mathbf{r}) \quad = \mathcal{L}_v^\alpha(\hat{p}^\alpha(\mathbf{r})) - \frac{\hat{p}^\alpha(\mathbf{r})}{\bar{\bar{Z}}_n(\mathbf{r})}, \tag{5.28c}$$

$$\mathbf{r} \in \Gamma_i^{(\alpha,\beta)} : \quad R_i^{(\alpha,\beta)}(\mathbf{r}) = \mathcal{L}_v^\alpha(\hat{p}^\alpha(\mathbf{r})) - \frac{\hat{p}^\alpha(\mathbf{r})}{\bar{Z}_i} + \mathcal{L}_v^\beta(\hat{p}^\beta(\mathbf{r})) + \frac{\hat{p}^\beta(\mathbf{r})}{\bar{Z}_i}. \tag{5.28d}$$

For each subdomain Ω^α, the boundary residual error functions involved (5.28) are orthogonalised with respect to weighting function $\tilde{p}$ or its normal derivative

$$-\int_{\Gamma_p^\alpha} \mathcal{L}_v^\alpha(\tilde{p})(\hat{p}^\alpha - \bar{p}) \, d\Gamma + \int_{\Gamma_v^\alpha} \tilde{p}^\alpha(\mathcal{L}_v^\alpha(\hat{p}^\alpha) - \bar{v}_n) \, d\Gamma + \int_{\Gamma_Z^\alpha} \tilde{p}^\alpha \left(\mathcal{L}_v^\alpha(\hat{p}^\alpha) - \frac{\hat{p}^\alpha}{\bar{\bar{Z}}_n} \right) d\Gamma$$

$$+ \sum_{\beta=1,\beta\neq\alpha}^{N_a} \left[\int_{\Gamma_i^{(\alpha,\beta)}} \tilde{p}^\alpha \left(\mathcal{L}_v^\alpha(\hat{p}^\alpha) - \frac{\hat{p}^\alpha}{\bar{Z}_i} + \mathcal{L}_v^\beta(\hat{p}^\beta) + \frac{\hat{p}^\beta}{\bar{Z}_i} \right) d\Gamma \right] = 0. \tag{5.29}$$

Using the Galerkin approach, the weighting functions are expanded in terms of the same basis functions $\mathbf{\Phi}$ as used for the pressure approximation $\hat{p}$ in (5.6)

$$\tilde{p}^\alpha(\mathbf{r}) = \sum_{i=1}^{M_a^\alpha} \tilde{c}_i^\alpha \Phi_i^\alpha(\mathbf{r}) = \mathbf{\Phi}^\alpha(\mathbf{r}) \, \tilde{\mathbf{c}}^\alpha, \tag{5.30}$$

where $\tilde{\mathbf{c}}$ represents an arbitrary weighting function contribution factor. Substituting the pressure approximation (5.13) and the weighting function (5.30) in the weighted residual formulation (5.29), together with the requirement that this relation should hold for any set of contribution factors $\tilde{\mathbf{c}}$, yields the acoustic wave model

$$
\begin{bmatrix} (\mathbf{A}^\alpha + \mathbf{C}_b^\alpha) & \mathbf{C}^{\alpha\beta} \\ \mathbf{C}^{\beta\alpha} & (\mathbf{A}^\beta + \mathbf{C}_b^\beta) \end{bmatrix} \begin{Bmatrix} \mathbf{p}^\alpha \\ \mathbf{p}^\beta \end{Bmatrix} = \begin{Bmatrix} \mathbf{b}^\alpha + \mathbf{c}_b^\alpha + \mathbf{c}^{\alpha\beta} \\ \mathbf{b}^\beta + \mathbf{c}_b^\beta + \mathbf{c}^{\beta\alpha} \end{Bmatrix} . \tag{5.31}
$$

The model contributions $\mathbf{A}^\alpha$ and $\mathbf{b}^\alpha$ represent the uncoupled matrices and vectors defined as follows

$$
\mathbf{A}^\alpha = \mathbf{A}_p^\alpha + \mathbf{A}_v^\alpha + \mathbf{A}_Z^\alpha \qquad \mathbf{b}^\alpha = \mathbf{b}_p^\alpha + \mathbf{b}_v^\alpha + \mathbf{b}_Z^\alpha \tag{5.32a}
$$

with   with

$$
\mathbf{A}_p^\alpha = -\int_{\Gamma_p} \mathcal{L}_v^\alpha(\mathbf{\Phi}^{\alpha\mathsf{T}})\mathbf{\Phi}^\alpha \, d\Gamma, \qquad \mathbf{b}_p^\alpha = -\int_{\Gamma_p} \mathcal{L}_v^\alpha(\mathbf{\Phi}^{\alpha\mathsf{T}})(\bar{p} - \hat{p}_q^\alpha) \, d\Gamma, \tag{5.32b}
$$

$$
\mathbf{A}_v^\alpha = \int_{\Gamma_v} \mathbf{\Phi}^{\alpha\mathsf{T}}\mathcal{L}_v^\alpha(\mathbf{\Phi}^\alpha) \, d\Gamma, \qquad \mathbf{b}_v^\alpha = \int_{\Gamma_v} \mathcal{L}_v^\alpha(\mathbf{\Phi}^{\alpha\mathsf{T}})(\bar{v}_n - \mathcal{L}_v^\alpha(\hat{p}_q^\alpha)) \, d\Gamma, \tag{5.32c}
$$

$$
\mathbf{A}_Z^\alpha = -\int_{\Gamma_Z} \mathbf{\Phi}^{\alpha\mathsf{T}}\mathcal{L}_Z^\alpha(\mathbf{\Phi}^\alpha) \, d\Gamma, \qquad \mathbf{b}_Z^\alpha = -\int_{\Gamma_Z} \mathbf{\Phi}^{\alpha\mathsf{T}}\mathcal{L}_Z^\alpha(\hat{p}_q^\alpha) \, d\Gamma. \tag{5.32d}
$$

The terms $\mathbf{C}_b^\alpha$, $\mathbf{C}_b^\beta$, $\mathbf{c}_b^\alpha$ and $\mathbf{c}_b^\beta$ represent the back-coupling matrices and vectors given by

$$
\mathbf{C}_b^\alpha = \int_{\Gamma_i} \mathbf{\Phi}^{\alpha\mathsf{T}} \left[\mathcal{L}_v^\alpha(\mathbf{\Phi}^\alpha) - \frac{\mathbf{\Phi}^\alpha}{\bar{Z}_i} \right] d\Gamma, \qquad \mathbf{c}_b^\alpha = -\int_{\Gamma_i} \mathbf{\Phi}^{\alpha\mathsf{T}} \left[\mathcal{L}_v^\alpha(\hat{p}_q^\alpha) - \frac{\hat{p}_q^\alpha}{\bar{Z}_i} \right] d\Gamma, \tag{5.33a}
$$

$$
\mathbf{C}_b^\beta = \int_{\Gamma_i} \mathbf{\Phi}^{\beta\mathsf{T}} \left[\mathcal{L}_v^\beta(\mathbf{\Phi}^\beta) + \frac{\mathbf{\Phi}^\beta}{\bar{Z}_i} \right] d\Gamma, \qquad \mathbf{c}_b^\beta = -\int_{\Gamma_i} \mathbf{\Phi}^{\beta\mathsf{T}} \left[\mathcal{L}_v^\beta(\hat{p}_q^\beta) + \frac{\hat{p}_q^\beta}{\bar{Z}_i} \right] d\Gamma. \tag{5.33b}
$$

The contributions $\mathbf{C}^{\alpha\beta}$, $\mathbf{C}^{\beta\alpha}$, $\mathbf{c}^{\alpha\beta}$ and $\mathbf{c}^{\beta\alpha}$ represent the coupling matrices and vectors given by

$$
\mathbf{C}^{\alpha\beta} = \int_{\Gamma_i} \mathbf{\Phi}^{\alpha\mathsf{T}} \left[\mathcal{L}_v^\beta(\mathbf{\Phi}^\beta) + \frac{\mathbf{\Phi}^\beta}{\bar{Z}_i} \right] d\Gamma, \qquad \mathbf{c}^{\alpha\beta} = -\int_{\Gamma_i} \mathbf{\Phi}^{\alpha\mathsf{T}} \left[\mathcal{L}_v^\beta(\hat{p}_q^\beta) + \frac{\hat{p}_q^\beta}{\bar{Z}_i} \right] d\Gamma, \tag{5.34a}
$$

$$
\mathbf{C}^{\beta\alpha} = \int_{\Gamma_i} \mathbf{\Phi}^{\beta\mathsf{T}} \left[\mathcal{L}_v^\alpha(\mathbf{\Phi}^\alpha) - \frac{\mathbf{\Phi}^\alpha}{\bar{Z}_i} \right] d\Gamma, \qquad \mathbf{c}^{\beta\alpha} = -\int_{\Gamma_i} \mathbf{\Phi}^{\beta\mathsf{T}} \left[\mathcal{L}_v^\alpha(\hat{p}_q^\alpha) - \frac{\hat{p}_q^\alpha}{\bar{Z}_i} \right] d\Gamma. \tag{5.34b}
$$

The wave model is assembled by minimising the approximation errors (5.28) in an integral sense. This involves a numerical integration of the integrals (5.32), (5.33) and (5.34), which is carried out by adopting the Gauss-Legendre quadrature rule in the practical implementation. To

select the number of Gauss points used for one boundary face per isoparametric coordinate, the following strategy is adopted

$$n_{gp} \geq 2 \max \left(\|k_{\bullet x}^{\alpha}\|, \|k_{\bullet y}^{\alpha}\|, \|k_{\bullet z}^{\alpha}\| \right), \qquad (5.35)$$

which is a three-dimensional extension of the selection rule (4.22) adopted in the formulation for plate bending problems. The resulting number of integration points applied for the actual boundary face in one direction is then obtained by multiplying n_{gp} with the length of the longest boundary edge of the corresponding face. The proposed selection strategy thus accounts for (i) the function in the solution set, which exhibits the highest oscillatory behaviour and (ii) the maximum length of the integration path. The integrands of these integrals consist of the products of wave functions $\boldsymbol{\Phi}$ and the differential operator $\mathcal{L}_v(\boldsymbol{\Phi})$ applied to these wave functions. In the proposed formulation of WBT, the wave functions are the propagating and evanescent plane waves, which are inherently frequency-dependent. As a result, the integrands may exhibit a highly oscillatory behaviour, which may further become spatially very localised. In addition, due to the global nature of the pressure expansion (5.6), these integrals need to be evaluated over large boundaries $\Gamma_{\bullet}$. Given an inherently poor conditioning of the WBT system matrix, special care must be taken during the numerical integration in order to calculate the matrix coefficients with sufficient accuracy (Van Hal, 2004).

5.3 Validation example: plane wave scattering by a rigid sphere

This section presents the validation of the wave based formulation for three-dimensional free-field problems. In the first validation example, a plane wave scattering on a rigid spherical obstacle is considered (Rejlek and Jiříček, 2004). The proposed validation example is chosen (i) for its geometrical simplicity and (ii) due to the existence of an analytical solution (Rayleigh, 1945). Moreover, selection of this validation example was also motivated because one vital requirement for a three-dimensional formulation of WBT for unbounded acoustic problems is carrying out the numerical integration of functions over the curved boundaries. Since the analytical solution of this simple configuration can be derived in a quite straightforward manner, a convergence analysis is carried out by considering the analytical solution as a reference.

5.3.1 Problem definition

Consider a rigid sphere of radius $R = 0.5$ m located in the origin of the coordinate system, which is exposed to a plane wave propagating in a positive z axis direction, see figure 5.4,

$$p_I = P e^{j\omega\left(t - \frac{z}{c}\right)} = P e^{jk(ct-z)} \qquad (5.36)$$

with $P = |P|e^{j\delta}$ the complex sound pressure magnitude. The scatterer is surrounded by air having the speed of sound $c = 343.8$ m/s and mass density $\rho = 1.2$ kg/m^3.
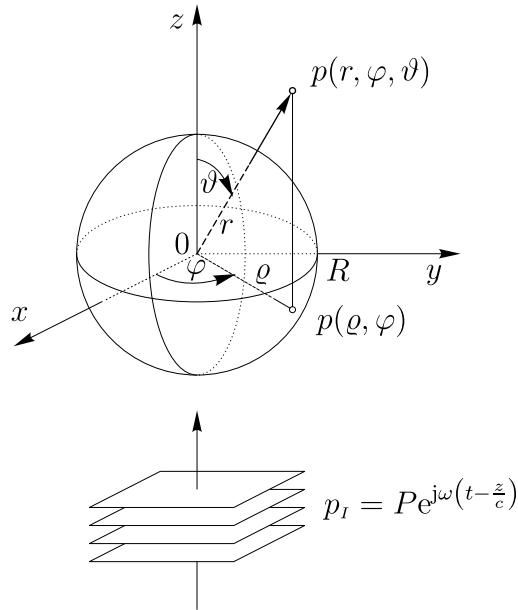
Figure 5.4: Plane wave scattering by a rigid sphere of radius R (Rejlek and Jiříček, 2004)

5.3.2 Analytical solution

Using the spherical coordinates

$$x = r \, \sin \vartheta \cos \varphi, \tag{5.37a}$$

$$y = r \, \sin \vartheta \sin \varphi, \tag{5.37b}$$

$$z = r \, \cos \vartheta, \tag{5.37c}$$

see figure 5.3(a), the equation (5.36) can be rewritten

$$p_I = P \mathrm{e}^{\mathrm{j}k(ct - r \cos \vartheta)}. \tag{5.38}$$

Assuming the axisymmetry of the scatterer shape, the resulting sound field can be obtained by solving an equivalent two-dimensional problem in the polar coordinates $p = p(r, \vartheta)$ defined by the Cartesian zx-plane, see figure 5.4. By expanding the term $\mathrm{e}^{-\mathrm{j}kr \cos \vartheta}$ by means of the spherical harmonics

$$\mathrm{e}^{-\mathrm{j}kr \cos \vartheta} = \sum_{n=0}^{\infty} \mathrm{P}_n(\cos \vartheta) h_n^{(2)}(kr) = \tag{5.39}$$

$$= h_0^{(2)}(kr) + \mathrm{P}_1(\cos \vartheta) h_1^{(2)}(kr) + \mathrm{P}_2(\cos \vartheta) h_2^{(2)}(kr) + \ldots + \mathrm{P}_n(\cos \vartheta) h_n^{(2)}(kr)$$

with $P_n(\eta)$ the Legendre polynomial of the nth order and argument η and $h_n^{(2)}(\zeta)$ the spherical Hankel function of the second kind of the nth order and argument ζ, the incident plane wave becomes

$$p_I = P \sum_{n=0}^{\infty} P_n(\cos\vartheta) h_n^{(2)}(kr) e^{j\omega t}. \tag{5.40}$$

The spherical Hankel function of the second kind is defined by

$$h_n^{(2)}(\zeta) = j_n(\zeta) - jn_n(\zeta), \tag{5.41}$$

where $j_n(\zeta)$ and $n_n(\zeta)$ are the spherical Bessel and spherical Neumann function of the nth order and argument ζ, respectively. The functions $j_n(\zeta)$ and $n_n(\zeta)$ are defined as follows

$$j_n(\zeta) = \sqrt{\frac{\pi}{2\zeta}} \, J_{n+\frac{1}{2}}(\zeta), \tag{5.42a}$$

$$n_n(\zeta) = \sqrt{\frac{\pi}{2\zeta}} \, N_{n+\frac{1}{2}}(\zeta) \tag{5.42b}$$

with $J_n(\zeta)$ and $N_n(\zeta)$ being the Bessel and Neumann functions of the nth order and argument ζ, respectively. Multiplying the term $e^{-jkr\cos\vartheta}$ by a Legendre polynomial $P_n(\eta)$, integrating with respect to ϑ on interval $\vartheta = -1$ to 1 and using equation (5.39) and identity

$$\int_{-1}^{1} P_m(\eta) P_n(\eta) d\eta = \begin{cases} 0 & \text{for } m \neq n, \\[2mm] \dfrac{2}{2n+1} & \text{for } m = n \end{cases} \tag{5.43}$$

yields

$$\int_{-1}^{1} P_n(\cos\vartheta) e^{-jkr\cos\vartheta} d\vartheta = h_n^{(2)}(kr) \int_{-1}^{1} P_n^2(\cos\vartheta) \, d\vartheta = \frac{2h_n^{(2)}(kr)}{2n+1}. \tag{5.44}$$

Using the equations (5.42), the right hand side of equation (5.44) may be rewritten as follows

$$\frac{2h_n^{(2)}(kr)}{2n+1} = (-j)^n \sqrt{\frac{\pi}{2kr}} \, J_{n+\frac{1}{2}}(kr) = (-j)^n j_n(kr). \tag{5.45}$$

Expressing the spherical Hankel function $h_n^{(2)}(kr)$ from equation (5.45) and substituting into equation (5.40) yields the equation for an incoming plane wave

$$p_I = P \sum_{n=0}^{\infty} (2n+1)(-j)^n P_n(\cos\vartheta) j_n(kr) e^{j\omega t}. \tag{5.46}$$

Scattering problems can be tackled by decomposing the total sound field p into an incoming p_I and a scattered wave p_{sc}

$$p = p_I + p_{sc}. \tag{5.47}$$

Assuming a rigid body, the scattered sound pressure becomes

$$p_{sc} = -P \sum_{n=0}^{\infty} (2n+1)(-j)^n P_n(\cos\vartheta) \frac{j'_n(kR)}{h'^{(2)}_n(kR)} h^{(2)}_n(kr) e^{j\omega t}. \tag{5.48}$$

Combining the equations (5.46), (5.47) and (5.48) yields the equation for the total sound pressure field

$$p(r,\vartheta) = P \sum_{n=0}^{\infty} j^{n+1}(2n+1) P_n(\cos\vartheta) \frac{j_n(kr)n'_n(kR) - n_n(kr)j'_n(kR)}{j'_n(kR) + jn'_n(kR)} e^{j\omega t}. \tag{5.49}$$

The angular term of (5.49) is often referred to as a directivity function, since it accounts for the directivity characteristics of the wave-scatterer configuration. Evaluating (5.49) at the surface of the sphere $r = R$ for $n = 0, 1, \ldots, 20$ and for different frequencies yields the directivity patterns of the plane wave scattering by a rigid sphere, see figure 5.5. The insert on the top left side indicates the relationship between the azimuthal angle ϑ and the incidence plane wave p_I.
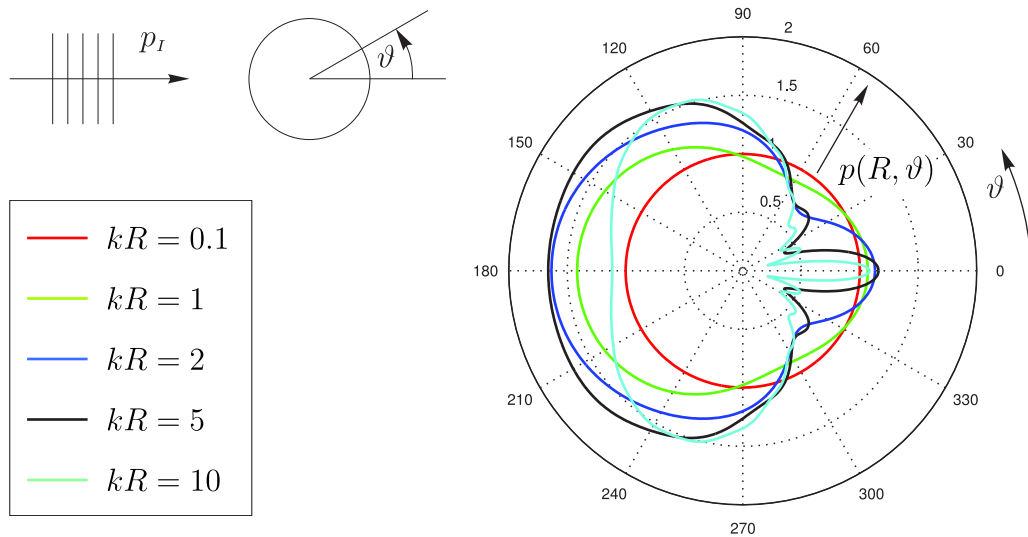
Figure 5.5: Directivity patterns of a plane wave scattering by a rigid sphere for different kR regimes

5.3.3 Numerical models

Several BE models have been created, which are based on either the direct or the indirect formulation. A generic BE set up of the problem considered consists of a discretised physical boundary Γ represented by a computational surface mesh, see figure 5.6(a). To evaluate the scattering effects, a field point mesh surrounding the sphere in the xz-plane is also considered.

Due to the spherical shape of the scatterer, the wave models are simply formed by the unbounded domain Ω^u, see figure 5.6(b). The physical boundary of the problem $\partial\Omega$ is congruent with the truncation boundary Γ_T in this particular case and consists of six spherical faces, see figure 5.7(a). Diwoky et al. (2008) developed the numerical integration of the functions on the doubly curved shells. Figure 5.7(b) captures the distribution of the integration Gauss points on such a shell, including the orientation of the local normal vectors.
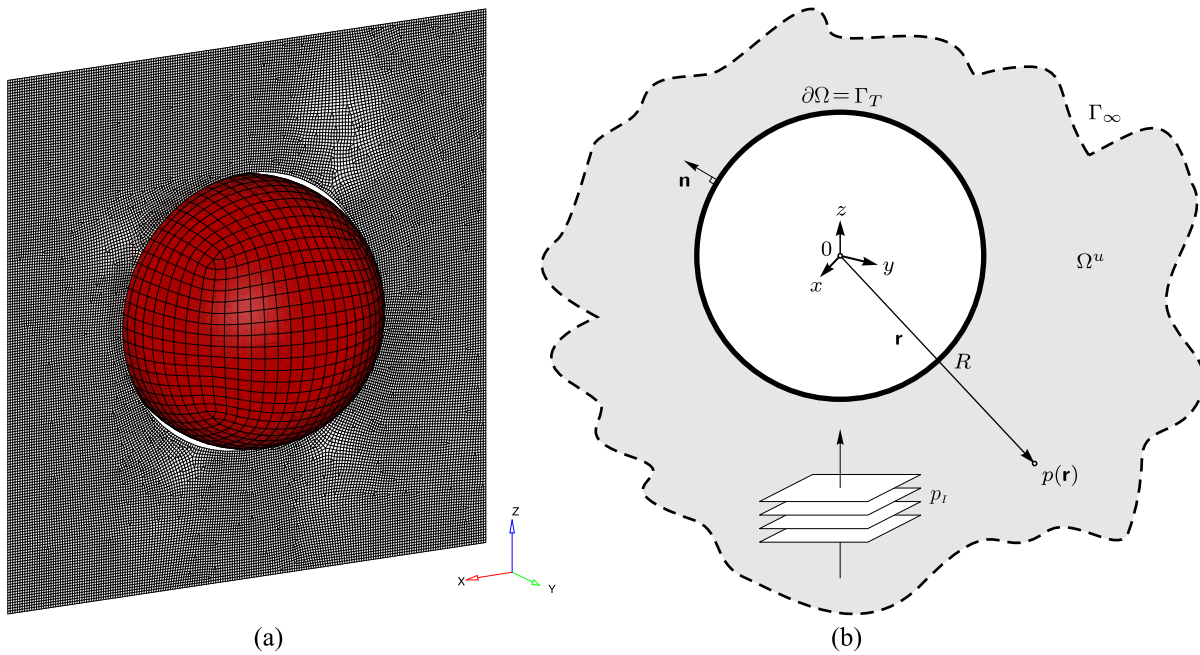
Figure 5.6: Plane wave scattering by a rigid sphere: (a) a generic acoustic BE set up – the computational BE mesh in red, the field point mesh in gray, (b) the corresponding wave based model

While both the BEM direct and indirect formulations rely on the commercial CAE tool *LMS Virtual.Lab* (LMS International, 2010), the WBT code is implemented in *MATLAB* (MathWorks, Inc., 2007). All calculations presented in this section are performed on a 2.26 GHz dual-core *Intel*-based computer using 4 Gbyte RAM and running the *Windows Vista 64-bit* operating system.
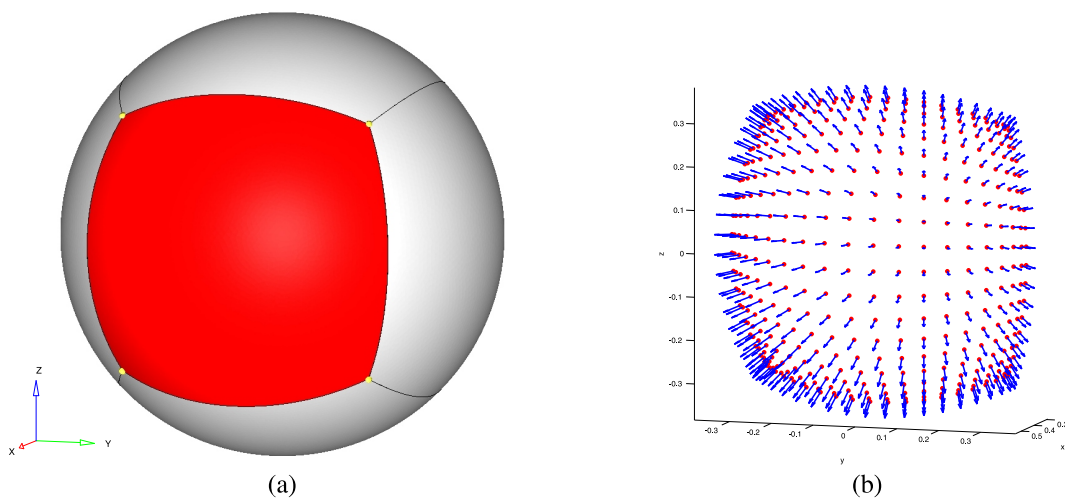
Figure 5.7: Plane wave scattering by a rigid sphere: (a) physical boundary of the wave based model $\partial\Omega$ decomposed into six spherical faces and (b) the distribution of both the integration Gauss points and normal vectors on one of these faces
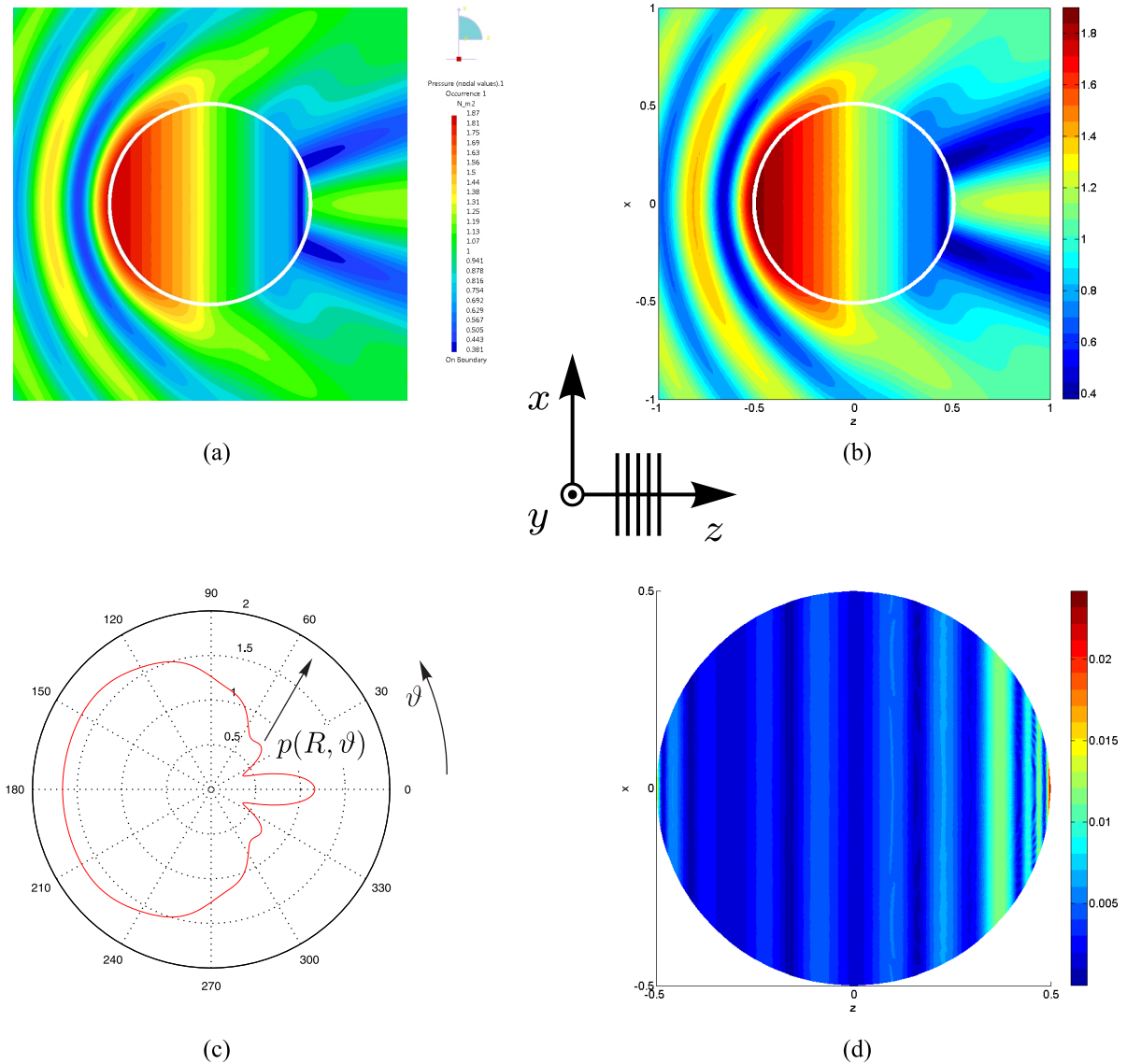
Figure 5.8: Plane wave scattering by a rigid sphere at $kR = 5$: pressure amplitude in [Pa] predicted by both (a) BEM (bem04) and (b) WBT (wbt02), (c) analytical solution of the directivity pattern $p = p(R, \vartheta)$ in [Pa] and (d) the relative WBT (wbt02) prediction error for pressure amplitude [-] (see tables 5.2 and 5.3 for model attributes)

5.3.4 Validation study

Figure 5.8 shows the pressure amplitude field for $kR = 5$, which is evaluated at both the surface of the sphere and the field point mesh around the scatterer by using the (a) BEM and (b) WBT. For these calculations the bem04 and wbt02 models, see table 5.2 and 5.3, are considered. Diagram 5.8(c) plots the directivity pattern $p = p(R, \vartheta)$ in [Pa] based on the analytical solution (5.49) for for $n = 0, 1, \ldots, 20$. Finally, figure 5.8(d) shows the relative pressure amplitude error for WBT evaluated at the surface of the sphere by using the analytical solution (5.49) as a reference, while figure 5.9 illustrates the case for $kR = 10$. Both figures 5.8 and 5.9 confirm the high accuracy of the proposed wave based methodology when tackling problems involving the integration of the wave function and its normal derivative over the curved boundaries. Therefore, the results constitute a basis for the further development of this solution scheme towards fully coupled vibro-acoustic problems involving three-dimensional unbounded domains.

(a)

(b)

(c)

(d)
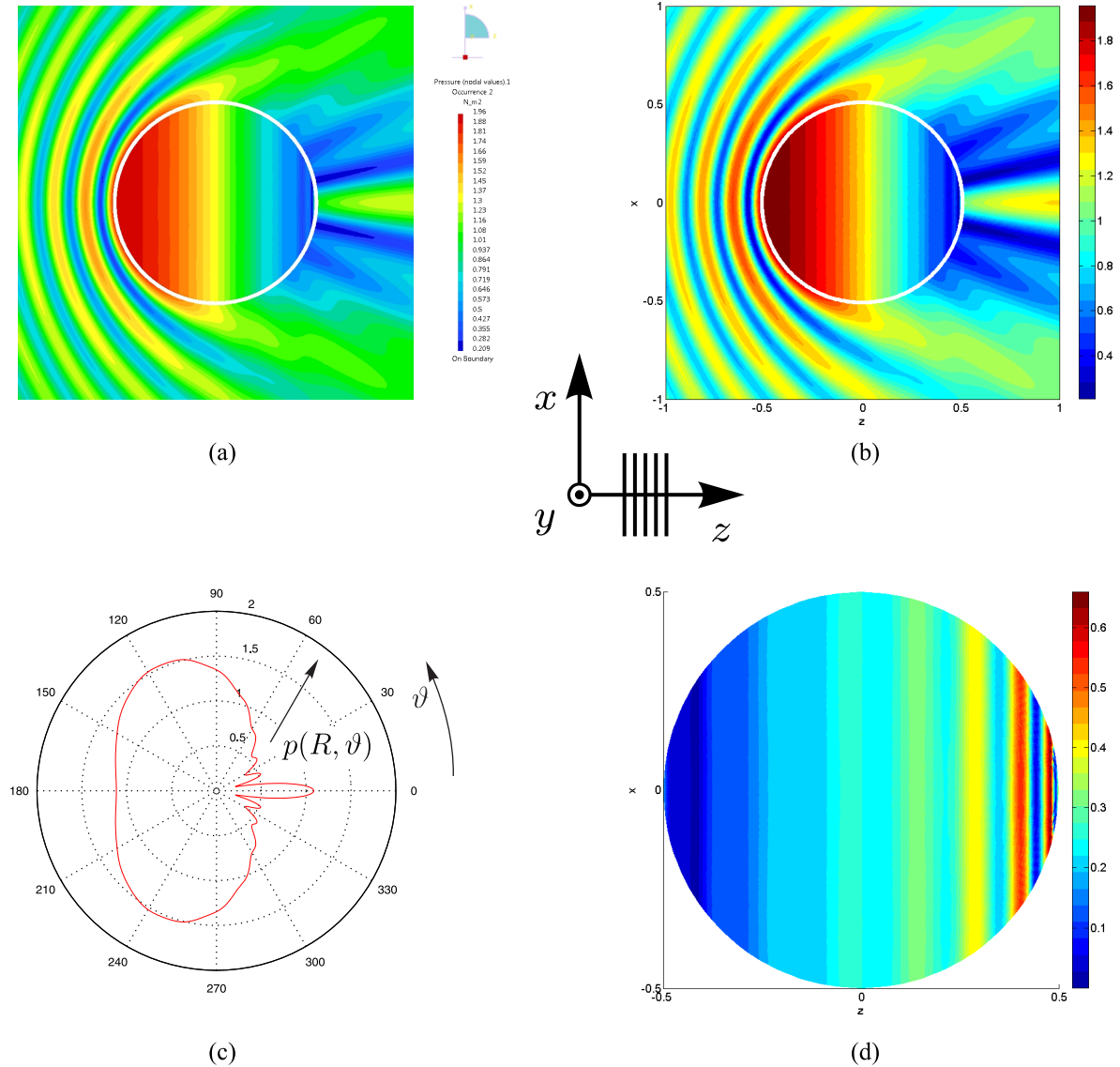
Figure 5.9: Plane wave scattering by a rigid sphere at $kR = 10$: pressure amplitude in [Pa] predicted by both (a) BEM (bem04) and (b) WBT (wbt02), (c) analytical solution of the directivity pattern $p = p(R, \vartheta)$ in [Pa] and (d) the relative WBT (wbt02) prediction error for pressure amplitude [-] (see tables 5.2 and 5.3 for model attributes)

5.3.5 Convergence analysis

Figure 5.10 plots the spatially averaged relative prediction error ε for the pressure amplitude versus the CPU time needed to carry out direct response calculation for both (a) $kR = 5$ and (b) $kR = 10$. This type of analysis employs different BE and WB models, see tables 5.2 and 5.3. The analytical solution of the problem (5.49) is used as a reference p_{REF}. The indicated CPU time for both BE and WB models comprises the time needed to perform the numerical integration in order to build up the matrix system, its solution and the postprocessing step. The size of all BE models is selected in order to make an in-core BE calculation admissible on the

computer platform indicated in section 5.3.3. The relative error ε is defined as follows

$$\varepsilon = \frac{1}{N} \sum_{i=1}^{N} \left| \frac{p_\bullet(\mathbf{r}_i) - p_{REF}(\mathbf{r}_i)}{p_{REF}(\mathbf{r}_i)} \right| \tag{5.50}$$

with $p_\bullet(\mathbf{r}_i)$ denoting the corresponding numerical solution (BEM direct/indirect or WBT) evaluated at N node positions located at the surface of the sphere. In the case of BEM, these positions correspond to nodes of an actual computational mesh based on table 5.2. For WBT, in contrast, these represent the N field points used to postprocess the wave function contribution factors $\mathbf{p}^\alpha$. The field point mesh used for the postprocessing of all WB models adopts the topology of the finest BE mesh (bem04/bem08). Figure 5.10 proves the high convergence rate of WBT compared with direct and indirect BEM.
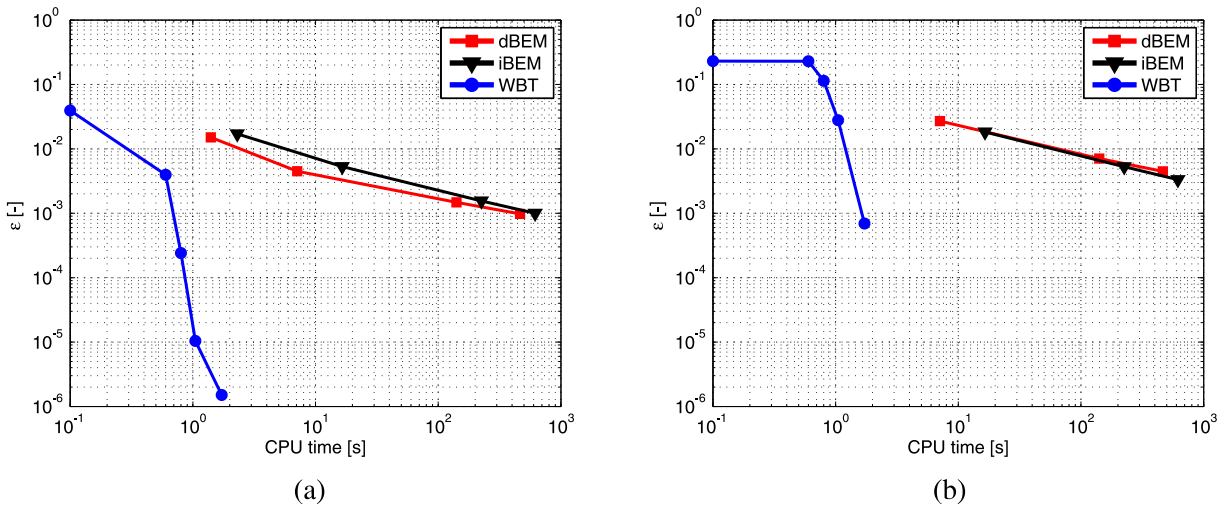
Figure 5.10: Plane wave scattering by a rigid sphere: pressure amplitude convergence curves for (a) $kR = 5$ and (b) $kR = 10$

model	formulation	#nod	#ele	topology	h_{max} [m]	$f_{max}^{\,1}$ [Hz]	CPU time [s] $kR = 5$	CPU time [s] $kR = 10$
bem01		378	384		0.1	≈ 573	1.4	N/A[2]
bem02	dBEM	1530	1536		0.05	≈ 1146	7.1	7.1
bem03	exterior	5766	5768		0.025	≈ 2292	141	141
bem04		9126	9128	quad4	0.02	≈ 2865	465	465
bem05		378	384	dominant	0.1	≈ 573	2.3	N/A[2]
bem06	iBEM	1530	1536		0.05	≈ 1146	16.5	16.5
bem07		5766	5768		0.025	≈ 2292	225	225
bem08		9126	9128		0.02	≈ 2865	617	617

Table 5.2: Plane wave scattering by a rigid sphere: attributes of the BE models

---

[1]Using the "six linear elements per wavelength" rule of thumb.
[2]Mesh too coarse.

model	L	$\dim\boldsymbol{\Phi}^u = \Sigma$ DOF	CPU time [s]
wbt01	6	49	0.1
wbt02	8	81	0.6
wbt03	10	121	0.8
wbt04	12	169	1.05
wbt05	16	289	1.72

Table 5.3: Plane wave scattering by a rigid sphere: attributes of the WB models

5.4 Validation example: baffled piston

The remaining validation examples presented in this chapter consider problems involving semi-infinite domains. The validation example discussed in this section represents a circular piston radiating sound into a semi-infinite acoustic domain. Similar to the previous test case presented in section 5.3, the validation example considered here was chosen due to the existence of an analytical solution, which can be derived in a closed-form. Once again, the analytical solution obtained is used as a reference in the convergence analysis, which compares the performance of both the BEM and WBT. The calculations are performed on a 3 GHz single-core, *Intel*-based computer using 1 Gbyte RAM and running the *Windows 2 000* operating system.

5.4.1 Problem definition

Consider a circular piston radiator of radius $R = 0.15\,\mathrm{m}$ mounted in an infinite rigid baffle, see figure 5.11(a). Assuming a piston-like motion, all points forming the surface of the radiator vibrate in-phase with the normal velocity of $v_n = 0.01\,\mathrm{m/s}$. The surrounding fluid is considered to be air with the speed of sound $c = 343.8\,\mathrm{m/s}$ and mass density $\rho = 1.2\,\mathrm{kg/m^3}$.
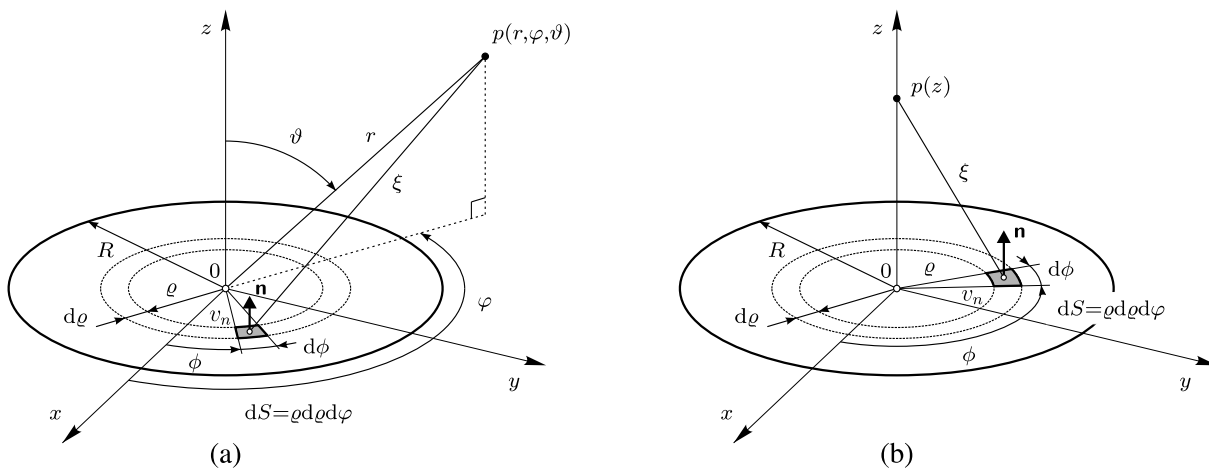
Figure 5.11: Baffled piston: (a) general radiator-observer problem and (b) simplified case $p = p(z)$ (Rejlek et al., 2008b)
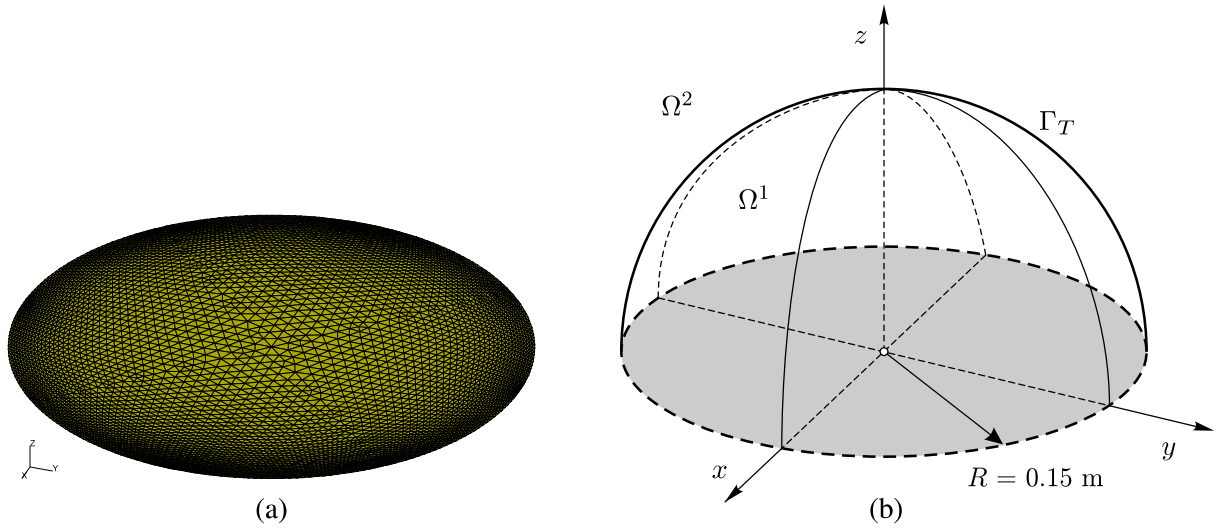
Figure 5.12: Baffled piston: (a) the boundary element and (b) the corresponding wave based model (Rejlek et al., 2008b)

5.4.2   Analytical solution

Sound radiation problems involving single or multiple planar radiators mounted in a rigid baffle can be investigated by evaluating the Rayleigh integral. In terms of differential calculus, each point on the surface of the radiator represents an elementary sound source inducing an infinitesimal pressure contribution to the overall sound pressure at a distance ξ

$$\mathrm{d}p(\xi) = \frac{\mathrm{j}k\rho c v_n}{2\pi} \frac{\mathrm{e}^{-\mathrm{j}k\xi}}{\xi} \mathrm{d}S. \tag{5.51}$$

ξ is measured between the infinitesimal radiating area $\mathrm{d}S$ on the surface of the radiator and the field point $\mathbf{r}$ located in the investigated semi-infinite domain above the baffle plane ($z > 0$)

$$\xi = \sqrt{r^2 + \varrho^2 - 2r\varrho \sin\vartheta \cos(\phi - \varphi)}. \tag{5.52}$$

At an arbitrary position $\mathbf{r}$, the sound pressure is determined by integrating all infinitesimal contributions (5.51) over the surface of the radiator

$$p(\mathbf{r}) = \frac{\mathrm{j}k\rho c}{2\pi} \iint_S v_n \frac{\mathrm{e}^{-\mathrm{j}k\xi}}{\xi} \mathrm{d}S \tag{5.53}$$

yielding the aforementioned Rayleigh integral. As the integrand of the Rayleigh integral (5.53) depends on both the position of the elementary source $\mathrm{d}S = \varrho\,\mathrm{d}\varrho\,\mathrm{d}\varphi$ and the field point $\mathbf{r}$, solving the general case involves an infinite series expansion. However, a significant simplification can be made by reducing the original problem to an axisymmetrical one, see figure 5.11(b). Since the pressure only depends on the z coordinate, the expression for the radiator-observer distance ξ becomes

$$\xi = \sqrt{\varrho^2 + z^2}. \tag{5.54}$$

Finally, by taking the piston-like vibrational behaviour into account, the evaluation of the Rayleigh integral (5.53) can be carried out in a straightforward way, which yields an analytical, closed-form solution

$$
p(z) = \frac{\mathrm{j}k\rho c v_n}{2\pi} \int_0^R \underbrace{\int_0^{2\pi} \frac{\mathrm{e}^{-\mathrm{j}k\xi}}{\xi}\mathrm{d}\phi}_{=2\pi} \varrho\mathrm{d}\varrho = \mathrm{j}k\rho c v_n \int_z^{\sqrt{R^2+z^2}} \mathrm{e}^{-\mathrm{j}k\xi}\mathrm{d}\xi =
$$
$$
= \rho c v_n \left[\mathrm{e}^{-\mathrm{j}kz} - \mathrm{e}^{-\mathrm{j}k\sqrt{R^2+z^2}}\right].
$$
(5.55)

5.4.3 Numerical models

The computational mesh used in the BE model consists of 4 729 nodes forming 9 216 triangular linear acoustic elements, see figure 5.12(a). The BE calculations are carried out in the commercial CAE tool *LMS/Sysnoise* Rev. 5.6 (LMS International, 2010) by applying a baffled direct collocational scheme.

Based on to the problem definition, a corresponding WB model is built up. As the radius of the truncation hemisphere Γ_T is chosen to coincide with the radius of the piston R, the resulting wave model consists merely of one convex Ω^1 and one semi-infinite domain Ω^2, see figure 5.12(b). The bounded part is formed by 294 degrees of freedom, while in the semi-infinite region 28 wave functions are applied.

5.4.4 Validation study

For the frequency response analyses two response points are selected $\mathrm{RP1} = (0,\ 0,\ 0.1)$ m and $\mathrm{RP2} = (0,\ 0,\ 1)$ m, which are located in the bounded and unbounded part of the WB model, respectively. Figure 5.13 plots the response spectra for the sound pressure calculated by the analytical formula (5.55) and the numerical methods at the response point (a) $\mathbf{r}_1$ and (b) $\mathbf{r}_2$. Similarly, the figures 5.14 and 5.15 capture the pressure field in the proximity of the radiator plotted on a field point mesh perpendicular to the baffle plane at 2 kHz and 4 kHz. The black solid line in the WB results indicates the truncation hemisphere Γ_T of the wave model.

Figures 5.13, 5.14 and 5.15 illustrate a perfect match between the WB and BE predictions across a wide frequency range. The pressure contours in figures 5.14 and 5.15, which are normal to the rigid baffle plane, further reveal that the normal velocity boundary condition has been taken into account correctly.

5.4.5 Convergence analysis

In order to provide a fair comparison between both numerical solution techniques, a convergence analysis is carried out. Figure 5.16 plots the spatially averaged relative prediction error ε for the sound pressure versus the CPU time needed for a direct response calculation at both (a)
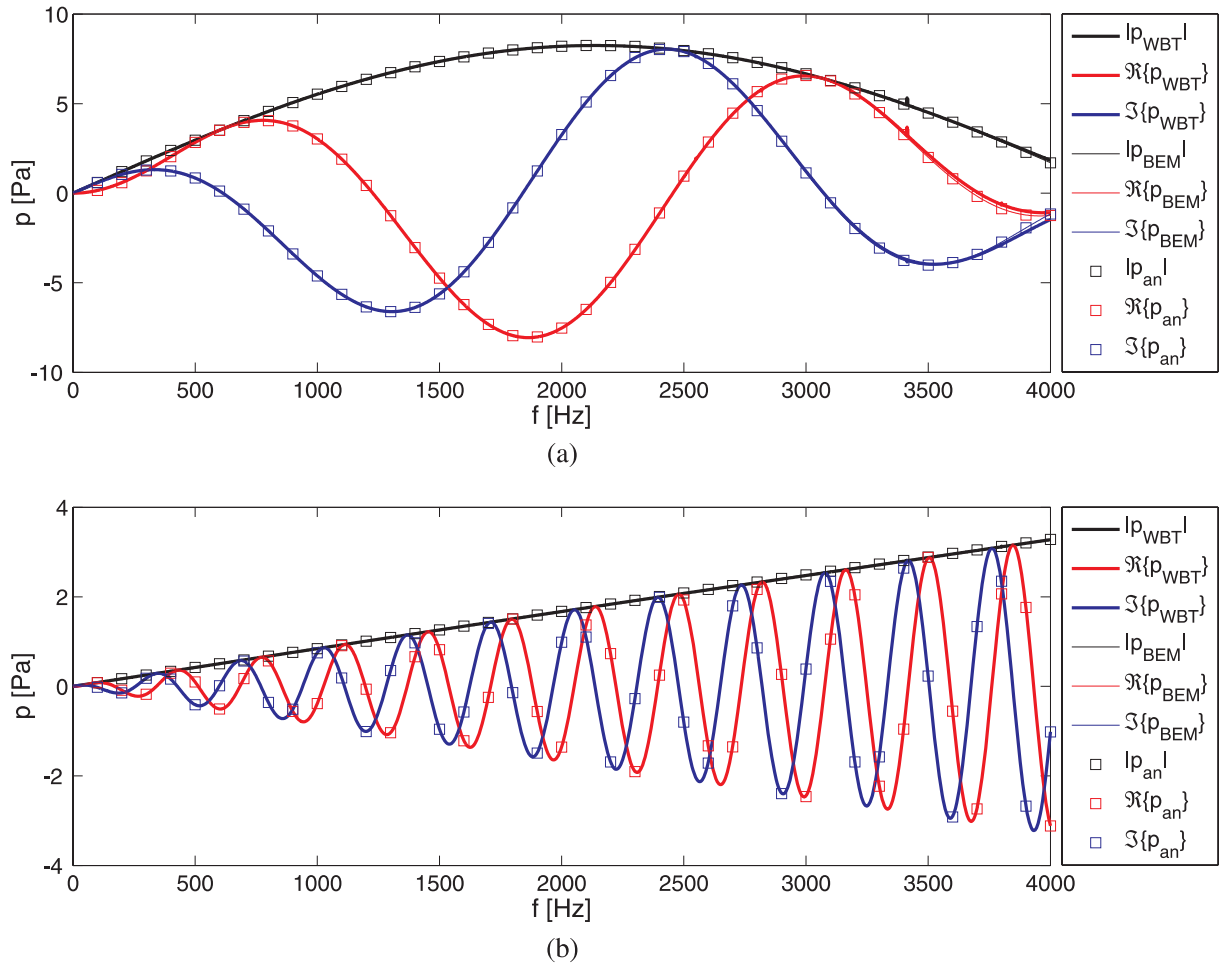
Figure 5.13: Baffled piston: sound pressure spectra up to 4 kHz evaluated at (a) RP1 and (b) RP2 (Rejlek et al., 2008b)

100 Hz and (b) 2 000 Hz. For the convergence study various BE and WB models, see tables 5.4 and 5.5, are utilised. The relative error ε is defined as follows

$$\varepsilon = \frac{1}{N} \sum_{i=1}^{N} \left| \frac{p_\bullet(\mathbf{r}_i) - p_{REF}(\mathbf{r}_i)}{p_{REF}(\mathbf{r}_i)} \right| \tag{5.56}$$

with $p_\bullet(\mathbf{r}_i)$ denoting the corresponding numerical solution evaluated at $N = 21$ different response points $\mathbf{r}_i$ located along the z axis in the range $z = \langle 0; 2 \rangle$ m with a step size of 0.1 m. The analytical solution of the problem (5.55) is used as a reference p_{REF}. The indicated CPU times for both BE and WB models represent the time to perform the numerical integration needed to build up the matrix system, its solution and the postprocessing step. The sizes of all BE models are chosen in order to enable an in-core BE calculation on the computer platform indicated in section 5.4.

Although WBT, similar to BEM, yields fully populated matrices with complex coefficients, the small size of the WB models and the favourable convergence rate make this technique more efficient than the element-based methods. Figure 5.16 confirms the findings of Desmet (1998) and Pluymers (2006) that the WBT achieves a higher convergence rate than to element-

BEM: Re{p}   WBT: Re{p}

(a) Real part of the sound pressure [Pa]

BEM: |p| WBT: |p|

(b) Sound pressure magnitude [Pa]
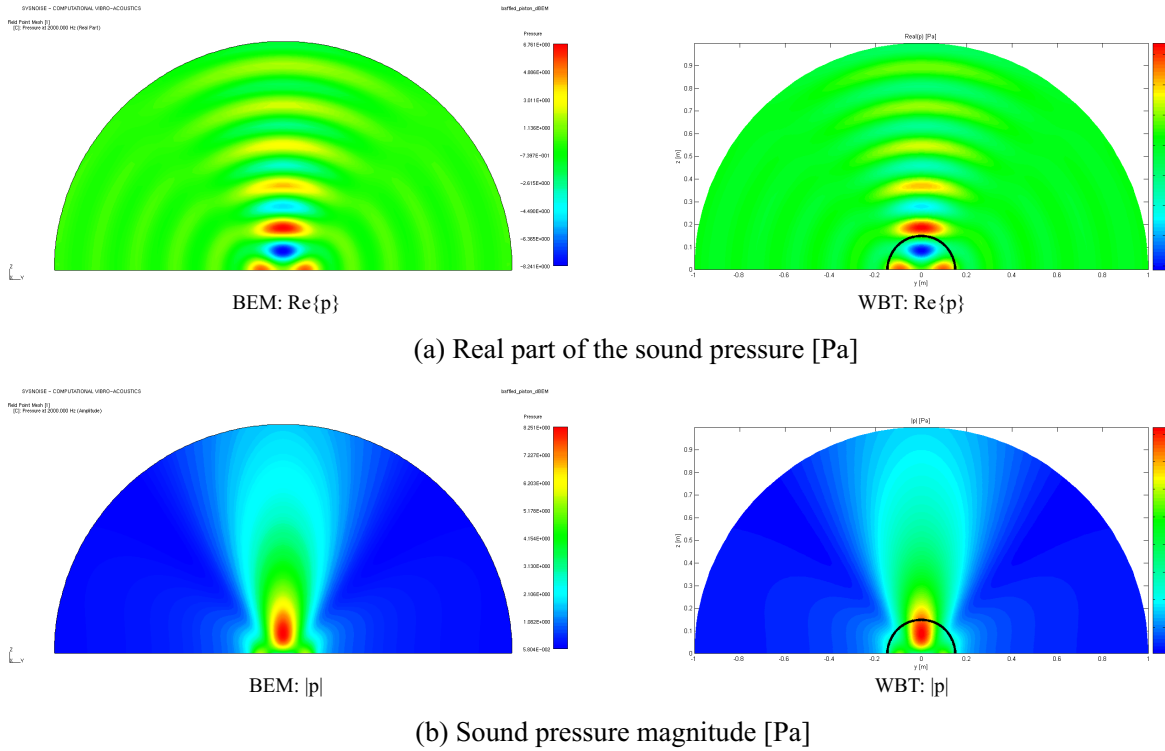
Figure 5.14: Baffled piston: sound pressure field at 2 kHz predicted by BEM and WBT (Rejlek et al., 2008b)

model	#nod	#ele	h_{max}[3] [m]	h_{min}[3] [m]	f_{max}[4] [Hz]	CPU time [s]
bem01	1 477	2 820	0.01	0.005	$\approx 2\,510$	40
bem02	2 949	5 708	0.01	0.002	$\approx 2\,690$	80
bem03	4 729	9 216	0.01	0.001	$\approx 2\,715$	410
bem04	8 117	15 916	0.0035	0.0035	$\approx 6\,500$	1 235

Table 5.4: Baffled piston: attributes of the BE models

model	$n_{r\bullet} = n_{s\bullet} = n_{t\bullet}$	L	$\dim\mathbf{\Phi}^b$	$\dim\mathbf{\Phi}^{si}$	Σ DOF	CPU time [s]
wbt01	2	6	54	28	82	0.34
wbt02	4	6	150	28	178	1.07
wbt03	4	8	150	45	195	1.15
wbt04	6	20	294	231	525	12.11
wbt05	8	22	486	276	762	36.42
wbt06	10	25	726	351	1 077	59.84

Table 5.5: Baffled piston: attributes of the WB models

based techniques. Particularly in the higher frequency range, the WBT provides more accurate predictions with much less computational effort.

---

[3]The maximum/minimum element edge length.

[4]Using the "twelve linear elements per wavelength" rule of thumb.

(a) Real part of the sound pressure [Pa]

(b) Sound pressure magnitude [Pa]
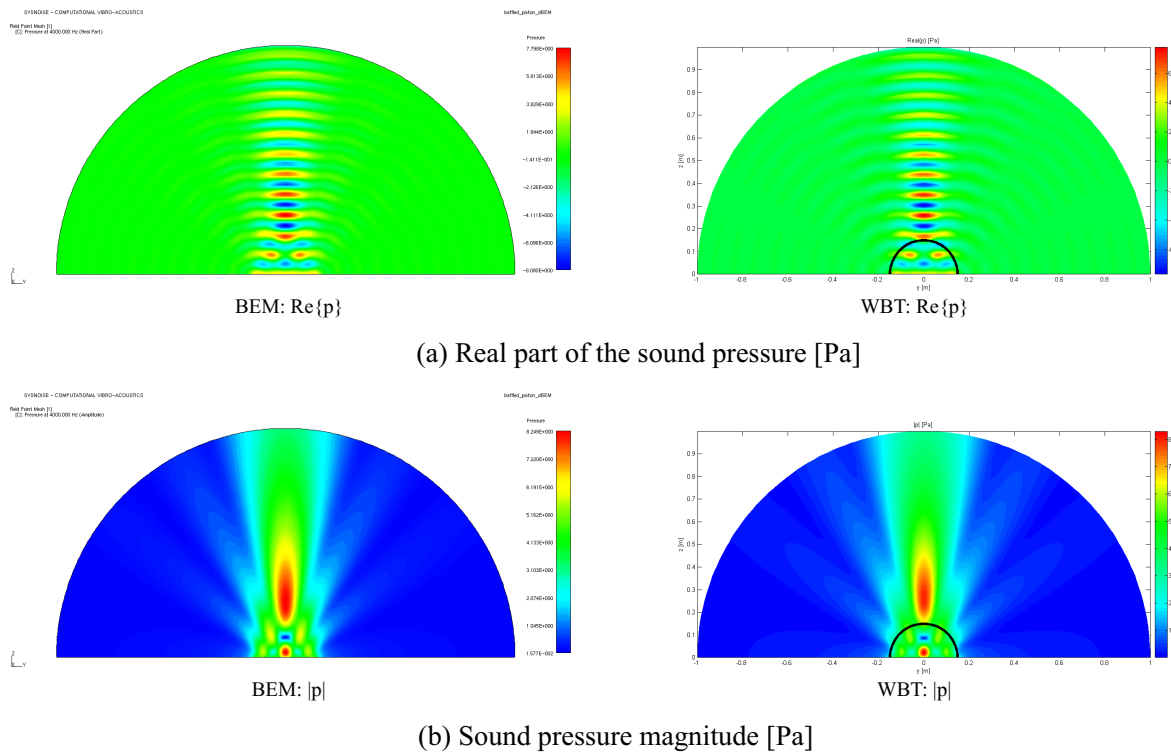
Figure 5.15: Baffled piston: sound pressure field at 4 kHz predicted by BEM and WBT (Rejlek et al., 2008b)
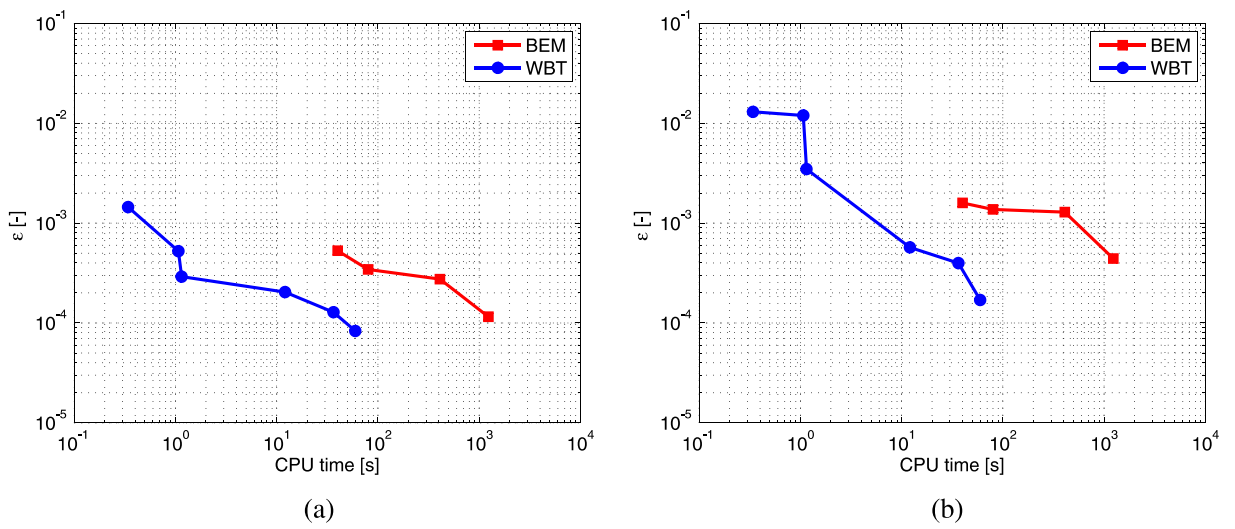
Figure 5.16: Baffled piston: pressure amplitude convergence curves at (a) 100 Hz and (b) 2 000 Hz calculated by BEM and WBT (Rejlek et al., 2008b)

5.5 Validation example: patch array

The next validation example considers a baffled problem involving a radiator of higher geometrical complexity. It consists of four rectangular planar radiators mounted in a baffle plane. All four patches radiate in-phase and form an array-like structure with the layout shown in figure 5.17. Each of the four radiators has the size of $a = 0.5$ m and shows a piston-like time-harmonic motion with a normal velocity of $v_n = 0.01$ m/s. The air has the speed of sound $c = 343.8$ m/s and the mass density $\rho = 1.2$ kg/m^3.

(a)   (b)
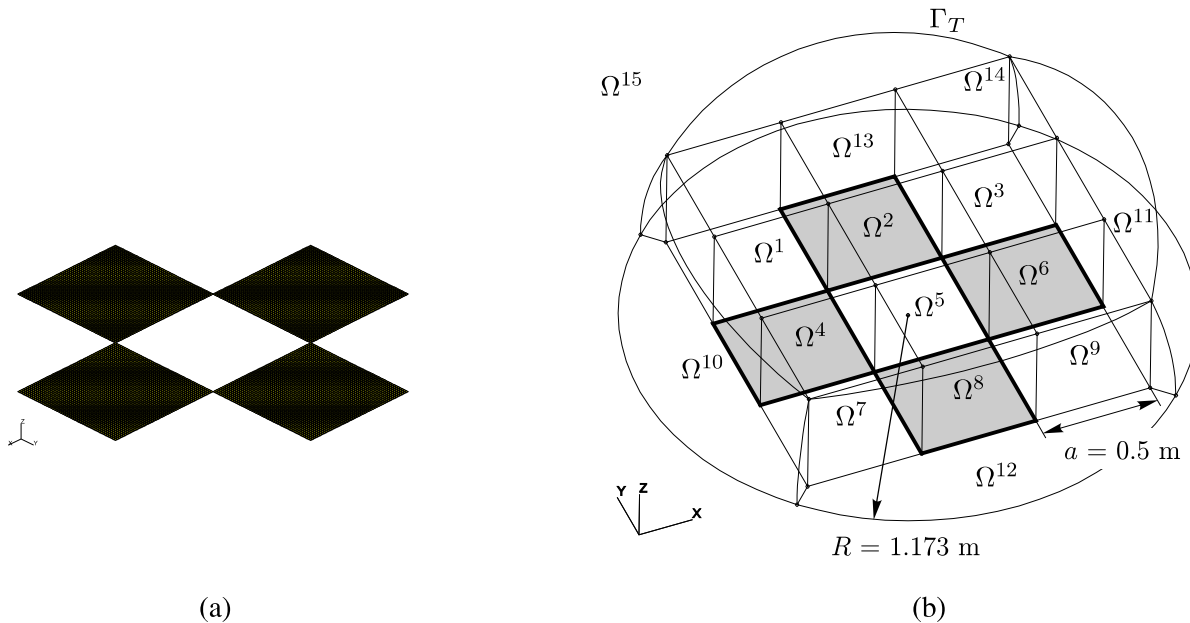
Figure 5.17: Patch array: (a) the boundary element and (b) the corresponding wave based model (Rejlek et al., 2008b)

attribute	denotation	value
solution scheme		BEM direct collocational baffled
number of nodes	#nod	10 400
number of elements	#ele	10 000
mesh topology	topo	quad4 dominant
maximum element edge size	h_{max}	0.01 m
degrees of freedom	DOF	10 400
FRF range	f_{min}, f_{max}	1–500 Hz
FRF step	Δf	1 Hz
CPU time needed for FRF	t_{FRF}	512 000 s

Table 5.6: Patch array: attributes of BE model

The BE mesh consists of 10 400 nodes forming 10 000 quadrilateral linear acoustic elements with a maximum element edge length of $h_{max} = 0.01$ m, see figure 5.17(a). Once again, the baffled direct collocational approach of the *LMS/Sysnoise* Rev. 5.6 (LMS International, 2010) is used to perform the BE calculations on the computer platform indicated in section 5.3.3.
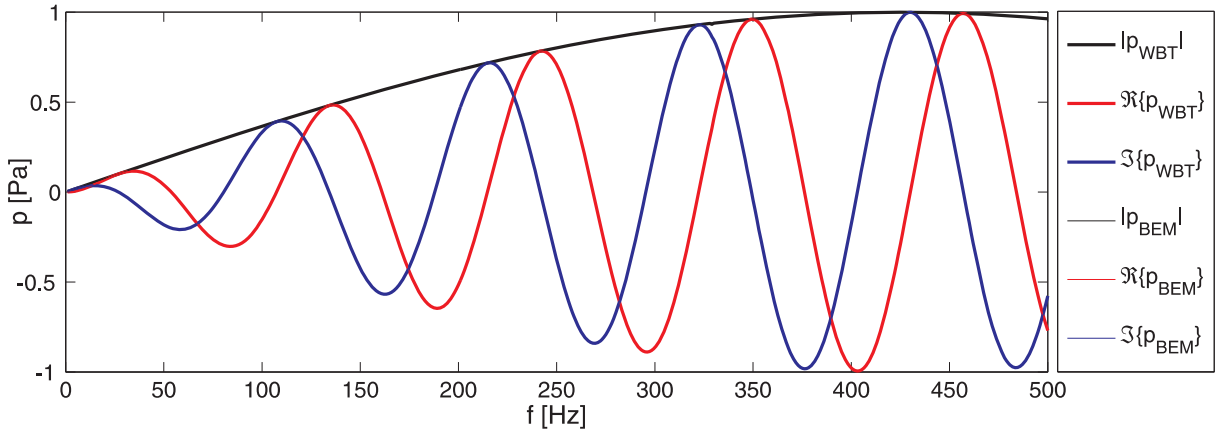
Figure 5.18: Patch array: sound pressure spectra up to 500 Hz evaluated at $RP1 = (0.1; 1; 3)$ m (Rejlek et al., 2008b)

Figure 5.17(b) depicts the WB model consisting of fourteen bounded subdomains Ω^1–Ω^{14} and one semi-infinite domain Ω^{15} located outside the truncation hemisphere Γ_T of radius $R = 1.173$ m. Each of the subdomains Ω^1–Ω^9 consists of 96 degrees of freedom, subdomains Ω^{10}–Ω^{14} are formed by 150 wave functions each, and in the semi-infinite domain Ω^{15} 66 wave functions are applied, which yield a total number of 1 680 wave functions.

Figure 5.18 shows the comparison of the pressure response spectra predicted by the WBT and BEM at response point $RP1 = (0.1, 1, 3)$ m. The attributes of the BE and WB model are listed in table 5.6 and 5.7, respectively. Figure 5.19 captures the distribution of the sound pressure on the baffle plane at 500 Hz as predicted with the BE and WB approaches. Once again, the WB results match the BE predictions and show that the continuity conditions prescribed at the interfaces between the subdomains have been correctly accounted for.

attribute	denotation	value
number of subdomains	N_a	14 bounded
	N_{si}	1 semi-infinite
truncation strategy		constant
truncation parameters	$n_{r\bullet}, n_{s\bullet}, n_{t\bullet}$	$n_{r\bullet}^{1-9} = n_{s\bullet}^{1-9} = n_{t\bullet}^{1-9} = 3$
		$n_{r\bullet}^{10-14} = n_{s\bullet}^{10-14} = n_{t\bullet}^{10-14} = 4$
	L	10
radius of truncation hemisphere	R	1.173 m
degrees of freedom	$\dim\boldsymbol{\Phi}$	1 680
FRF range	f_{min}, f_{max}	1–500 Hz
FRF step	Δf	1 Hz
CPU time needed for FRF	t_{FRF}	75 750 s

Table 5.7: Patch array: attributes of WB model

BEM: Re{p}   WBT: Re{p}

(a) Real part of the sound pressure [Pa]

BEM: |p| WBT: |p|

(b) Sound pressure magnitude [Pa]
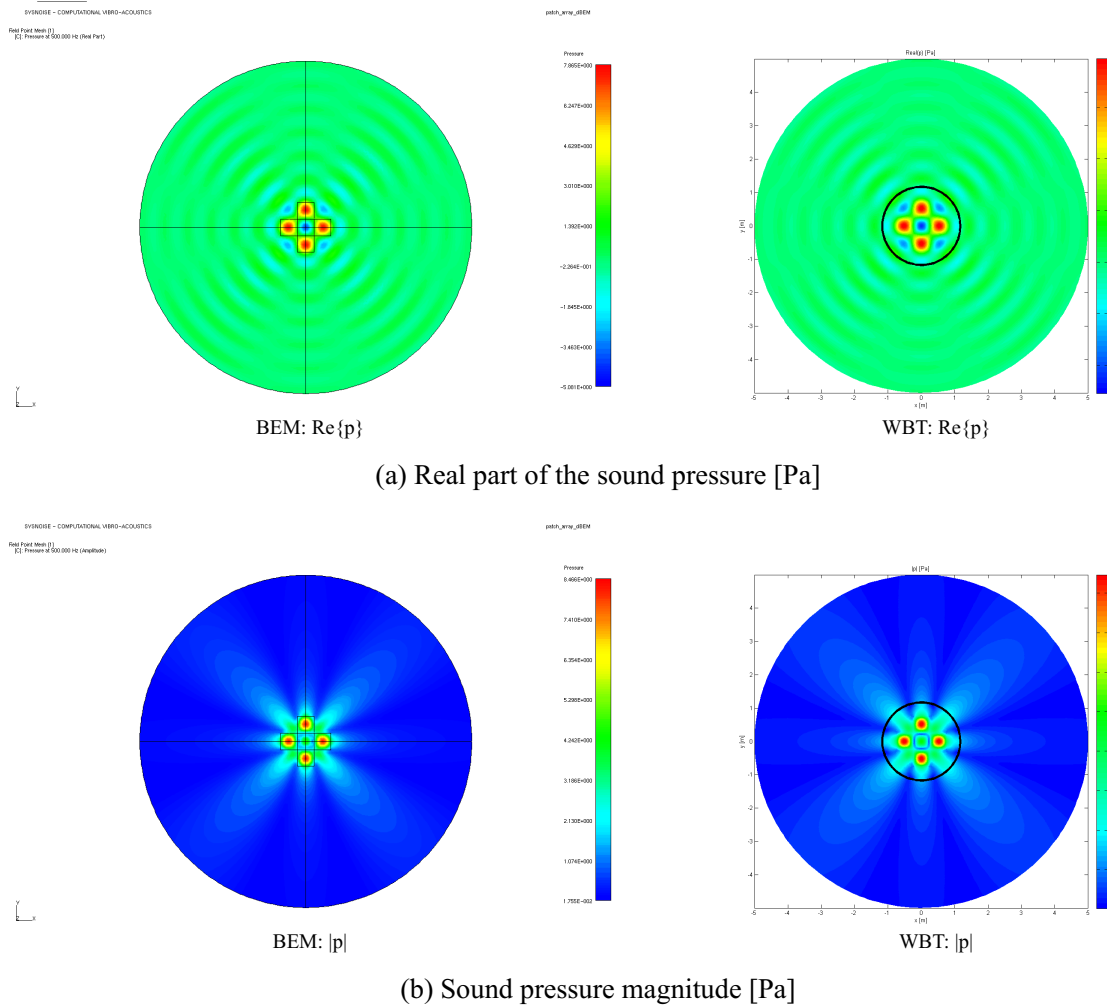
Figure 5.19: Patch array: sound pressure on the baffle at 500 Hz predicted by BEM and WBT (Rejlek et al., 2008b)

5.6 Validation example: engine bay

The last validation example in this chapter considers application to an industry-sized problem and demonstrates the practical applicability of the wave based approach to baffled non-planar problems. The problem represents a simplified engine bay of an executive car with the dimensions indicated in figure 5.20. The structure is located at $z = 0.18$ m above the rigid plane and is considered to be rigid except for the inner side of the upper panel, which has a prescribed normal velocity boundary condition of $v_n = 0.01 \, \text{m/s}$.

The computational mesh of the BE model consists of 7 648 nodes forming 7 531 quad4 linear acoustic elements with the maximum element edge size of $h_{max} = 0.025$ m, see figure 5.21. Since the problem exhibits an open boundary, an indirect variational solution scheme is chosen with the jump of pressure boundary condition prescribed along the free edge located at the bottom of the structure. This additional boundary condition is essential in the indirect variational formulation of BEM in order to ensure the continuity of acoustic pressure along the free edges. The BE analysis is performed in *LMS Virtual.Lab* CAE system running the *LMS/SYSNOISE* Rev. 5.6 solver (LMS International, 2010) on a computational platform matching the specifi-
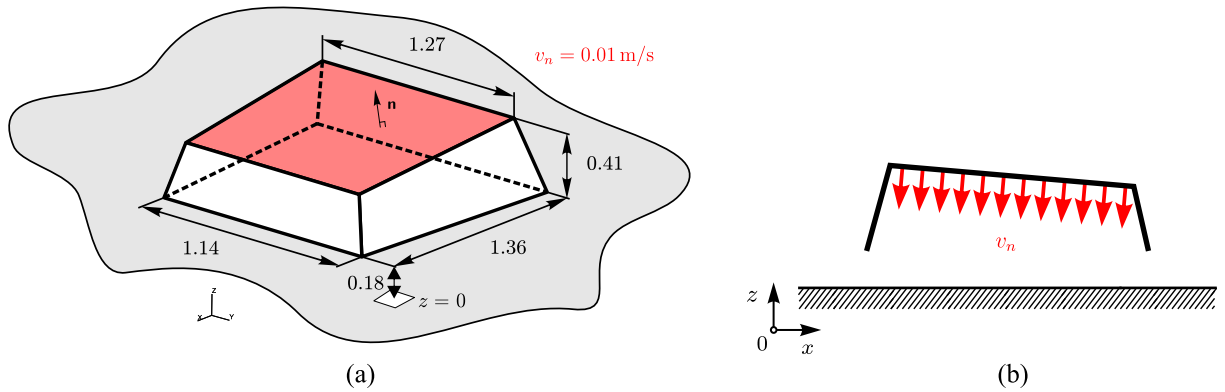
Figure 5.20: Engine bay: (a) problem definition with dimensions in [m], (b) the side view

cations outlined in section 5.4. Figure 5.22 shows the corresponding WB model consisting of eleven bounded subdomains Ω^1–Ω^{11} and an additional semi-infinite domain Ω^{12}. The truncation hemisphere Γ_T dividing the wave model into the bounded and unbounded part has the radius of $R = 1$ m.

Figures 5.23 and 5.24 capture the predicted sound pressure fields at 500 Hz and 1 000 Hz, respectively. The real part of the acoustic pressure is plotted at the field point mesh located in the zx-plane. In the WB results the bold solid lines denote the physical boundary, while the dashed line stands for a truncation hemisphere Γ_T. The contour plots prove that the normal velocity boundary condition at both the rigid plane and the physical boundary including the coupling conditions at the common interfaces between the adjacent subdomains have been accurately taken into account.

For the frequency response analyses, two response points are selected. While the first point
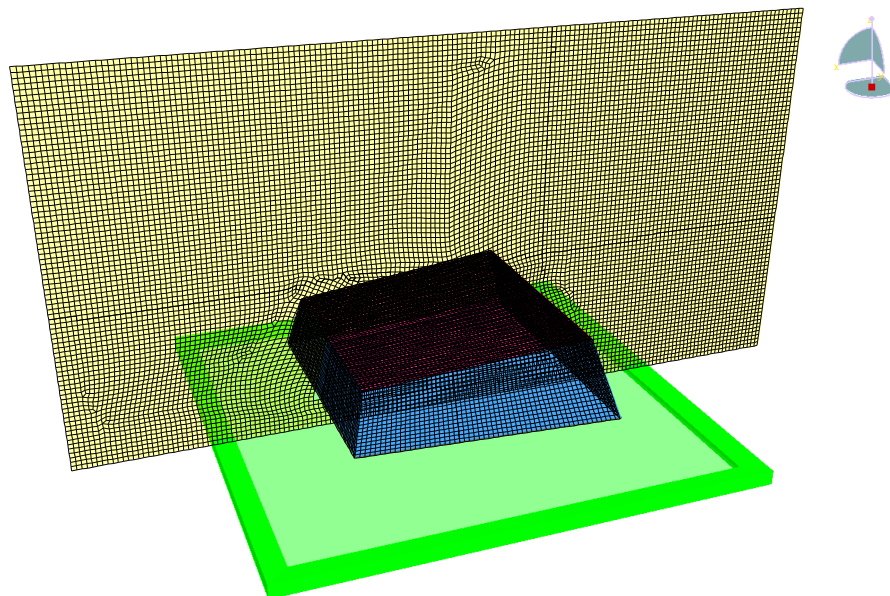
Figure 5.21: Engine bay: the BE model – the computation BE mesh indicated in blue, the field point mesh indicated in ochre, the symmetry plane representing a rigid plane indicated in green
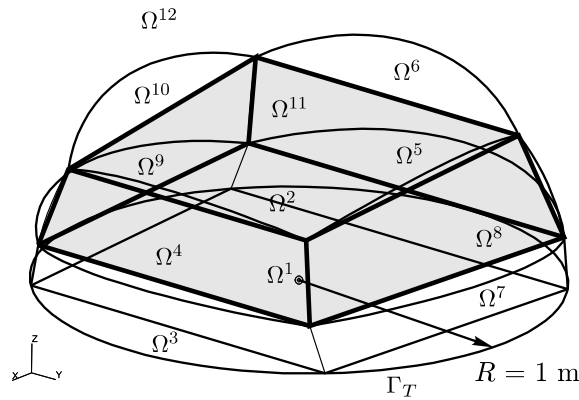
Figure 5.22: Engine bay: the WB model consisting of eleven bounded and one semi-infinite subdomain

$RP1 = (0.06,\ 0.04,\ 0.3)$ m is located inside the engine bay, the latter one $RP2 = (0,\ 7.5,\ 1)$ m is located in the semi-infinite domain of the WB model and represents the reference microphone position used during the pass-by noise scenarios. Figures 5.25 and 5.26 plot the pressure response spectra determined by the BE model (red curve) and the WB model (blue curve), see, respectively, tables 5.8 and 5.9 for the detailed model set ups. While the WB model performs faster than its BE counterpart, the WB prediction matches the reference BE solution roughly up to a frequency of 800 Hz for both response points. Above this frequency, the WB solution
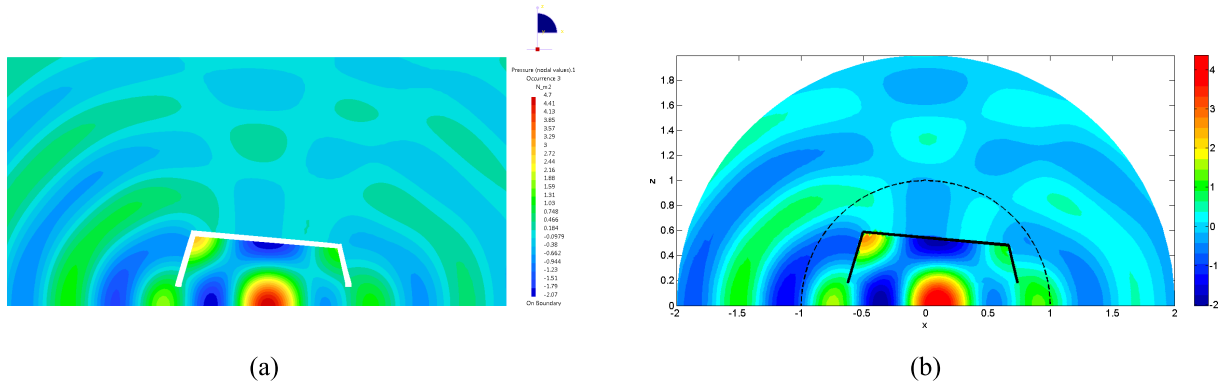
Figure 5.23: Engine bay: real part of sound pressure at 500 Hz predicted by (a) BEM and (b) WBT
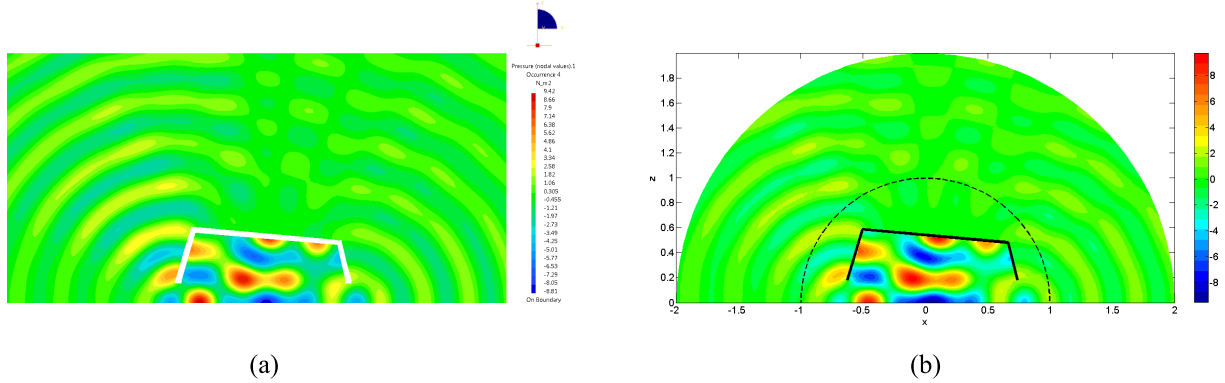
Figure 5.24: Engine bay: real part of sound pressure at 1 000 Hz predicted by (a) BEM and (b) WBT

begins to deteriorate slightly, mainly due to the insufficient number of wave functions applied in both the bounded and semi-infinite domains. Increasing the truncation parameters applied in the bounded acoustic domains to $n_{r\bullet} = n_{s\bullet} = n_{t\bullet} = 9$ yields a wave model consisting of 6 831 degrees of freedom with a predicted response represented by the gray solid curve. Although this model needs 163 550 s in order to run the frequency response analysis, an increased accuracy can be observed in the higher frequency range above 800 Hz. A further increase of the model size to $n_{r\bullet} = n_{s\bullet} = n_{t\bullet} = 10$ and $L = 30$ yields the wave model consisting of 8 482 degrees of freedom, which is represented by the black dashed curve in figures 5.25 and 5.26. This model requires roughly 457 000 s to obtain the frequency response predictions, which match the reference BEM solution across the whole frequency range.

attribute	denotation	value
solution scheme		BEM indirect variational
number of nodes	#nod	7 648
number of elements	#ele	7 531
mesh topology	topo	quad4
maximum element edge size	h_{max}	0.025 m
degrees of freedom	DOF	10 400
FRF range	f_{min}, f_{max}	1–1 000 Hz
FRF step	Δf	1 Hz
CPU time needed for FRF	t_{FRF}	168 100 s

Table 5.8: Engine bay: attributes of BE model

attribute	denotation	value
number of subdomains	N_a	11 bounded
	N_{si}	1 semi-infinite
truncation strategy		constant
truncation parameters	$n_{r\bullet}, n_{s\bullet}, n_{t\bullet}$	7
	L	25
radius of truncation hemisphere	R	1 m
degrees of freedom	dim$\mathbf{\Phi}$	4 575
FRF range	f_{min}, f_{max}	1–1 000 Hz
FRF step	Δf	1 Hz
CPU time needed for FRF	t_{FRF}	100 600 s

Table 5.9: Engine bay: attributes of the baseline WB model

5.7 Summary

This chapter reported on the basic concepts and the application of the WBT for three-dimensional, uncoupled, unbounded acoustic problems. Four validation examples were considered. The first validation case addressed the application to wave scattering problems, namely a plane wave scattering by a rigid sphere. Due to the simple geometry of the scatterer, it was possible to derive an analytical solution, which was then used as a reference for the convergence study.
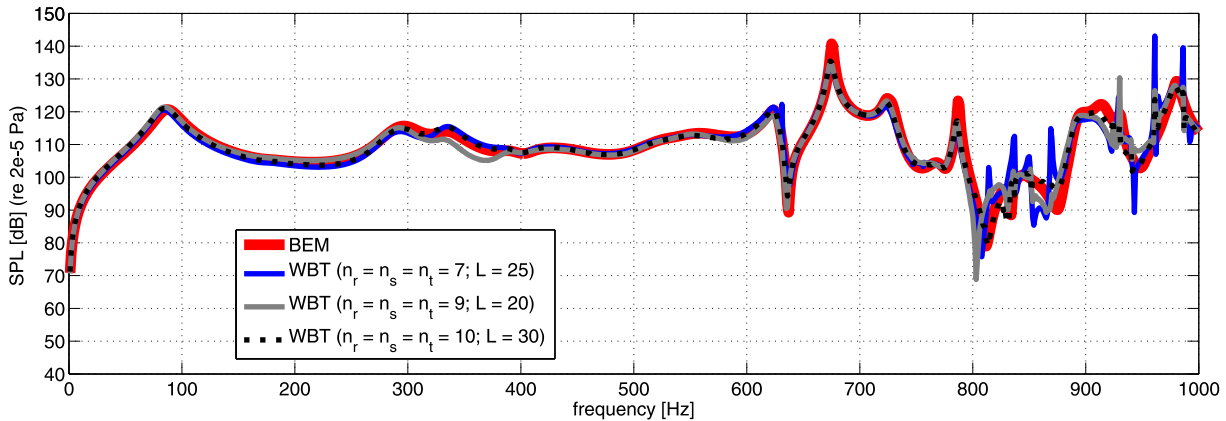
Figure 5.25: Engine bay: pressure response spectra at point RP1
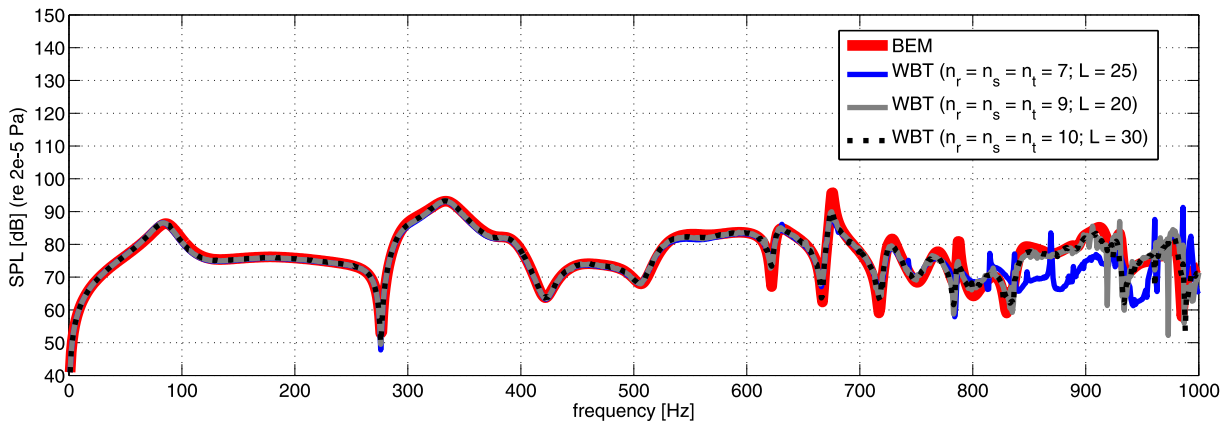
Figure 5.26: Engine bay: pressure response spectra at point RP2

The remaining validation examples involved semi-infinite solution domains. The WBT was successively applied to three semi-infinite problems of increasing complexity. The simplest validation problem considered a sound radiation analysis of a baffled piston radiator. In this particular case, it was once again possible to derive an analytical solution, which became the reference for the convergence study. The next validation example presented a more complex problem, which involved the domain decomposition strategy in the bounded part of the wave model. The radiator consisted of an array of four vibrating patches. The last validation example presented an application to an industry-sized problem by considering a non-planar baffled problem.

All of the validation examples have demonstrated the suitability of WBT for tackling steady-state, unbounded acoustic problems involving both the free-field and semi-infinite domains. Finally, both convergence studies have proven that the computational performance of WBT is higher than that of BEM. Nevertheless, as already indicated in chapter 4, the computational efficiency of the WBT has not yet been fully exploited. Thus, by using an optimised coding in high-performance programming language, WBT gains a further advantage in computational efficiency over BEM. In addition, to prevent increase of the computational burden for unbounded problems involving complex geometries, a direct FE–WB coupling scheme (Pluymers, 2006; Silar, 2007) could be further adopted. Moreover, the hybrid modelling framework recently developed by Van Genechten (2010), which employs a modally reduced finite element model, is even more advantageous for modelling of geometrically complex problems.

Chapter 6

The Wave Based Technique for fully coupled, unbounded vibro-acoustic problems

This chapter presents the concepts and applications of the wave based technique for a steady-state analysis of three-dimensional, fully coupled, unbounded vibro-acoustic problems. In a wide variety of real-life problems, the mutual coupling interaction between the structure and fluid is no longer negligible, which implies that the both parts of problem have to be considered simultaneously. The vibrating structure influences the adjacent acoustic domain, while the pressure waves in fluid induce the structural vibrations at the same time. As a consequence, it is no longer possible to assume the structure as independent of fluid, and vice versa, so the whole problem must be considered as one (fully) coupled system. In this type of formulation, both the structural thin plate bending problem and the unbounded acoustic problem are described by means of a coupled wave based model.

For the reader's convenience, section 6.1 first restates the definition of a general, coupled, unbounded vibro-acoustic problem. Section 6.2 then outlines the concept of the wave based technique for the coupled problems by introducing some additional coupling terms, which account for the mutual interaction between the structural and acoustic parts, and the WBT is applied on three different coupled problems. Section 6.3 presents the application of WBT to an academic example involving a free-field, unbounded acoustic domain. Section 6.4 considers the application of WBT to an industry-sized problem consisting of a simplified car-like geometry involving a semi-infinite acoustic domain. In the last validation example, see section 6.5, the WBT is applied for a coupled analysis of the so-called distributed mode loudspeaker, which involve both the free-field and semi-infinite acoustic domains. Section 6.6 concludes the chapter with a summary.

6.1   Problem definition

Consider a general three-dimensional, fully coupled, unbounded vibro-acoustic problem. The structural part Ω_s consists of a thin flat plate (Vanmaele, 2007) subjected to (i) boundary conditions imposed at the physical boundary Γ_s, (ii) a point force F acting in the out-of-plane

direction at the position $\mathbf{r}_F$ and (iii) the acoustic pressure loading p arising from the coupling to an acoustic domain along the structural-acoustic interface Γ_{sa}. In the structural problem, the structural-acoustic coupling effects are incorporated as a distributed transverse force by extending the particular solution function of the governing differential equation. The acoustic part Ω_a consists of a closed physical boundary Γ_a surrounded by fluid, which forms an unbounded acoustic domain (Diwoky et al., 2008). The acoustic part is subjected to (i) boundary conditions defined at Γ_a, (ii) the point source having an acoustic volume velocity strength amplitude q located at $\mathbf{r}_q$ and (iii) the normal velocity distributed at the structural-acoustic interface Γ_{sa} accounting for the coupling effects resulting from plate dynamics. An additional normal velocity boundary condition applied at Γ_{sa} accounts for these acoustic-structural coupling effects.

The dynamic excitations show a time-harmonic behaviour $e^{j\omega t}$ with a circular frequency ω. The corresponding time-harmonic response of the vibro-acoustic system is thus described in terms of steady-state out-of-plane displacement w_z and the acoustic pressure field p.

6.1.1 Structural part

The structural displacement field $w_z(\mathbf{r})$ is governed by the steady-state dynamic equation

$$\nabla^4 w_z(\mathbf{r}') - k_b^4 w_z(\mathbf{r}') = \frac{p}{D} + \frac{F}{D}\delta(\mathbf{r}'_F), \ \forall \mathbf{r} \in \Omega_s \tag{6.1}$$

based on Kirchhoff thin plate theory for the out-of-plane bending motion (Leissa, 1993). The problem consists of a plate Ω_s characterised by its density ρ_s, Young's modulus E, material loss factor η, the Poisson's ratio ν and the thickness t. The dynamic field variables are expressed in terms of a local coordinate system (x', y', z'), see figure 2.3. The plate is subjected to a point force F acting at position $\mathbf{r}_F$ directed in the out-of-plane direction z'. In (6.1) ∇ is the Nabla operator

$$\nabla^4 = \frac{\partial^4}{\partial x^4} + 2\frac{\partial^4}{\partial x^2 \partial y^2} + \frac{\partial^4}{\partial y^4}, \tag{6.2}$$

δ is the Dirac delta function and k_b and D are the bending wave number and bending stiffness, respectively, which are defined as follows

$$k_b = \sqrt[4]{\frac{\rho_s t \omega^2}{D}}, \tag{6.3}$$

$$D = \frac{Et^3(1 + j\eta)}{12(1 - \nu^2)} \tag{6.4}$$

with $j = \sqrt{-1}$ the imaginary unit. In order for the problem to be well-posed, a non-overlapping set of boundary conditions is prescribed $\partial\Omega_s = \Gamma_s = \Gamma_{w\theta} \cup \Gamma_{MV} \cup \Gamma_{wM} \cup \Gamma_{\theta V}$ at the physical boundary. The possible boundary conditions are as follows:

- kinematic boundary conditions $\forall \mathbf{r}' \in \Gamma_{w\theta}$:

$$w_z(\mathbf{r}') = \bar{w}(\mathbf{r}), \tag{6.5a}$$

$$\mathcal{L}_\theta(w_z(\mathbf{r}')) = \bar{\theta}_n(\mathbf{r}), \tag{6.5b}$$

- mechanical boundary conditions $\forall \mathbf{r}' \in \Gamma_{MV}$:

$$\mathcal{L}_M(w_z(\mathbf{r}')) = \bar{M}_n(\mathbf{r}), \tag{6.5c}$$

$$\mathcal{L}_V(w_z(\mathbf{r}')) = \bar{V}_n(\mathbf{r}), \tag{6.5d}$$

- mixed boundary conditions type 1 $\forall \mathbf{r}' \in \Gamma_{wM}$:

$$w_z(\mathbf{r}') = \bar{w}(\mathbf{r}), \tag{6.5e}$$

$$\mathcal{L}_M(w_z(\mathbf{r}')) = \bar{M}_n(\mathbf{r}), \tag{6.5f}$$

- mixed boundary conditions type 2 $\forall \mathbf{r}' \in \Gamma_{\theta V}$:

$$\mathcal{L}_\theta(w_z(\mathbf{r}')) = \bar{\theta}_n(\mathbf{r}), \tag{6.5g}$$

$$\mathcal{L}_V(w_z(\mathbf{r}')) = \bar{V}_n(\mathbf{r}), \tag{6.5h}$$

where $\mathcal{L}_\bullet(w_z(\mathbf{r}'))$ are the differential operators defined in (A.28) in terms of a generalised plate coordinate system (n, s), with $\mathbf{n}'$ and $\mathbf{s}'$ the direction tangential and normal to the plate boundary, respectively, see figure 2.3.

6.1.2 Acoustic part

The Helmholtz equation governing the steady-state acoustic pressure perturbation field in the fluid domain

$$\nabla^2 p(\mathbf{r}) + k^2 p(\mathbf{r}) = -\mathrm{j}\rho_a \omega q \delta(\mathbf{r}, \mathbf{r}_q), \quad \forall \mathbf{r} \in \Omega_a \tag{6.6}$$

forms the acoustic part of the problem with ρ_a the fluid mass density, $k = \omega/c$ the acoustic wave number and c the speed of sound. Once again, the appropriate boundary conditions have to be imposed in order for the problem to be well-posed. The following boundary condition types forming a non-overlapping set $\partial\Omega_a = \Gamma_a = \Gamma_p \cup \Gamma_v \cup \Gamma_Z \cup \Gamma_{sa}$ are defined at the physical boundary:

- pressure boundary condition (Dirichlet/essential) $\forall \mathbf{r} \in \Gamma_p$:

$$p(\mathbf{r}) = \bar{p}(\mathbf{r}), \tag{6.7a}$$

- normal velocity boundary condition (Neumann/natural) $\forall \mathbf{r} \in \Gamma_v$:

$$\mathcal{L}_v(p(\mathbf{r})) = \bar{v}_n(\mathbf{r}), \tag{6.7b}$$

- normal impedance boundary condition (Robin/mixed) $\forall \mathbf{r} \in \Gamma_Z$:

$$\mathcal{L}_v(p(\mathbf{r})) = \frac{p(\mathbf{r})}{\bar{Z}_n(\mathbf{r})}, \tag{6.7c}$$

- normal displacement continuity condition at the fluid-structure interface (Neumann/natural) $\forall \mathbf{r} \in \Gamma_{sa}$:

$$\mathcal{L}_v(p(\mathbf{r})) = \mathrm{j}\omega w_z(\mathbf{r}) \tag{6.7d}$$

with the differential operator $\mathcal{L}_v(p(\mathbf{r}))$ as defined in (B.36b). As the acoustic domain Ω_a is unbounded, an additional Sommerfeld radiation condition has to be imposed $\forall \mathbf{r} \in \Gamma_\infty$:

$$\lim_{|\mathbf{r}|\to\infty} \left[|\mathbf{r}| \left(\frac{\partial p(\mathbf{r})}{\partial |\mathbf{r}|} + \mathrm{j}kp(\mathbf{r}) \right) \right] = 0. \tag{6.8}$$

6.2 Basic concepts of the Wave Based Technique

As shown in sections 6.1.1 and 6.1.2, the thin flat plate is described in terms of a local coordinate system (x', y', z'), while the acoustic domain is defined in a global coordinate system (x, y, z). The following coordinate transformation is introduced here

$$\forall \mathbf{r}(x', y') = \mathbf{r}(x, y, z) : \begin{cases} x = u_x(x', y') = u_{x,0} + u_{x,x'}x' + u_{x,y'}y' \\ y = u_y(x', y') = u_{y,0} + u_{y,x'}x' + u_{y,y'}y' \\ z = u_z(x', y') = u_{z,0} + u_{z,x'}x' + u_{z,y'}y', \end{cases} \tag{6.9}$$

which allows the geometry of the plate middle surface to be described in terms of a global coordinate system, see figure 6.1.
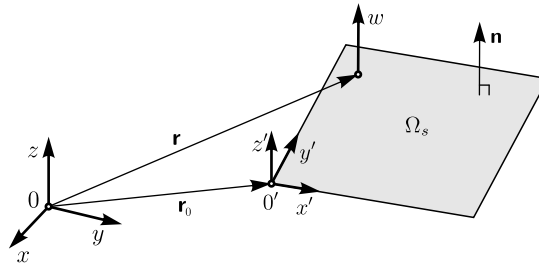
Figure 6.1: Transformation between the global and local plate coordinate system (Rejlek and Priebsch, 2010)

6.2.1 Field variable expansion

Since the structural-acoustic interaction appears as an additional boundary condition (6.7d) imposed at Γ_{sa}, the Helmholtz equation governing the steady-state pressure field in the acoustic part of a coupled problem has the same form as for the unbounded case. Therefore, the solution expansion approximating the exact pressure within each subdomain Ω^α can still be used

$$p^\alpha(\mathbf{r}) \approx \hat{p}^\alpha(\mathbf{r}) = \mathbf{\Phi}^\alpha(\mathbf{r})\,\mathbf{p}^\alpha + \hat{p}_q^\alpha(\mathbf{r}) \tag{6.10}$$

with $\boldsymbol{\Phi}^{\alpha}(\mathbf{r})$ the acoustic wave function set and $\mathbf{p}^{\alpha}$ the unknown contribution factors to an acoustic part of the coupled model, as proposed by Desmet (1998). In the structural part of a coupled problem, the acoustic-structural coupling effects arise from the distributed transverse load p acting on the plate. In the WBT formulation, these effects are incorporated as additional particular solution functions in the Kirchhoff equation (6.1). The out-of-plane displacement approximation is given by

$$w(\mathbf{r}) \approx \hat{w}(\mathbf{r}) = \boldsymbol{\Psi}(\mathbf{r})\,\mathbf{w} + \hat{w}_F(\mathbf{r}) + \hat{\mathbf{w}}_a(\mathbf{r})\mathbf{p} + \hat{w}_q(\mathbf{r}), \tag{6.11}$$

where $\boldsymbol{\Psi}(\mathbf{r})$ is the structural wave function set, and $\mathbf{w}$ are the unknown contribution factors to a structural part of the coupled model. In the solution expansion (6.11), $\hat{\mathbf{w}}_a(\mathbf{r})\mathbf{p}$ accounts for the pressure loading resulting from the homogeneous part of the pressure approximation $\boldsymbol{\Phi}(\mathbf{r})\mathbf{p}$, while $\hat{w}_q(\mathbf{r})$ represents the loading effects due to the acoustic volume velocity point source (Van Hal, 2004). In (6.11), the particular solution functions $\hat{\mathbf{w}}_a$ and $\hat{w}_q$ are given by

$$\hat{\mathbf{w}}_a(\mathbf{r}') = \int_{\Gamma_{sa}} \hat{w}_f(\|\mathbf{r}' - \mathbf{r}'_f\|)\boldsymbol{\Phi}(\mathbf{r}'_f)\,\mathrm{d}x'_f\,\mathrm{d}y'_f, \tag{6.12a}$$

$$\hat{w}_q(\mathbf{r}') = \int_{\Gamma_{sa}} \hat{w}_f(\|\mathbf{r}' - \mathbf{r}'_f\|)\hat{p}_q(\mathbf{r}'_f)\,\mathrm{d}x'_f\,\mathrm{d}y'_f \tag{6.12b}$$

with $\hat{w}_f$ the particular solution function representing the response of an infinitely large plate to a point force. Due to the flat shape of the plate, however, an alternative formulation for the particular function $\hat{\mathbf{w}}_a$ can be expressed in form (Desmet et al., 2002; Pluymers et al., 2002)

$$\hat{\mathbf{w}}_a(x', y') = \frac{\boldsymbol{\Phi}}{D[(A_{x'}^2 + A_{y'}^2)^2 - k_b^4]} \tag{6.13}$$

with

$$A_{x'} = k_x u_{x,x'} + k_y u_{y,x'} + k_z u_{z,x'}, \tag{6.14a}$$

$$A_{y'} = k_x u_{x,y'} + k_y u_{y,y'} + k_z u_{z,y'}. \tag{6.14b}$$

For the particular case $x \equiv x'$ and $y \equiv y'$, the expression (6.13) may be rewritten in the form

$$\hat{\mathbf{w}}_a(x', y') = \begin{cases} \hat{w}_{a_r}(x', y') = \dfrac{\Phi_r(x', y')}{D[(k_{rx}^2 + k_{ry}^2)^2 - k_b^4]} \\[2ex] \hat{w}_{a_s}(x', y') = \dfrac{\Phi_s(x', y')}{D[(k_{sx}^2 + k_{sy}^2)^2 - k_b^4]} \\[2ex] \hat{w}_{a_t}(x', y') = \dfrac{\Phi_t(x', y')}{D[(k_{tx}^2 + k_{ty}^2)^2 - k_b^4]}. \end{cases} \tag{6.15}$$

6.2.2 Domain decomposition

Similar to the uncoupled acoustic problem, the generally non-convex acoustic part of the coupled problem Ω_a needs to be subdivided into a number of non-overlapping convex subdomains in order to meet the convergence requirements of the WBT. Thus, at the common interfaces Γ_i between two acoustic subdomains (α, β), the following set of coupling conditions is applied

- coupling condition type 1 $\forall \mathbf{r} \in \Gamma_i^{(\alpha,\beta)}$:

$$\mathcal{L}_v^\alpha(p^\alpha(\mathbf{r})) - \frac{p^\alpha(\mathbf{r})}{\bar{Z}_{int}} = -\mathcal{L}_v^\beta(p^\beta(\mathbf{r})) - \frac{p^\beta(\mathbf{r})}{\bar{Z}_{int}}, \tag{6.16a}$$

- coupling condition type 2 $\forall \mathbf{r} \in \Gamma_i^{(\beta,\alpha)}$:

$$\mathcal{L}_v^\beta(p^\beta(\mathbf{r})) - \frac{p^\beta(\mathbf{r})}{\bar{Z}_{int}} = -\mathcal{L}_v^\alpha(p^\alpha(\mathbf{r})) - \frac{p^\alpha(\mathbf{r})}{\bar{Z}_{int}} \tag{6.16b}$$

with $\bar{Z}_{int} = \rho_a c$ the impedance coupling factor. The structural part of the coupled problem consists of convex subdomain Ω_s.

6.2.3 Evaluation of boundary and interface conditions

The pressure approximation (6.10) used in the acoustic part satisfies the governing differential equation (6.6), but violates the boundary conditions (6.7) and the interface conditions (6.16). The following weighted residual formulation enforces the residual errors to zero in an integral sense

$$\mathrm{WRF}_{a,uncoup} + \int_{\Gamma_{sa}^\alpha} \tilde{p}^\alpha (\mathcal{L}_v^\alpha(\hat{p}^\alpha) - \mathrm{j}\omega\hat{w})\, \mathrm{d}\Gamma = 0 \tag{6.17}$$

with $\mathrm{WRF}_{a,uncoup}$ the terms representing the weighted residual formulation of the uncoupled acoustic problem defined in (5.28), extended by the integral term taking the structural-acoustic interaction into account.

The out-of-plane displacement approximation (6.11) used in the structural part satisfies the governing differential equation (6.1) extended by the structural-acoustic coupling terms, but it violates the boundary conditions (6.5). The following weighted residual formulation enforces the involved residual errors to zero in an integral sense

$$\mathrm{WRF}_{s,uncoup} = 0, \tag{6.18}$$

where $\mathrm{WRF}_{s,uncoup}$ represents the weighted residual formulation of the uncoupled structural problem given by (4.13). Similar to uncoupled problems, the Galerkin approach is applied, in which the weighting functions are the linear combination of the same Trefftz basis functions as those used for the approximation functions. Substitution of the pressure approximation (6.10), the out-of-plane displacement approximation (6.11) and the weighting functions in the weighted

residual formulations (6.17) and (6.18), together with the requirement that these relations should hold for any set of contribution factors, yields the following vibro-acoustic wave model

$$
\begin{bmatrix}
(\mathbf{A}_a^\alpha + \mathbf{C}_{ab}^\alpha) \, \mathbf{C}_{as}^\alpha & \mathbf{C}_a^{\alpha\beta} \\
\mathbf{C}_{sa}^\alpha & \mathbf{A}_s & \mathbf{C}_{sa}^\beta \\
\mathbf{C}_a^{\beta\alpha} & \mathbf{C}_{as}^\beta \, (\mathbf{A}_a^\beta + \mathbf{C}_b^\beta)
\end{bmatrix}
\begin{Bmatrix}
\mathbf{p}^\alpha \\
\mathbf{w} \\
\mathbf{p}^\beta
\end{Bmatrix}
=
\begin{Bmatrix}
\mathbf{b}_a^\alpha + \mathbf{c}_{ab}^\alpha + \mathbf{c}_{as}^\alpha + \mathbf{c}_a^{\alpha\beta} \\
\mathbf{b}_s + \mathbf{c}_{sa}^\alpha + \mathbf{c}_{sa}^\beta \\
\mathbf{b}_a^\beta + \mathbf{c}_{ab}^\beta + \mathbf{c}_{as}^\beta + \mathbf{c}_a^{\beta\alpha}
\end{Bmatrix}.
\tag{6.19}
$$

In (6.19), the model contributions $\mathbf{A}^\alpha$ and $\mathbf{b}^\alpha$ represent the uncoupled acoustic matrices and vectors of the corresponding acoustic subdomain Ω^α. The model contributions $\mathbf{A}_s$ and $\mathbf{b}_s$ stand for the uncoupled structural matrices and vectors. These uncoupled terms were already defined in (5.32), (4.18) and (4.19). The model contributions $\mathbf{C}_{ab}$ and $\mathbf{c}_{ab}$ are the acoustic back-coupling terms given by

$$
\mathbf{C}_{ab} = \int_{\Gamma_{sa}} \mathbf{\Phi}^{\mathsf{T}} (\mathcal{L}_v(\mathbf{\Phi}) - j\omega \hat{\mathbf{w}}_a) \, d\Gamma,
\tag{6.20a}
$$

$$
\mathbf{c}_{ab} = -\int_{\Gamma_{sa}} \mathbf{\Phi}^{\mathsf{T}} (\mathcal{L}_v(\hat{p}_q) - j\omega \hat{w}_q) \, d\Gamma.
\tag{6.20b}
$$

The model contributions $\mathbf{C}_{as}$ and $\mathbf{c}_{as}$ represent the acoustic-structural coupling matrix and vector expressed as follows

$$
\mathbf{C}_{as} = -\int_{\Gamma_{sa}} j\omega \mathbf{\Phi}^{\mathsf{T}} \mathbf{\Psi} \, d\Gamma,
\tag{6.21a}
$$

$$
\mathbf{c}_{as} = \int_{\Gamma_{sa}} j\omega \mathbf{\Phi}^{\mathsf{T}} \hat{w}_F \, d\Gamma,
\tag{6.21b}
$$

while the $\mathbf{C}_{sa}$ and $\mathbf{c}_{sa}$ are the structural-acoustic coupling terms given by

$$
\begin{aligned}
\mathbf{C}_{sa} = {} & \int_{\Gamma_{w\theta} \cup \Gamma_{wM}} \mathcal{L}_V(\mathbf{\Psi}^{\mathsf{T}}) \hat{\mathbf{w}}_a \, ds && + \sum_{c_w=1}^{n_{cw}} \llbracket \mathcal{L}_{Ms}^\alpha(\mathbf{\Psi}^{\mathsf{T}}) \rrbracket_{c_w} \hat{\mathbf{w}}_a|_{c_w} + \dots \\
& \dots + \int_{\Gamma_{w\theta} \cup \Gamma_{\theta V}} \mathcal{L}_M(\mathbf{\Psi}^{\mathsf{T}}) \mathcal{L}_\theta(\hat{\mathbf{w}}_a) \, ds && + \dots \\
& \dots - \int_{\Gamma_{wM} \cup \Gamma_{MV}} \mathcal{L}_\theta(\mathbf{\Psi}^{\mathsf{T}}) \mathcal{L}_M(\hat{\mathbf{w}}_a) \, ds && + \dots \\
& \dots - \int_{\Gamma_{mV} \cup \Gamma_{\theta V}} \mathbf{\Psi}^{\mathsf{T}} \mathcal{L}_V(\hat{\mathbf{w}}_a) \, ds && - \sum_{c_V=1}^{n_{cV}} \mathbf{\Psi}^{\mathsf{T}}|_{c_V} \llbracket \mathcal{L}_{Ms}(\hat{\mathbf{w}}_a) \rrbracket_{c_V},
\end{aligned}
\tag{6.22a}
$$

$$\mathbf{c}_{sa} = \int_{\Gamma_{w\theta} \cup \Gamma_{wM}} \mathcal{L}_V(\boldsymbol{\Psi}^\mathsf{T})\hat{w}_q \, \mathrm{d}s \qquad + \sum_{c_w=1}^{n_{cw}} [\![\mathcal{L}_{Ms}(\hat{w}_q)]\!]_{c_w} \hat{w}_q|_{c_w} + \dots$$

$$\dots - \int_{\Gamma_{w\theta} \cup \Gamma_{\theta V}} \mathcal{L}_M(\boldsymbol{\Psi}^\mathsf{T})\mathcal{L}_\theta(\hat{w}_q) \, \mathrm{d}s \quad + \dots$$

$$\dots - \int_{\Gamma_{wM} \cup \Gamma_{MV}} \mathcal{L}_\theta(\boldsymbol{\Psi}^\mathsf{T})\mathcal{L}_M(\hat{w}_q) \, \mathrm{d}s \quad + \dots \tag{6.22b}$$

$$\dots - \int_{\Gamma_{mV} \cup \Gamma_{\theta V}} \boldsymbol{\Psi}^\mathsf{T}\mathcal{L}_V(\hat{w}_q) \, \mathrm{d}s \qquad - \sum_{c_V=1}^{n_{cV}} \boldsymbol{\Psi}^\mathsf{T}|_{c_V} [\![\mathcal{L}_{Ms}(\hat{w}_q)]\!]_{c_V} \, .$$

Furthermore, consider a coupled vibro-acoustic system in which the plate is surrounded by fluid on both sides, see figure 6.2. Although the two acoustic subsystems are physically separated by the plate, the WBT incorporates an explicit indirect cavity-cavity coupling in such cases. The related model contributions are defined as follows (Van Hal, 2004)

$$\mathbf{C}_a^{\alpha\beta} = -\int_{\Gamma_{sa}} \mathrm{j}\omega \boldsymbol{\Phi}^{\alpha\mathsf{T}}\hat{\mathbf{w}}_a^\beta \, \mathrm{d}\Gamma, \qquad \mathbf{c}_a^{\alpha\beta} = \int_{\Gamma_{sa}} \mathrm{j}\omega \boldsymbol{\Phi}^{\alpha\mathsf{T}}\hat{w}_q^\beta \, \mathrm{d}\Gamma, \tag{6.23a}$$

$$\mathbf{C}_a^{\beta\alpha} = -\int_{\Gamma_{sa}} \mathrm{j}\omega \boldsymbol{\Phi}^{\beta\mathsf{T}}\hat{\mathbf{w}}_a^\alpha \, \mathrm{d}\Gamma, \qquad \mathbf{c}_a^{\beta\alpha} = \int_{\Gamma_{sa}} \mathrm{j}\omega \boldsymbol{\Phi}^{\beta\mathsf{T}}\hat{w}_q^\alpha \, \mathrm{d}\Gamma. \tag{6.23b}$$
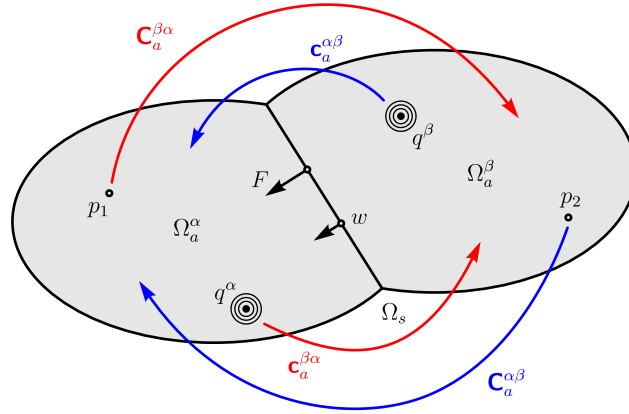
Figure 6.2: Indirect cavity-cavity coupling phenomena and the related wave model contributions (Rejlek and Priebsch, 2010)

6.3 Validation example: box-backed plate

The first validation example considers two simple academic problems consisting of a flexible rectangular plate backed first by a closed cavity and then by an open rigid box (Rejlek and Priebsch, 2010). The workflow is thus divided into two phases. In the first phase, only the flexible plate backed by the air-filled cavity is considered, without taking into account any sound

propagation into an unbounded acoustic domain. The purpose of this phase is simply to pretest the coupled formulation to verify that the underlying theory has been correctly accounted for. In the next step, the interior acoustic problem is further extended by introducing the truncation geometry and the unbounded acoustic domain, which is modelled explicitly in the wave based approach.

6.3.1 Problem definition

Consider a rigid box of dimensions $0.7 \times 0.3 \times 0.5$ m as illustrated in figure 6.3. A rectangular clamped plate constituting the bottom part of the box is made of aluminium having the mass density $\rho_s = 2\,700$ kg/m^3, the Young's modulus $E = 72 \cdot 10^9$ Pa and the Poisson's ratio $\nu = 0.3$. The plate has a thickness $t = 0.001$ m and is excited by a point force $F = 1$ N applied at the position $\mathbf{r}_F = (0.2,\, 0.1)$ m in the positive z direction. Depending on the problem, the box is either closed or open, refer to figure 6.3(a) and 6.3(b), respectively. The box is filled and, if applicable, also surrounded by air having the speed of sound $c = 343.8$ m/s and the mass density $\rho_a = 1.2$ kg/m^3.
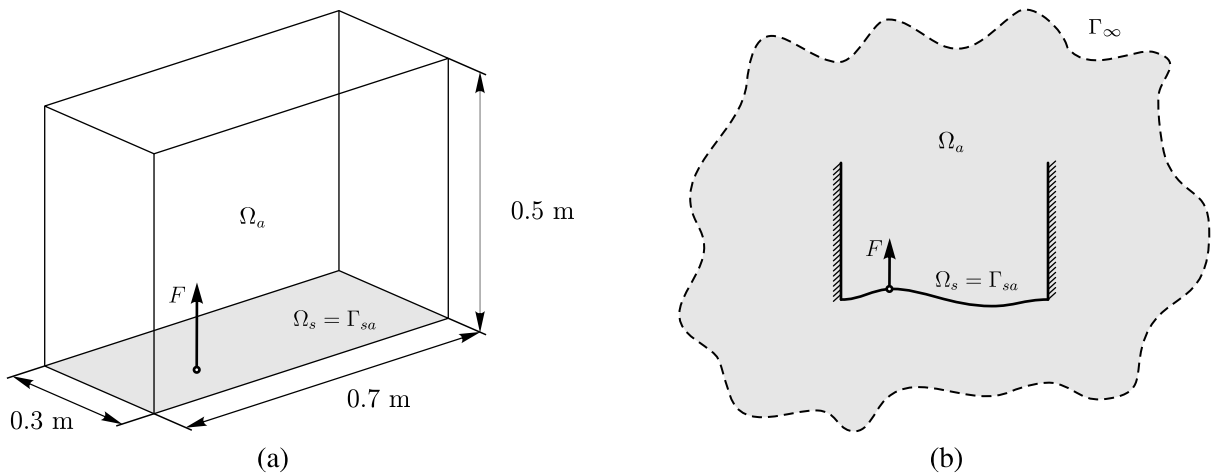
Figure 6.3: (a) Cavity and (b) open box-backed plate problem (Rejlek and Priebsch, 2010)

6.3.2 Cavity-backed plate

The first phase considers an interior coupled problem consisting of a cavity-backed plate validation example, see figure 6.3(a). As a reference, two different coupled FE–FE models calculated by the *Abaqus/Standard* solver (SIMULIA Dassault Systèmes, 2011) are utilised. The coarse FE model consists of $10\,118$ nodes forming $2\,100$ linear quadrilateral shell elements and $6\,720$ linear hexahedral acoustic elements, with a maximum element edge size of $h_{max,s} = 0.01$ m and $h_{max,a} = 0.025$ m, respectively. Although the fine FE model uses the same mesh density, it employs higher-order elements for both the structural and acoustic parts. The $36\,910$ nodes form $2\,100$ quadratic quadrilateral shell elements and $6\,720$ quadratic hexahedral acoustic elements, see figure 6.4(a). The FE calculations are performed using the direct solution method. Due to the low geometrical complexity of the problem, the corresponding wave based model consists of only one structural and one acoustic subdomain, see figure 6.5(a). The WBT code is
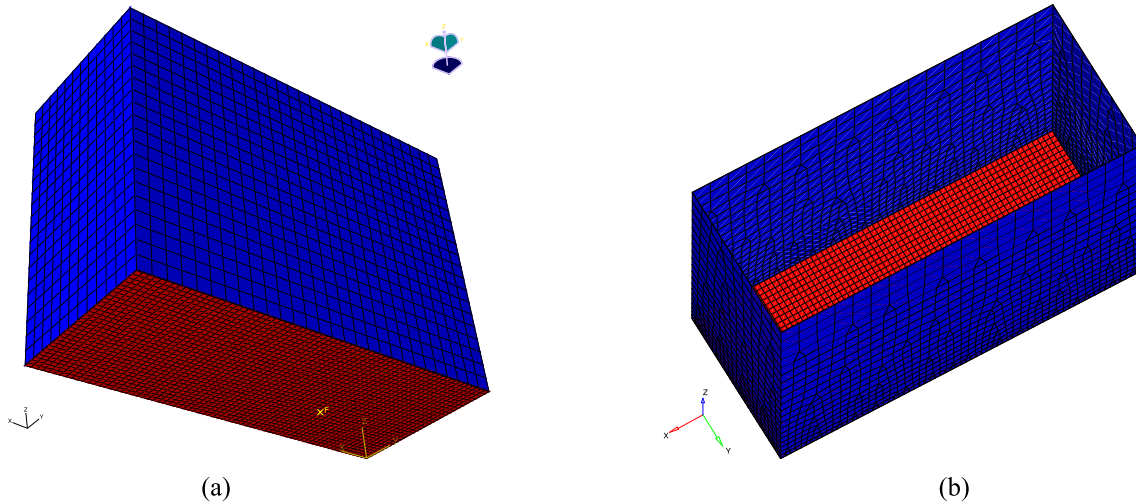
Figure 6.4: Box-backed plate: (a) FE–FE and (b) FE–BE model (Rejlek and Priebsch, 2010)

implemented in *MATLAB* (MathWorks, Inc., 2007). All calculations presented in this chapter are performed on a 2.26 GHz dual-core *Intel*-based computer using 4 Gbyte RAM and running the *Windows Vista 64-bit* operating system.

Figure 6.8 plots the acoustic frequency response functions (p/F) in the range 1–1 000 Hz with the resolution of 1 Hz obtained at the response point $\text{RP1} = (0.4, 0.2, 0.3)$ m by the different models. The linear FE model requires 3 483 s to obtain the frequency response function, while the quadratic one requires 36 367 s to perform the same type of analysis, see table 6.1. The wave model employs the frequency-dependent strategy with $T = 2$ to truncate both the acoustic and structural wave function sets. This yields 24–348 acoustic and 16–176 structural degrees of freedom and the WB model needs 12 223 s to carry out the frequency response calculation, see table 6.2.
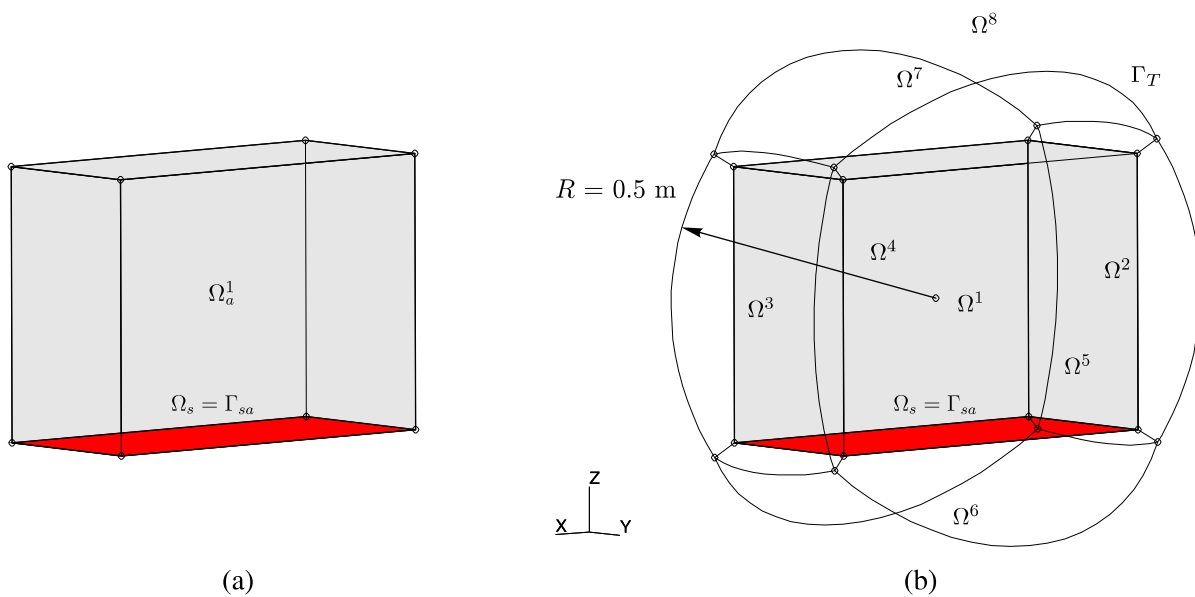
Figure 6.5: Box-backed plate: (a) interior and (b) unbounded WB model (Rejlek and Priebsch, 2010)

FEM: Re{p}　　　　　　　　　WBT: Re{p}

FEM: Re{w}　　　　　　　　　WBT: Re{w}
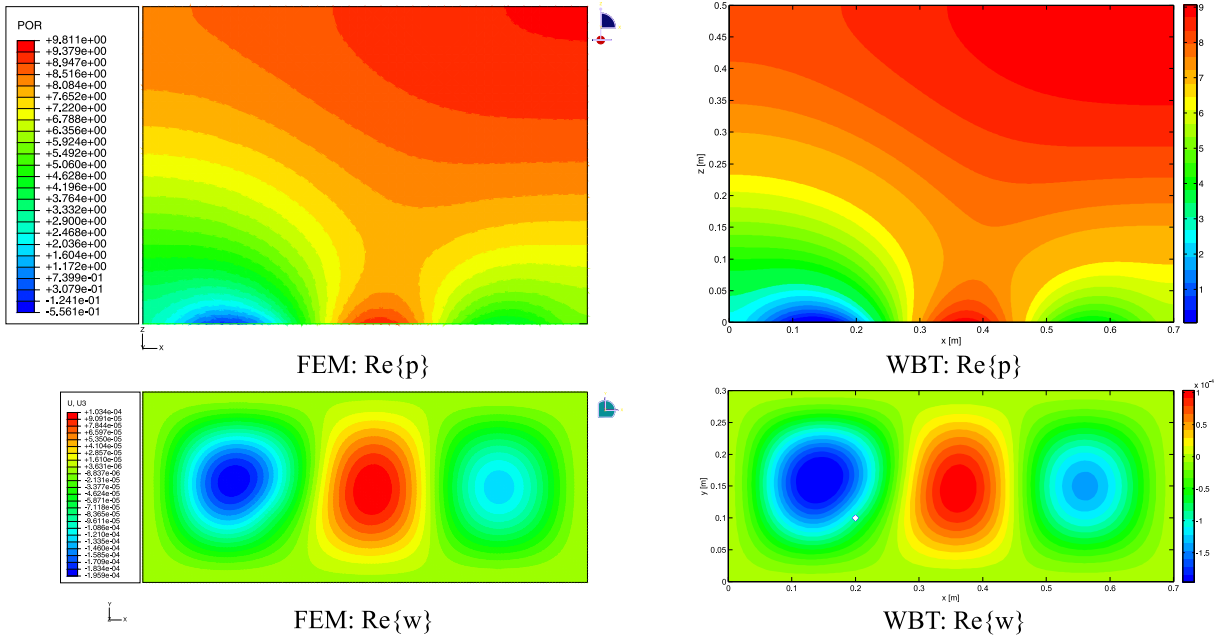
Figure 6.6: Cavity-backed plate: the real part of acoustic pressure plotted in $y = 0.2$ m plane and the out-of-plane displacement at 105 Hz predicted by quadratic FEM and WBT (Rejlek and Priebsch, 2010)

Up to a frequency of approximately 500 Hz, all three models provide comparable predictions. In the higher frequency range, however, the linear FE prediction clearly suffers from the dispersion error. On the other hand, both the quadratic FE and WB results, maintain the same prediction accuracy within the whole frequency range of interest.

FEM: Re{p}　　　　　　　　　WBT: Re{p}

FEM: Re{w}　　　　　　　　　WBT: Re{w}
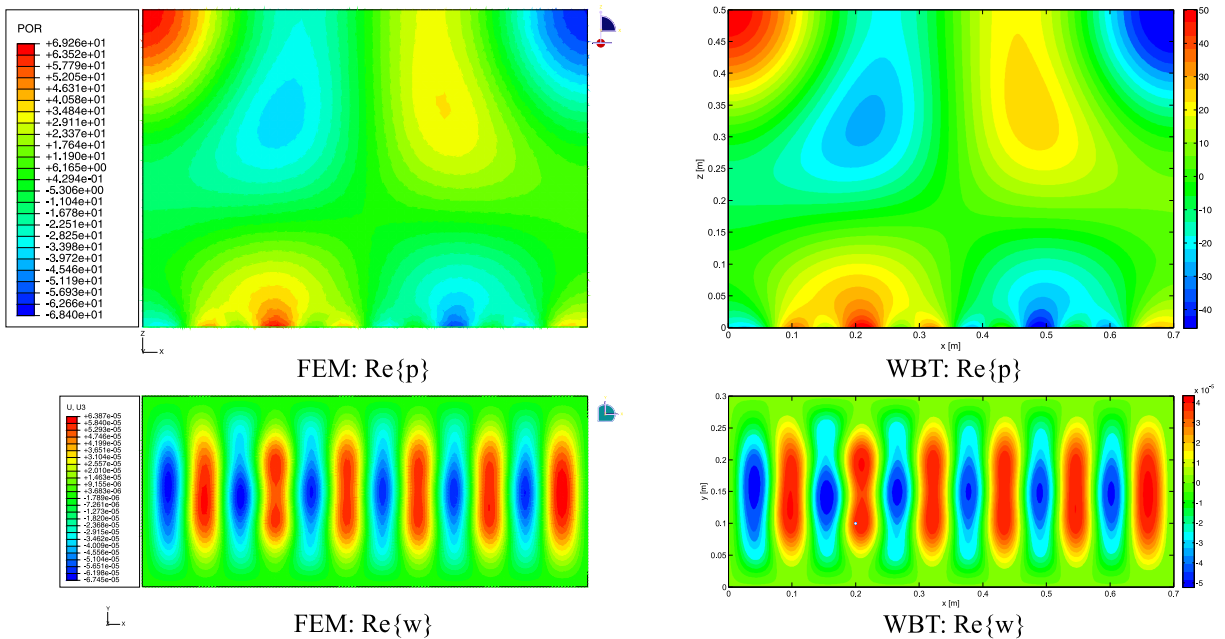
Figure 6.7: Cavity-backed plate: the real part of acoustic pressure plotted in $y = 0.2$ m plane and the out-of-plane displacement at 784 Hz predicted by quadratic FEM and WBT (Rejlek and Priebsch, 2010)

attribute	denotation	value	
		structural	acoustic
solution scheme		FEM–FEM direct	
number of nodes	#nod	6 501	30 409
number of elements	#ele	2 100	6 720
mesh topology	topo	quad8	hexa20
maximum element edge size	$h_{max,s}$, $h_{max,a}$	0.01 m	0.025 m
degrees of freedom	DOF	321 296	
FRF range	f_{min}, f_{max}	1–1 000 Hz	
FRF step	Δf	1 Hz	
number of modes up to f_{max}	#mod	53	21
CPU time needed for FRF	t_{FRF}	36 367 s	

Table 6.1: Cavity-backed plate: attributes of the FE–FE model

attribute	denotation	value	
		structural	acoustic
solution scheme		fully coupled WBT	
number of subdomains	N_s, N_a	1	1
truncation strategy		frequency-dependent	
truncation parameter	T_s, T_a	2	
degrees of freedom	dimΨ, dimΦ	16–176	24–348
FRF range	f_{min}, f_{max}	1–1 000 Hz	
FRF step	Δf	1 Hz	
CPU time needed for FRF	t_{FRF}	12 223 s	

Table 6.2: Cavity-backed plate: attributes of the WB model
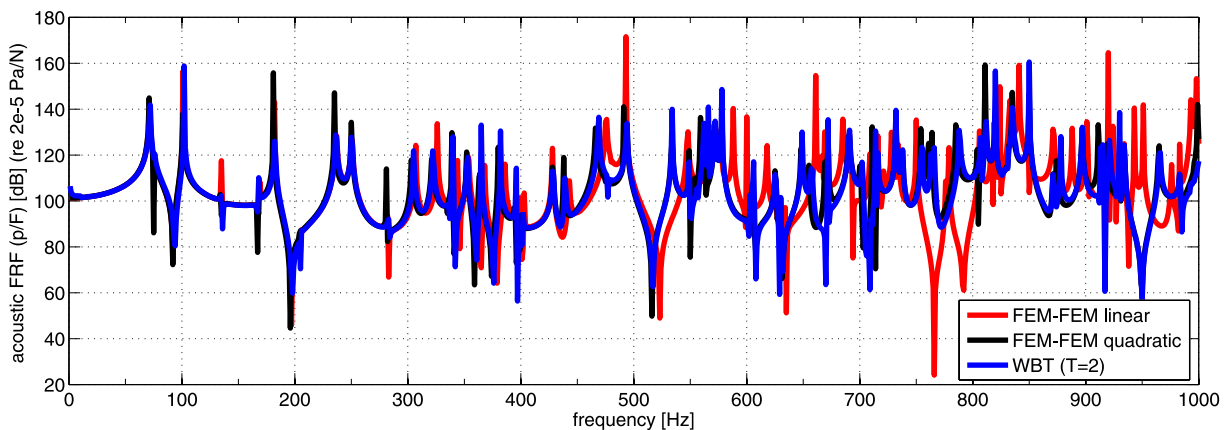
Figure 6.8: Cavity-backed plate: frequency response functions at point RP1 (Rejlek and Priebsch, 2010)

Figures 6.6 and 6.7 show the predicted fields at 105 Hz and 784 Hz, respectively. Each figure plots the real part of both the structural out-of-plane displacement field and the acoustic pressure field in the plane $y = 0.2$ m, as predicted by quadratic FEM and WBT. At 105 Hz, the

wave model employs 378 acoustic and 168 structural degrees of freedom, while at 784 Hz 732 acoustic and 300 structural degrees of freedom are utilised. In the WB predictions, both the displacement patterns and the pressure fields prove that the structural and acoustic boundary conditions have been correctly accounted for.

6.3.3   Open box-backed plate

Removing the top side of the box from the previous problem yields the open box-backed plate validation example, see figure 6.3(b), which represents a three-dimensional extension of a 2D example presented by Pluymers et al. (2004). To validate the WB model, a coupled FE–BE model is considered as a reference. It consists of a modally reduced structural FE model and the acoustic indirect BE model and is built up in a commercial CAE system *LMS Virtual.Lab* running the *LMS/SYSNOISE* Rev. 5.6 solver (LMS International, 2010), see figure 6.4(b). The structural FE part consists of 2 201 nodes forming 2 100 linear quadrilateral shell elements with a maximum element edge size of $h_{max,s} = 0.01$ m. The modal base of the structural problem comprises the eigenmodes calculated by the *MSC.Nastran* solver (MSC Software Corporation, 2008) up to the frequency of 2 000 Hz. The acoustic BE part consists of 4 279 nodes forming a quad4 dominant mesh having 4 378 linear quad4 and tria3 elements, with a maximum element edge size of $h_{max,a} = 0.05$ m. Both meshes have identical node positions at the structural-acoustic coupling interface. The corresponding wave based model consists of one structural subdomain, as well as one unbounded and seven bounded acoustic subdomains, see figure 6.5(b).

attribute	denotation	value	
		structural	acoustic
solution scheme		FEM modal	BEM indirect variational
number of nodes	#nod	2 201	4 279
number of elements	#ele	2 100	4 378
mesh topology	topo	quad4	quad4 dominant
maximum element edge size	$h_{max,s}, h_{max,a}$	0.01 m	0.05 m
degrees of freedom	DOF	12 006	4 397
number of modes up to 2 000 Hz	#mod	118	–
CPU time for modal extraction	t_{mod}	22 s	–
FRF range	f_{min}, f_{max}	–	1–1 000 Hz
FRF step	Δf	–	1 Hz
CPU time needed for FRF	t_{FRF}	–	75 000 s

Table 6.3: Open box-backed plate: attributes of the FE–BE model

Figure 6.9(a) plots the acoustic frequency response functions (p/F) in the range 1–1 000 Hz with the resolution of 1 Hz obtained at the response point $RP2 = (0.35, 0.15, 1)$ m by the FE–BE and WB model, see tables 6.3 and 6.4. The FE–BE model utilises the same computational mesh throughout the calculation and thus uses a constant number of degrees of freedom over the frequency. It requires roughly 75 000 s to perform the frequency response analysis. The wave model, on the other hand, employs the frequency-dependent strategy with $T_a = T_u = T_s = 2$ to truncate the acoustic bounded, acoustic unbounded and structural wave function sets and needs 30 309 s for the prediction. Figure 6.9(b) plots the evolution of both the number of the acoustic
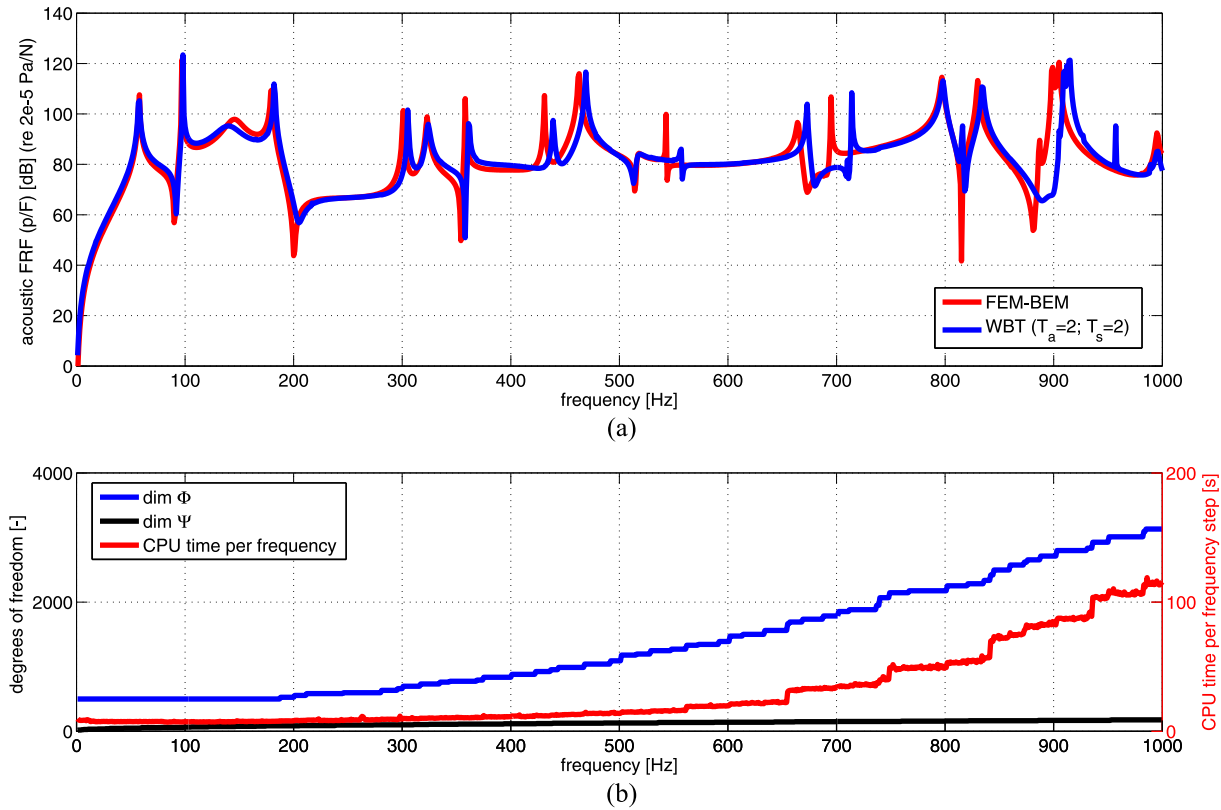
Figure 6.9: Open box-backed plate: (a) frequency response functions at point RP2 and (b) the number of WB acoustic and structural degrees of freedom with the related CPU time needed to solve one frequency step (Rejlek and Priebsch, 2010)

and structural WB degrees of freedom and the related CPU time over the frequency involved in solving the wave model. The frequency-dependent rule (5.21) is applied for the truncation of the wave function set used in the acoustic unbounded domain.

attribute	denotation	value	
		structural	acoustic
solution scheme		fully coupled WBT	
number of subdomains	N_s, N_a	1	7
	N_u	–	1
truncation strategy		frequency-dependent	
truncation parameter	T_s, T_a, T_u	2	
radius of truncation sphere	R	–	0.5 m
degrees of freedom	dim$\boldsymbol{\Psi}$, dim$\boldsymbol{\Phi}$	16–176	499–3132
FRF range	f_{min}, f_{max}	1–1 000 Hz	
FRF step	Δf	1 Hz	
CPU time needed for FRF	t_{FRF}	30 309 s	

Table 6.4: Open box-backed plate: attributes of the WB model

Figures 6.10 and 6.11 show the predicted sound radiation patterns at 200 Hz and 400 Hz, respectively. Both figures plot the sound pressure level (SPL) field in the plane $y = 0.15$ m as predicted by FE–BE and WB model. For the acoustic part, the WB model uses $n_{r\bullet} = n_{s\bullet} = n_{t\bullet} = 10$

(a)   (b)
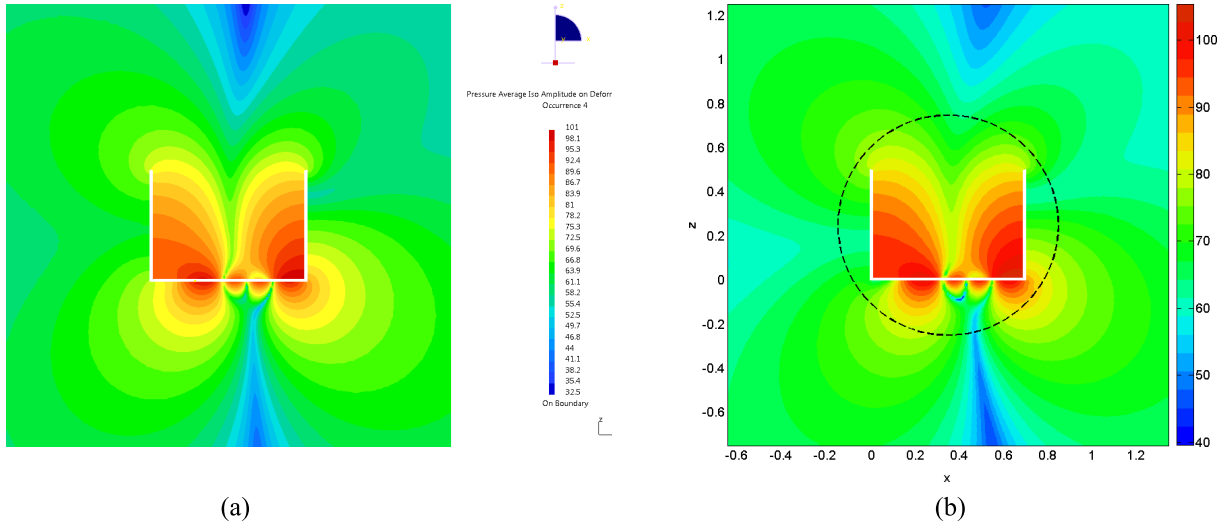
Figure 6.10: Open box-backed plate: the sound pressure level in [dB] (re $2 \cdot 10^{-5}$ Pa) at 200 Hz predicted by (a) the coupled FE–BE model and (b) the WBT (Rejlek and Priebsch, 2010)

(a)   (b)
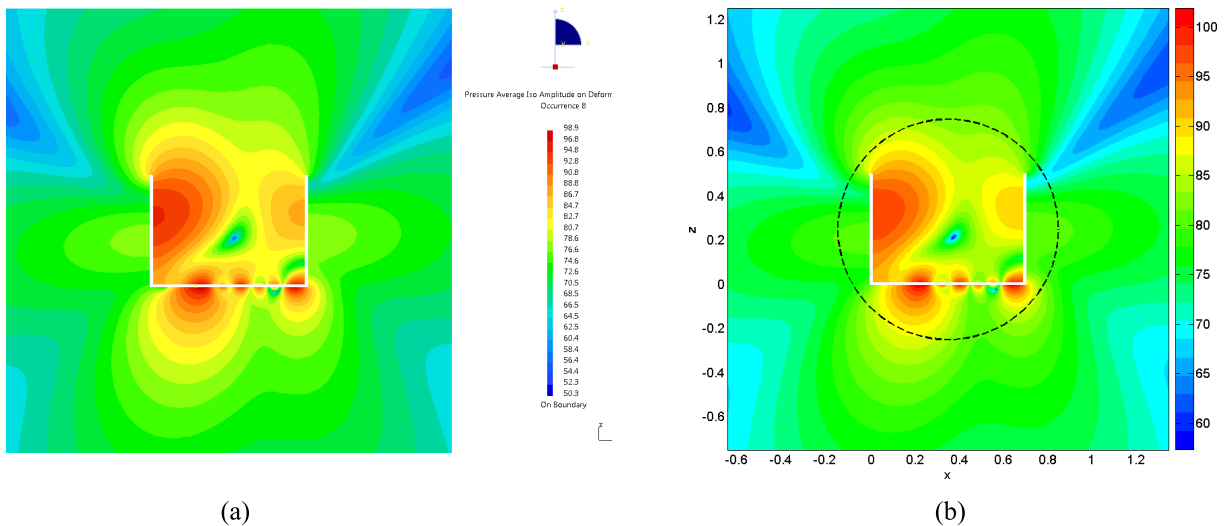
Figure 6.11: Open box-backed plate: the sound pressure level in [dB] (re $2 \cdot 10^{-5}$ Pa) at 400 Hz predicted by (a) the coupled FE–BE model and (b) the WBT (Rejlek and Priebsch, 2010)

and $L = 20$ to truncate the bounded and unbounded acoustic wave function sets, respectively, and $n'_r = n'_s = 50$ truncation numbers for the structural wave function set. This yields $5\,523$ acoustic and 408 structural degrees of freedom. The coupled FE–BE model needs 600 s to calculate one frequency step including the postprocessing of primary results at the field point mesh, whereas the wave model requires about 137 s. The BE solution time, however, does not include the computational efforts spent on performing the FE-based structural modal analysis used in the subsequent coupled FE–BE calculation. The WB CPU time, on the other hand, comprises the solution of the fully coupled system, including both the structural and acoustic parts of the problem. The dashed lines in the WB contour plots denote the truncation sphere Γ_T. The contour plots show a good match between the FE–BE and WB predictions. Moreover, the WB pressure patterns prove that both the normal velocity boundary condition at the rigid parts of the physical boundary and the coupling conditions at the structural-acoustic interface have been accurately fulfilled.

6.4 Validation example: soundbrick convertible

The previous two validation examples verified the ability of WBT to tackle fully coupled vibro-acoustic problems involving both the interior and exterior formulation. Encouraged by the results obtained for a simple academic example, the next validation example applies the WBT to an industry-sized problem involving a semi-infinite acoustic domain (Rejlek and Priebsch, 2010). The problem consists of a simplified, car-like structure with an open boundary of dimensions, as displayed in figure 6.12. The structure of the car is considered to be rigid, except for the floor panel, which consists of a thin flat plate of thickness $t = 0.003$ m made of aluminium having the mass density $\rho_s = 2\,700$ kg/m^3, the Young's modulus $E = 72 \cdot 10^9$ Pa and the Poisson's ratio $\nu = 0.3$. The clamped plate is excited by a point force $F = 1$ N applied in a normal direction at the position $\mathbf{r}_F = (0.6,\ 0.4)$ m. The structure rests on a rigid baffle and is surrounded by air having the speed of sound $c = 343.8$ m/s and mass density $\rho_a = 1.2$ kg/m^3.
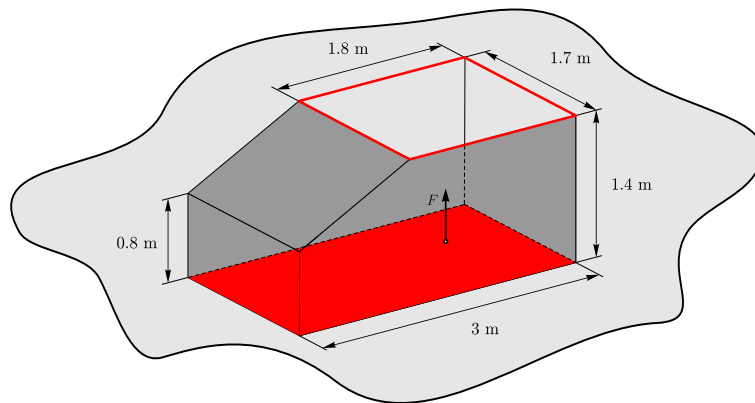
Figure 6.12: Soundbrick convertible (Rejlek and Priebsch, 2010)

Similar to the previous validation case a coupled FE–BE model is considered as a reference solution. The fully coupled model consists of a modally reduced structural FE model and the acoustic indirect BE baffled model. The model is built up in a commercial CAE system *LMS*
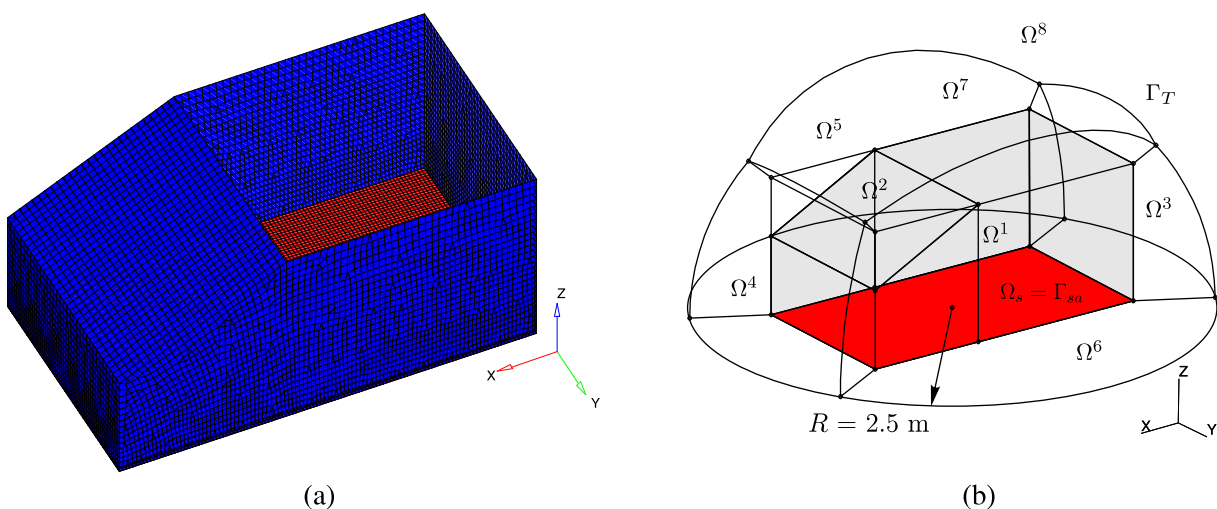
Figure 6.13: Soundbrick convertible: (a) FE–BE and (b) WB model (Rejlek and Priebsch, 2010)
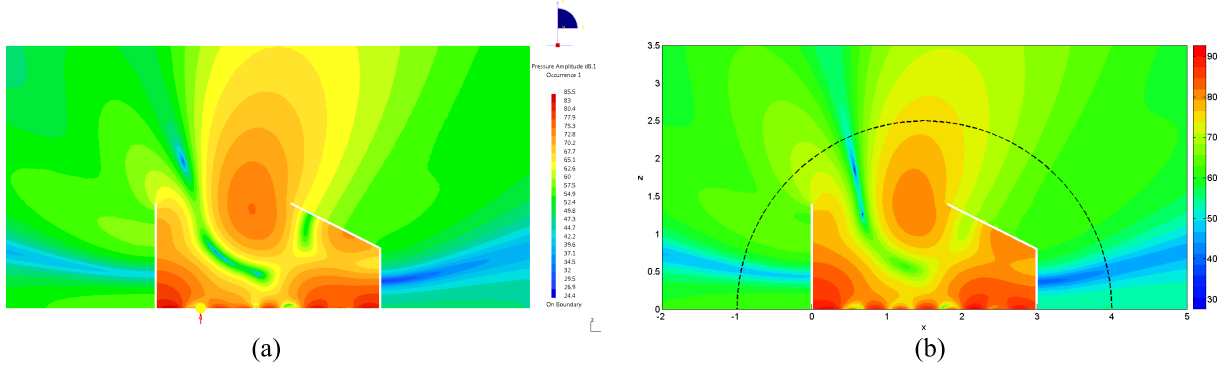
Figure 6.14: Soundbrick convertible: the sound pressure level in [dB] (re $2 \cdot 10^{-5}$ Pa) at 200 Hz predicted by (a) the coupled FE–BE model and (b) the WBT (Rejlek and Priebsch, 2010)
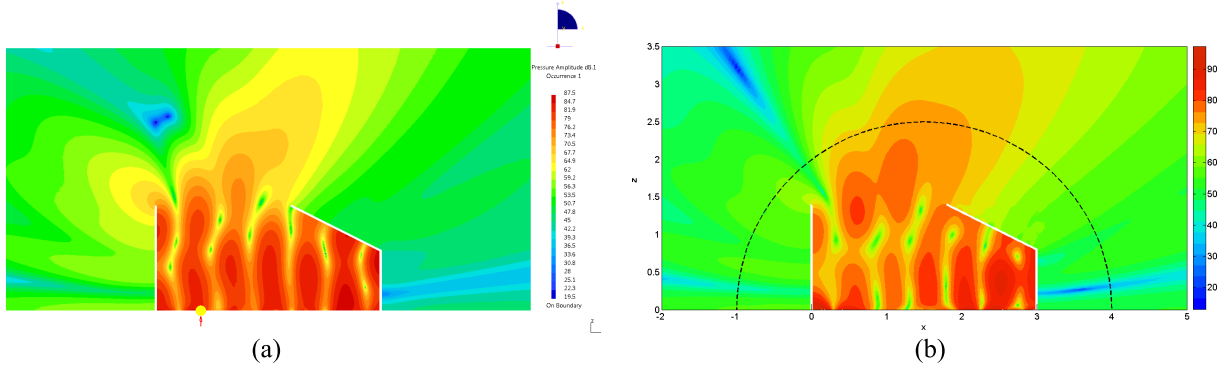
Figure 6.15: Soundbrick convertible: the sound pressure level in [dB] (re $2 \cdot 10^{-5}$ Pa) at 400 Hz predicted by (a) the coupled FE–BE model and (b) the WBT (Rejlek and Priebsch, 2010)

Virtual.Lab running the *LMS/SYSNOISE* Rev. 5.6 solver (LMS International, 2010), see figure 6.13(a). The structural FE part consists of 8 349 nodes forming 8 160 linear quadrilateral shell elements with a maximum element edge size of $h_{max,s} = 0.025$ m. The modal base comprises the structural eigenmodes calculated by the *MSC.Nastran* solver (MSC Software Corporation, 2008) up to the frequency of 1 500 Hz. The acoustic BE part consists of 15 378 nodes forming a quad4 dominant mesh topology having 15 417 linear quad4 and tria3 elements with a maximum element edge size of $h_{max,a} = 0.05$ m. Both computational meshes use congruent node positions at the structural-acoustic coupling interface. The corresponding wave model, see figure 6.13(b), consists of one structural (indicated in red) and seven bounded acoustic subdomains, which are truncated by the hemisphere Γ_T of radius $R = 2.5$ m.

Figures 6.14 and 6.15 show the predicted sound radiation patterns at 200 Hz and 400 Hz, respectively. Both figures plot the SPL field in the plane $y = 0.85$ m calculated by FE–BE and the WB model. For the acoustic part, the WB model uses $n_{r\bullet} = n_{s\bullet} = n_{t\bullet} = 12$ and $L = 20$ to truncate both the bounded and unbounded acoustic wave function sets and $n'_r = n'_s = 50$ truncation numbers for the structural wave function set. This yields 7 329 acoustic and 408 structural degrees of freedom. The coupled FE–BE approach needs nearly 11 870 s (approximately 3.3 hours) to calculate one frequency step, including the postprocessing of primary results at the field point mesh, while the wave model, which employs a constant wave function set truncation over the frequency, requires about 340 s. Once again, the BE solution time does not include the subsequent computational time needed for an FE calculation of the structural

attribute	denotation	value	
		structural	acoustic
solution scheme		FEM modal	BEM indirect variational baffled
number of nodes	#nod	8 349	15 378
number of elements	#ele	8 160	15 417
mesh topology	topo	quad4	quad4 dominant
maximum element edge size	$h_{max,s}$, $h_{max,a}$	0.025 m	0.05 m
degrees of freedom	DOF	47 838	16 195
number of modes up to 1500 Hz	#mod	817	–
CPU time for modal extraction	t	345 s	–
FRF range	f_{min}, f_{max}	–	1–400 Hz
FRF step	Δf	–	1 Hz
CPU time needed for FRF	t_{FRF}	–	~ 39 days[1]

Table 6.5: Soundbrick convertible: attributes of the FE–BE model

attribute	denotation	value	
		structural	acoustic
solution scheme		fully coupled WBT	
number of subdomains	N_s, N_a	1	7
	N_{si}	–	1
truncation strategy		constant	
truncation parameter	(n'_r, n'_s), $(n_{r\bullet}, n_{s\bullet}, n_{t\bullet})$	50	8
	L	–	20
radius of truncation hemisphere	R	–	2.5 m
degrees of freedom	$\dim\boldsymbol{\Psi}$, $\dim\boldsymbol{\Phi}$	408	3 633
FRF range	f_{min}, f_{max}	1–400 Hz	
FRF step	Δf	1 Hz	
CPU time needed for FRF	t_{FRF}	26 000 s	

Table 6.6: Soundbrick convertible: attributes of the WB model

modes used in the coupled FE–BE analysis. The WB CPU time, on the other hand, includes the solution of the whole coupled system. The dashed lines in the WB contour plots denote the truncation hemisphere Γ_T. Both contour plots indicate a fair match between the FE–BE and WB predictions. The WB pressure patterns also demonstrate that the model has properly accounted for the normal velocity boundary condition at both the rigid parts of the physical boundary and the rigid baffle plane, as well as the continuity condition at the structural-acoustic interface.

Figures 6.16 and 6.17 plot the acoustic frequency response functions (p/F) estimated by the FE–BE and WB model up to 400 Hz at the positions of $\mathrm{RP1} = (1.5, 0.85, 1)$ m and $\mathrm{RP2} = (1.5, 8.35, 1)$ m, see tables 6.5 and 6.6, respectively. The response point RP1 is located inside the car structure and corresponds to a driver's ear position, whereas the point RP2 is located in the far-field and represents the reference microphone position used during the pass-by noise

---

[1]Estimated value.

measurements. The WB calculation is carried out with the frequency resolution of 1 Hz (blue solid curve), while a frequency step of 5 Hz is initially applied in the case of the coupled FE–BE model, due to the huge computational load involved in solving this problem. The same FE–BE model is utilised, as used for the prediction of the dynamic fields discussed above, which requires roughly $8\,400$ s to perform one frequency step. Hence, it takes almost eight days in total to calculate the frequency spectrum consisting of 80 frequency steps on the computer described in section 6.3.2. For this reason, the narrow-band frequency response analysis adopting the frequency step of $\Delta f = 1$ Hz is carried out on a more computationally efficient platform. The whole frequency range is split into eight jobs, each consisting of 50 frequency steps, which are distributed among two quad-core CPUs of a high-performance *HP Z800* workstation equipped with 2.4 GHz *Intel Xeon E5620* quad-core dual processor, 48 Gbyte RAM and running *Windows 7 64-bit*-operating system. The whole calculation is run in parallel by submitting one job per core, which takes about 5.5 days – an equivalent of almost 39 days on the original dual-core laptop used before. Postprocessing of each of the eight jobs yields the final FE–BE frequency response functions (red solid curve), see 6.16 and 6.17.

The wave model uses $n_{r\bullet} = n_{s\bullet} = n_{t\bullet} = 8$ and $L = 20$ to truncate both the bounded and unbounded acoustic wave function sets and $n'_r = n'_s = 50$ truncation numbers for the structural wave function set. This yields $3\,633$ acoustic and 408 structural degrees of freedom constantly
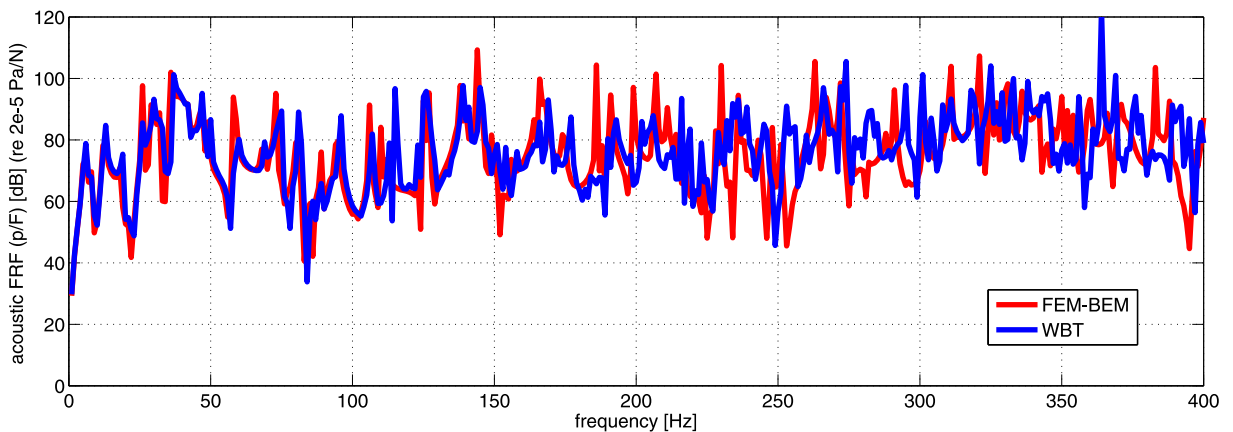
Figure 6.16: Soundbrick convertible: frequency response functions at point RP1
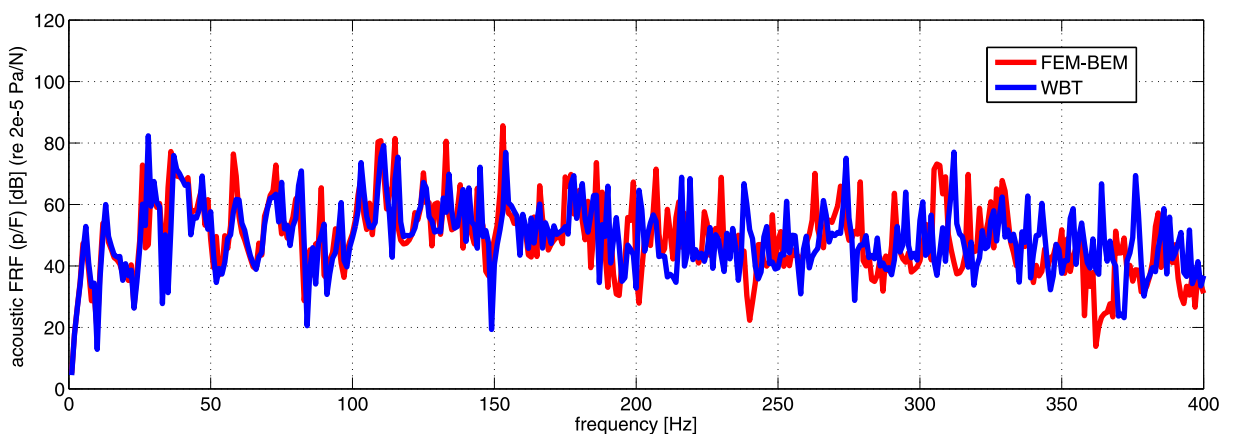
Figure 6.17: Soundbrick convertible: frequency response functions at point RP2

across the frequency range, which requires about 65 seconds to solve one frequency step. The comparison shows a good match between both models up to a frequency of approximately 200 Hz. At higher frequencies the WB response begins to deteriorate slightly, which is, however, related to the relatively low number of acoustic wave functions $\mathbf{\Phi}$ used in the bounded part of the model.

6.5 Validation example: distributed mode loudspeaker

The last validation example in this chapter considers the application of the WBT to a so-called distributed mode loudspeaker (DML) (Harris and Hawksford, 1997; Azima and Mapp, 1998; Azima, 1998; Panzer, 1998) involving both the free-field and semi-infinite acoustic domains. The DMLs (also sometimes referred to as diffuse radiators, due to their superb broadband omnidirectional characteristics) present a novel loudspeaker design in contrast to conventional speakers, which are based on a piston-like vibrating diaphragm driven by a moving coil transducer. A comparative study on the directivity characteristics of a DML and a conventionally designed speaker is presented as well.

6.5.1 DML principle

The DML technology was originally developed and patented worldwide by a British company named NXT in the mid of 1990s (Azima, 1998). The actual invention of the underlying DML principle, however, dates back to the end of 1980s and resulted (coincidentally) from defense research on lightweight composites conducted by Britain's Defence Evaluation & Research Agency (DERA). The basic concept of DML is best explained by comparing it with the principle of a classic speaker. In a conventional speaker, the diaphragm undergoes a piston-like motion, meaning all points of the diaphragm are considered to vibrate in-phase, at least within a limited frequency range. This fact causes many problems, which have been addressed in the field of speaker design over the last fifty years. Although some of those problems have been more or less successfully resolved, the major drawbacks remain unresolved, primarily due to their inherent nature. Since the diaphragm moves as a rigid whole, the compression on one side inherently induces the rarefaction of the fluid on the other side. Thus, in order to avoid the acoustic short circuit effects that mainly occur at low frequencies, the speaker has to be mounted in a cabinet.
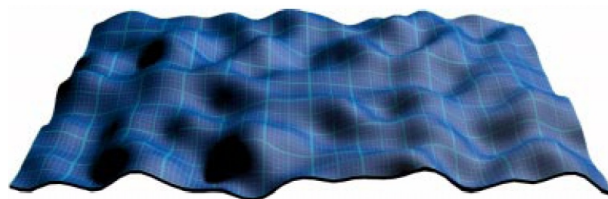
Figure 6.18: A quasi-random deflection shape of a DML-panel (image courtesy of NXT plc)

Moreover, conventional speakers are mass controlled, meaning the transducer provides a constant force across the frequency range, while the diaphragm has to resist a constant mass, irrespective of frequency – its own plus the mass of the displaced air load. This means that the speaker operates with a constant acceleration across the frequency range, and the displacement therefore decreases with increasing frequency. The radiation impedance of the speaker, on the

(a)   (b)

Figure 6.19: Distributed mode loudspeaker: (a) typical configuration and (b) possible plaster-in instal-
lation (images courtesy of Amina Technologies Ltd.)

other hand, increases with the frequency at exactly the same rate as the displacement decreases. Thus, the acoustic power remains constant. This is valid as long as the acoustic wavelength remains large compared to the characteristic dimension of the diaphragm. As the frequency increases, the wavelength shortens once it becomes comparable with the diaphragm dimensions. In this range, however, the radiation impedance reaches its maximum and becomes almost constant for all higher frequencies, see figure 6.28. Accordingly, the acoustic power starts to drop at the same rate as the diaphragm displacement decreases with the frequency[2]. The radiation pattern becomes more directional, and the acoustic output becomes confined to progressively narrower solid angles. This also explains the common design of conventional loudspeakers – large diaphragms provide the volume displacement necessary to reproduce low frequencies, while small diaphragms take over at higher frequencies before the output of the larger units becomes too directional. Even so, the directivity of the speaker still varies significantly over frequency, which remains one of the biggest issues – the off-axis response has a crucial effect on what the listener actually hears. The direct, reflected and reverberant sound fields of the listening room all have different tonal balances, which means that the sound heard becomes distorted by effects such as imaging aberration.

Rather than aiming to achieve an ideal piston-like membrane movement, the DML-panel appears to vibrate in uncoordinated, random fashion. It behaves like an array of individually radiating elements, which vibrate with an uncorrelated phase. In fact, the diaphragm undergoes a quasi-random motion, see figure 6.18, in which the uncorrelated contributions from each vibrating element interfere constructively, as seen from the far-field response point. Thus, no global interference occurs and the panel behaves like a diffuse radiator emitting the sound equally in all directions. Clearly, there are many corollary advantages over conventional speaker designs as well. Another significant feature is that the dimensions of a panel no longer control its directivity – even for wavelengths shorter than the panel itself, the radiation pattern is still almost

---

[2]12 dB per octave.

perfectly omnidirectional. Similarly, there is no inherent restriction on the moving mass of the whole system, see figure 6.19(a), that determines the high frequency bound, as is common in conventional tweeters. Thus, it is possible to create easily a full-range speaker of any size with a high broadband performance, using a single panel.

In addition, since the panel vibrates in uncorrelated fashion, the short circuit phenomenon does not take place in the case of free-field installation. As a consequence, the driver unit no longer has to be mounted in a cabinet – the panel behaves as a bipolar transducer radiating the sound efficiently into both directions. However, if it is necessary or desirable to install the DML in a baffle, it offers unique placement versatility combined with new aesthetic features, such as attractive flat design, paints/finishes, or even a plaster-in installation, see figure 6.19(b).

6.5.2 Validation study

The following sections consider two validation cases that involve both the free-field and baffled installations of a DML-panel. In the practical applications, the loudspeaker panel is usually made of a composite material consisting of an aluminium honeycomb core layered with a paper skin on both sides. The resulting structure is thus stiff, yet extremely lightweight, which implies that the critical frequency is lower than that of a homogenous structure of the same weight (but, indeed, lower stiffness) (Fahy, 2000). As a consequence, the useful frequency range of a DML lies above the coincidence frequency where the panel already behaves as a good sound radiator. However, since the WBT relies on the Kirchhoff thin plate theory, see section A.2.1, only homogenous flat structures are admissible in the wave based formulation for the plate bending problems. As such, the composite structure is represented by an equivalent homogenous plate of the same macroscopic physical properties.
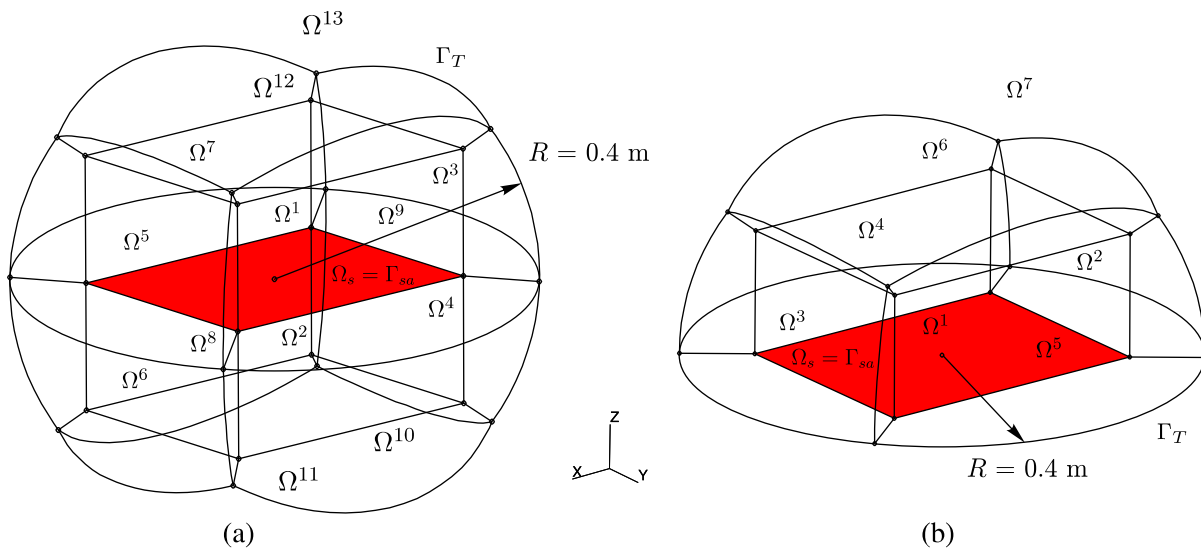
Figure 6.20: Distributed mode loudspeaker: WB models representing (a) the free-field and (b) the baffled problem (Rejlek and Priebsch, 2011)

The problem consists of a $t = 0.003$ m thin rectangular panel of dimensions 0.45×0.35 m having the equivalent mass density $\rho_s = 40$ kg/m³, the equivalent Young's modulus $E = 20 \cdot 10^9$ Pa and the equivalent Poisson's ratio $\nu = 0.45$. These material parameters have been estimated using the available material data (Panzer, 1998). The panel is excited by a point

force $F = 1$ N applied in a normal direction to the plate at the position $\mathbf{r}_F = (0.2,\ 0.1)$ m. All boundary edges are clamped and the panel is surrounded by air having the speed of sound $c = 343.8$ m/s and the mass density $\rho_a = 1.2\ \mathrm{kg/m^3}$.

6.5.2.1   Free-field installation

In order to validate the proposed wave based formulation a coupled FE–BE analysis is considered as a reference solution. The fully coupled problem consists of a modally reduced structural FE model and the acoustic indirect BE model. The resulting model is assembled in a commercial CAE system *LMS Virtual.Lab* running the *LMS/SYSNOISE* Rev. 5.6 solver (LMS International, 2010). The structural FE part consists of 25 521 nodes forming 25 200 linear quadrilateral shell elements with a maximum element edge size of $h_{max,s} = 0.0025$ m. The modal base contains the structural eigenmodes calculated by the *MSC.Nastran* solver (MSC Software Corporation, 2008) up to the frequency of 8 000 Hz. The acoustic BE part consists of 6 461 nodes forming 6 300 linear quad4 elements with a maximum element edge size of $h_{max,a} = 0.005$ m. As the two computational meshes are incompatible, a structural-acoustic mapping approach is applied at the common interface. The corresponding wave model, see figure 6.20(a), consists of one structural (indicted in red) subdomain and one unbounded and twelve bounded acoustic subdomains. Outside the truncation boundary Γ_T, the unbounded subdomain Ω^{13} explicitly accounts for the infinite extent of the solution domain (Rejlek and Priebsch, 2011).

(a)   (b)
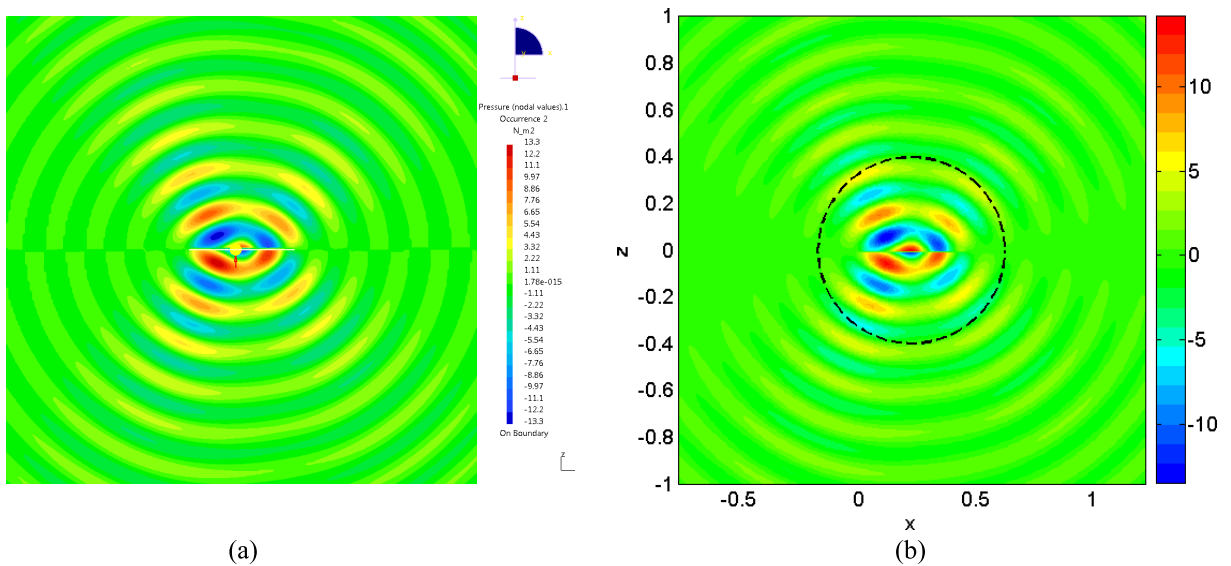
Figure 6.21: Free-field DML: real part of sound pressure field at 2 kHz predicted by (a) FEM–BEM and (b) WBT

Figures 6.21 and 6.22 show the predicted sound radiation patterns at 2 and 4 kHz, respectively. The figures plot the real part of the sound pressure field in the plane $y = 0.175$ m as predicted by the FE–BE and WB models. For the acoustic part, the WB model uses $n_{r\bullet} = n_{s\bullet} = n_{t\bullet} = 9$ and $L = 40$ to truncate both the bounded and unbounded acoustic wave function sets, while $n'_r = n'_s = 60$ is applied for the truncation of the structural wave function set. This yields 8 881 acoustic and 488 structural degrees of freedom. The coupled FE–BE model needs 890 s to calculate one frequency step, including the postprocessing of primary results at the field point mesh. The wave model employing constant wave function set truncation over the frequency

(a)   (b)
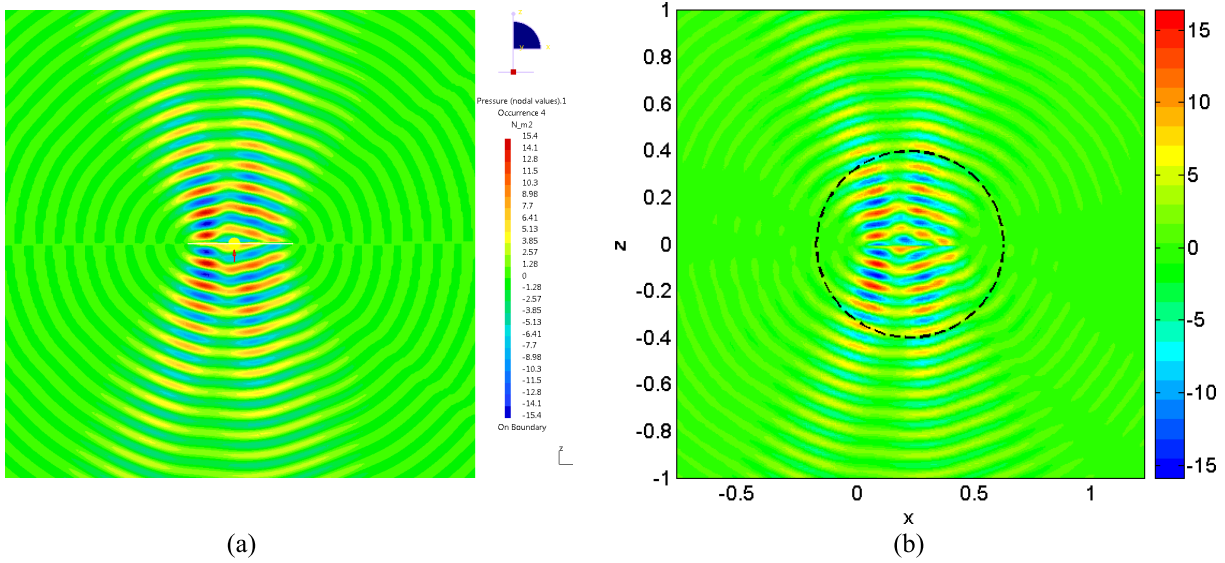
Figure 6.22: Free-field DML: real part of sound pressure field at 4 kHz predicted by (a) FEM–BEM and (b) WBT (Rejlek and Priebsch, 2011)

(a)

(b)
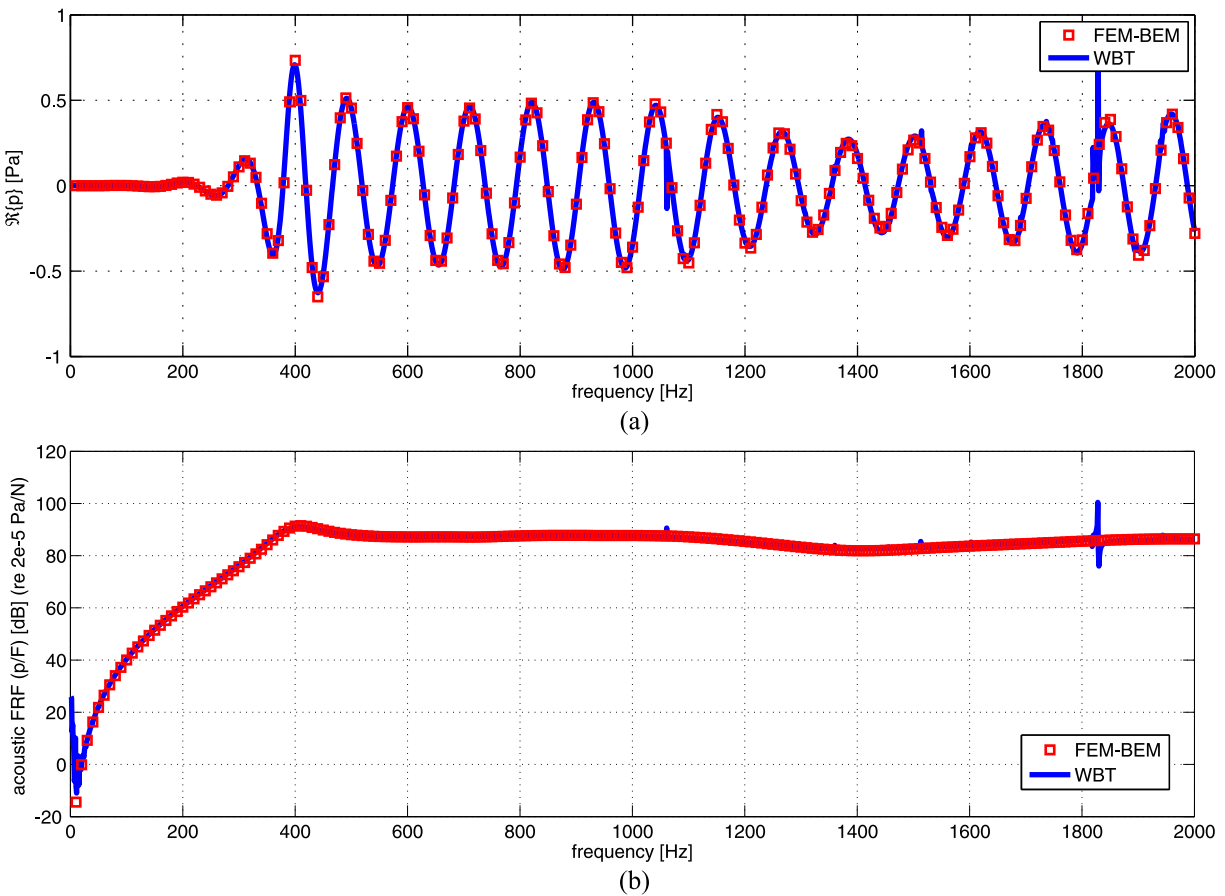
Figure 6.23: Free-field DML: (a) pressure response spectra (real part of the sound pressure) and (b) acoustic frequency response functions predicted by FEM–BEM and WBT up to 2 kHz at point RP1 (Rejlek and Priebsch, 2011)

attribute	denotation	value	
		structural	acoustic
solution scheme		FEM modal	BEM indirect variational
number of nodes	#nod	25 521	6 461
number of elements	#ele	25 200	6 300
mesh topology	topo	quad4	
maximum element edge size	$h_{max,s}$, $h_{max,a}$	0.0025 m	0.005 m
degrees of freedom	DOF	149 286	6 480
number of modes up to 8 000 Hz	#mod	19	–
CPU time for modal extraction	t_{mod}	60 s	–
FRF range	f_{min}, f_{max}	–	1–2 000 Hz
FRF step	Δf	–	10 Hz
CPU time per Δf	$t_{\Delta f}$	–	165 s

Table 6.7: Free-field DML: attributes of the FE–BE model

requires about 400 s. Similar to the previous example presented in this chapter, the BE solution time does not include the computational efforts necessary for performing the structural modal analysis using FEM. The time needed to solve the wave model, on the other hand, includes the solution of the fully coupled system. The dashed lines in the WB contour plots denote the truncation sphere Γ_T. The contour plots indicate a close match between the FE–BE and WB predictions. As no physical boundaries other than the vibrating panel occur in the model, the problem is obviously antisymmetric with respect to $z = 0$. The pressure fields predicted by WBT reveal that the antisymmetric nature of the sound radiation pattern has been correctly accounted for.

attribute	denotation	value	
		structural	acoustic
solution scheme		fully coupled WBT	
number of subdomains	N_s, N_a	1	12
	N_u	–	1
truncation strategy		constant	
truncation parameter	(n'_r, n'_s), $(n_{r\bullet}, n_{s\bullet}, n_{t\bullet})$	50	6
	L	–	20
radius of truncation sphere	R	–	0.4 m
degrees of freedom	dim$\boldsymbol{\Psi}$, dim$\boldsymbol{\Phi}$	408	3 969
FRF range	f_{min}, f_{max}	1–2 000 Hz	
FRF step	Δf	1 Hz	
CPU time per Δf	$t_{\Delta f}$	42 s	

Table 6.8: Free-field DML: attributes of the WB model

In addition to the response fields studies, a frequency response analysis in the range of 1–2 000 Hz is carried out using the FE–BE and WB approaches. Figure 6.23(a) captures the real part of the sound pressure evaluated at the response point RP1 = (0, 0, 3) m, while fig-

ure 6.23(b) plots the acoustic frequency response functions (p/F). The WB calculation is carried out with the frequency resolution of 1 Hz, while a frequency step of 10 Hz is used for the coupled FE–BE model, in order to reduce the computational load. The same FE–BE model employed to predict the dynamic fields discussed above is used, which requires roughly 165 s to perform one frequency step, see table 6.7. The wave model with the detailed attributes listed in table 6.8 uses $n_{r\bullet} = n_{s\bullet} = n_{t\bullet} = 6$ and $L = 20$ to truncate both the bounded and unbounded acoustic wave function sets and $n'_r = n'_s = 50$ truncation numbers for the structural wave function set. This yields 3 969 acoustic and 408 structural degrees of freedom constantly across the frequency range and requires about 42 seconds to solve one frequency step. The comparisons show a perfect match between both predictions in the whole frequency range of interest.

6.5.2.2 Baffled installation

For the baffled analysis, the unbounded FE–BE model as presented in section 6.5.2.1, is used as a starting point. The only distinction is the introduction of a rigid baffle located in the $z = 0$ plane. The wave model, on the other hand, consists of one structural subdomain, as well as one unbounded and six bounded acoustic subdomains, see figure 6.20(b).

FEM-BEM: Re{p}   WBT: Re{p}

(a) Real part of the sound pressure [Pa]

FEM-BEM: 20 log |p|/p$_{ref}$ WBT: 20 log |p|/p$_{ref}$

(b) Sound pressure level [dB re $2 \cdot 10^{-5}$ Pa]
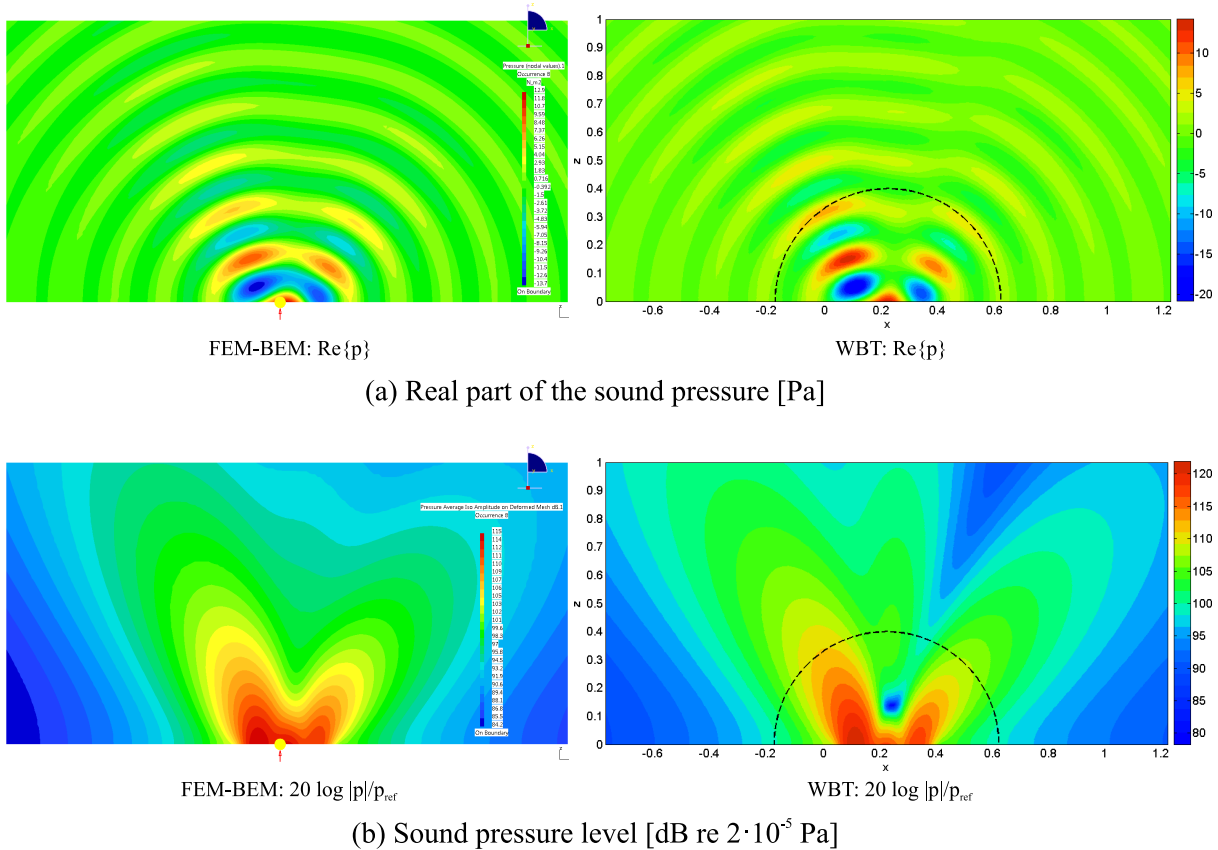
Figure 6.24: Baffled DML: sound pressure fields at 2 kHz predicted by (a) FEM–BEM and (b) WBT

Figures 6.24 and 6.25 show the predicted sound radiation patterns at 2 and 4 kHz, respectively. The figures plot the field of both the real part of the sound pressure and the SPL in the plane $y = 0.175$ m, as predicted by the FE–BE and WB models. The structural part of the wave model uses $n'_r = n'_s = 60$ to truncate the wave function set. For the acoustic subdomains located within the

FEM-BEM: Re{p}   WBT: Re{p}

(a) Real part of the sound pressure [Pa]

FEM-BEM: 20 log |p|/p$_{\text{ref}}$ WBT: 20 log |p|/p$_{\text{ref}}$

(b) Sound pressure level [dB re $2 \cdot 10^{-5}$ Pa]
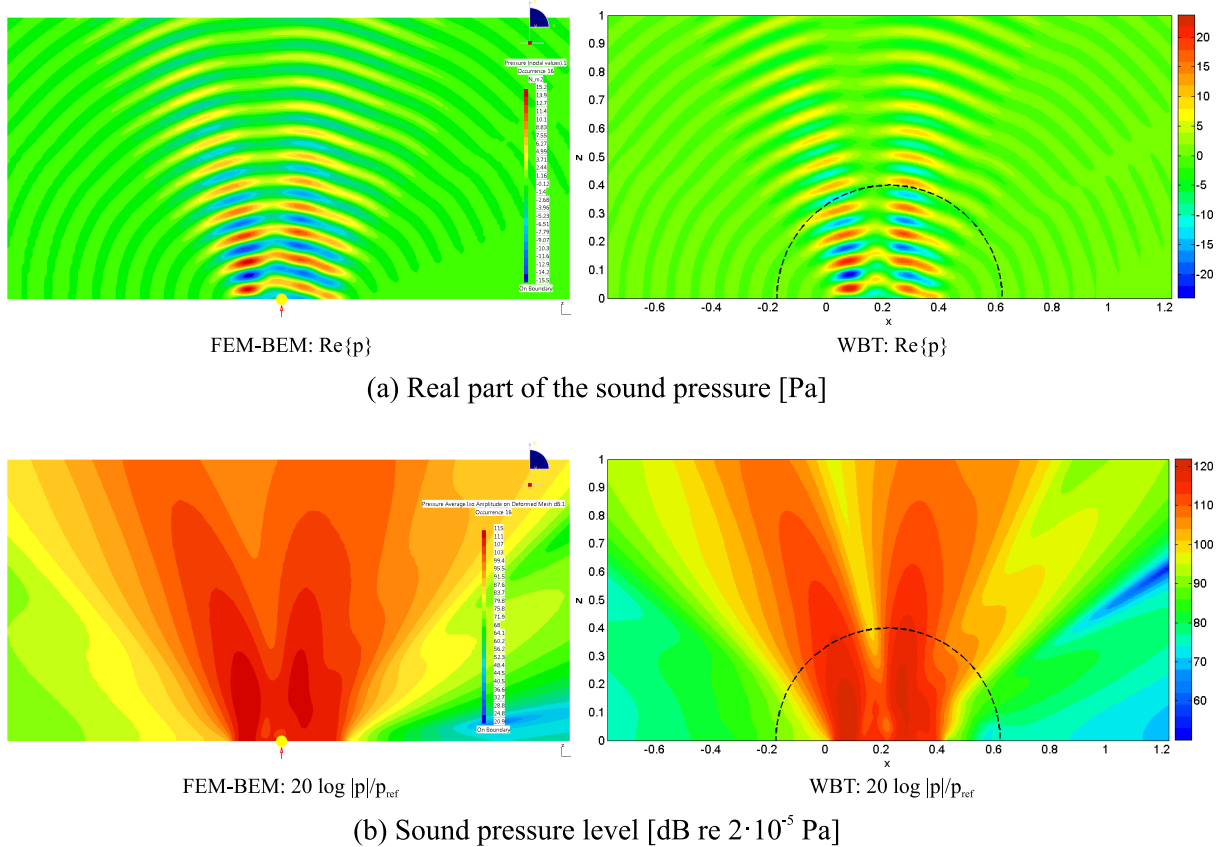
Figure 6.25: Baffled DML: sound pressure fields at 4 kHz predicted by (a) FEM–BEM and (b) WBT

bounded region of the wave model, $n_{r\bullet}^1 = n_{s\bullet}^1 = n_{t\bullet}^1 = 14$ and $n_{r\bullet}^{(2-6)} = n_{s\bullet}^{(2-6)} = n_{t\bullet}^{(2-6)} = 13$ truncation numbers are applied, while the semi-infinite wave function expansion is truncated at order of $L = 25$. This yields a total of 7 581 acoustic and 488 structural degrees of freedom.

attribute	denotation	value	
		structural	acoustic
solution scheme		FEM modal	BEM indirect variational baffled
number of nodes	#nod	25 521	6 461
number of elements	#ele	25 200	6 300
mesh topology	topo	quad4	
maximum element edge size	$h_{max,s}$, $h_{max,a}$	0.0025 m	0.005 m
degrees of freedom	DOF	149 286	6 480
number of modes up to 8 000 Hz	#mod	19	–
CPU time for modal extraction	t_{mod}	60 s	–
FRF range	f_{min}, f_{max}	–	1–2 000 Hz
FRF step	Δf	–	1 Hz
CPU time per Δf	t_{coup}	–	70 s

Table 6.9: Baffled DML: attributes of the FE–BE model
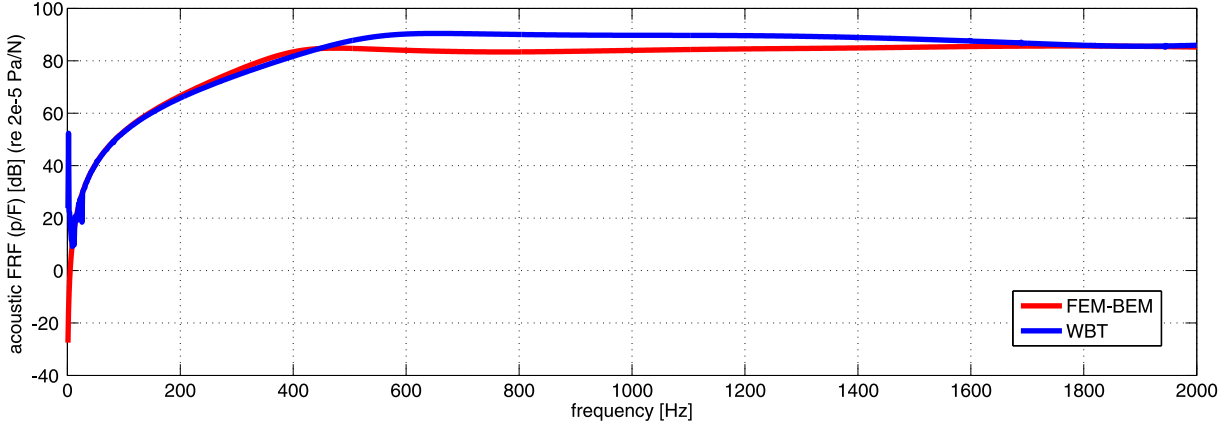
Figure 6.26: Baffled DML: frequency response functions predicted up to 2 kHz at point RP1

The coupled FE–BE needs roughly 707 s to calculate one frequency step, including the postprocessing of primary results at the field point mesh. The wave model, which employs a constant wave function set truncation across the frequency range, requires about 340 s. The BE solution time, however, does not include the computational efforts necessary for calculating the structural modes. The WBT, on the other hand, solves the whole coupled system simultaneously. The dashed lines in the WB contour plots indicate the truncation hemisphere Γ_T. The contour plots show a fair match between the FE–BE and WB predictions. Moreover, the WB pressure patterns demonstrate that the normal velocity boundary condition at both the rigid parts of the physical boundary and the rigid baffle plane have been properly accounted for. In addition, the pressure fields also reveal that both the structural-acoustic coupling condition at Γ_{sa} and the continuity conditions enforced at the interfaces between the acoustic subdomains are fulfilled exactly.

attribute	denotation	value	
		structural	acoustic
solution scheme		fully coupled WBT	
number of subdomains	N_s, N_a	1	6
	N_{si}	–	1
truncation strategy		constant	
truncation parameter	(n_r', n_s'), $(n_{r\bullet}, n_{s\bullet}, n_{t\bullet})$	60	$n_\bullet^1 = 10$
			$n_\bullet^{2-6} = 8$
	L	–	20
radius of truncation hemisphere	R	–	0.4 m
degrees of freedom	$\dim\boldsymbol{\Psi}$, $\dim\boldsymbol{\Phi}$	488	3 387
FRF range	f_{min}, f_{max}	1–2 000 Hz	
FRF step	Δf	1 Hz	
CPU time per Δf	t	35 s	

Table 6.10: Baffled DML: attributes of the WB model

Figure 6.26 plots the acoustic frequency response functions (p/F) determined at the response point $\mathrm{RP1} = (0, 0, 3)$ m by the FEM–BEM and WBT. Once again, the same FE–BE model applied for the prediction of the response fields is used, see table 6.9, which requires roughly 70 s to perform one frequency step. In the wave model, see table 6.10, $n_{r\bullet}^1 = n_{s\bullet}^1 = n_{t\bullet}^1 = 10$

and $n_{r\bullet}^{2-6} = n_{s\bullet}^{2-6} = n_{t\bullet}^{2-6} = 8$ truncation parameters are applied within the bounded acoustic subdomains, while $L = 20$ is used for the truncation of the solution expansion in the semi-infinite domain. The structural wave function set is truncated from above with $n_r' = n_s' = 60$. The resulting wave model has 3 387 acoustic and 488 structural degrees of freedom in total, which are constant across the frequency range. Such a WB model requires about 35 seconds to solve one frequency step. The comparison of the estimated frequency response functions shows a good match in the range up to 400 Hz and then again in the high frequency range from 1800 Hz onwards. In between, however, the WB prediction overestimates the FE–BE one. One reason for this could be the effect of fluid loading acting on the structural plate. While in FE–BE model the fluid acts from both sides of the plate, in the wave model, on the other hand, only the semi-infinite fluid domain located above the plate is explicitelly modelled.

6.5.3   Directivity characteristics

As mentioned previously, among the most remarkable features of a DML concept are the broad-band omnidirectional radiation characteristics. This section therefore presents a comparative study of the directional properties of a DML-panel and a conventional speaker. In this type of investigation, only a baffled installation is considered. The analyses are conducted by means of the wave models introduced in section 5.4 and 6.5.2.

(a)   (b)
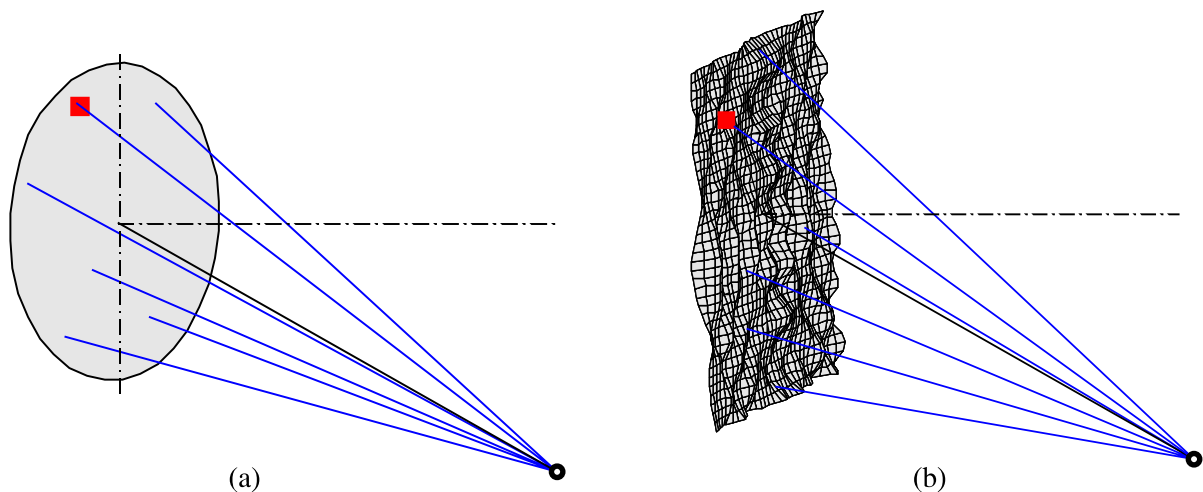
Figure 6.27: Velocity distribution on (a) conventional loudspeaker diaphragm (circular piston-like radiator) and (b) DML-panel (diffuse radiator) (Azima, 1998)

The conventional speaker is represented by the baffled piston validation example described in section 5.4. The circular diaphragm undergoes a piston-like motion, in which all points of the radiator vibrate in-phase with a constant velocity magnitude. Thus, the directivity depends solely on the path lengths between the infinitesimal radiating element and the response point, see figure 6.27(a), or, more specifically, on the phase shifts of the incoming waves, which determine whether the contributions will interfere in a constructive or destructive way. As long as the wavelength of the acoustic wave remains substantially larger than the dimensions of the diaphragm, the piston behaves as a point source and radiates sound efficiently in all directions, see directivity diagram in figure 6.28 for range of $kR < 1$. A major change occurs, however, once the wavelength reaches the range of diaphragm dimensions, at which point the radiated power begins to decrease and the radiation pattern becomes more directional, see the directivity pattern in $kR \gg 1$ regime plotted in figure 6.28.
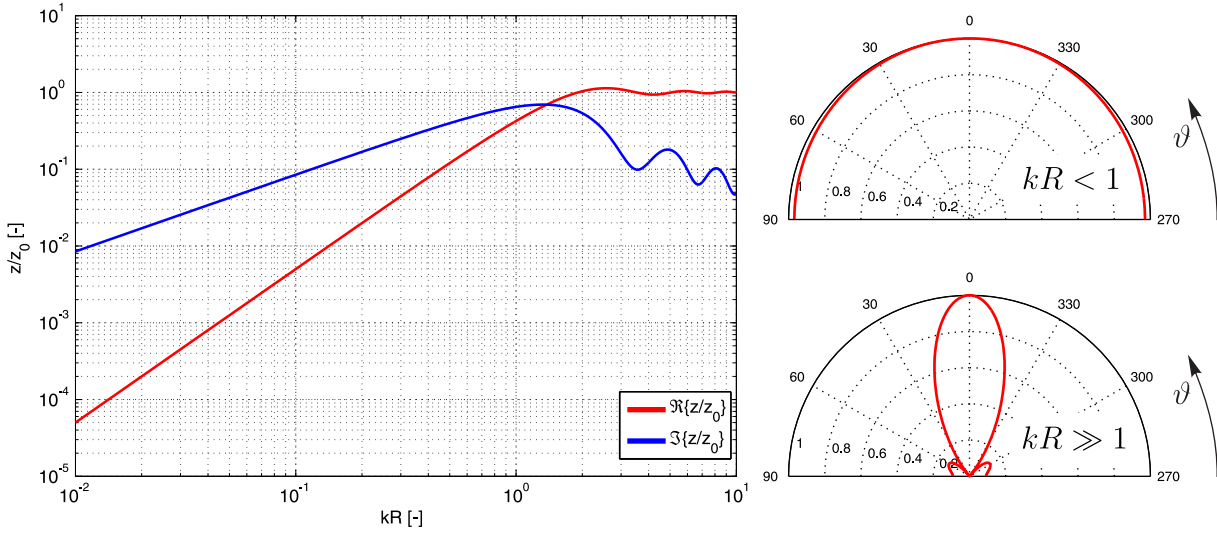
Figure 6.28: Baffled piston: the radiation impedance as a function of kR – the inserts on the right hand side indicate the directivity patterns $\eta(\vartheta)$ for different kR regimes

In figure 6.28, the normalised radiation impedance z/z_0 of a baffled piston is given by

$$z = z_0 \left[1 - \frac{\mathrm{J}_1(2kR)}{kR} + \mathrm{j}\frac{\mathrm{H}_1(2kR)}{kR} \right] \tag{6.24}$$

with $z_0 = \rho c$ the specific impedance and $\mathrm{H}_1(\bullet)$ the first-order Struve function. The directivity patterns plotted on the right hand side of figure 6.28 are defined by (Williams, 1999)

$$\eta(\vartheta) = \left| \frac{2\mathrm{J}_1(kR\sin\vartheta)}{kR\sin\vartheta} \right|. \tag{6.25}$$

In the DML, on the other hand, each infinitesimal element vibrates in an uncorrelated fashion independently of the others, i.e. the motion of the panel is incoherent. More precisely, the panel undergoes a quasi-random motion, see figure 6.18, in which the motion between the infinitesimal elements is uncorrelated with respect to magnitude and phase. As such, the uncorrelated contributions from each vibrating element interfere constructively, as seen from the far-field response point. Thus, no global interference occurs, and the panel behaves as a diffuse radiator emitting the sound equally in all directions.

Figures 6.29 and 6.30 plot the directivity patterns of both radiators at 2 and 4 kHz, respectively, with the directivity defined as follows

$$D(\vartheta,\varphi) = 20\log\frac{|p(\vartheta,\varphi)|}{p_{REF}}, \tag{6.26}$$

where $p_{REF} = 2 \cdot 10^{-5}$ Pa is the reference value for the sound pressure. Figure 6.29 confirms the initial assumptions – the radiation characteristic of a circular radiator becomes strongly directional for the Helmholtz number reaching the range $kR \gg 1$, while the DML achieves a substantially more uniform radiation pattern even with slightly larger dimensions. At the higher frequencies, see figure 6.30, the difference between the directional performances of the two transducers becomes even more pronounced.
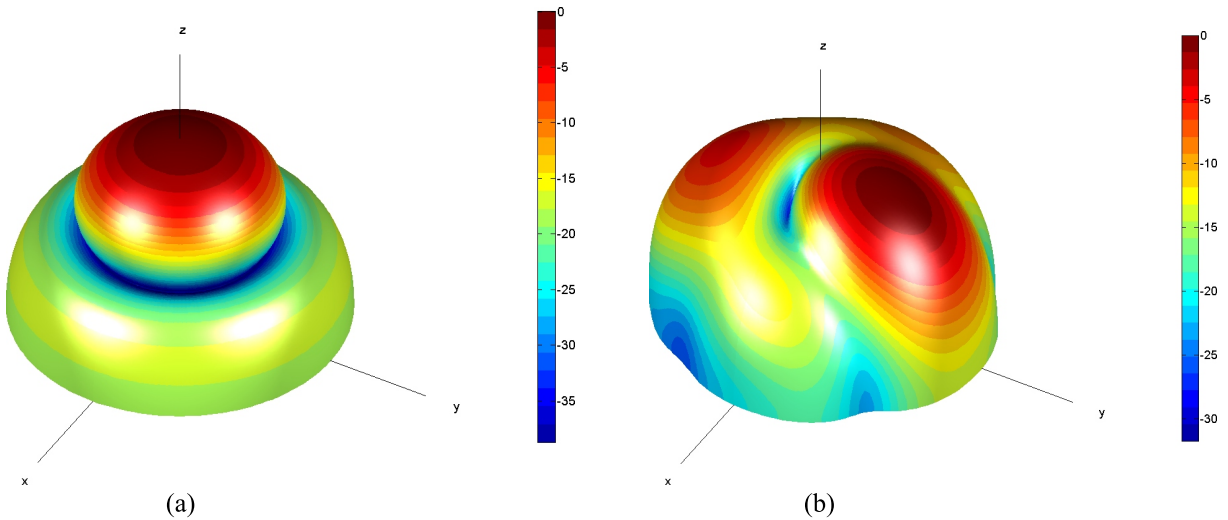
Figure 6.29: Directivity patterns at 2 kHz predicted by WBT: (a) baffled piston, (b) baffled DML-panel
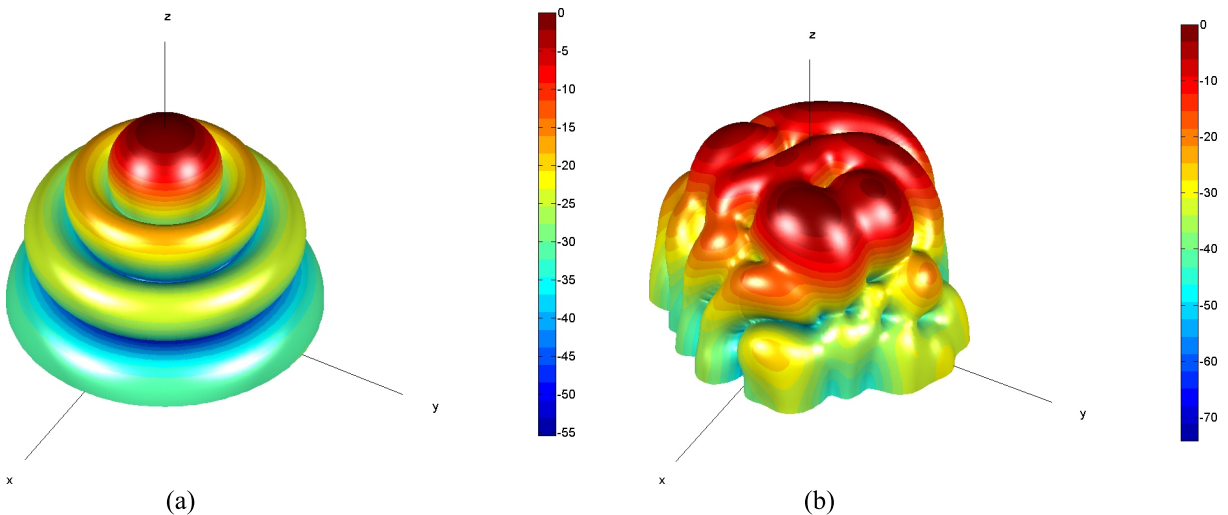
Figure 6.30: Directivity patterns at 4 kHz predicted by WBT: (a) baffled piston, (b) baffled DML-panel

6.6   Summary

This chapter reported on the basic concepts and the application of the WBT for a steady-state analysis of three-dimensional, fully coupled, unbounded vibro-acoustic problems. Three test cases were considered in order to validate the coupled formulation of WBT. The first validation example presented the application of WBT to an academic example involving a free-field, unbounded acoustic domain. As such, the initial investigation was divided into two stages. The first pretesting stage only considered the coupled structural-acoustic formulation of an interior problem, and this formulation was further extended towards unbounded problems by introducing the artificial truncation geometry in the second stage. The first test case provided the necessary validation of the coupled formulation and illustrated the increased computational efficiency of this approach.

Encouraged by the first promising results, the coupled scheme was next applied to an industry-sized problem consisting of a simplified car-like geometry involving a semi-infinite acoustic

domain. The second validation example aimed to demonstrate the practical applicability of the WBT to real-life engineering problems. In the last validation example, the WBT was applied for a coupled analysis of the so-called distributed mode loudspeaker (DML) involving both the free-field and semi-infinite acoustic domains. Besides the numerical validation, a study of the directivity characteristics of this novel loudspeaker were carried out using WBT.

The various validation examples have demonstrated the efficiency of this novel approach compared with the state-of-the-art technologies based on the finite and boundary element methods. Even though the WBT has proven to be very efficient, its ability to tackle problems of higher geometrical complexity is still restricted. This is due to the global nature of the approximation functions adopted in the framework of this method. To ease this limitation, the coupling of WBT with a conventional element based method could be applied, which would combine both the superior computational efficiency of WBT and the high geometrical flexibility of FEM and/or BEM into one coupled scheme. The second limiting factor for industrial utilisation of WBT is the lack of an advanced, dedicated preprocessing tool. Currently, the wave models are still being built up manually by the user. To reach an industrial level of maturity, however, a semi- or fully automated preprocessor must be employed.

Chapter 7

The Wave Based Technique for one-way-coupled, unbounded vibro-acoustic problems

This chapter discusses the methodology and application of the wave based technique for a steady-state analysis of three-dimensional, one-way, (weak) coupled unbounded vibro-acoustic problems. Whenever a structure is surrounded by fluid, the vibro-acoustic behaviour of the system is influenced by the mutual coupling interaction between the two subsystems. A specific class of problems, however, allows the strong mutual coupling to be omitted and both subsystems to be considered weak-coupled. In this class of problems, the vibrating structure can still be regarded as independent of external pressure loading arising from the surrounding acoustic domain (Desmet, 1998). One example is the uncoupled vibro-acoustic analysis of elastic high-stiffness structure surrounded by low-density fluid, such as the radiation of engine block noise into a surrounding air domain. Atalla and Bernhard (1994) proposed a dimensionless measure to determine the strength of the mutual coupling interaction in a vibro-acoustic system. It is vitally important to distinguish between strongly and weakly coupled systems, particularly from the computational point of view.

Section 7.1 recaps a general, one-way-coupled, unbounded vibro-acoustic problem. Section 7.2 outlines the concept of the so-called multi-local-velocities algorithm (MLV), which is used to couple the structural FE model with an unbounded acoustic WB counterpart by adopting a geometrical mapping technique. The MLV approach is applied to two validation examples involving both the free-field and semi-infinite acoustic domains. The first validation case, covered in section 7.3, considers a free-field noise radiation analysis of a four cylinder car engine with a gearbox. Section 7.4 reports on the application of the MLV for a semi-infinite, structure-borne noise radiation analysis of a truck exhaust muffler. In the latter example, experimental measurement campaigns complement the numerical validation study. Section 7.5 summarises this chapter.

7.1   Problem definition

Consider a three-dimensional, one-way-coupled, unbounded structural-acoustic problem. The structural part consists of a closed boundary, which constitutes the wetted surface Γ_{sa}. The system is excited by a harmonic point force F applied in a normal direction to the boundary at the position $\mathbf{r}_F$. The acoustic part consists of a closed boundary surrounded by fluid, which forms an unbounded acoustic domain Ω_a, see figure 2.4(b). Assuming that the system is linear, the fluid is inviscid and the process adiabatic, the steady-state pressure response $p(\mathbf{r}, t) = p(\mathbf{r})\mathrm{e}^{\mathrm{j}\omega t}$ at an arbitrary position $\mathbf{r}$ within the solution domain Ω_a is governed by the Helmholtz equation

$$\nabla^2 p(\mathbf{r}) + k^2 p(\mathbf{r}) = -\mathrm{j}\rho_a \omega q \delta(\mathbf{r}, \mathbf{r}_q), \quad \forall \mathbf{r} \in \Omega_a. \tag{7.1}$$

At the boundary of the problem $\partial\Omega_a = \Gamma_v$ the normal velocity boundary condition is imposed $\forall \mathbf{r} \in \Gamma_v$:

$$\mathcal{L}_v(p(\mathbf{r})) = \frac{\mathrm{j}}{\rho_a \omega} \frac{\partial p(\mathbf{r})}{\partial n} = \bar{v}_n(\mathbf{r}) \tag{7.2}$$

with $\frac{\partial}{\partial n}$ the normal derivative and $\bar{v}_n(\mathbf{r})$ the prescribed normal velocity originating from the structural part of the problem. Again, as the solution domain Ω_a is unbounded, an additional Sommerfeld radiation condition has to be imposed at Γ_∞ in order to ensure that no acoustic energy reflections occur at infinity $\forall \mathbf{r} \in \Gamma_\infty$:

$$\lim_{|\mathbf{r}| \to \infty} \left[|\mathbf{r}| \left(\frac{\partial p(\mathbf{r})}{\partial |\mathbf{r}|} + \mathrm{j}k p(\mathbf{r}) \right) \right] = 0. \tag{7.3}$$

7.2   Concept of the Multi–Local–Velocities approach

As the problem introduced in section 7.1 involves an unbounded acoustic domain an additional modification of the wave based scheme is once again required. Similar to the problem presented in section 5.1, the acoustic domain is divided into a bounded and an unbounded part $\Omega_a = \Omega^b \bigcup \Omega^u$ by introducing an artificial truncation boundary Γ_T , see figure 7.1(a). The corresponding solution expansions for the two regions of the acoustic domain were already introduced in section 5.2.2, see equations (5.6) and (5.18).

To couple the structural and acoustic problems, which are based on different computational techniques and thus use incompatible numerical models, a generic multi–local–velocity (MLV) algorithm is utilised (Hepberger et al., 2004), see figure 7.1(b). First, a user-specified region of the FE mesh is assigned to each WB boundary part Γ_v^i. Within this target region, a corresponding finite element is sought, where the projection of the Gauss point (GP) onto the FE mesh meets some algorithm-specific criteria. Once the corresponding finite element counterpart has been found, the velocity vector $\mathbf{v}(\mathbf{r})$ for the given FE–GP mapping pair is determined by interpolating the nodal FE velocities by using the corresponding FE shape functions. Finally, only the normal component of the velocity vector $\mathbf{v}_n(\mathbf{r})$ is mapped onto the physical boundary Γ_v^i and as such is imposed as a spatially variant normal velocity boundary condition $\bar{v}_n(\mathbf{r})$.
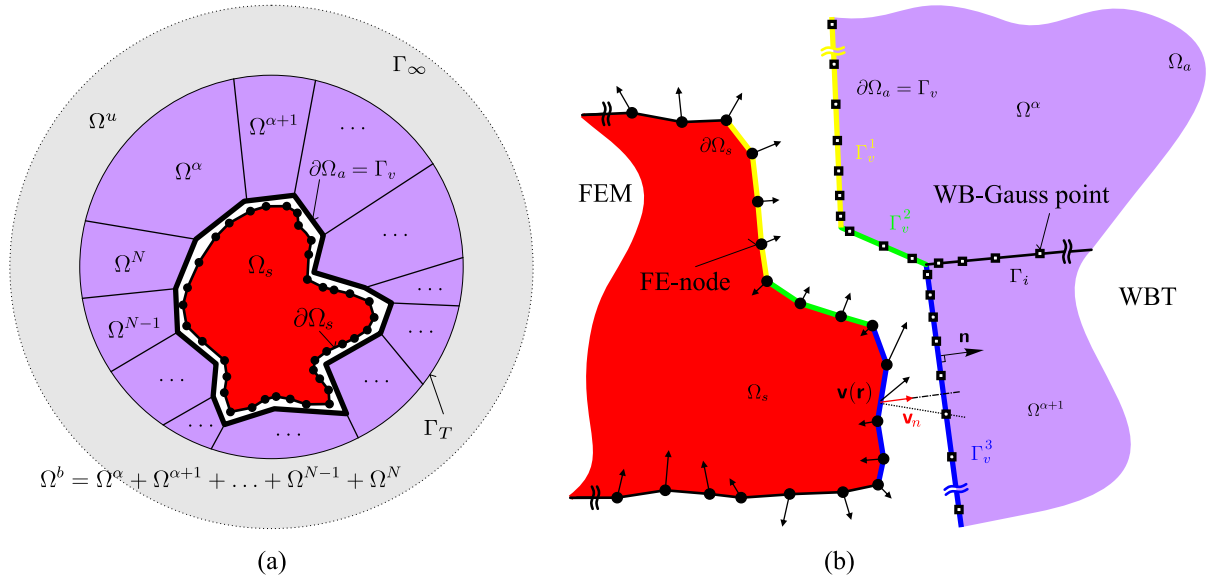
Figure 7.1: The application of WBT for one-way-coupled, unbounded vibro-acoustic problems: (a) the concept of a truncation boundary Γ_T and (b) the generic MLV algorithm (Rejlek et al., 2009)

7.3   Validation example: four cylinder engine

Rejlek et al. (2009) demonstrated the applicability of the proposed approach to an industry-sized problem. The noise radiation analysis of an assembly, which consists of a four cylinder car engine block and gearbox having the main dimensions of $0.995 \times 0.523 \times 0.535$ m, is considered as the first validation example, see figure 7.2(a). Due to intellectual property rights, it is a common practice in the industrial engineering environment to exchange the data on an FE model level only. In this way, an FE model is often the only available data containing the geometrical information. In most cases, however, these models originate from different analysis fields, such as structural dynamic or fatigue simulation. Since these simulation procedures pose specific requirements on the computational meshes, these models are not necessarily well-suited for a noise radiation analysis, in which some geometrical features (e.g. small holes and ribs) have a negligible effect. In this respect, the initial rather complex FE model, which consists of shell and volumetric elements, is simplified for validation purposes. The engine brackets are omitted, and the original FE model is wrapped in a coarser mesh consisting of linear triangular shell elements, see figure 7.2(b).

In figure 7.2(b), the different colours refer to groups of clustered structural elements based on the geometric features of the model. Later on, these panels are linked to a corresponding part of the physical wave based boundary. The structural model is made of aluminium having the mass density $\rho_s = 2\,700$ kg/m^3, the Young's modulus $E = 7 \cdot 10^9$ Pa, the Poisson's ratio $\nu = 0.3$, the material loss factor $\eta = 0.008$ and an element thickness of $t = 0.001$ m. The model is clamped at three discrete positions and excited by a harmonic point force $F = 1$ N applied at the valve cover, see figure 7.2(b). The dynamic behaviour of the structural problem is analysed in the frequency range up to $1\,000$ Hz by means of a standard FE software package *MSC.Nastran* (MSC Software Corporation, 2008) according to Reissner-Mindlin thick plate theory, see figure 7.4.
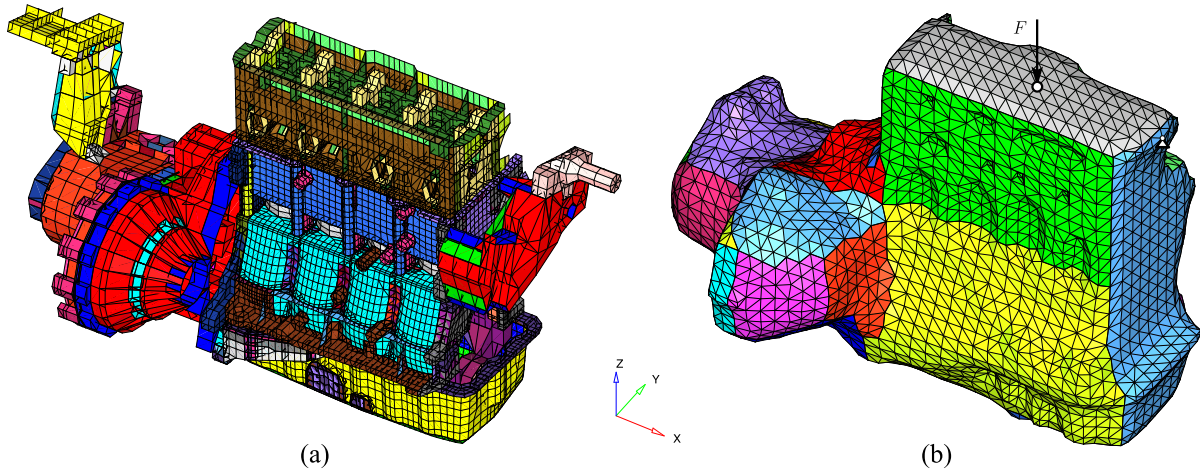
Figure 7.2: The car engine block–gearbox assembly: (a) the initial and (b) the simplified structural FE model, with the colours indicating the FE panels defined in accordance with the subdivision of an acoustic WB model (Rejlek et al., 2009)

The structural problem is surrounded by air with a speed of sound $c = 343.8$ m/s and the mass density $\rho_a = 1.2$ kg/m^3. The wave based modelling strategy involves the subdivision of the entire acoustic domain Ω_a into different regions, see figure 7.3(a). First, the structural FE model is accommodated within a fictitious rectangular box, which is a part of the bounded region of the wave model. The colours in figure 7.3(b) indicate the actual partitioning of this rectangular domain into a number of convex subdomains. On top of the rectangular domain, the wave model is further extended by six spherical subdomains, which constitute the truncation boundary Γ_T, see figure 7.3(a). Finally, the solution expansion (5.18) is applied to the unbounded part of the model Ω^u. The WBT routines are implemented in *Fortran90* programming language (Press
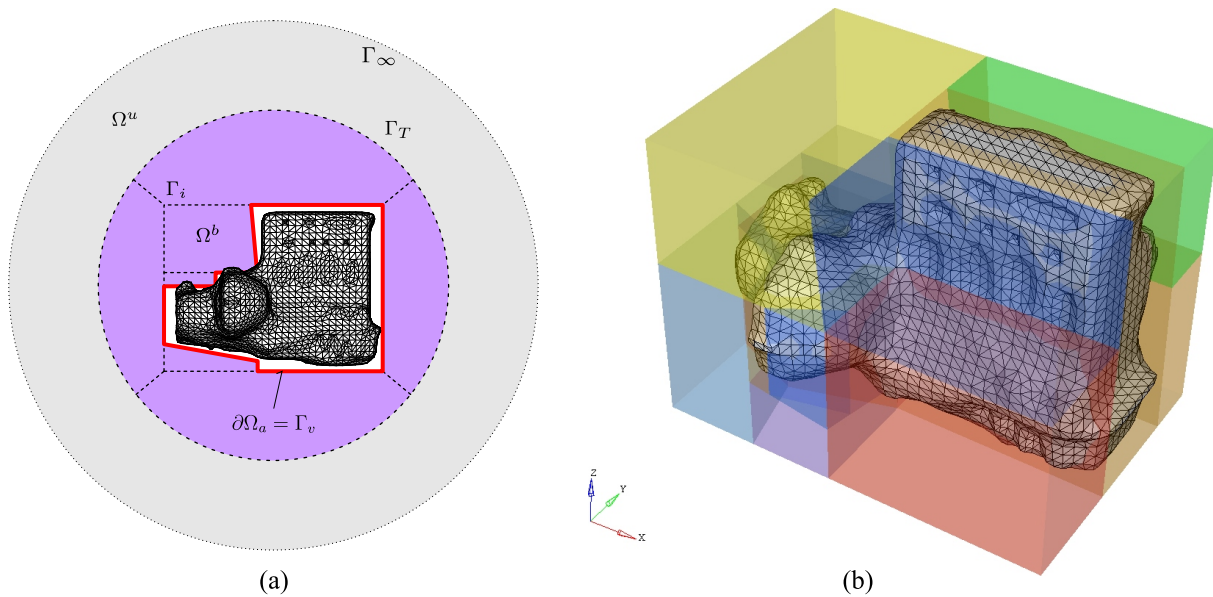
Figure 7.3: Four cylinder engine - the MLV modelling strategy: (a) subdivision of the acoustic domain into different regions, and (b) a detailed view of the wave model partitioning into convex subdomains inside the fictitious rectangular box (Rejlek et al., 2009)

et al., 1992). All calculations presented in this section are performed on a 2.26 GHz dual-core *Intel*-based computer using 4 Gbyte RAM and running the *Windows Vista 64-bit* operating system.
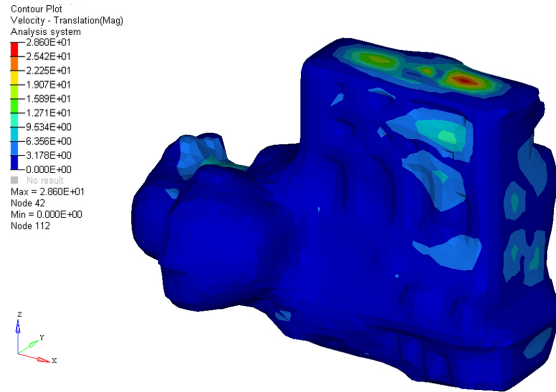
Figure 7.4: Four cylinder engine: the structural velocity magnitude calculated by the FEM and plotted at 697 Hz on a deflected shape [mm/s] (Rejlek et al., 2009)

In order to validate the proposed wave based approach, a commercial CAE system *LMS Virtual.Lab* running the *LMS/SYSNOISE* Rev. 5.6 solver (LMS International, 2010) is applied. The BE indirect model is based on the same mesh that was used for the structural FE analysis, see figure 7.2(b). As the radiating body constitutes a closed surface, an additional normal impedance boundary condition is prescribed at the inner side of the BE mesh in order to mitigate the effect of the non-uniqueness problem, see section 3.2. The primary BE results are postprocessed on a rectangular field point mesh with the dimensions of 2×2 m, which intersects the acoustic domain Ω_a parallel to the xz-plane. Figure 7.5 captures the sound radiation pattern (sound pressure level in [dB] (re $2 \cdot 10^{-5}$ Pa)) predicted at 697 Hz by the boundary element and wave based approaches. As such, these patterns correspond to a deflection shape of the structural problem shown in figure 7.4, which is affected by the shape of the mode num-

(a)   (b)
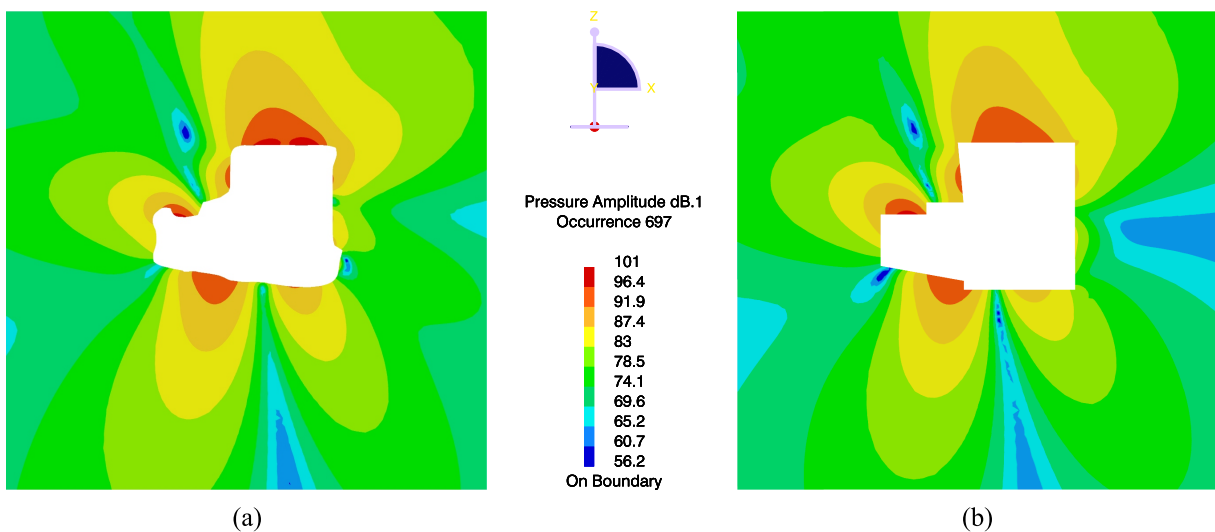
Figure 7.5: Four cylinder engine: sound pressure level in [dB] (re $2 \cdot 10^{-5}$ Pa) at 697 Hz predicted by (a) FEM–BEM and (b) FEM–WBT (Rejlek et al., 2009)

ber 42 with the eigenfrequency of 698.2 Hz. The overall sound radiation behaviour shows a good agreement between the two methodologies. However, as the two field point meshes vary somewhat in the vicinity of the vibrating structure due to the model-specific discretisation, the near field results are resolved with a slightly different accuracy.

attribute	denotation	value	
		structural	acoustic
solution scheme		FEM direct	BEM indirect variational
number of nodes	#nod	2 762	
number of elements	#ele	5 520	
mesh topology	topo	tria3	
maximum element edge size	h_{max}	0.035 m	
degrees of freedom	DOF	16 554	2 762
FRF range	f_{min}, f_{max}	1–1 000 Hz	
FRF step	Δf	1 Hz	
number of modes up to f_{max}	#mod	70	–
CPU time needed for FRF	t_{FRF}	1 552 s	231 312 s

Table 7.1: Four cylinder engine: attributes of the FE–BE model

For the frequency response analyses, two response points are selected. The first point is located at position RP1 = $(0, 0, 1.43)$ m one meter above the engine and corresponds to a reference microphone at a distance of one meter. The second microphone has a position of RP2 = $(0, 7.5, 0)$ m and represents the reference microphone used during the pass-by noise measurements. Figures 7.6 and 7.7 plot the acoustic frequency response functions (p/F) determined by the BE (red curve) and WB (blue curve) models, see tables 7.1 and 7.2, respectively, for the detailed model attributes. The wave based prediction, which requires less than one fifth of the total solution time of the BE run up, provides an adequate prediction across the whole frequency range of interest. The wave model uses a frequency-dependent strategy for the truncation of the wave function set using the parameter $T = 2 (WF + 1)$. As a result, each of the determined truncation parameters $n_{r\bullet}^{\alpha}$, $n_{s\bullet}^{\alpha}$ and $n_{t\bullet}^{\alpha}$ is increased by one $(WF+1)$ in this strategy.
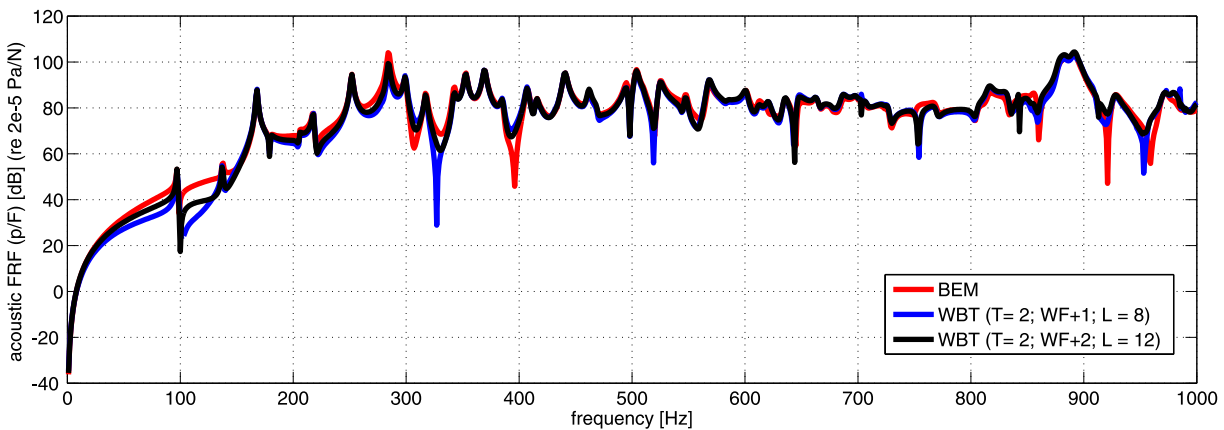
Figure 7.6: Four cylinder engine: frequency response functions at point RP1
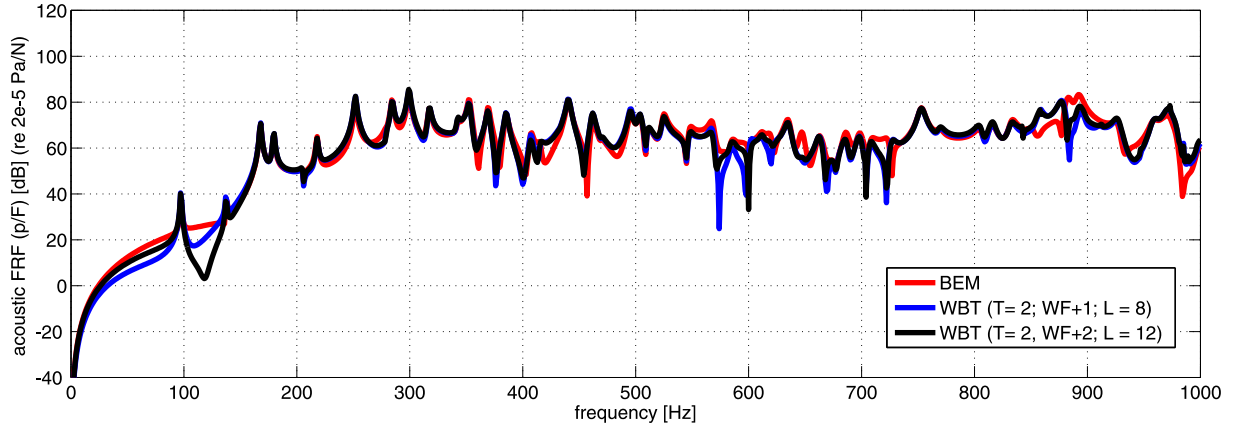
Figure 7.7: Four cylinder engine: frequency response functions at point RP2

attribute	denotation	value	
		structural	acoustic
solution scheme		FEM direct	WBT
number of nodes	#nod	2 762	−
number of elements	#ele	5 520	−
mesh topology	topo	tria3	−
maximum element edge size	h_{max}	0.035 m	−
number of subdomains	N_a	−	19 bounded
	N_u	−	1 unbounded
truncation strategy		−	frequency-dependent
truncation parameter	T	−	$2\,(WF+1)$
	L		8
radius of truncation sphere	R	−	0.6 m
degrees of freedom	DOF, $\dim\mathbf{\Phi}$	16 554	1 905–2 857
FRF range	f_{min}, f_{max}	1–1 000 Hz	
FRF step	Δf	1 Hz	
number of modes up to f_{max}	#mod	70	−
CPU time needed for FRF	t_{FRF}	1 552 s	41 691 s

Table 7.2: Four cylinder engine: attributes of the baseline FE–WB model

Applying a more strict truncation rule within the bounded acoustic domains $T = 2\,(WF+2)$, and increasing the number of wave functions used in the unbounded domain $L = 12$ yields a wave model consisting of 3 019–4 171 degrees of freedom over the frequency range. This model takes approximately 87 735 s to carry out the frequency response prediction, which is plotted in black solid curve in figures 7.6 and 7.7. The estimated response functions show an almost perfect match with the reference BE solution.

7.4 Validation example: truck exhaust muffler

Truck exterior noise has a significant impact on the competitiveness of transportation vehicles, not only due to the increasing customer demand for vibro-acoustic comfort, but also due to the tightening legal regulations regarding noise emissions (Pratellesi et al., 2011). Typically, a so-called pass-by noise standardised procedure is used to measure vehicle noise emissions. A vehicle drives under specified driving conditions in an open environment, and the acoustic pressure responses in a number of locations along the path of the vehicle are measured (ISO, 2007). For a better understanding and a reduction in the number of physical tests, numerical simulations are increasingly being used in parallel to these measurements.

The exhaust system represents a critical part of modern truck design. On the one hand, it is one of the most dominant noise sources during the standardised pass-by noise measurement, which is an important criterion for assessing the environmental impact of a vehicle. A proper design of the exhaust system, on the other hand, has a significant impact on both fuel efficiency and the reduction of exhaust gas emissions. For these main reasons, the truck exhaust system has been selected as a representative test case for the validation of the proposed emerging computational techniques in course of the EU project MID-MOD[1] (Rejlek et al., 2011). Both the CAD data and the physical muffler used for the experimental testing have been kindly provided by *VOLVO Technology AB*.
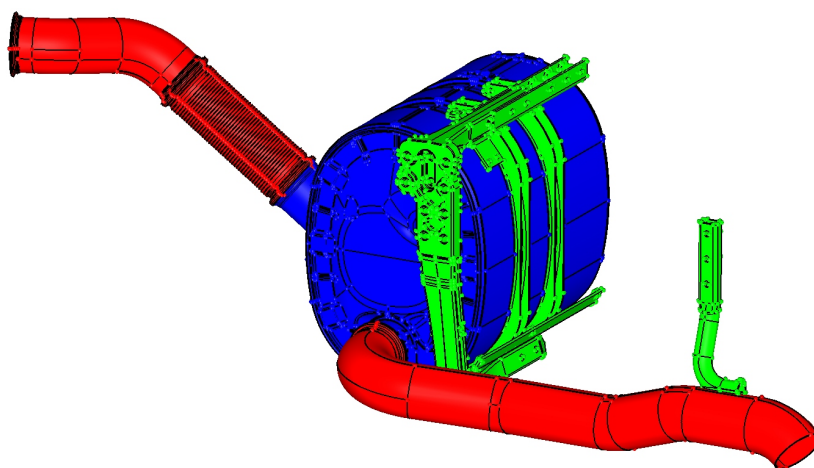
Figure 7.8: Truck exhaust system: the main muffler in blue, the inlet (left) and outlet (right) pipe in red, and the attachment frame in green (Rejlek et al., 2011)

7.4.1 Problem definition

The truck exhaust system, see figure 7.8, consists of the main muffler, the inlet and outlet pipes and the attachment frame used to mount the muffler to a vehicle chassis. The exhaust muffler consists of four chambers, see figure 7.9(a), which are interconnected with perforated pipes and selective catalytic reduction (SCR) elements, see figure 7.9(b). The design of the muffler adopts a double wall arrangement, in which the space enclosed by the two steel walls is filled with an e-glass damping layer to increase the sound insulation and to reduce the outer wall temperature. The muffler has the main dimensions of $0.67 \times 0.62 \times 0.46$ m and the weight of 74 kg. The walls are made of steel, while ceramic is used for the SCR catalysts.

---

[1]FP7 Research & Technical Development collaborative project, EC grant agreement no. SCP7-2008-218508.

Based on the experimental campaigns, a unified coordinate system is chosen for the numerical models, see figure 7.19, in which the lowest point located on the edge close to the outlet is projected onto the ground. This yields the reference point, and the muffler is therefore located 0.3 m above the rigid ground, which corresponds to the position used in the real truck.

(a)   (b)
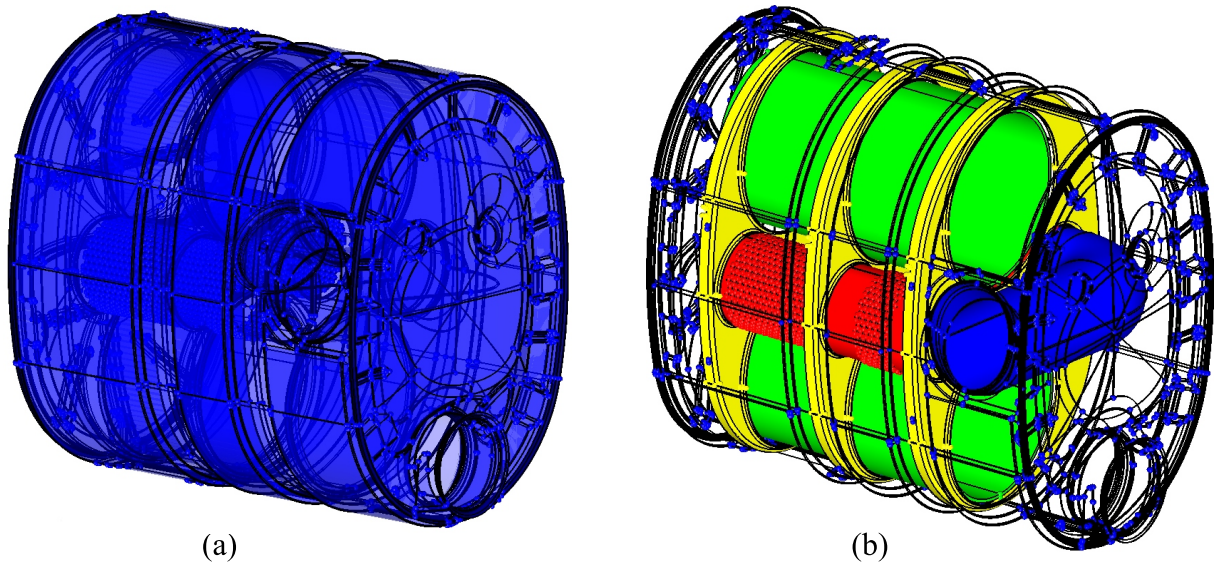
Figure 7.9: Truck exhaust muffler: (a) x-ray view and (b) the inner components – red the perforated pipes, in green the selective catalytic reduction (SCR) catalysts (Rejlek et al., 2011)

Figure 7.10 shows the workflow adopted for both the experimental measurements and the numerical analyses. First, a structural FE model is used for uncoupled frequency response analysis. Next, the acoustic WB and BE models are built up. The velocities predicted by the FEM on an outer surface of the vibrating body are coupled with both acoustic models in a weak manner. As such, the velocity field is applied as a normal velocity boundary condition on the physical boundary of the acoustic problem. In order to validate the computational models, experimental measurement campaigns complement the numerical analyses.
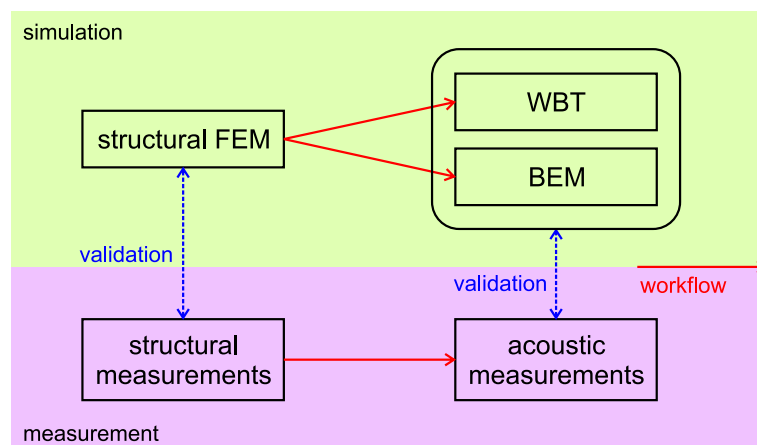
Figure 7.10: Truck exhaust muffler: the workflow (Rejlek et al., 2012)

7.4.2 Structural part

The muffler test case includes experimental measurement campaigns used in the subsequent validation study. Figure 7.11(a) shows the measurement set up used for the updating of the structural FE model – the muffler is suspended from an auxiliary frame by the flexible lightweight cords and the structure is excited in the direction normal to the surface by the impulse hammer equipped with a force cell. The deflection shape at the outer surface of the structure is captured by a set of uniaxial accelerometers. As the whole surface of the muffler consists of 126 measurement points, while only a limited number of accelerometers is available, the sensors are moved over the surface of the muffler until the entire structure has been captured. At the void measurement positions with no sensors attached during the particular measurement run, dummy masses are applied to account for the effect of the added mass due to the accelerometers.

(a)

(b)
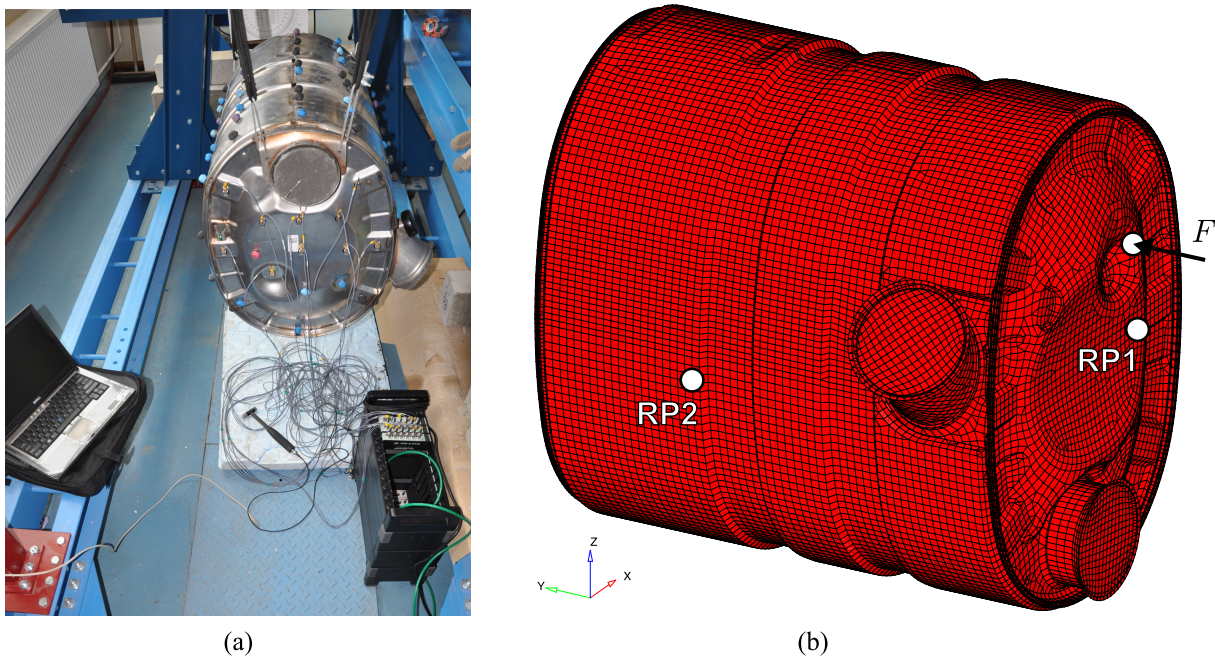
Figure 7.11: Truck exhaust muffler: (a) experimental set up (image courtesy of *The Institute of Vehicles, Warsaw University of Technology*), and (b) the corresponding FE model with the indicated positions of the excitation and response points (Rejlek et al., 2012)

In parallel with the measurement campaign, a corresponding structural FE model is created based on the provided CAD data, see figure 7.11(b). Due to the fairly complex nature of the muffler interior, a combined shell/solid finite element modelling strategy is utilised. While the steel components are modelled by shell elements, both the e-glass damping layers and the SCR catalysts are represented by the solid elements. The walls are made of steel having the mass density $\rho_s = 7\,900 \, \text{kg/m}^3$, the Young's modulus $E = 2.1 \cdot 10^{11}$ Pa, the Poisson's ratio $\nu = 0.28$ and a thickness varying between $t = 0.0012$ m and $t = 0.0015$ m. For the perforated pipes, a homogeneous structure having equivalent macroscopic physical properties is applied. The spotwelds used to join the steel walls of the muffler are modelled by the rigid body elements (rbe2), while the additional masses applied due to the attached sensors are accounted for by the concentrated mass element connections (conm2) applied at the discrete measurement positions. The FE calculations are carried out by a standard FE software package *MSC.Nastran* (MSC Software Corporation, 2008) on a 2.26 GHz dual-core *Intel*-based computer using 4 Gbyte RAM and running the *Windows Vista 64-bit* operating system.
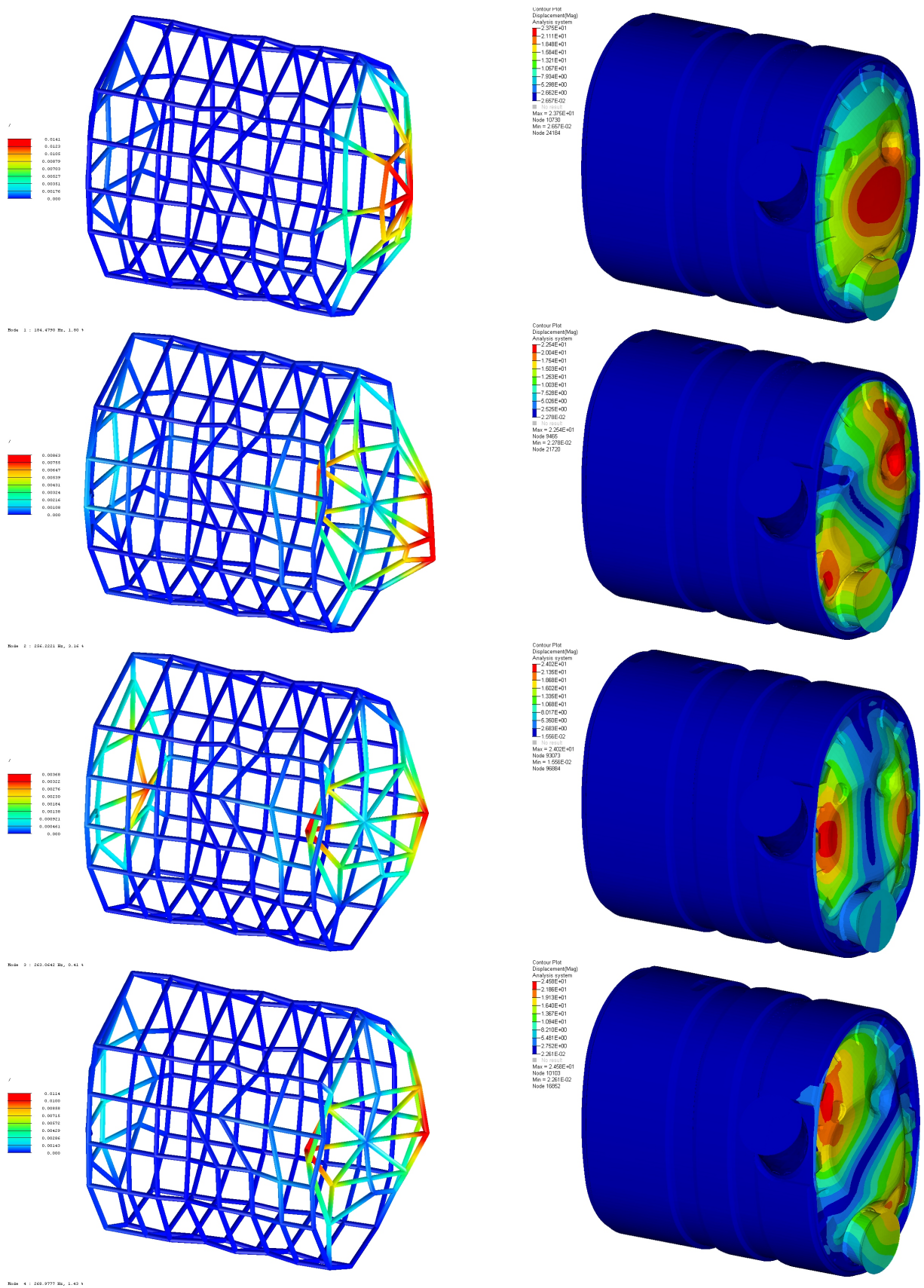
Figure 7.12: Truck exhaust muffler: shapes of the first four mode pairs – experimental measurement (left) and FE analysis (right) (Rejlek et al., 2011)

First, an FE modal analysis is carried out up to 1 600 Hz, and the predicted mode shapes are compared with their experimentally captured counterparts. Figure 7.12 shows the shapes of the first four mode pairs. Although the order of modes shapes is somewhat shuffled, the FE model is able to capture the first four modes of the structure fairly accurately. For this reason, the modal assurance criterion comparison shows some off-diagonal terms, see figure 7.13, even though the MAC-values themselves for the selected modes are relatively high. As such, the experimental measurement data is used for the correlation of the FE model.
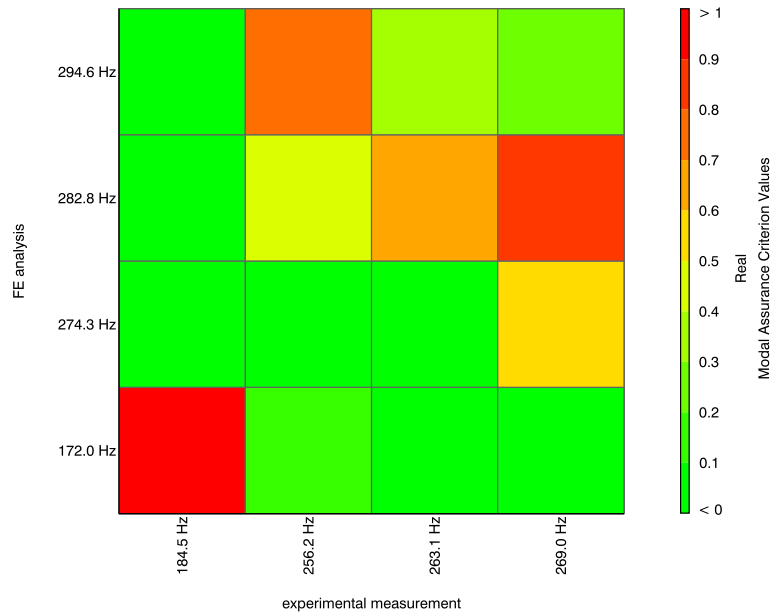
Figure 7.13: Truck exhaust muffler: modal assurance criterion for the first four calculated modes (Rejlek et al., 2011)

Next, the predicted modal base is used for a frequency response analysis up to 1 000 Hz, which adopts the modal superposition approach. The structure is excited by a point force $F = 1$ N applied in a positive y direction at the position $\mathbf{r}_F = (0.107, 0, 0.721)$ m, see figure 7.11(b). For the evaluation of the structural frequency response functions, two response points are selected $\mathrm{RP1} = (0.106, 0, 0.613)$ m and $\mathrm{RP2} = (-0.229, 0.429, 0.58)$ m. Figures 7.14 and 7.15 show the comparison of the predicted and measured structural response functions (a/F) up to 1 000 Hz. The FE predictions show, that the first structural modes are captured fairly good. However from a frequency of roughly 250 Hz onwards, the FE transfer functions start to deteriorate, where they mostly remain within the 10 dB tolerance range compared to experimental measurements. The reason for this is the high damping of the structure due to the adopted double-wall arrangement and the e-glass damping layers applied in between. As a result, the vibrational behaviour becomes highly localised. This can be observed in figure 7.14, which captures response at the position RP1 located close to the excitation point. The first mode with the eigenfrequency of 172 Hz has very localised behaviour and is thus less pronounced at the point RP2, see figure 7.15, which is located at a more distant position from the excitation point. Nevertheless, the global dynamic behaviour of the analysed structure is captured with an acceptable accuracy. Finally, the velocity field predicted at the outer surface of the muffler is applied as a boundary condition on the acoustic WB model.
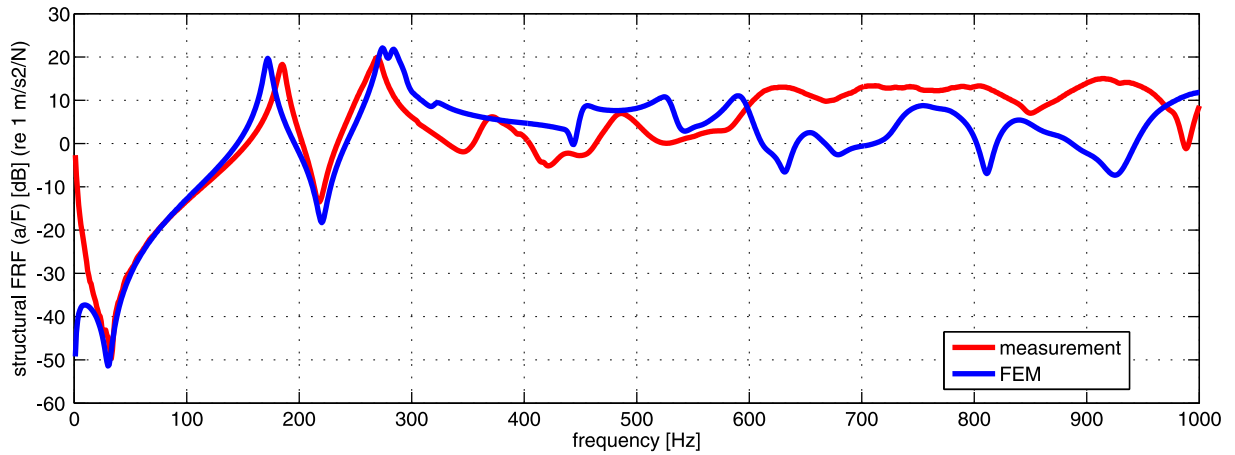
Figure 7.14: Truck exhaust muffler: structural frequency response functions at point RP1 (Rejlek et al., 2011)
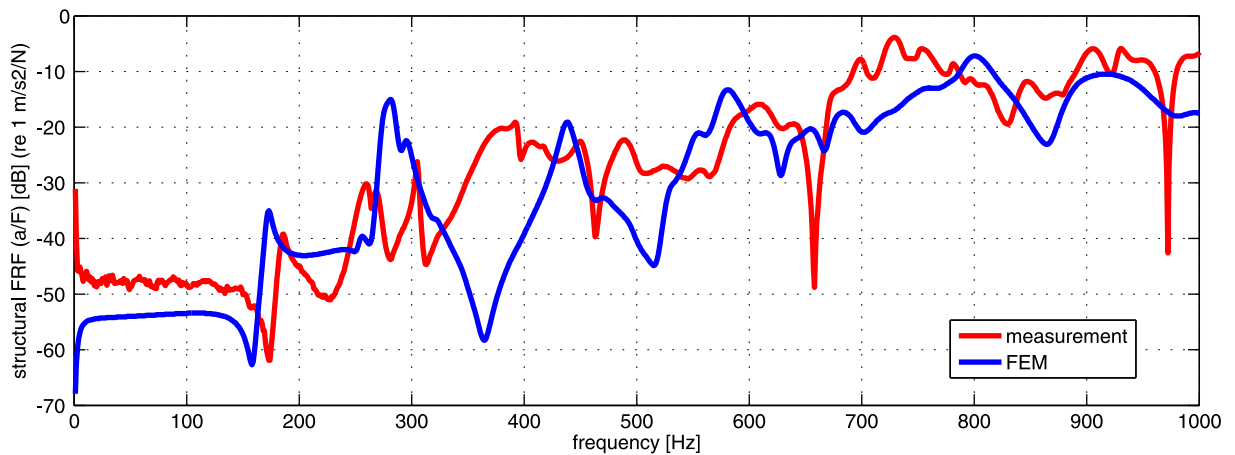
Figure 7.15: Truck exhaust muffler: structural frequency response functions at point RP2 (Rejlek et al., 2011)

7.4.3 Acoustic part

The muffler is surrounded by air having the speed of sound $c = 343.8$ m/s and mass density $\rho_a = 1.2$ kg/m^3 and is located 0.3 m above the rigid ground plane, which corresponds to its position in a real truck. As a baseline approach, a one-way-coupled FE–BE model is built up in a commercial CAE system *LMS Virtual.Lab* running the *LMS/SYSNOISE* Rev. 5.6 solver (LMS International, 2010), see figure 7.16(a). It consists of the structural velocity field predicted by the FE model and the acoustic indirect BE model. The structural FE part consists of 103 639 nodes forming 221 030 linear shell and solid elements with a maximum element edge size of $h_{max,s} = 0.01$ m. For the acoustic part, the initial rather fine FE mesh is coarsened, which yields a simplified BE wrap mesh consisting of 9 664 nodes forming 9 657 linear quad4 elements with a maximum element edge size of $h_{max,a} = 0.015$ m. As the two computational meshes are incompatible, a geometrical mapping technique is applied to couple the FE and BE models along the structural-acoustic interface. Since a semi-infinite problem is considered, a symmetry plane located at $z = 0$ is introduced in the BE model to account for the effect of an infinite rigid plane.
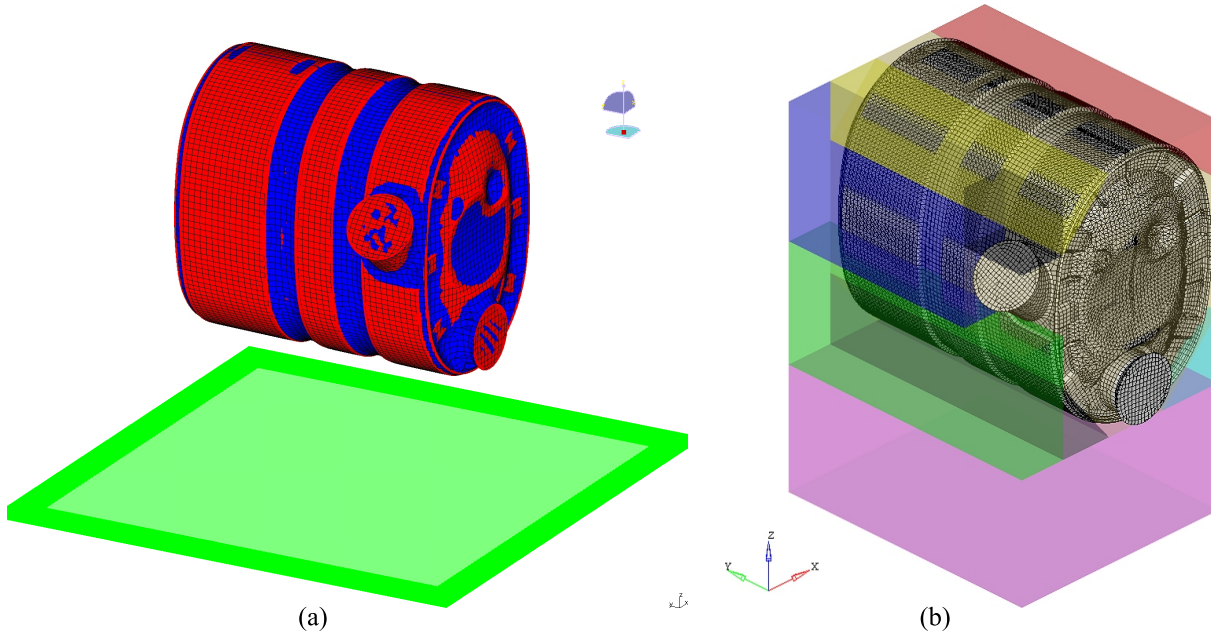
Figure 7.16: Truck exhaust muffler: (a) the BEM indirect model – the structural FE mesh in red, the simplified BE wrap mesh in blue, and the symmetry plane in green; and (b) a detailed view of the wave model partitioning into convex subdomains inside the fictitious rectangular box (Rejlek et al., 2011)

Since the physical boundary of the acoustic problem constitutes a closed body, the so-called non-uniqueness problem may occur, see section 3.2. This phenomenon is purely related to the mathematical formulation of BEM, which may result in a non-uniqueness of the solution at certain critical frequencies. As a consequence, the solution becomes numerically polluted at these critical frequencies. In order to overcome this problem, an additional impedance boundary condition has to be prescribed at the inner side of the acoustic boundary in order to damp those fictitious resonances. As a rule of thumb, D'Amico (2009) proposed a value of $Z = -\rho_a c$ to be used in order to efficiently mitigate the cavity resonances. Nevertheless, those additional treatments invoke the assembly the impedance matrix, which is, however, computationally highly demanding part of the overall BE solution procedure and therefore compromises the computational efficiency of BEM for the undamped case.

The very first BE model did not take this phenomenon into account, which yielded a strongly polluted solution with spurious peaks in the frequency response. In the next model, the $Z = -\rho_a c$ impedance has been imposed at the whole inner side of the muffler. However, the slow down due to the additional computational effort required to assemble the impedance matrix in order of magnitudes compromised the BE solution. Finally, a pragmatic approach was adopted, which consisted of the application of the impedance at roughly 18.5 % of the inner surface, which yields very good results with a still reasonable computational load.

As a next step, the acoustic wave model of the surrounding fluid domain is assembled by adopting the following modeling strategy (Rejlek et al., 2012). First, the radiating structure is virtually accommodated inside a fictitious rectangular box, and the fluid confined is disretised into convex acoustic subdomains, see figure 7.16(b). Please note that the figure 7.16(b) only shows a part of the whole acoustic WB model – on top of the fictitious rectangular box, 5 spherical acoustic subdomains are created at the solver level and thus do not have to be explicitly mod-

elled by the user. The outer surfaces of these 5 subdomains constitute the artificial truncation boundary Γ_T. Beyond this boundary, the solution expansion (5.26) approximates the pressure field in the semi-infinite acoustic domain. The resulting wave model consists of 13 bounded subdomains and one semi-infinite acoustic subdomain and adopts the MLV mapping strategy to couple the structural and acoustic fields in a weak manner.

The MLV allows a standard FE code to be adopted for the analysis of the structural part of the vibro-acoustic problem. In this particular case, the commercially available FE package *MSC.Nastran* was used for the uncoupled structural calculation. The so-called *Nastran* punch file is used as an interface format for the exchange of the velocity data, which implies that quite a substantial amount of data needs to be transferred between the FEM and WBT. To alleviate the manipulation of the huge result files and thereby increase the computational efficiency, only the outer surface of the vibrating structure needs to be exchanged between the FEM and WBT. This reduces the amount of data to be transferred to almost one fifth of its original size.

(a)   (b)
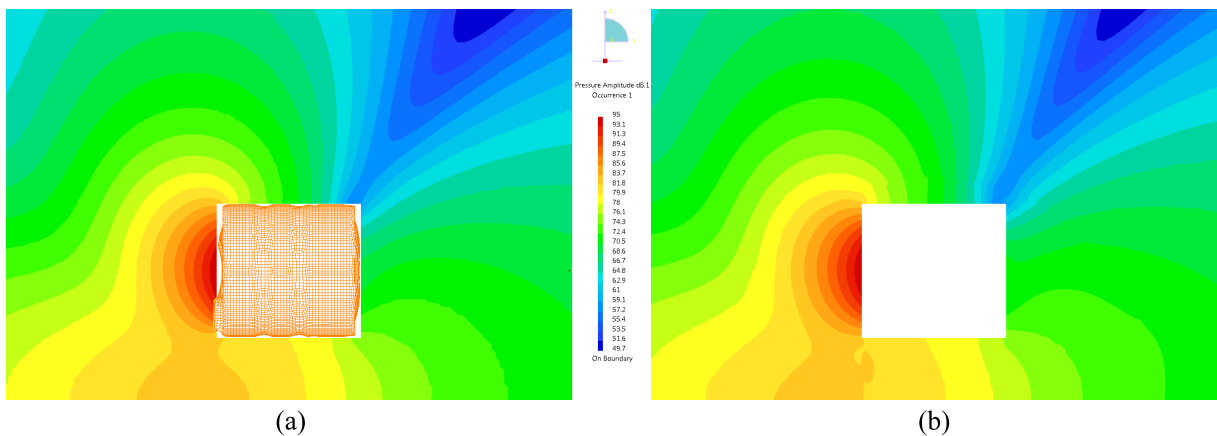
Figure 7.17: Truck exhaust muffler: sound pressure level in [dB] (re $2 \cdot 10^{-5}$ Pa) at 172 Hz predicted by (a) FEM–BEM (with BE mesh plotted in orange) and (b) FEM–WBT (Rejlek et al., 2011)

(a)   (b)
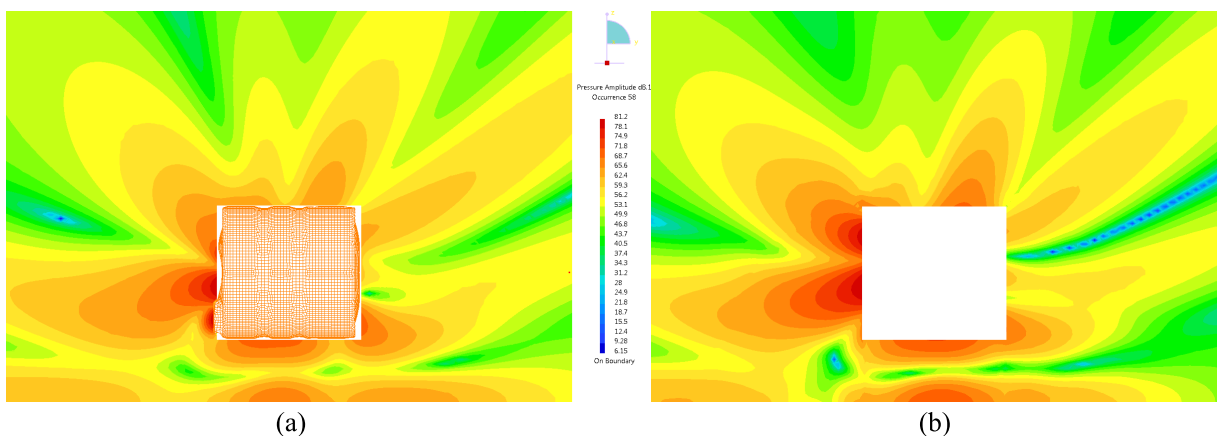
Figure 7.18: Truck exhaust muffler: sound pressure level in [dB] (re $2 \cdot 10^{-5}$ Pa) at 726 Hz predicted by (a) FEM–BEM (with BE mesh plotted in orange) and (b) FEM–WBT (Rejlek et al., 2011)

Figure 7.17 shows the sound radiation pattern predicted by the BEM and WBT at a frequency of 172 Hz, which corresponds to the first structural eigenfrequency. Similarly, figure 7.18 shows the radiated pressure fields at 726 Hz, which is driven by the shape of the structural mode number 51 with the eigenfrequency of 727.4 Hz. The two figures show a very good match at the two different frequencies.
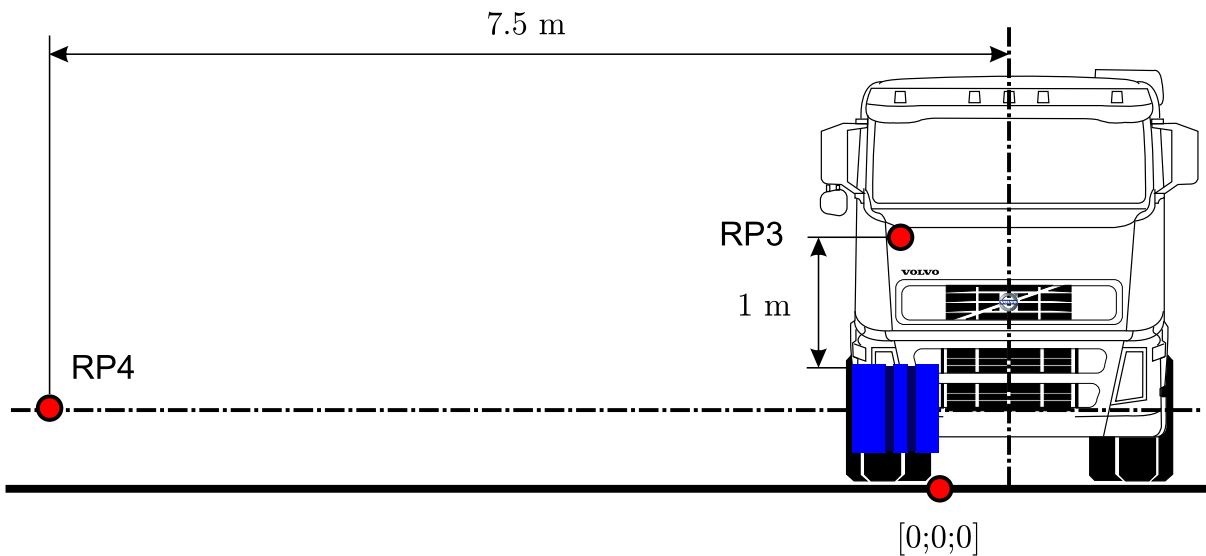
Figure 7.19: Truck exhaust muffler: definition of acoustic response points (Rejlek et al., 2011)

<div align="center">(a)   (b)</div>

Figure 7.20: Truck exhaust muffler: (a) experimental set up in a semi-anechoic chamber, and (b) close-up of an impact hammer excitation (images courtesy of *Institut für Kraftfahrzeuge, RWTH Aachen University*) (Rejlek et al., 2012)

For the acoustic frequency response analyses, two response points are selected, see figure 7.19. The first point is located at position RP3 = (0, 0.283, 1.925) m one meter above the muffler and corresponds to a reference microphone positioned one meter away. The second one has a position of RP4 = (0, 6.862, 0.614) m and represents the reference microphone used during the pass-by noise measurements.

The numerical validation study is complemented by the experimental measurement campaign carried out in a semi-anechoic chamber, see figure 7.20. The muffler is suspended from the ceiling by the flexible lightweight cords and the structure is excited in the direction normal to the surface by the impulse hammer equipped with a force cell. The radiated sound is measured by pressure microphones located in the positions indicated in figure 7.19.

Figures 7.21 and 7.22 plot the acoustic frequency response functions (p/F) up to 1000 Hz determined at point RP3 (reference 1 m microphone) and RP4 (reference pass-by noise microphone) by the two computational techniques (BE in red, WBT in blue) and compared with the experimental data (black). Tables 7.3 and 7.4 list the detailed attributes of the numerical models involved. Except for the low frequency range up to approximately 100 Hz, the two predicted results match the experimental data fairly well. The deterioration of the measurement data in the very low frequency range is clearly related to rather poor coherence, see figure 7.23, which is related to an insufficient excitation of the structure due to the high damping.

attribute	denotation	value	
		structural	acoustic
solution scheme		FEM modal	BEM indirect variational
number of nodes	#nod	103 639	9 664
number of elements	#ele	221 030	9 657
mesh topology	topo	tria3, quad4, hexa8, tetra4, penta6	quad4
maximum element edge size	h_{max}	0.01 m	0.015 m
degrees of freedom	DOF	nodal: 469 323 modal[2]: 9 144	9 664
FRF range	f_{min}, f_{max}	1–1 000 Hz	
FRF step	Δf	1 Hz	
number of modes up to f_{max}	#mod	120[3]	–
CPU time needed for FRF	t_{FRF}	13 558 s	$\sim 500\,000$ s

Table 7.3: Truck exhaust muffler: attributes of the FE–BE model

In contrast to the FE–BE model, which uses invariant computational meshes over the frequency and thus involves a constant number of degrees of freedom, the WB model adopts a frequency-dependent strategy for the truncation of the wave function set with the parameter $T = 2$. For the semi-infinite domain, $L = 20$ is applied for the truncation of the pressure expansion over the frequency range of interest. As a consequence, the wave based prediction requires only one tenth of the total solution time of the BE calculation on an identical computer platform. In addition to that, the WBT solution time includes the efforts spent on reading the huge structural

---

[2]Modal superposition technique adopted.
[3]Non-rigid body modes.
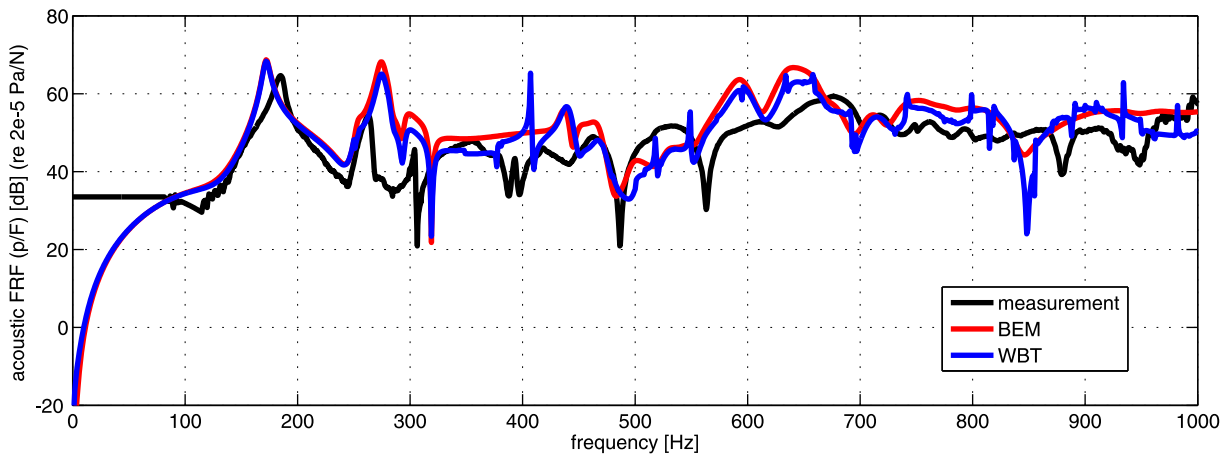
Figure 7.21: Truck exhaust muffler: acoustic frequency response functions at point RP3 (Rejlek et al., 2011)
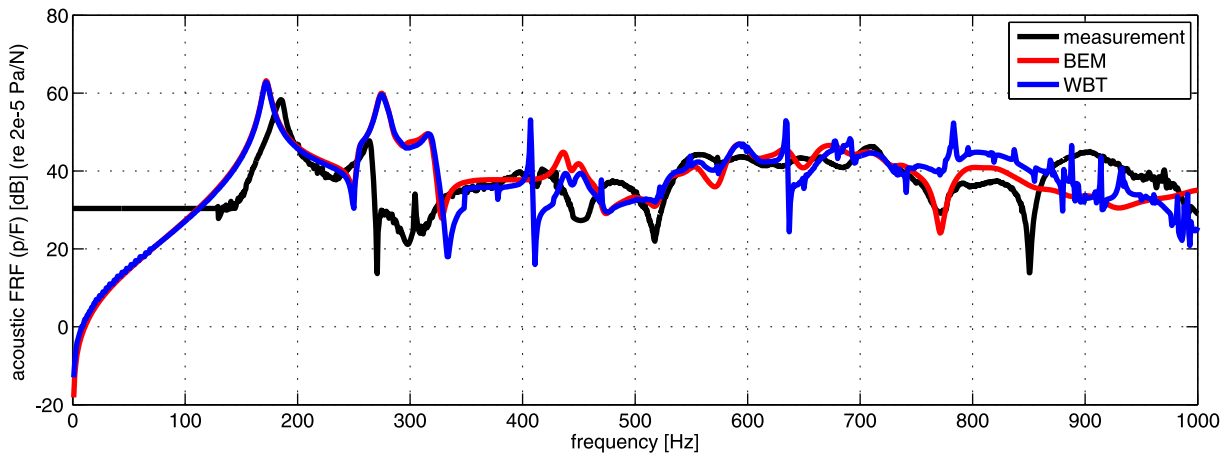
Figure 7.22: Truck exhaust muffler: acoustic frequency response functions at point RP4 (Rejlek et al., 2011)
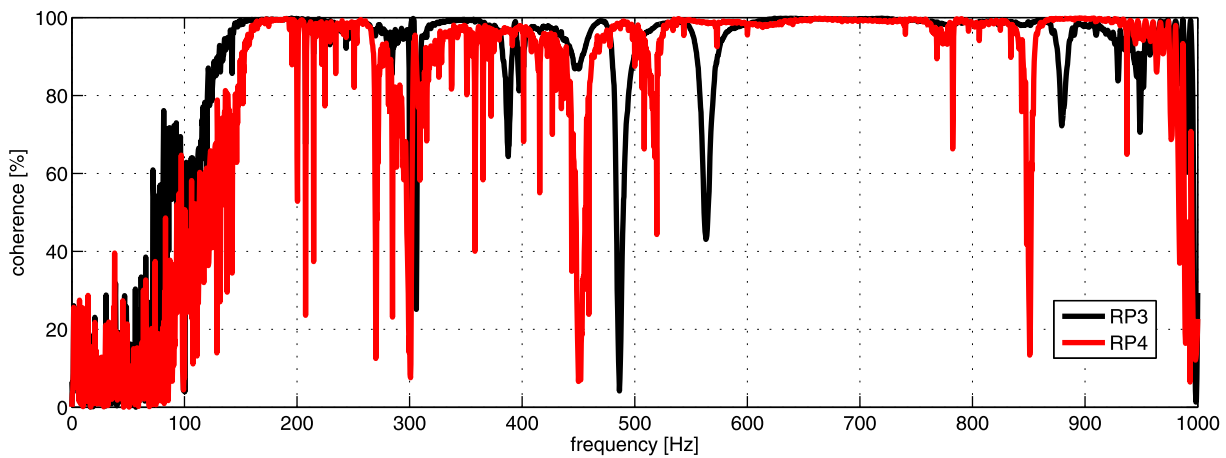
Figure 7.23: Truck exhaust muffler: coherence of the structure-borne noise measurements (Rejlek et al., 2011)

attribute	denotation	value	
		structural	acoustic
solution scheme		FEM modal	WBT
number of nodes	#nod	103 639	–
number of elements	#ele	221 030	–
mesh topology	topo	tria3, quad4, hexa8, tetra4, penta6	–
maximum element edge size	h_{max}	0.01 m	–
number of subdomains	N_a	–	13 bounded
	N_{si}	–	1 semi-infinite
truncation strategy		–	frequency-dependent
truncation parameter	T	–	2
	L		20
radius of truncation hemisphere	R	–	1.05 m
degrees of freedom	DOF	nodal: 469 323 modal: 9 144	2431–2 563
FRF range	f_{min}, f_{max}	1–1 000 Hz	
FRF step	Δf	1 Hz	
number of modes up to f_{max}	#mod	120	–
CPU time needed for FRF	t_{FRF}	13 558 s	50 791 s

Table 7.4: Truck exhaust muffler: attributes of the FE–WB model

velocity file, which is, however, not the case with BEM. When comparing WBT to BEM, the WB predictions match the BE results accurately up to a frequency of 300 Hz for both response points (RP3 and RP4). At higher frequencies, the WB predictions start to deteriorate, which is however related to a relatively low order of the pressure expansion used in the semi-infinite domain.

7.5 Summary

This chapter described the application of the wave based approach for the analysis of one-way-coupled, unbounded vibro-acoustic problems. The WBT was applied to two industry-sized problems, in which it proved its suitability for tackling real-life engineering problems. It adopts a geometrical mapping technique (MLV) to weakly couple a structural finite element model with an unbounded acoustic WB counterpart. In this respect, the WBT overcomes the biggest inherent limitation concerning its applicability to problems exhibiting geometrically complex boundaries.

The first validation example considered a free-field noise radiation analysis of a car engine block–gearbox assembly. The standard *MSC.Nastran* FE solver was utilised to carry out the structural dynamic analysis. The calculated velocity field was then mapped onto the acoustic wave based model using the MLV. The resulting WB results were compared with a baseline BEM approach considered in the validation study. Across the whole frequency range of interest, the WBT achieved almost the same prediction accuracy as BEM, however, with a substantially lower computational load.

The second example presented the application of WBT for a noise radiation analysis involving a semi-infinite acoustic problem. The truck exhaust muffler was selected as a representative test case to assess the performance of the wave based approach in the mid-frequency range. In addition to a numerical validation study based on the finite and boundary element methods, experimental measurement campaigns were also carried out. The experimental testing included both the structural correlation and the noise radiation measurements in a semi-anechoic chamber. Although the muffler was initially considered to be an engineering problem that is relatively easy to model, it turned out that the validation with the experimental data was quite challenging. One reason for this is its fairly complex interior and the joining technique used to connect the large number of inner components made of different materials. As the muffler was analysed in a non-destructive way, the only available data for the definition of an FE model was the supplied CAD data. However, the uncertainty in a proper definition of the boundary conditions may be the reason for the differences, in particular in the higher frequency range. Another reason is a relatively high damping of the whole structure due to the applied e-glass layers. In this way, the structural measurements might become less precise, since one cannot efficiently excite the structure on its outer surface, which is highly damped due to the double-wall design strategy. The vibrational behaviour thus becomes highly localised. Once the structural FE model had been correlated with the test data, the predicted FE velocity field was mapped onto acoustic BE and WB models, which were then employed for the acoustic response analysis. For the problem considered, the utilised baseline BE model becomes prohibitively large and involves a huge computational burden. The WBT, on the other hand, achieves a comparable prediction accuracy with a significantly lower computational effort, when run on an identical computational platform.

Part III

CONCLUSIONS

Chapter 8

General conclusions and future developments

This chapter gives a summary of the main results achieved within the scope of this doctoral research project and provides some recommendations for future research on this topic.

8.1 Main contributions and conclusions

This dissertation further develops a novel prediction technique for numerical mid-frequency modelling of unbounded vibro-acoustic problems. The topic of this research is the wave based technique, which is a promising deterministic scheme that aims to relax the common limitations of conventional state-of-the-art methods for mid-frequency modelling. Desmet (1998) introduced the WBT for analysis of three-dimensional, steady-state, vibro-acoustic problems. He proposed the basic concepts of this technique by selecting the appropriate sets of basis functions for both the structural and acoustic problems, which ensure the high convergence rate of this method. His work was further extended by Van Hal (2004), who incorporated new types of multi-physical coupling effects and formulated some guidelines considering an efficient wave based modelling. Pluymers (2006) proposed the concept of a truncation geometry, which allows the analysis of two-dimensional acoustic problems involving unbounded spatial domains. In addition, he applied a modification of the solution scheme for tackling 2D semi-infinite problems, in which the rigid baffle plane is introduced implicitly. In this respect, the presented dissertation continues the work initiated by these authors and focuses on the following two main objectives.

- The novel formulation and development of the WBT for a steady-state analysis of fully coupled, three-dimensional, unbounded vibro-acoustic problems including problems involving semi-infinite acoustic domains.

- Extensding of the applicability of the WBT towards industrial one-way-coupled three-dimensional, unbounded vibro-acoustic problems, which utilise a geometrical mapping strategy to couple the structural FE and acoustic WB model.

Based on the findings obtained in the course of this research project, the following general conclusions can be drawn.

- Inherently, the size of the WB models is substantially smaller than the corresponding element-based counterparts, which has a favourable effect on the computational efficiency of WBT. For all of the uncoupled and coupled vibro-acoustic problems presented in the framework of this dissertation, the WBT outperforms the baseline FE and/or BE models in terms of both the solving time and the memory requirements, while achieving a comparable level of prediction accuracy on the same computational platform. Additionally, the convergence analyses performed on selected validation examples prove the convergence rate of WBT to be substantially higher compared to conventional deterministic methods.

- The WBT solution does not suffer from the dispersion error, which is an inherent characteristic of FEM and BEM. At higher frequencies, the wave models, which are significantly smaller (in terms of degrees of freedom) than theei element-based counterparts, yield more accurate predictions of response spectra.

- The efficiency of the wave based approach strongly depends on the geometrical complexity of the problem. The assembly of the wave model involves a numerical integration of the basis functions and their spatial derivatives, which is, however, the most time-consuming step in the whole WBT solution procedure. In order to maintain the computational efficiency of WBT, the number of integration surfaces has to kept adequately low, which also implies that the problem must be moderately sized.

8.1.1   WBT formulation of thin plate bending problems

In order to comply with the first objective of this doctoral research, the WBT was first implemented and applied for the analysis of plate bending motion according to Kirchhoff thin plate theory. This class of problems constitutes a necessary basis for a further extensions towards fully coupled vibro-acoustic systems. The proposed approach is generalised by considering the multi-domain strategy for tackling general non-convex problems. Different validation examples proved that the wave based technique provides a faster prediction, while maintaining the same level of accuracy as the finite element method. Nevertheless, since only flat structures are admissible for a description according to Kirchhoff thin plate theory, the applicability of the proposed methodology remains restricted to simple plates.

8.1.2   WBT for three-dimensional semi-infinite acoustic problems

This research was a continuation of the work initiated by Diwoky et al. (2008) on the application of WBT for three-dimensional free-field acoustic problems. By using some properties of the solution expansion, which was originally proposed by Jegorovs (2007) for the pressure approximation in the unbounded domain, the solution scheme was adapted for the analysis of baffled semi-infinite problems. The formulation was implemented and validated by various test cases. All of the presented validation examples proved, that the WBT outperforms the conventional techniques, such as the coupled FE–BE approach. Validation examples for which an analytical solution exists also demonstrated the favourable convergence rate of this method.

8.1.3 Fully coupled, unbounded vibro-acoustic wave model

In the initial stage of this research project, the WBT was implemented and successfully validated for the analysis of uncoupled thin plate bending and unbounded acoustic problems. Both uncoupled problems demonstrated the increased computational efficiency of the proposed wave based modelling approach over state-of-the-art techniques. By synthesising the formulations of the thin plate bending and the unbounded acoustic problems, a general fully coupled unbounded vibro-acoustic wave model was introduced.

First, the coupled structural-acoustic formulation of WBT was implemented and tested by means of an interior acoustic problem. This involved some additional indirect multi-physical coupling effects which needed to be accounted for. Once the formulation had been validated, the problem was explicitly extended by the unbounded acoustic domain. Various validation examples involving both the free-field and semi-infinite spatial domains were considered in the validation study. These examples demonstrated the enhanced computational efficiency of WBT compared to baseline techniques.

In the final example, the WBT was applied for the coupled analysis of a so-called distributed mode loadspeaker (DML). Using the proposed wave based formulation to tackle the fully coupled problems, a comparative study was conducted that investigated the directional characteristics of a conventional speaker and the novel DML speaker.

8.1.4 WBT for one-way-coupled vibro-acoustic problems

The inherent restriction of WBT with respect to its limited capability for tackling problems involving geometrically complex boundaries was alleviated by adopting a coupled FE–WB scheme. In this approach, the structural part of the one-way-coupled vibro-acoustic problem is tackled by a standard FE package, whereas the acoustic fluid domain is analysed by WBT. The concept of geometrical mapping between the structural FE and acoustic WB model, which was originally introduced by Hepberger et al. (2004) for a weak-coupled analysis of interior vibro-acoustic problems, was further extended for problems involving unbounded acoustic domains. Thereafter, the MLV coupling algorithm was utilised for an industrial application of WBT to real-life engineering problems.

First, the WBT was applied to a free-field noise radiation analysis of a powertrain unit consisting of four cylinder car engine with gearbox. The wave based approach is validated in a numerical manner utilising a state-of-the-art method. Compared with the baseline BE approach, the WBT achieved higher computational efficiency on an identical computational platform.

The second example considered a study of the structure-borne noise radiation of a truck exhaust muffler involving a semi-infinite acoustic domain. A truck exhaust muffler was selected as a representative test case to assess the performance of the wave based approach in the mid-frequency range. Extensive experimental measurement campaign complemented the numerical validation work based on BEM. The structural response was analysed by means of an FE model, which was correlated by the experimental test data. By employing the MLV strategy, the predicted structural FE results were projected onto the WB model and compared with the measurements carried out in a semi-anechoic chamber. When comparing the two computational methods in the frequency range considered, the WBT clearly outperformed the baseline BE model, which already involved a huge computational burden. The WBT, in contrast, achieved a prediction accuracy comparable to BEM. In this way, the WBT showed its practical applicability to cope

with industrial problems and demonstrated its enhanced computational efficiency compared to state-of-the-art techniques.

The solving time gained due to the increased computational efficiency is, however, partially offset by the higher preprocessing efforts spent on WB modelling. However, since the concept of the coupled FE–WB approach adopts a similar modelling strategy as that commonly applied in the conventional FE–BE models, the only additional preprocessing time is involved in the assembly of the acoustic wave model, which has not been fully automated yet.

8.2   Recommendations for further developments

- The formulation of WBT for the analysis of plate bending problems adopts the Kirchhoff thin plate theory. However, the Reissner-Mindlin thick plate model provides a more generic concept by accounting for the effects of both the shear stresses and the rotatory inertia. Implementation of WBT for the Reisner-Mindlin plate model and extension of its formulation towards single and double curved shells and general 3D solid problems will further extend the application field of this method. Nevertheless, since WBT, as any other indirect Trefftz approach, relies on exact solutions of the governing equation, the future research should focus on definition of complete function sets, which allow a fast convergence of the method.

- Except for the one-way-coupled FE–WB approach, the current implementation of WBT is written in *MATLAB*, mainly due to the availability of the commonly used routines and the general flexibility of this open platform. However, since *MATLAB* cannot be considered a high-performance programming language, the superior computational efficiency of WBT has not yet been fully exploited. Implementation of the code in a high-performance programming language, such as *Fortran* or *C++*, would further increase the computational efficiency of WBT. Since the existing *MATLAB*-based implementation already routinely achieves comparable or even shorter solution times than conventional baseline methods which employ high-end solvers, there remains a huge potential for the further enhancement of the computational efficiency of the WBT.

- At present, the wave model preprocessing still relies mainly on the user's knowledge and has to be performed manually. For some cases, such as the application of WBT for one-way-coupled problems, the model assembly process is facilitated to a certain extent by employing a standard FE preprocessor. However, to reach an industrial level of maturity, a semi- or fully automated preprocessing has to be established.

- In order to allow the application of WBT on real-life engineering problems, poroelastic materials must be included into WB solution scheme. The first formulations of WBT for tackling the poroelastic domains based on Biot material model have shown the potential. Research on this topic is currently ongoing (Deckers et al., 2012).

- Currently, the dynamic selection of the appropriate number of basis functions is based on a frequency-dependent rule of thumb. However, a more sophisticated a priori estimator (e.g. by adopting a residual error-controlled adaptive strategy), would provide a more robust and efficient self-adaptive wave based scheme.

- In terms of the application of WBT for one-way-coupled problems which adopt the MLV mapping strategy, future research will focus on the enhancement of the coupling compatibility. In this way, the wave based method can be coupled with an experimentally acquired data and/or fully resolved powertrain simulation results based on a hybrid multi body/finite element time-domain analysis, which would incorporate the actual engine dynamics. Future research will also address the automation of the MLV approach. For the particular case of strongly incompatible computational meshes, the robustness of the proposed technique needs to be further investigated.

- Future research should also address accurate acoustic source modelling and possibly account for the effects of uncertainty and variability in the numerical vibro-acoustic analysis. By including non-determinism into the wave models in either parametric or non-parametric way, the WB prediction can be enhanced for the analysis of physical phenomena that are not completely known in a deterministic sense. This would allow a numerical analysis of uncertain and variable processes, which provides information on ranges of possible system behaviour rather than unique predictions.

References

Allard, J. F. and Atalla, N. (**2009**). *Propagation of Sound in Porous Media: Modelling Sound Absorbing Materials, Second Edition*. John Wiley & Sons, Ltd. ISBN 978-0-470-746615-0.

Astley, R. J. (**2000**). Infinite elements for wave problems: a review of current formulations and an assessment of accuracy. *International Journal for Numerical Methods in Engineering*, **49**(7):951–976. ISSN 1097–0207. doi:10.1002/1097-0207(20001110)49:7<951::AID-NME989>3.0.CO;2-T.

Astley, R. J., Macaulay, G. J. and Coyette, J. P. (**1994**). Mapped Wave Envelope Elements for Acoustical Radiation and Scattering. *Journal of Sound and Vibration*, **170**(1):97–118. ISSN 0022-460X. doi:10.1006/jsvi.1994.1048.

Atalla, N. and Bernhard, R. (**1994**). Review of numerical solutions for low-frequency structural-acoustic problems. *Applied Acoustics*, **43**(3):271–294. ISSN 0003-682X. doi:10.1016/0003-682X(94)90050-7.

Atalla, N., Panneton, R. and Debergue, P. (**1998**). A mixed displacement-pressure formulation for poroelastic materials. *Journal of the Acoustical Society of America*, **104 (3)**:1444–1452.

Azima, H. (**1998**). NXT Technology – When a Little Chaos is Good For You. *Audio Magazine*.

Azima, H. and Mapp, P. (**1998**). Diffuse-Field Distributed-Mode Radiators and Their Associated Early Reflections. In *Audio Engineering Society Convention 104*. URL http://www.aes.org/e-lib/browse.cfm?elib=8421.

Babuška, I., Ihlenburg, F., Paik, E. T. and Sauter, S. A. (**1995**). A Generalized Finite Element Method for solving the Helmholtz equation in two dimensions with minimal pollution. *Computer Methods in Applied Mechanics and Engineering*, **128**(3–4):325–359. ISSN 0045-7825. doi:10.1016/0045-7825(95)00890-X.

Berenger, J.-P. (**1994**). A Perfectly Matched Layer for the Absorption of Electromagnetic Waves. *Journal of Computational Physics*, **114**(2):185–200. ISSN 0021-9991. doi:10.1006/jcph.1994.1159.

Berenger, J.-P. (**1996**). Three-Dimensional Perfectly Matched Layer for the Absorption of Electromagnetic Waves. *Journal of Computational Physics*, **127**(2):363–379. ISSN 0021-9991. doi:10.1006/jcph.1996.0181.

Bergen, B. (**2011**). *Wave based modelling techniques for unbounded acoustic problems*. Ph.D. thesis, Katholieke Universiteit Leuven, division PMA, 2011D07. ISBN 978-94-6018-392-8.

Bettess, P. (**1992**). *Infinite Elements*. Penshaw Press. ISBN 0-9518806-0-8.

Biot, M. A. (**1956**). Theory of the Propagation of Elastic Waves in a Fluid-Saturated Porous Solid. I. Low frequency range. II. Higher frequency range. *Journal of the Acoustical Society of America*, **28**(2):168–191.

CALM network (**2004**). Research for a Quieter Europe in 2020 – An Updated Strategy Paper of the CALM Network – Oct. 2004. European Commission Research Directorate-General. ISBN 3-200-00224-7.

Clough, R. W. and Wilson, E. L. (**1999**). Early Finite Element Research at Berkeley. *Fifth U.S. National Conference on Computational Mechanics, August 4-6*.

Collino, F. and Monk, P. B. (**1998**). Optimizing the perfectly matched layer. *Computer Methods in Applied Mechanics and Engineering*, **164**(1–2):157–171. ISSN 0045-7825. doi:10.1016/S0045-7825(98)00052-8.

Cremer, L., Heckl, M. and Petersson, B. A. T. (**2005**). *Structure-Borne Sound: Structural Vibrations and Sound Radiation at Audio Frequencies (3rd edition)*. Springer-Verlag Berlin Heidelberg. ISBN 9783540226963.

D'Amico, R. (**2009**). *Fast Multipole Boundary Element Formulation for the Vibro-Acoustic Analysis of the Automotive and Railway Structures*. Master's thesis, Università degli Studi di Firenze.

Deckers, E., Hörlin, N.-E., Vandepitte, D. and Desmet, W. (**2012**). A Wave Based Method for the efficient solution of the 2D poroelastic Biot equations. *Computer Methods in Applied Mechanics and Engineering*, **201–204**:245–262. ISSN 0045-7825. doi:10.1016/j.cma.2011.09.015.

Deckers, E., Van Genechten, B., Vandepitte, D. and Desmet, W. (**2010**). Efficient treatment of stress singularities in poroelastic wave based models using special purpose enrichment functions. *Computers & Structures*. ISSN 00457949. doi:10.1016/j.compstruc.2010.11.012.

Desmet, W. (**1998**). *A wave based prediction technique for coupled vibro-acoustic analysis*. Ph.D. thesis, Katholieke Universiteit Leuven, division PMA, 98D12. ISBN 90-5682-151-2.

Desmet, W., Van Hal, B., Sas, P. and Vandepitte, D. (**2002**). A computationally efficient prediction technique for the steady-state dynamic analysis of coupled vibro-acoustic systems. *Advances in Engineering Software*, **33**:527–540.

Diwoky, F., Hepberger, A., Mócsai, T., Pramberger, H. and Priebsch, H.-H. (**2008**). Application of the Wave Based Method to 3D radiation problems. In *proceedings of the 5th International Workshop on Trefftz Methods (Trefftz.08), March 31–April 2, Leuven, Belgium*, pages 157–166.

Donders, S. (**2008**). *Computer-Aided Engineering Methodologies for Robust Automotive NVH Design*. Ph.D. thesis, Katholieke Universiteit Leuven, division PMA, 2008D02. ISBN 978-90-5682-882-0.

d'Udekem, D., Saitoh, M., den Nieuwenhof, B. V. and Yamamoto, T. (**2011**). Numerical Prediction of the Exhaust Noise Transmission to the Interior of a Trimmed Vehicle by Using the Finite/Infinite Element Method. In *proceedings of the SAE 2011 Noise and Vibration Conference and Exhibition, May 16–19, Grand Rapids, Michigan, USA*. doi:10.4271/2011-01-1710.

Duval, A., Baratier, J., Morgenstern, C., Dejaeger, L., Kobayashi, N. and Yamaoka, H. (**2008**). Trim FEM simulation of a dash and floor insulator cur out modules with structureborne and airborne excitations. In *proceedings of the Euronoise 2008, June 29–July 4, Paris, France*, pages 3777–3782.

European Commission (**1996**). Future Noise Policy, European Commission Green Paper, COM(96) 540 final. European Commission.

Fahy, F. (**2000**). *Sound and Structural Vibration: Radiation, Transmission and Response*. Academic Press. ISBN 0122476719.

Fischer, M., Gauger, U. and Gaul, L. (**2004**). A multipole Galerkin boundary element method for acoustics. *Engineering Analysis with Boundary Elements*, **28**(2):155–162. ISSN 0955-7997. doi:10.1016/j.enganabound.2003.07.001.

Gerdes, K. (**1998**a). A summary of Infinite Element formulations for exterior Helmholtz problems. *Computer Methods in Applied Mechanics and Engineering*, **164**(1–2):95–105. ISSN 0045-7825. doi:10.1016/S0045-7825(98)00048-6.

Gerdes, K. (**1998**b). The conjugated vs. the unconjugated infinite element method for the Helmholtz equation in exterior domains. *Computer Methods in Applied Mechanics and Engineering*, **152**(1–2):125–145. ISSN 0045-7825. doi:10.1016/S0045-7825(97)00186-2.

Givoli, D. and Cohen, D. (**1995**). Nonreflecting Boundary Conditions Based on Kirchhoff-Type Formulae. *Journal of Computational Physics*, **117**(1):102–113. ISSN 0021-9991. doi:10.1006/jcph.1995.1048.

Givoli, D., Neta, B. and Patlashenko, I. (**2003**). Finite element analysis of time-dependent semi-infinite wave-guides with high-order boundary treatment. *International Journal for Numerical Methods in Engineering*, **58**(13):1955–1983. ISSN 1097-0207. doi:10.1002/nme.842.

Gladwell, G. (**1965**). A finite element method for acoustics. In *proceedings of the Fifth International Congress of Acoustics, Liège, Belgium, Paper L33*, pages 1–4.

Greengard, L. and Rokhlin, V. (**1987**). A Fast Algorithm for Particle Simulations. *Journal of Computational Physics*, **135**(2):280–292. ISSN 0021-9991. doi:10.1006/jcph.1997.5706.

Grote, M. J. and Kirsch, C. (**2007**). Nonreflecting boundary condition for time-dependent multiple scattering. *Journal of Computational Physics*, **221**(1):41–62. ISSN 0021-9991. doi:10.1016/j.jcp.2006.06.007.

Guj, L., Courtois, T. and Bertolini, C. (**2011**). A FE Based Procedure for Optimal Design of Damping Package, with Presence of the Insulation Trim. In *proceedings of the SAE 2011 Noise and Vibration Conference and Exhibition, May 16–19, Grand Rapids, Michigan, USA*. doi:10.4271/2011-01-1693.

Harari, I. (**2006**). A survey of finite element methods for time-harmonic acoustics. *Computer Methods in Applied Mechanics and Engineering*, **195**(13–16):1594–1607. ISSN 0045-7825. doi:10.1016/j.cma.2005.05.030. A Tribute to Thomas J.R. Hughes on the Occasion of his 60th Birthday.

Harari, I., Patlashenko, I. and Givoli, D. (**1998**). Dirichlet-to-Neumann Maps for Unbounded Wave Guides. *Journal of Computational Physics*, **143**(1):200–223. ISSN 0021-9991. doi: 10.1006/jcph.1998.5960.

Harris, N. and Hawksford, M. O. (**1997**). The Distributed-Mode Loudspeaker (DML) as a Broad-Band Acoustic Radiator. In *Audio Engineering Society Convention 103*. URL http://www.aes.org/e-lib/browse.cfm?elib=7253.

Haug, E. (**1981**). Engineering safety analysis via destructive numerical experiments. *EU-ROMECH 121, Polish Academy of Sciences, Engineering Transactions*, **29(1)**:39–49.

Haug, E. (**2005**). Can you Crash Moore's Law ?! *Pam TALK*, **29**:20–21. ISSN 1635-866X.

Haug, E., Scharnhorst, T. and Du Bois, P. (**1986**). FEM-Crash, Berechnung eines Fahrzeugfrontalaufpralls. *VDI Berichte*, **613**:479–505.

Hepberger, A., Diwoky, F., Jalics, K. and Priebsch, H. (**2004**). Application of Wave Based Technique for a cavity considering forced excitation at boundaries and effects of absorption material. In *proceedings of International Conference on Noise and Vibration Engineering (ISMA2004), September 20–22, Leuven, Belgium*, pages 1501–1512.

ISO (**2007**). ISO 362-1:2007 Measurement of noise emitted by accelerating road vehicles – Engineering method – Part 1: M and N categories. International Organization for Standardization.

Jegorovs, J. (**2007**). *The Optimal Shape of the Reflex Tube of a Bass Loudspeaker*. Ph.D. thesis, Universität Kaiserslautern, D 386.

Jiroušek, J. and Leon, N. (**1977**). A powerful finite element for plate bending. *Computer Methods in Applied Mechanics and Engineering*, **12**(1):77–96. ISSN 0045-7825. doi:10.1016/0045-7825(77)90052-4.

Jiroušek, J. and Wroblewski, A. (**1995**). T-elements: a finite element approach with advantages of boundary solution methods. *Advances in Engineering Software*, **24**(1–3):71–88. ISSN 0965-9978. doi:10.1016/0965-9978(95)00060-7.

Jiroušek, J. and Zielinski, A. P. (**1997**). Survey of trefftz-type element formulations. *Computers & Structures*, **63**(2):225–242. ISSN 0045-7949. doi:10.1016/S0045-7949(96)00366-5.

Juhl, P. M. (**1993**). *The Boundary Element Method For Sound Field Calculations*. Ph.D. thesis, The Acoustics Laboratory, Technical University of Denmark.

Kirkup, S. (**1998**). *The Boundary Element Method in Acoustics (reprint 2007)*. Integrated Sound Software. ISBN 0-953-4031-06.

KU Leuven (**2007**). ISAAC 18 course: "Advanced Techniques in Applied and Numerical Acoustics", Lecture notes. Katholieke Universiteit Leuven, division PMA.

Lalor, N. and Priebsch, H.-H. (**2007**). The prediction of low- and mid-frequency internal road vehicle noise: A literature survey. In *proceedings of the Institution of Mechanical Engineers, Part D: Journal of Automobile Engineering*, volume 221, pages 245–269. doi: 10.1243/09544070JAUTO199.

Lanoye, R. (**2007**). *Assessment of the absorption performance of sound absorbing materials. Use of the Trefftz's method and of a new dual particle velocity-pressure sensor*. Ph.D. thesis, Katholieke Universiteit Leuven, afdeling bouwfysica akoestiek en thermische fysica, D/2007/7515/29. ISBN 978-90-5682-795-3.

Leissa, A. (**1993**). *Vibration of Plates*. Acoustical Society of America, Woodbury, NY. ISBN 978-1563962943.

LMS International (**2010**). *Virtual.Lab Acoustics, Rev. 9-SL3*. Interleuvenlaan 68, 3001 Leuven, Belgium.

Lyon, R. H. and DeJong, R. G. (**1995**). *Theory and Application of Statistical Energy Analysis (2nd edition)*. Butterworth-Heinemann, Boston. ISBN 9780750691116.

Marburg, S. (**2002**). Six boundary elements per wavelength: is that enough? *Journal of Computational Acoustics (JCA)*, **10**:25–51. ISSN 1134-3060. doi:10.1142/S0218396X02001401.

MathWorks, Inc. (**2007**). *Matlab & Simulink R2007b Online Product Documentation*. 3 Apple Hill Drive, Natick, Massachusetts 01760, USA. URL http://www.mathworks.com/help/techdoc/.

Mócsai, T., Priebsch, H.-H., Diwoky, F. and Hepberger, A. (**2009**). Engine Radiation Simulation up to 3 kHz using the Wave Based Technique. In *proceedings of the 16th International Congress on Sound and Vibration (ICSV2009), Kraków, Poland*.

MSC Software Corporation (**2008**). *MSC Nastran 2008 r1 Quick Reference Guide*. 2 MacArthur Place, Santa Ana, California 92707, USA.

Panzer, N., Joerg; Harris (**1998**). Distributed-Mode Loudspeaker Radiation Simulation. In *Audio Engineering Society Convention 105*. URL http://www.aes.org/e-lib/browse.cfm?elib=8397.

Pluymers, B. (**2006**). *Wave based modelling methods for steady-state vibro-acoustics*. Ph.D. thesis, Katholieke Universiteit Leuven, division PMA, 2006D4. ISBN 90-5682-696-4.

Pluymers, B., Desmet, W., Vandepitte, D. and P., S. (**2005**). On the use of a wave based prediction technique for steady-state structural-acoustic radiation analysis. *Journal of Computer Modeling in Engineering & Sciences (CMES)*, **7**(2):173–184. doi:10.3970/cmes.2005.007.173.

Pluymers, B., Desmet, W., Vandepitte, D. and Sas, P. (**2002**). Application of the wave based prediction technique for the analysis of the coupled vibro-acoustic behaviour of a 3D cavity. In *proceedings of the International Conference on Noise and Vibration Engineering (ISMA2002), September 16–18, Leuven, Belgium*, pages 891–900.

Pluymers, B., Desmet, W., Vandepitte, D. and Sas, P. (**2004**). Application of an efficient wave-based prediction technique for the analysis of vibro-acoustic radiation problems. *Journal of Computational and Applied Mathematics*, **168**(1–2):353–364. ISSN 0377-0427. doi: 10.1016/j.cam.2003.05.020. Selected Papers from the Second International Conference on Advanced Computational Methods in Engineering (ACOMEN 2002).

Pluymers, B., Van Hal, B., Vandepitte, D. and Desmet, W. (**2007**). Trefftz-based methods for time-harmonic acoustics. *Archives of Computational Methods in Engineering (ARCME)*, **14**:343–381. ISSN 1134-3060. doi:10.1007/s11831-007-9010-x.

Pratellesi, A., Donders, S., Orlando, S., Van Genechten, B., Rejlek, J., Englund, T., Nordström, L., Pluymers, B., von Werne, D. and Tournour, M. (**2011**). *Deliverable D8.3 – Concluding report on mid-frequency challenges and solutions for trucks*. Technical report, EU project MID-MOD (FP7 RTD collaborative project, EC grant no. 218508).

Press, W. H., Flannery, B. P., Teukolsky, S. A. and Vetterling, W. T. (**1992**). *Numerical Recipes in Fortran 77: The Art of Scientific Computing (2nd edition)*. Cambridge University Press. ISBN 9780521430647.

Rayleigh, J. W. S. (**1945**). *The Theory of Sound*. Dover Publications New York (2nd edition 1894, reprint 1945). ISBN 0486602923 (Volume One), 0486602931 (Volume Two).

Rejlek, J. (**2008**). The mid-frequency gap – a real challenge in the numerical vibro-acoustic modelling. Poster, Marie Curie Conference, Euroscience Open Forum (ESOF2008), July 17–22, Barcelona, Spain.

Rejlek, J., Diwoky, F., Hepberger, A. and Pluymers, B. (**2008**a). Wave Based Technique: enrichment of the set of basis functions. In *proceedings of the International Conference on Noise and Vibration Engineering (ISMA2008), September 15–17, Leuven, Belgium*, pages 1595–1608. ISBN 978-90-7380-286-5.

Rejlek, J., Englund, T., Nordström, L., Pratellesi, A., Roeck, W. D., Ruschmeyer, S., Hagen, D., Galezia, A. and D'Amico, R. (**2011**). *Deliverable D4.3 – Exterior truck applications – validation report*. Technical report, EU project MID-MOD (FP7 RTD collaborative project, EC grant no. 218508).

Rejlek, J. and Jiříček, O. (**2004**). Numerical Modelling Of The Head-Related Transfer Function Using The Boundary Element Method. In *proceedings of the 33rd International Congress and Exposition on Noise Control Engineering (INTER-NOISE 2004), August 22–25, Prague, Czech Republic*.

Rejlek, J., Mócsai, T., Šilar, P., Hepberger, A. and Priebsch, H.-H. (**2009**). Wave Based Prediction Technique for Sound Radiation Analysis. In *proceedings of the International Conference on Acoustics (NAG/DAGA2009), March 23–26, Rotterdam, The Netherlands*, pages 206–209. ISBN 978-3-9808659-6-8.

Rejlek, J., Ohenhen, G., Šilar, P., Priebsch, H.-H., Galezia, A., Hagen, D. and Ruschmeyer, S. (**2012**). A weak-coupled finite element–wave based technique formulation: application for a noise radiation analysis of a truck exhaust muffler. *Paper submitted for the Noise and Vibration: Emerging Methods (NOVEM 2012) conference, April 1–4, 2012, Sorrento, Italy*.

Rejlek, J., Pluymers, B., Diwoky, F., Hepberger, A., Priebsch, H.-H. and Desmet, W. (**2007**). Validation of the wave based technique for the analysis of 2D steady-state acoustic radiation problems. In *proceedings of the International Conference on Engineering Dynamics (ICED2007), April 16–18, Carvoeiro, Algarve, Portugal*.

Rejlek, J., Pluymers, B., Hepberger, A., Priebsch, H.-H. and Desmet, W. (**2008**b). Application of the Wave Based Technique for steady-state semi-infinite sound radiation analysis. *Computer Assisted Mechanics and Engineering Sciences (CAMES)*, **15**(3–4):337–351. ISSN 1232-308X.

Rejlek, J. and Priebsch, H.-H. (**2010**). Wave based technique for the analysis of fully coupled structural-acoustic unbounded problems. In *proceedings of the International Conference on Noise and Vibration Engineering (ISMA2010), September 20–22, Leuven, Belgium*, pages 2407–2424. ISBN 978-90-7380-287-2.

Rejlek, J. and Priebsch, H.-H. (**2011**). On the Use of the Wave Based Technique for a Three-Dimensional Noise Radiation Analysis of Coupled Vibro-Acoustic Problems. In *proceedings of the SAE 2011 Noise and Vibration Conference and Exhibition, May 16–19, Grand Rapids, Michigan, USA*. doi:10.4271/2011-01-1713.

Schenck, H. A. (**1968**). Improved Integral Formulation for Acoustic Radiation Problems. *Journal of the Acoustical Society of America*, **44**(1):41–58. ISSN 00014966. doi:10.1121/1.1911085.

Shorter, P. and Langley, R. (**2005**). Vibro-acoustic analysis of complex systems. *Journal of Sound and Vibration*, **288**(3):669–699. ISSN 0022-460X. doi:10.1016/j.jsv.2005.07.010. Uncertainty in structural dynamics.

Silar, P. (**2007**). *Direkte hybride Kopplung von Wave Based Technik und Finite Elemente Methode zur Simulation des Innengeräusches von Fahrzeugen*. Ph.D. thesis, Technische Universität Graz.

SIMULIA Dassault Systèmes (**2011**). *Abaqus 6.11, Abaqus/CAE User's Manual*. Rising Sun Mills, 166 Valley Street, Providence, RI 02909-2499, USA.

Thompson, L. L. (**2006**). A review of finite-element methods for time-harmonic acoustics. *Journal of the Acoustical Society of America*, **119**(3):1315–1330. ISSN 00014966. doi:10.1121/1.2164987.

Thompson, L. L. and Huan, R. (**1999**). Computation of transient radiation in semi-infinite regions based on exact nonreflecting boundary conditions and mixed time integration. *The Journal of the Acoustical Society of America*, **106**(6):3095–3108. ISSN 0001-4966. doi:10.1121/1.428163.

Tournour, M. A., Kosaka, F. and Shiozaki, H. (**2007**). Fast Acoustic Trim Modeling using Transfer Admitance and Finite Element Method. In *proceedings of the SAE 2007 Noise and Vibration Conference and Exhibition, May 15–17, St. Charles, Illinois, USA*. doi:10.4271/2007-01-2166.

Trefftz, E. (**1926**). Ein Gegenstück zum Ritzschen Verfahren. In *proceedings of the 2nd International Congress on Applied Mechanics, Zürich, Switzerland*, pages 131–137.

Turner, M. J., Clough, R. W., Martin, H. C. and Topp, L. P. (**1956**). Stiffness and deflection analysis of complex structures. *Journal of the Aeronautical Sciences*, **23**:805–823.

Van Genechten, B. (**2010**). *Trefftz-based Mid-frequency Analysis of Geometrically Complex Vibro-acoustic Systems – Hybrid Methodologies and Multi-level Modelling*. Ph.D. thesis, Katholieke Universiteit Leuven, division PMA, 2010D08. ISBN 978-94-6018-199-3.

Van Hal, B. (**2004**). *Automation and performance optimization of the wave based method for interior structural-acoustic problems*. Ph.D. thesis, Katholieke Universiteit Leuven, division PMA, 2004D7. ISBN 90-5682-536-4.

Van Hal, B., Desmet, W., Vandepitte, D. and Sas, P. (**2000**). Application of the efficient wave based prediction technique for the steady-state dynamic analysis of flat plates. pages 607–614.

Vanmaele, C. (**2007**). *Development of a wave based prediction technique for the efficient analysis of low- and mid-frequency structural vibrations*. Ph.D. thesis, Katholieke Universiteit Leuven, division PMA, 2007D11. ISBN 978-90-5682-834-9.

Vanmaele, C., Vandepitte, D. and Desmet, W. (**2007**). An efficient wave based prediction technique for plate bending vibrations. *Computer Methods in Applied Mechanics and Engineering*, **196**(33–34):3178–3189. ISSN 0045-7825. doi:10.1016/j.cma.2007.03.002.

Vergote, K., Genechten, B. V., Vandepitte, D. and Desmet, W. (**2011**). On the analysis of vibro-acoustic systems in the mid-frequency range using a hybrid deterministic-statistical approach. *Computers & Structures*, **89**(11–12):868–877. ISSN 0045-7949. doi:10.1016/j.compstruc.2011.03.002.

Von Estorff, O. (**2000**). *Boundary Elements in Acoustics: Advances and Applications*. WIT-press. ISBN 978-1-85312-556-0.

Williams, E. G. (**1999**). *Fourier acoustics : sound radiation and nearfield acoustical holography*. Academic Press. ISBN 0127539603.

World Health Organization (**2011**). Burden of disease from environmental noise – Quantification of healthy life years lost in Europe. The Regional Office for Europe of the World Health Organization. ISBN 978-92-890-0229-5.

Zienkiewicz, O. C., Taylor, R. L., Zhu, J. Z. and Nithiarasu, P. (**2005**). *The Finite Element Method Set (6th edition)*. Butterworth-Heinemann. ISBN 978-0-7506-6431-8.

Part IV

ADDENDA

Appendix A

Uncoupled structural problems

Plates constitute an important portion of the structural components used in various industrial applications. They represent a special class of general three-dimensional solids with the characteristic feature that one of the dimensions the thickness t, is much smaller that the other ones. This feature is made use of when deriving the appropriate mathematical models from a general three-dimensional theory of elasticity by incorporating some assumptions regarding their structural behaviour.

Section A.1 shows that the deformation of a plate can be decomposed into the in-plane and out-of-plane components, after which these two phenomena can be investigated separately. However, as only the out-of-plane bending motion radiates sound efficiently in the case of planar structures, see section A.2, the in-plane plate membrane problems are beyond the scope of this dissertation. Therefore, these problems are briefly summarised in the section A.3, for the sake of completeness.

A.1   General concepts

To start with, a consistent notation is introduced here which is used throughout the dissertation. According to the general theory of elasticity, positive normal stresses are tensile. Positive shear stresses are those oriented in positive directions of the coordinate system and that act on the positive faces of the element, see figure A.1(a).

Consider a plate of thickness t positioned such that the undeformed middle surface of the plane coincides with the xy-plane, see figure A.1(b). This plane, which is called a *neutral plane*, lies midway through its thickness for homogeneous plates, which are considered in this dissertation. The deformation is described by the translational displacements

$$\mathbf{w} = \begin{Bmatrix} w_x \\ w_y \\ w_z \end{Bmatrix} \tag{A.1}$$
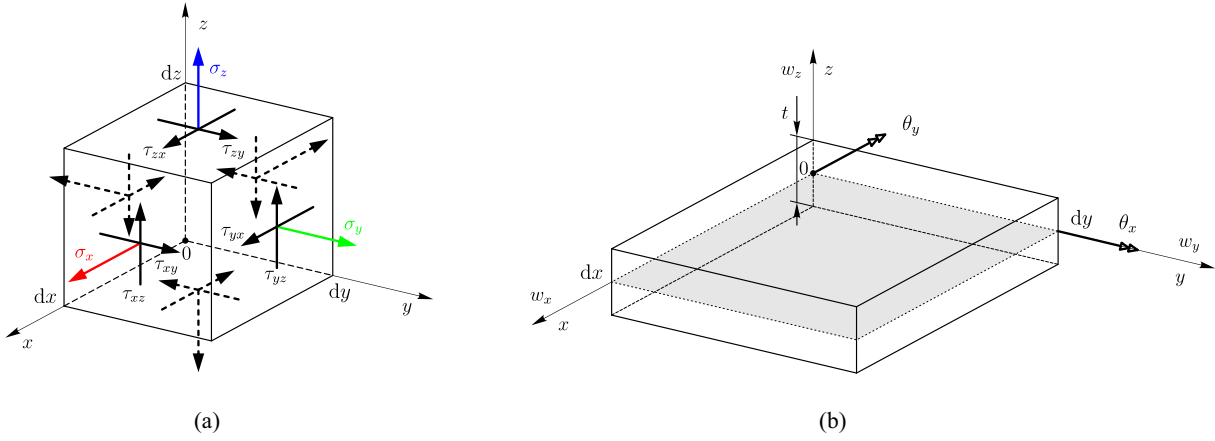
Figure A.1: Sign convention for (a) positive stresses acting on an infinitesimal element and (b) the translational displacements and rotations in a general flat plate problem

and the rotations

$$\boldsymbol{\theta} = \begin{Bmatrix} \theta_x \\ \theta_y \end{Bmatrix} \tag{A.2}$$

according to the sign conventions defined in figure A.1(b). In generalised plate theory, the following assumptions are introduced:

(i) The sections normal to the middle plane of the undeformed plate remain planar during the deformation. This implies that the w_x and w_y vary linearly through the thickness of the plate (Leissa, 1993).

(ii) As the stresses in the z direction are small, the strains in the z direction are negligible and thus the plane stress state ($\sigma_z = 0$) is assumed to hold in each lamina.

By utilising these assumptions, the deformation of a plate is fully described by means of displacements and rotations of the middle plane, see figure A.2,

$$w_x(x, y, z) = w_x^m(x, y) + z\theta_x^b(x, y) \tag{A.3a}$$

$$w_y(x, y, z) = w_y^m(x, y) + z\theta_y^b(x, y) \tag{A.3b}$$

$$w_z(x, y, z) = w_z^b(x, y) \tag{A.3c}$$

with $\bullet^m$ and $\bullet^b$ denoting the in-plane membrane and out-of-plane bending motion components. In a plate made of material having symmetrical properties with respect to the middle plane, the bending (out-of-plane) and membrane (in-plane longitudinal and in-plane transverse) waves may be decoupled and investigated separately.
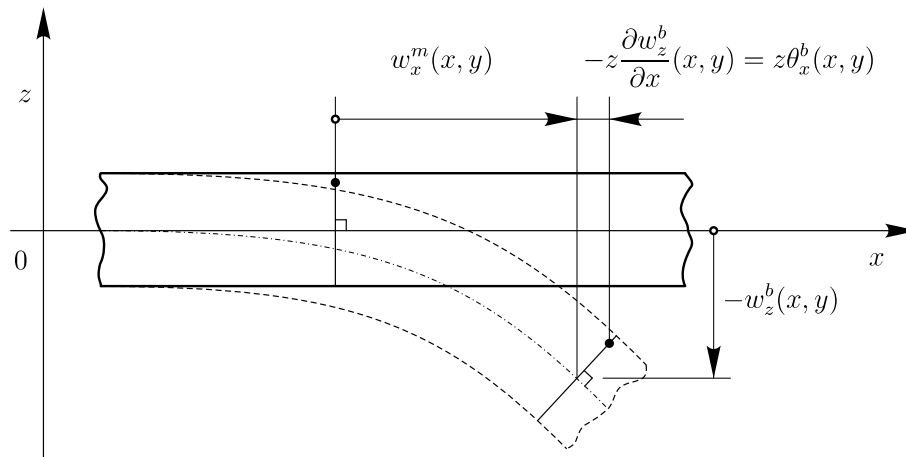
Figure A.2: Kinematics of the plate deformation

A.2   Plate bending problems

Two plate bending theories have been developed over the last two centuries – first the Kirchhoff thin plate theory[1] (1850) and then the Reissner-Mindlin formulation (1945, 1951) for thick plates. The main distinction between the two theories is that the Kirchhoff formulation omits both the effect of transverse shear stresses and the effects of rotatory inertia, as illustrated in figure A.3. These assumptions are valid as long as the thickness of the plate is smaller than the bending wavelength[2]. Despite the additional limitations introduced in the Kirchhoff thin plate theory, this mathematical model is preferred for its simplicity and its adequate applicability for a large number of problems. It was selected for the later formulation of the WBT for the plate bending problems for the following reasons:

(i) The Kirchhoff plate theory describes the deformation by means of a single quantity, while the Reissner-Mindlin model employs three independent variables. As a consequence, adopting the Kirchhoff theory leads to a considerable reduction of the problem size, which yields substantially smaller numerical models.

(ii) Using the Kirchhoff plate theory, an analytical solution can be derived in a quite straight-forward manner. This is an essential requirement for the formulation of the WBT, since its basis functions have to be the exact solutions of the governing differential equation. In the Reissner-Mindlin plate model, on the other hand, the dynamic behaviour is described by three coupled equations. In order to obtain an analytical solution, these equations have to be first decoupled, which may, however, lead to stability problems.

Vanmaele (2007) carried out a qualitative comparison of the two theories, which proved that the Kirchhoff plate model tends to overestimate the eigenfrequencies compared to the Reissner-Mindlin theory. However, since these effects are considered negligible for the applications presented within the scope of this dissertation, the Kirchhoff plate theory was selected as the underlying mathematical model used to formulate the WBT.

---

[1]Sometimes also referred to as a Classical Plate Theory.
[2]Cremer et al. (2005) proved, that the range of validity approximately holds for $\lambda_b > 6t$.
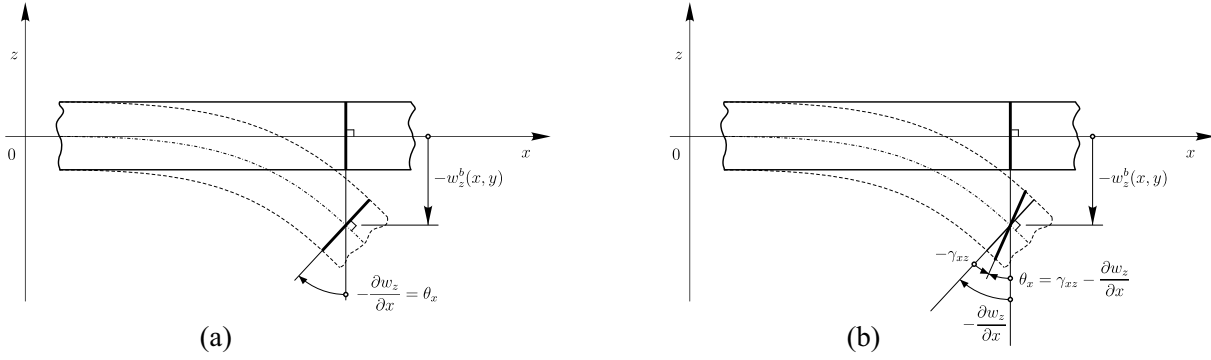
Figure A.3: The (a) Kirchhoff and (b) Reissner-Mindlin plate bending models

A.2.1 Kirchhoff theory

The assumption introduced by Kirchhoff states that the normals to the middle plane remain normal to it during the deformation, hence the shear deformations are omitted ($\gamma_{xz} = \gamma_{yz} = 0$), which yields

$$\boldsymbol{\theta} = -\nabla w_z = - \begin{Bmatrix} \dfrac{\partial w_z}{\partial x} \\ \dfrac{\partial w_z}{\partial y} \end{Bmatrix}. \tag{A.4}$$

As the rotations can be expressed by means of transverse displacement, the Kirchhoff theory describes the state of deformation with only one quantity. Assuming the strains are much less than one[3] and substituting the out-of-plane bending components $\bullet^b$ from the equations (A.3) yields the strain-displacement relations (Leissa, 1993)

$$\varepsilon_x = \frac{\partial w_x}{\partial x} \qquad = -z \frac{\partial^2 w_z}{\partial x^2} \tag{A.5a}$$

$$\varepsilon_y = \frac{\partial w_y}{\partial y} \qquad = -z \frac{\partial^2 w_z}{\partial y^2} \tag{A.5b}$$

$$\gamma_{xy} = \frac{\partial w_x}{\partial x} + \frac{\partial w_y}{\partial y} = -2z \frac{\partial^2 w_z}{\partial x \partial y} \tag{A.5c}$$

written in matrix form

$$\boldsymbol{\varepsilon} = \begin{Bmatrix} \varepsilon_x \\ \varepsilon_y \\ \gamma_{xy} \end{Bmatrix} = z \begin{bmatrix} \dfrac{\partial}{\partial x} & 0 \\ 0 & \dfrac{\partial}{\partial y} \\ \dfrac{\partial}{\partial y} & \dfrac{\partial}{\partial x} \end{bmatrix} \begin{Bmatrix} \theta_x \\ \theta_y \end{Bmatrix} = z \mathbf{L} \boldsymbol{\theta} = -z \begin{Bmatrix} \dfrac{\partial^2}{\partial x^2} \\ \dfrac{\partial^2}{\partial y^2} \\ 2\dfrac{\partial^2}{\partial x \partial y} \end{Bmatrix} w_z = -z \boldsymbol{\chi} w_z \tag{A.6}$$

---

[3]For small shear strain angles $\gamma_{1,2}$ an assumption $\tan \gamma_{1,2} \approx \gamma_{1,2}$ can be used.

with **L** the strain differential operator and $\boldsymbol{\chi} = \{\chi_x \ \chi_y \ \chi_{xy}\}^\mathsf{T}$ the vector of bending curvatures. Assuming an isotropic and elastic material that obeys Hooke's law, the stress-strain relation is given by

$$\sigma_x = \frac{E(1 + \mathrm{j}\eta)}{1 - \nu^2}(\varepsilon_x + \nu\varepsilon_y) \tag{A.7a}$$

$$\sigma_y = \frac{E(1 + \mathrm{j}\eta)}{1 - \nu^2}(\varepsilon_y + \nu\varepsilon_x) \tag{A.7b}$$

$$\tau_{xy} = G\gamma_{xy}, \tag{A.7c}$$

with E the Young's modulus, η the material loss factor, ν the Poisson's ratio and

$$G = \frac{E(1 + \mathrm{j}\eta)}{2(1 + \nu)} \tag{A.8}$$

the transverse shear modulus. Equations (A.7) may be rewritten in a matrix form

$$\boldsymbol{\sigma} = \begin{Bmatrix} \sigma_x \\ \sigma_y \\ \tau_{xy} \end{Bmatrix} = \frac{E(1 + \mathrm{j}\eta)}{1 - \nu^2} \begin{bmatrix} 1 & \nu & 0 \\ \nu & 1 & 0 \\ 0 & 0 & \dfrac{1 - \nu}{2} \end{bmatrix} \begin{Bmatrix} \varepsilon_x \\ \varepsilon_y \\ \gamma_{xy} \end{Bmatrix}. \tag{A.9}$$

Consider a plate element of thickness t and infinitesimal dimensions $\mathrm{d}x$ and $\mathrm{d}y$, with the stresses acting on the element faces as shown in figure A.4(a). Integrating these stresses over the thickness of the plate and substituting the strain-displacement (A.5) and the stress-stain relations (A.7) yields the bending M_x, M_y and torsional moments M_{xy}

$$M_x = \int_{-t/2}^{t/2} z\sigma_x \, \mathrm{d}z = -D\left(\frac{\partial^2 w_z}{\partial x^2} + \nu\frac{\partial^2 w_z}{\partial y^2}\right) \tag{A.10a}$$

$$M_y = \int_{-t/2}^{t/2} z\sigma_y \, \mathrm{d}z = -D\left(\frac{\partial^2 w_z}{\partial y^2} + \nu\frac{\partial^2 w_z}{\partial x^2}\right) \tag{A.10b}$$

$$M_{xy} = \int_{-t/2}^{t/2} z\tau_{xy} \, \mathrm{d}z = -D(1 - \nu)\frac{\partial^2 w_z}{\partial x\partial y}. \tag{A.10c}$$

These moments have dimensions of moment per unit length. Although the transverse shear stresses are negligible ($\gamma_{xz} = \gamma_{yz} = 0$), their corresponding integral resultants – the transverse shear forces are required for the subsequent formulation of the constitutive equation

$$Q_x = \int\limits_{-t/2}^{t/2} \tau_{xz}\,\mathrm{d}z \tag{A.11a}$$

$$Q_y = \int\limits_{-t/2}^{t/2} \tau_{yz}\,\mathrm{d}z. \tag{A.11b}$$

The transverse shear forces have the dimensions of force per unit length. Figure A.4(b) depicts the resulting integral quantities related to the midplane of the plate.
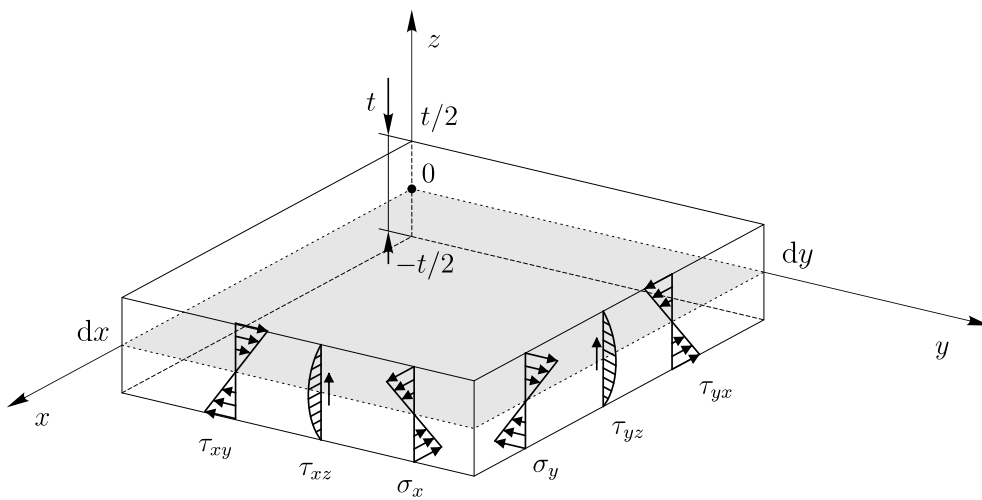
(a)
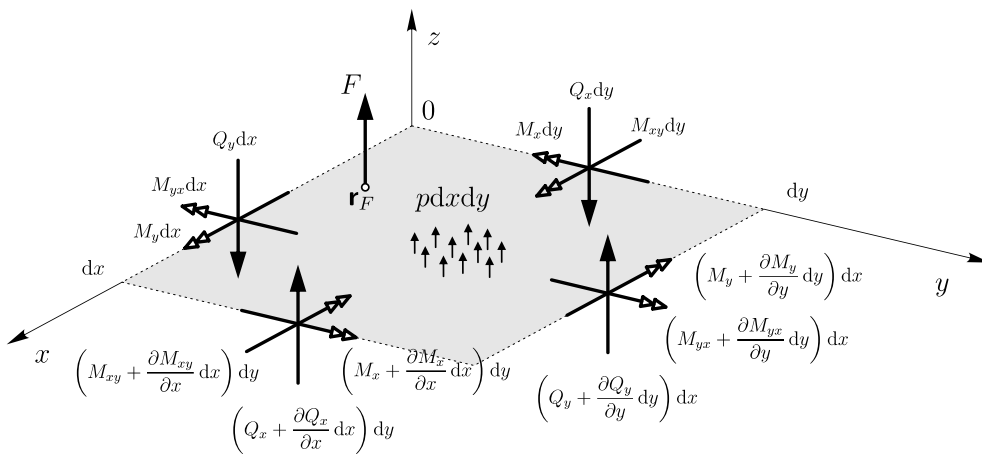
(b)

Figure A.4: Plate bending problem: (a) stresses acting on an infinitesimal element of the plate and (b) their integral resultants

Rewriting the equations for moments (A.10) using the matrix notation for the strain-displacement (A.6) and the stress-strain relations (A.9) gives

$$\mathbf{M} = \begin{Bmatrix} M_x \\ M_y \\ M_{xy} \end{Bmatrix} = \int_{-t/2}^{t/2} z\boldsymbol{\sigma}\mathrm{d}z = \mathbf{D}\mathbf{L}\boldsymbol{\theta} = -\mathbf{D}\boldsymbol{\chi}w_z \tag{A.12}$$

with the elasticity matrix

$$\mathbf{D} = D \begin{bmatrix} 1 & \nu & 0 \\ \nu & 1 & 0 \\ 0 & 0 & \dfrac{1-\nu}{2} \end{bmatrix} \tag{A.13}$$

and the bending stiffness

$$D = \frac{Et^3(1+\mathrm{j}\eta)}{12(1-\nu^2)}. \tag{A.14}$$

The dynamic equation governing the plate bending motion is derived by expressing the constitutive relations for the dynamic equilibrium of forces and moments acting on an infinitesimal portion of the plate $t\mathrm{d}x\mathrm{d}y$, see figure A.4(b). First, consider the steady-state dynamic force equilibrium in the z direction by assuming a time-harmonic response of the field variables $w_z(x,y,t) = w_z(x,y)\mathrm{e}^{\mathrm{j}\omega t}$ with ω the circular frequency

$$\left(\frac{\partial Q_x}{\partial x}\,\mathrm{d}x\right)\mathrm{d}y + \left(\frac{\partial Q_y}{\partial y}\,\mathrm{d}y\right)\mathrm{d}x + p\mathrm{d}x\mathrm{d}y = -\rho t\mathrm{d}x\mathrm{d}y\omega^2 w_z. \tag{A.15}$$

Dividing the equation by an infinitesimal area of the plate $\mathrm{d}x\mathrm{d}y$ yields

$$\frac{\partial Q_x}{\partial x} + \frac{\partial Q_y}{\partial y} + p + \rho t\omega^2 w_z = 0. \tag{A.16}$$

The second constitutive relation is the steady-state dynamic equilibrium of moments with respect to y axis

$$\left(\frac{\partial M_x}{\partial x}\,\mathrm{d}x\right)\mathrm{d}y + \left(\frac{\partial M_{yx}}{\partial y}\,\mathrm{d}y\right)\mathrm{d}x - \left(Q_x + \frac{\partial Q_x}{\partial x}\,\mathrm{d}x\right)\mathrm{d}y\mathrm{d}x = -\frac{\rho t^3}{12}\mathrm{d}x\mathrm{d}y\omega^2\theta_x \tag{A.17}$$

and in an analogous way with respect to the x axis. Omitting the term on the right hand side, which accounts for the rotatory inertia and the higher-order differentials, yields the simplified form of moment equilibrium equation (A.17) with respect to the corresponding axis

$$Q_x = \frac{\partial M_x}{\partial x} + \frac{\partial M_{yx}}{\partial y} \tag{A.18a}$$

$$Q_y = \frac{\partial M_y}{\partial y} + \frac{\partial M_{xy}}{\partial x}. \tag{A.18b}$$

Combining equations (A.18) and (A.16) yields

$$p + \rho t \omega^2 w_z + \chi^\mathsf{T} \left\{ \begin{array}{c} M_x \\ M_y \\ M_{xy} \end{array} \right\} = 0. \tag{A.19}$$

Substituting the equation for moments (A.12) into (A.19) gives

$$p + \rho t \omega^2 w_z - \chi^\mathsf{T} \mathbf{D} \chi w_z = 0. \tag{A.20}$$

Dividing the equation (A.20) by the bending stiffness D and expanding the term $\chi^\mathsf{T} \mathbf{D} \chi$ involving the products yields the equation governing a steady-state thin plate bending motion

$$\nabla^4 w_z(\mathbf{r}) - k_b^4 w_z(\mathbf{r}) = \frac{p}{D} + \frac{F}{D} \delta(\mathbf{r}_F), \quad \forall \mathbf{r} \in \Omega, \tag{A.21}$$

where

$$\nabla^4 = \frac{\chi^\mathsf{T} \mathbf{D} \chi}{D} = \frac{\partial^4}{\partial x^4} + 2 \frac{\partial^4}{\partial x^2 \partial y^2} + \frac{\partial^4}{\partial y^4} \tag{A.22}$$

and

$$k_b = \sqrt[4]{\frac{\rho t \omega^2}{D}} \tag{A.23}$$

is the bending wave number with ρ the mass density. In equation (A.21), $\mathbf{r}$ is the position vector, p is the external transverse load having the dimension force per unit area (e.g. the pressure loading or gravitational field), F is the point force acting at position $\mathbf{r}_F$, and δ is the Dirac delta function, see figure A.5.
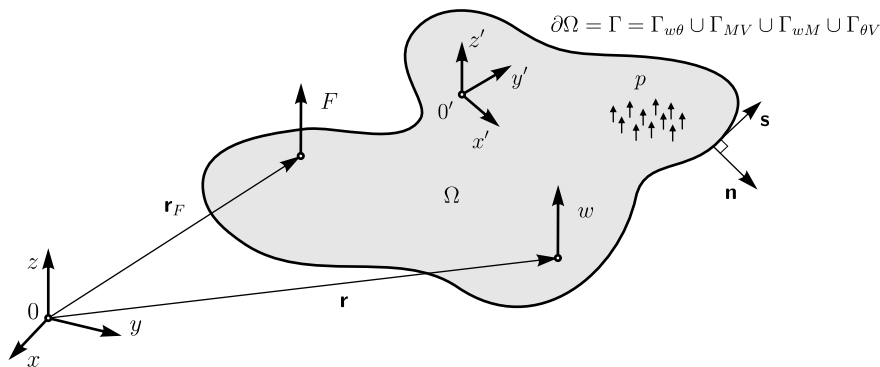
Figure A.5: A general thin plate bending problem

Since the governing equation (A.21) is a fourth-order partial differential equation, two boundary conditions have to be imposed at each point of the boundary in order for the problem to be well-posed. The following types of boundary condition forming a non-overlapping set $\Gamma = \Gamma_{w\theta} \cup \Gamma_{MV} \cup \Gamma_{wM} \cup \Gamma_{\theta V}$ can be imposed at the boundary $\partial \Omega = \Gamma$ of the problem, in which the quantities w_z, θ_n, M_n and V_n are defined in terms of a generalised local coordinate system (n, s), see figure A.6:

- Kinematic boundary conditions $\forall \mathbf{r} \in \Gamma_{w\theta}$:

$$w_z(\mathbf{r}) = \bar{w}(\mathbf{r}) \tag{A.24a}$$

$$\mathcal{L}_\theta(w_z(\mathbf{r})) = \bar{\theta}_n(\mathbf{r}) \tag{A.24b}$$

with $\bar{w}(\mathbf{r})$ and $\bar{\theta}_n(\mathbf{r})$ the prescribed values for the transverse out-of-plane displacement and the normal rotation. The boundary condition (A.24a) inherently implies that the condition for tangential rotation has also been fulfilled

$$\bar{\theta}_s = -\frac{\partial w_z}{\partial s}.$$

The boundary conditions (A.24) are imposed, for example, at a clamped edge, see figure A.8(a).

- Mechanical boundary conditions $\forall \mathbf{r} \in \Gamma_{MV}$:

$$\mathcal{L}_M(w_z(\mathbf{r})) = \bar{M}_n(\mathbf{r}) \tag{A.25a}$$

$$\mathcal{L}_V(w_z(\mathbf{r})) = \bar{V}_n(\mathbf{r}) \tag{A.25b}$$

with $\bar{M}_n(\mathbf{r})$ the prescribed bending moment. As the mechanical type of boundary conditions implies that all three mechanical quantities are prescribed simultaneously, while only two conditions are admissible to be imposed at any point of the boundary, the effect of the torsional moment M_{ns} along the boundary is combined with the transverse shear force Q_n into one edge condition, which yields

$$V_n = Q_n + \frac{\partial M_{ns}}{\partial s},$$

see figure A.7. The force resultant $\bar{V}_n(\mathbf{r})$ acting on the edge is referred to as a generalised shear force or just an edge reaction. The boundary conditions (A.25) are defined, for example, at a free edge, see figure A.8(b).

- Mixed boundary conditions type 1 $\forall \mathbf{r} \in \Gamma_{wM}$:

$$w_z(\mathbf{r}) = \bar{w}(\mathbf{r}) \tag{A.26a}$$

$$\mathcal{L}_M(w_z(\mathbf{r})) = \bar{M}_n(\mathbf{r}) \tag{A.26b}$$

with $\bar{w}(\mathbf{r})$ and $\bar{M}_n(\mathbf{r})$ the prescribed values for the transverse out-of-plane displacement and the bending moment. The boundary conditions (A.26) arise, for instance, at a simply supported edge, see figure A.8(c).

- Mixed boundary conditions type 2 $\forall \mathbf{r} \in \Gamma_{\theta V}$:

$$\mathcal{L}_\theta(w_z(\mathbf{r})) = \bar{\theta}_n(\mathbf{r}) \tag{A.27a}$$

$$\mathcal{L}_V(w_z(\mathbf{r})) = \bar{V}_n(\mathbf{r}) \tag{A.27b}$$

with $\bar{\theta}_n(\mathbf{r})$ and $\bar{V}_n(\mathbf{r})$ the prescribed normal rotation and the generalised shear force, respectively. The boundary conditions (A.27) are imposed, for example, at a symmetry edge, see figure A.8(d). Table A.1 lists the common types of structural boundary conditions. The differential operators involved in the formulation of the boundary conditions (A.24)-(A.27) are defined as follows

$$\theta_n = \mathcal{L}_\theta(w) \quad = -\frac{\partial w}{\partial n} \tag{A.28a}$$

$$M_n = \mathcal{L}_M(w) \ = -D\left(\frac{\partial^2 w}{\partial n^2} + \nu\frac{\partial^2 w}{\partial s^2}\right) \tag{A.28b}$$

$$M_{ns} = \mathcal{L}_{Ms}(w) = -D(1-\nu)\frac{\partial^2 w}{\partial n\partial s} \tag{A.28c}$$

$$Q_n = \mathcal{L}_Q(w) \ = -D\frac{\partial}{\partial n}\left(\frac{\partial^2 w}{\partial n^2} + \frac{\partial^2 w}{\partial s^2}\right) \tag{A.28d}$$

$$V_n = \mathcal{L}_V(w) \ = -D\frac{\partial}{\partial n}\left(\frac{\partial^2 w}{\partial n^2} + (2-\nu)\frac{\partial^2 w}{\partial s^2}\right) = Q_n + \frac{\partial M_{ns}}{\partial s}. \tag{A.28e}$$
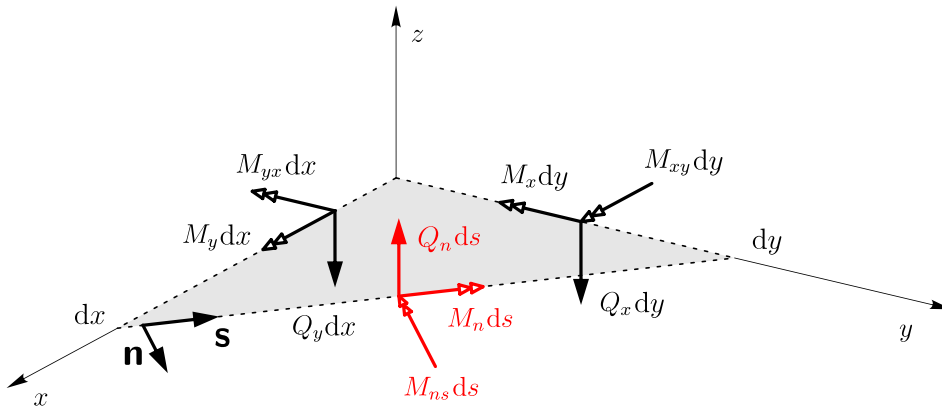
Figure A.6: Generalised quantities related to local coordinate system (n, s)
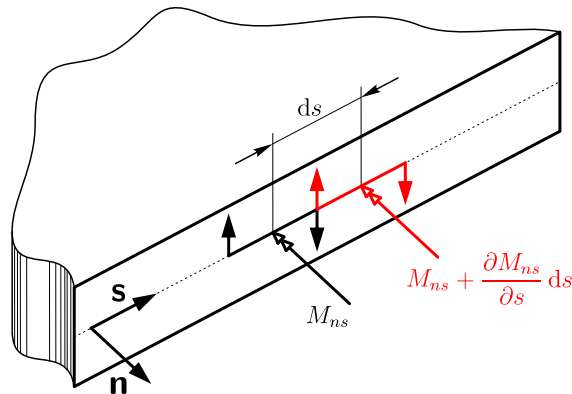
Figure A.7: Generalised shear force

| type of | prescribed quantities | | | | example |
boundary condition	w_z	θ_n	M_n	V_n	
kinematic at $\Gamma_{w\theta}$	✓	✓			clamped edge
mechanical at Γ_{MV}			✓	✓	free edge
mixed type 1 at Γ_{wM}	✓		✓		simply supported edge
mixed type 2 at $\Gamma_{\theta V}$		✓		✓	symmetry edge

Table A.1: Thin plate bending problem: boundary conditions
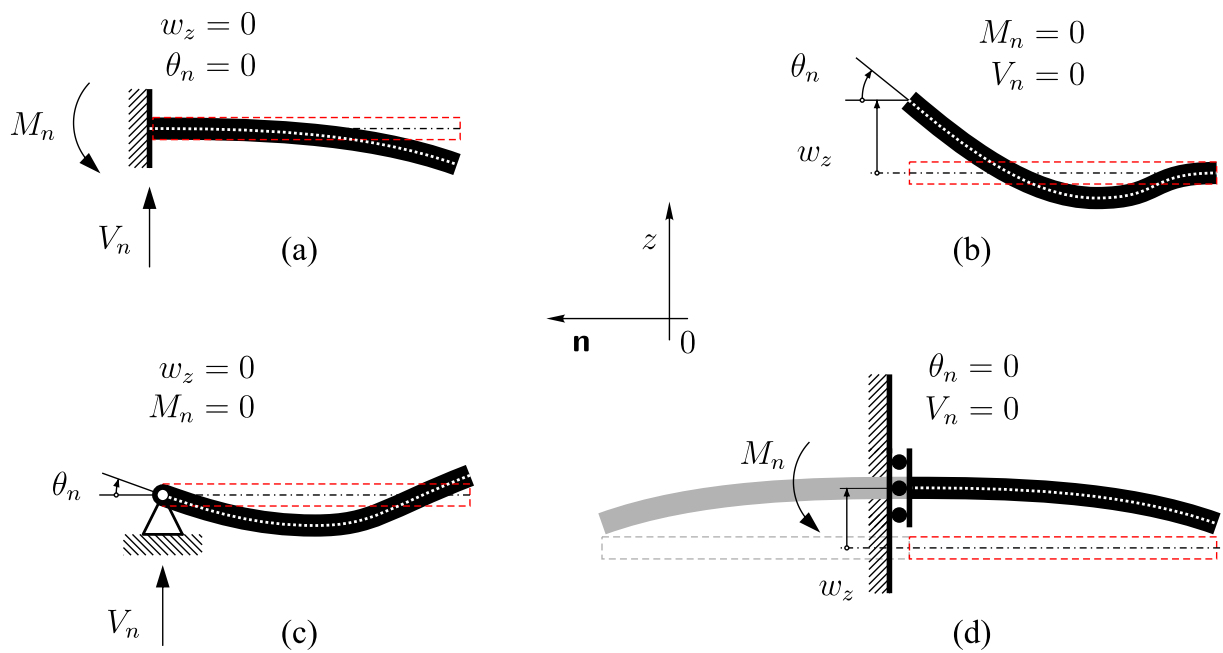
Figure A.8: The common boundary conditions arising in a thin plate bending problem: (a) clamped edge, (b) free edge, (c) simply supported edge and (d) symmetry edge

A.2.2 Reissner-Mindlin theory

The Reissner-Mindlin plate bending model is a further generalisation of Kirchhoff's classical plate theory to thick plates, where the shear deformations and the effects of the rotatory inertia are no longer negligible. As a thick plate exhibits non-zero transverse shear strains $\gamma_{xz} \neq 0$ and $\gamma_{yz} \neq 0$, the cross-sections of the plate are no longer normal to the midplane yielding the transverse shear strains

$$\boldsymbol{\gamma} = \begin{Bmatrix} \gamma_{xz} \\ \gamma_{yz} \end{Bmatrix} = \begin{Bmatrix} \dfrac{\partial w_z}{\partial x} \\ \dfrac{\partial w_z}{\partial y} \end{Bmatrix} + \begin{Bmatrix} \theta_x \\ \theta_y \end{Bmatrix} = \nabla w_z + \boldsymbol{\theta}, \tag{A.29}$$

see figure A.3(b). The resulting transverse shear stresses are given as

$$\boldsymbol{\tau} = \begin{Bmatrix} \tau_{xz} \\ \tau_{yz} \end{Bmatrix} = \kappa^2 \mathbf{G} \boldsymbol{\gamma}, \tag{A.30}$$

with $\mathbf{G}$ the matrix of transverse shear moduli and κ^2 a shear correction coefficient used to reduce the transverse shear stiffness[4]. The governing differential equation for the bending motion can be obtained in an analogous way to the thin plate problem discussed above. Once again, by assembling the constitutive relations for the dynamic equilibrium of forces and moments related to an infinitesimal element of plate one can derive the differential equations and the corresponding boundary conditions. Furthermore, the model enhances the Kirchhoff plate theory by incorporating the effects of the transverse shear forces and the rotatory inertia.

Although the concept of the Reissner-Mindlin theory presents a more general dynamic plate model, the full derivation of this mathematical model is not further considered in the framework of this doctoral thesis. For more details, the reader is referred to the work of Vanmaele (2007).

A.3   Plate membrane problems

The in-plane plate membrane motion is described by means of the displacement field w_x and w_y. Since the displacement components in both the x and y directions are invariant in the z direction, the in-plane strain-displacement relation is

$$\boldsymbol{\varepsilon} = \begin{Bmatrix} \varepsilon_x \\ \varepsilon_y \\ \gamma_{xy} \end{Bmatrix} = \begin{bmatrix} \dfrac{\partial}{\partial x} & 0 \\ 0 & \dfrac{\partial}{\partial y} \\ \dfrac{\partial}{\partial x} & \dfrac{\partial}{\partial y} \end{bmatrix} \begin{Bmatrix} w_x \\ w_y \end{Bmatrix} = \mathbf{L} \begin{Bmatrix} w_x \\ w_y \end{Bmatrix} \tag{A.31}$$

with $\mathbf{L}$ the differential strain operator as already described in section A.2. Assuming a linear elastic material, the stress-strain relation is governed by Hooke's law

$$\boldsymbol{\sigma} = \begin{Bmatrix} \sigma_x \\ \sigma_y \\ \tau_{xy} \end{Bmatrix} = \mathbf{D} \boldsymbol{\varepsilon}, \tag{A.32}$$

with $\mathbf{D}$ the elasticity matrix

$$\mathbf{D} = \frac{E(1 + \mathrm{j}\eta)}{1 - \nu^2} \begin{bmatrix} 1 & \nu & 0 \\ \nu & 1 & 0 \\ 0 & 0 & \dfrac{1 - \nu}{2} \end{bmatrix}. \tag{A.33}$$

---

[4]To account for non-constant shears arising in real plates, while considering constant displacement and rotations throughout the thickness, the transverse shear stiffness has to be reduced by factor κ^2 in order to obtain a zero value of the strain at the free surfaces of the plate $z = \pm t/2$. Reissner (1945) introduced a value of $\kappa^2 = 5/6$ in his work on static theory, while Mindlin (1951) proposed to chose $\kappa^2 = \pi^2/12$ in order to make the dynamic theory consistent.

The quantities E, ν and η were already introduced in section A.2. Integrating the stresses over the thickness t yields the stress resultants

$$\mathbf{N} = \left\{ \begin{array}{c} N_x \\ N_y \\ N_{xy} \end{array} \right\} = \int\limits_{-t/2}^{t/2} \boldsymbol{\sigma} \mathrm{d}z = t\mathbf{DL} \left\{ \begin{array}{c} w_x \\ w_y \end{array} \right\}, \tag{A.34}$$

where N_x and N_y are the in-plane longitudinal and N_{xy} in-plane shear forces, see figure A.9. Establishing the constitutive relations for the equilibrium of the steady-state dynamic forces acting on an infinitesimal element of plate $t\mathrm{d}x\mathrm{d}y$ in the x and y directions yields

(a)

(b)
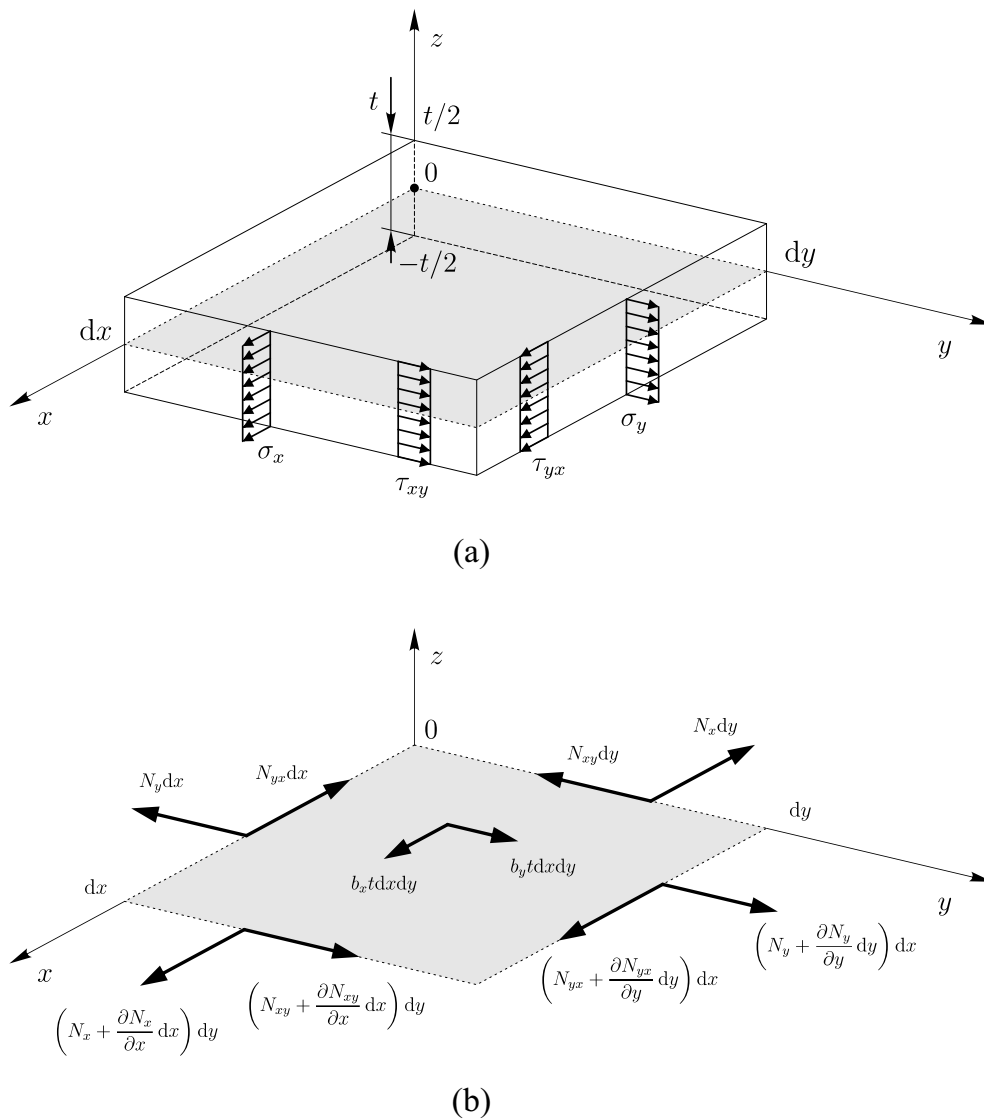
Figure A.9: Plate membrane problem: (a) stresses acting on an infinitesimal element of plate and (b) their integral resultants

$$\frac{\partial N_x}{\partial x} + \frac{\partial N_{yx}}{\partial y} + tb_x + \rho t\omega^2 w_x = 0 \tag{A.35a}$$

$$\frac{\partial N_y}{\partial y} + \frac{\partial N_{xy}}{\partial x} + tb_y + \rho t\omega^2 w_y = 0 \tag{A.35b}$$

with $\mathbf{b} = \{b_x b_y\}^{\mathsf{T}}$ the distributed body forces per unit volume. Substituting the in-plane forces (A.34) into equations (A.35) yields the coupled steady-state dynamic Navier equations governing the in-plane motion behaviour

$$\frac{\partial^2 w_x}{\partial x^2} + \frac{1-\nu}{2}\frac{\partial^2 w_x}{\partial y^2} + \frac{1+\nu}{2}\frac{\partial^2 w_y}{\partial x\partial y} + \frac{\rho(1-\nu^2)\omega^2}{E(1+\mathrm{j}\eta)}w_x + \frac{1-\nu^2}{E(1+\mathrm{j}\eta)}b_x = 0 \tag{A.36a}$$

$$\frac{\partial^2 w_y}{\partial y^2} + \frac{1-\nu}{2}\frac{\partial^2 w_y}{\partial x^2} + \frac{1+\nu}{2}\frac{\partial^2 w_x}{\partial x\partial y} + \frac{\rho(1-\nu^2)\omega^2}{E(1+\mathrm{j}\eta)}w_y + \frac{1-\nu^2}{E(1+\mathrm{j}\eta)}b_y = 0 \tag{A.36b}$$

or rewritten in a matrix form

$$\mathbf{L}^{\mathsf{T}}\mathbf{DL}\begin{Bmatrix} w_x \\ w_y \end{Bmatrix} + \rho\omega^2\begin{Bmatrix} w_x \\ w_y \end{Bmatrix} + \begin{Bmatrix} b_x \\ b_y \end{Bmatrix} = 0, \quad \forall \mathbf{r} \in \Omega. \tag{A.37}$$

In order to provide an analytical solution of the homogeneous governing differential equation, which is an essential requirement for the formulation of the WBT, the equations (A.36) have to be transformed into a set of two uncoupled ones. Assuming that no body forces occur, two transformation strategies can be employed.

A.3.1   Displacement potentials

The first transformation adopts the Helmholtz theorem for the decomposition of a vector field. Provided the vector field is piecewise differentiable, employing this technique allows an arbitrary vector field to be decomposed into an irrotational and solenoidal part. Applying this theorem to an in-plane displacement field leads to

$$\begin{Bmatrix} w_x \\ w_y \end{Bmatrix} = \nabla\phi + \nabla \times \psi, \tag{A.38}$$

with ϕ and ψ the irrotational and solenoidal potential, respectively. Using this transformation, the Navier equations (A.36) can be converted into uncoupled equations

$$\nabla^2\phi + k_l^2\phi = 0, \quad \forall \mathbf{r} \in \Omega \tag{A.39a}$$

$$\nabla^2\psi + k_t^2\psi = 0 \quad \forall \mathbf{r} \in \Omega \tag{A.39b}$$

with k_l and k_t the in-plane longitudinal and shear wave numbers defined as follows

$$k_l = \omega \sqrt{\frac{\rho(1 - \nu^2)}{E(1 + \mathrm{j}\eta)}} = 0 \tag{A.40a}$$

$$k_l = \omega \sqrt{\frac{2\rho(1 + \nu)}{E(1 + \mathrm{j}\eta)}} = 0. \tag{A.40b}$$

A.3.2 Dilatational and rotational strain

The second decoupling strategy decomposes the displacement field into a dilatational strain e and a rotational strain Ω

$$e = \frac{\partial w_x}{\partial x} + \frac{\partial w_y}{\partial y} \tag{A.41a}$$

$$\Omega = \frac{\partial w_y}{\partial x} - \frac{\partial w_x}{\partial y}, \tag{A.41b}$$

which yields

$$\begin{Bmatrix} w_x \\ w_y \end{Bmatrix} = -\frac{1}{k_l^2}\nabla e + \frac{1}{k_t^2}\nabla \times \Omega, \tag{A.42}$$

with k_l and k_t the wave numbers as defined in (A.40). The Navier equations (A.36) are reformulated as follows

$$\nabla^2 e + k_l^2 e = 0, \quad \forall \mathbf{r} \in \Omega \tag{A.43a}$$

$$\nabla^2 \Omega + k_t^2 \Omega = 0, \quad \forall \mathbf{r} \in \Omega. \tag{A.43b}$$

The two transformation techniques are similar except for the relative weighting between the dilatational and rotational component. For a detailed discussion of these decomposition strategies, including the types of boundary conditions imposed in the plate membrane problem, the reader is referred to (Vanmaele, 2007).

Appendix B

Uncoupled acoustic problems

This appendix presents the full derivation of the mathematical model, which governs the propagation of small disturbances through a homogeneous, compressible, inviscid fluid. After introducing some initial assumptions in section B.1, the steady-state form of the general wave equation is derived from the general continuum mechanics in section B.2. This mathematical model is further applied to uncoupled, interior and unbounded acoustic problem, see sections B.3 and B.4.

B.1   General concepts

The total pressure field $p(\mathbf{r}, t)$, mass density field $\rho(\mathbf{r}, t)$ and the velocity vector field $\mathbf{v}(\mathbf{r}, t)$ are the underlying physical quantities that describe an arbitrary acoustic problem. Decomposing the total field into a perturbation and ambient part yields

$$p(\mathbf{r}, t) = p'(\mathbf{r}, t) + p_0(\mathbf{r}, t) \tag{B.1a}$$

$$\rho(\mathbf{r}, t) = \rho'(\mathbf{r}, t) + \rho_0(\mathbf{r}, t) \tag{B.1b}$$

$$\mathbf{v}(\mathbf{r}, t) = \mathbf{v}'(\mathbf{r}, t) + \mathbf{v}_0(\mathbf{r}, t) \tag{B.1c}$$

with the primed variables the acoustic fluctuations, which are superposed onto the ambient quantities. The acoustic components $p'(\mathbf{r}, t)$, $\rho'(\mathbf{r}, t)$ and $\mathbf{v}'(\mathbf{r}, t)$ represent the propagation of a mechanical disturbance through a homogeneous, inviscid, compressible fluid, while the ambient fields correspond to an equilibrium state of the fluid

$$p_0(\mathbf{r}, t) \equiv b \tag{B.2a}$$

$$\rho_0(\mathbf{r}, t) \equiv \rho \tag{B.2b}$$

$$\mathbf{v}(\mathbf{r}, t) \equiv \mathbf{0} \tag{B.2c}$$

with b the barometric pressure and ρ the mean density. Thus, the ambient fields are considered to be spatially and temporally invariant.

B.2   Wave equation

The fundamental differential equation governing the acoustic perturbation fields – the wave equation – is derived by applying the law of conservation of momentum and mass to an infinitesimal control volume $\mathrm{d}x\mathrm{d}y\mathrm{d}z$ by considering the thermodynamic nature of the processes in fluid. The next paragraphs introduce the three underlying equations, which constitute a basis from which the wave equation will be derived at a later stage.

Conservation of momentum *(Equation of motion)*

Applying Newton's second law of motion to the infinitesimal element $\mathrm{d}V = \mathrm{d}x\mathrm{d}y\mathrm{d}z$

$$\mathrm{d}F = \mathrm{d}m\frac{\mathrm{d}\mathbf{v}}{\mathrm{d}t} \tag{B.3}$$

and establishing the constitutive relations for the equilibrium of the dynamic forces acting in the y direction, see figure B.1, yields

$$\rho\mathrm{d}x\mathrm{d}y\mathrm{d}z\frac{\mathrm{d}v_y}{\mathrm{d}t} = -\frac{\partial p}{\partial y}\,\mathrm{d}y\mathrm{d}x\mathrm{d}z. \tag{B.4}$$

Expressing the force balance relations for the x and z directions, the conservation of momentum may be rewritten as a vector equation

$$-\nabla p = \rho\frac{\mathrm{d}\mathbf{v}}{\mathrm{d}t}, \tag{B.5}$$

where the substantial time derivative of the velocity vector may be decomposed into the local and convective terms as follows

$$\frac{\mathrm{d}\mathbf{v}}{\mathrm{d}t} = \frac{\partial\mathbf{v}}{\partial t} + (\mathbf{v}\cdot\nabla)\mathbf{v}. \tag{B.6}$$

The first *local* term on the right hand side of (B.6) represents the variation of velocity with respect to time at a fixed point of fluid, while the second *convective* term stands for a time rate of change of velocity of the control volume due to its translation along the trajectory. By substituting (B.6) into (B.5), the expression for the conservation of momentum applied on an infinitesimal element of fluid becomes

$$-\nabla p = \rho\left(\frac{\partial\mathbf{v}}{\partial t} + (\mathbf{v}\cdot\nabla)\mathbf{v}\right). \tag{B.7}$$

Equation (B.7), also referred to as the Eulerian equation of motion for an inviscid flow, is a non-linear partial differential equation due to the presence of the convective term $(\mathbf{v}\cdot\nabla)\mathbf{v}$.
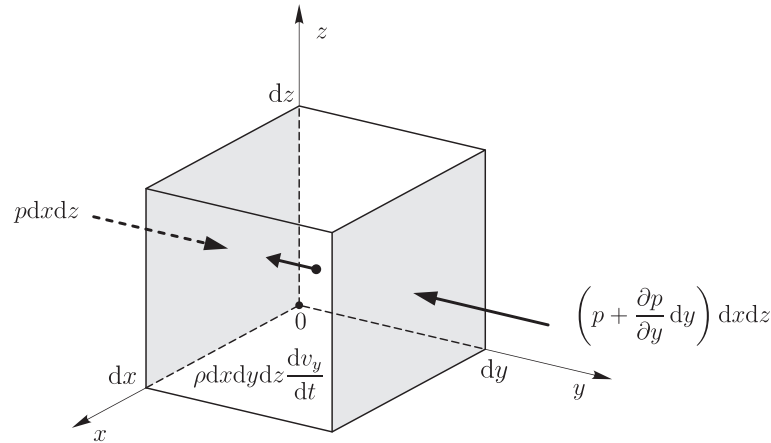
Figure B.1: The equilibrium of the dynamic forces acting on an infinitesimal fluid element $\mathrm{d}x\mathrm{d}y\mathrm{d}z$ in the y direction

Conservation of mass *(Continuity equation)*

The second fundamental relation is obtained by applying the law of conservation of mass to an infinitesimal volume of fluid $\mathrm{d}V = \mathrm{d}x\mathrm{d}y\mathrm{d}z$. Expressing the constitutive relation for the mass flows passing through the control volume by considering the effect of an acoustic volume velocity point source $q(\mathbf{r}, t) = q'(\mathbf{r}, t) + q_0(\mathbf{r}, t)'$, see figure B.2, the conservation of mass is given by

$$\frac{\partial \rho}{\partial t}\mathrm{d}x\mathrm{d}y\mathrm{d}z = \left(\rho q - \frac{\partial(\rho v_x)}{\partial x} + \frac{\partial(\rho v_y)}{\partial y} + \frac{\partial(\rho v_z)}{\partial z}\right)\mathrm{d}x\mathrm{d}y\mathrm{d}z, \tag{B.8}$$

which may be rewritten using the divergence operator $\nabla\cdot$ in form

$$\nabla \cdot (\rho\mathbf{v}) - \rho q = -\frac{\partial \rho}{\partial t}. \tag{B.9}$$

The continuity equation (B.9) states that the time rate of change of density equals the net mass of fluid entering the control volume per unit time, i.e. divergence of the mass flux $\nabla \cdot \rho\mathbf{v}$ plus the additional mass flow induced in the fluid due to the effect of an external acoustic source.

Using a vector calculus identity

$$\nabla \cdot (\rho\mathbf{v}) = \rho\nabla \cdot \mathbf{v} + \mathbf{v} \cdot \nabla\rho \tag{B.10}$$

and by dividing the equation (B.9) by density ρ, the continuity equation may be expressed as follows

$$q - \nabla \cdot \mathbf{v} = \frac{1}{\rho}\left(\frac{\partial \rho}{\partial t} + \mathbf{v} \cdot \nabla\rho\right). \tag{B.11}$$

Using the expression for a substantial derivative of the fluid velocity vector (B.6) introduced in a previous paragraph, the expression between the parentheses on the right hand side of equation

(B.11) may be rewritten as follows

$$\frac{\mathrm{d}\rho}{\mathrm{d}t} = \frac{\partial\rho}{\partial t} + \mathbf{v}\cdot\nabla\rho. \tag{B.12}$$

Again, the convective term $\mathbf{v}\cdot\nabla\rho$ in (B.11) causes the non-linearity in the continuity equation.
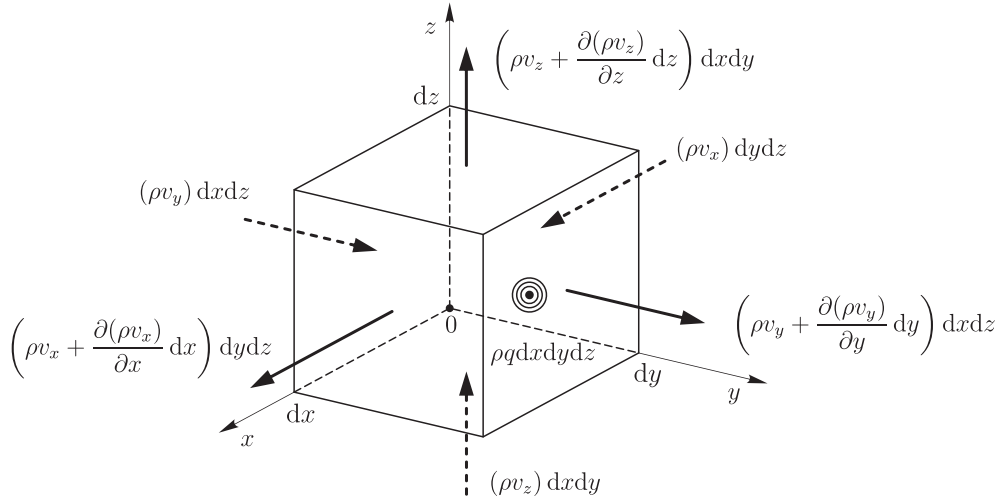
Figure B.2: Mass flux through a control volume $\mathrm{d}V$

Thermodynamic processes in fluid *(Equation of state)*

So far, two fundamental constitutive relations obeying the laws of conservation of momentum and mass have been established. Thus, one has four equations[1] featuring five variables, namely all three components of the velocity $\mathbf{v}(\mathbf{r}, t) = v_x(\mathbf{r}, t)\mathbf{i} + v_y(\mathbf{r}, t)\mathbf{j} + v_z(\mathbf{r}, t)\mathbf{k}$, pressure p and the mass density ρ. To tackle this problem, one must define out the relation between the pressure and density $p = p(\rho)$. Obviously, the missing part for assembling the wave equation is related to the thermodynamic processes taking place in the fluid. To start with, first recall the first law of thermodynamics

$$\mathrm{d}U = \delta Q + \delta A, \tag{B.13}$$

which states that an infinitesimal increase of the internal energy of a system $\mathrm{d}U$ equals an infinitesimal amount of energy added by heating the system δQ and the infinitesimal amount of work done on the system δA. The mechanical work done on the system invokes a change of the volume of gas, see figure B.3,

$$\delta A = -F\,\mathrm{d}x = -pS\,\mathrm{d}x = -p\,\mathrm{d}V, \tag{B.14}$$

which implies a change of pressure. In (B.14), the minus sign denotes that by compressing the gas the mechanical work done on the system is positive, while the work done by the system is

---

[1]One Eulerian vector equation of motion for each of the threee Cartesian coordinates plus one continuity equation.

negative. In an ideal gas, the internal energy depends merely on the thermodynamic temperature Θ and the specific heat at a constant volume C_V

$$U = \frac{m}{M} C_V \,\Theta, \tag{B.15}$$

with M the molar mass. For the change of the internal energy (B.15) holds

$$\mathrm{d}U = \frac{m}{M} C_V \,\mathrm{d}\Theta. \tag{B.16}$$

Assuming the thermodynamic processes in the fluid occur sufficiently fast that no heat transfer takes place between the regions undergoing the compression and rarefaction, the system is considered to be adiabatic

$$\delta Q = 0. \tag{B.17}$$

Substituting (B.14) and (B.17) into (B.13) yields

$$\frac{m}{M} C_V \,\mathrm{d}\Theta + p \,\mathrm{d}V = 0 \tag{B.18}$$

meaning the mechanical work can be either done by or on the system. Since an ideal gas obeys the equation of state

$$pV = nR\Theta, \tag{B.19}$$

with $n = m/M$ the amount of substance, the thermodynamic temperature Θ may be eliminated from equation (B.18). Differentiating an equation of state (B.19)

$$p \,\mathrm{d}V + V \,\mathrm{d}p = nR \,\mathrm{d}\Theta \tag{B.20}$$

and its substitution into (B.20) yields

$$(C_V + R) \, p \,\mathrm{d}V + C_V V \,\mathrm{d}p = 0, \tag{B.21}$$

with R being the universal gas constant.

Since $\kappa = C_p/C_V$ and $C_V + R = C_p$ (Mayer's relation), equation (B.21) may be simplified as follows

$$\kappa \frac{\mathrm{d}V}{V} + \frac{\mathrm{d}p}{p} = 0. \tag{B.22}$$
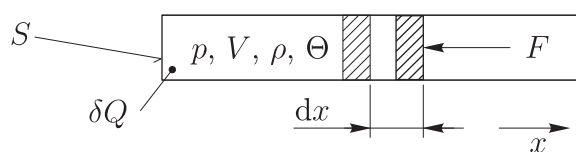
Figure B.3: The first law of thermodynamics

Integrating (B.22) yields the Poisson's equation for an ideal fluid undergoing an adiabatic process

$$pV^{\kappa} = C \tag{B.23}$$

or rewritten in terms of density using the inverse proportionality relation between volume and density $V \sim \rho^{-1}$

$$p\rho^{-\kappa} = C, \tag{B.24}$$

with C an arbitrary constant. Due to the power of κ, the pressure-density relation (B.24) is, however, non-linear.

Linearised steady-state wave equation *(The Helmholtz equation)*

In the previous section, three fundamental equations governing the relations between the pressure p, mass density ρ and fluid velocity **v** in an inviscid fluid were derived. For the reader's convenience, the set of equations is repeated here:

- the Eulerian equation of motion

$$-\nabla p = \rho \left(\frac{\partial \mathbf{v}}{\partial t} + (\mathbf{v} \cdot \nabla)\mathbf{v} \right), \tag{B.25a}$$

- the continuity equation

$$q - \nabla \cdot \mathbf{v} = \frac{1}{\rho} \left(\frac{\partial \rho}{\partial t} + \mathbf{v} \cdot \nabla \rho \right), \tag{B.25b}$$

- the Poisson's equation

$$p = C\rho^{\kappa}. \tag{B.25c}$$

Despite the initial considerations concerning the fluid properties all three equations (B.25) are non-linear. Consider a Taylor-series expansion of a function $f(x)$ around a point a

$$f(x) = \sum_{n=0}^{\infty} \frac{f^{(n)}(a)}{n!}(x - a)^n, \tag{B.26}$$

with a denoting point the derivative of f is evaluated at, which is located in the vicinity of x. Representing the pressure-density relation (B.25c) expressed for an ambient state $C = b/\rho^{\kappa}$ in terms of a Taylor-series expansion (B.26) yields

$$p' = \frac{\kappa p}{\rho}\rho' + \frac{\kappa(\kappa - 1)}{2\rho_0^2}(\rho')^2 + \dots \quad . \tag{B.27}$$

If one retains only the first order terms in (B.27), assumes that there is no ambient external flow $(q_0 \equiv 0)$, assumes a linear perturbation, i.e. a sufficiently small variation of the variables with respect to ambient fields

$$p'(\mathbf{r}, t) \ll b \tag{B.28a}$$

$$\rho'(\mathbf{r}, t) \ll \rho \tag{B.28b}$$

and omits the convective terms in favour of the local derivatives in equations (B.25a) and (B.25b), then the linearised set of equations (B.25) becomes

$$-\nabla p' = \rho \frac{\partial \mathbf{v}'}{\partial t}, \tag{B.29a}$$

$$q' - \nabla \cdot \mathbf{v}' = \frac{1}{\rho} \frac{\partial \rho'}{\partial t}, \tag{B.29b}$$

$$p' = \frac{\kappa b}{\rho} \rho'. \tag{B.29c}$$

As the pressure $p' = p(\mathbf{r}, t)$ and density $\rho' = \rho(\mathbf{r}, t)$ are the functions of time at a certain position in fluid $\mathbf{r}$, the rate of change of pressure and density is given by differentiating (B.29c) with respect to time

$$\frac{\partial p}{\partial t} = \frac{\kappa b}{\rho} \frac{\partial \rho}{\partial t}. \tag{B.30}$$

As the instantaneous acoustic pressure p' is considered to be the principal physical quantity describing an arbitrary acoustic perturbation field, the density $\rho' = \rho'(\mathbf{r}, t)$ may be eliminated from equation (B.29b) by substituting (B.30). Applying the divergence operator $\nabla\cdot$ on (B.29a) and differentiating (B.29b) with respect to time yields the wave equation for acoustic pressure

$$\nabla^2 p - \frac{1}{c^2} \frac{\partial^2 p}{\partial t^2} = -\rho \frac{\partial q'}{\partial t}, \tag{B.31}$$

where c denotes the phase speed of an acoustic wave in fluid

$$c = \sqrt{\frac{\kappa b}{\rho}}. \tag{B.32}$$

Using the equation of state for an ideal gas (B.19), the relation (B.32) may be rewritten

$$c = \sqrt{\frac{\kappa R \Theta}{M}}, \tag{B.33}$$

in which κ, R and M are material constants, so that the speed of sound merely depends on a thermodynamic state of fluid. By assuming a time-harmonic variation of the field variables, i.e. $p'(\mathbf{r}, t) = p'(\mathbf{r})e^{j\omega t}$ for pressure as the primary variable, while the same applies for mass density

fluctuations ρ' and acoustic velocity $\mathbf{v}'$, the wave equation (B.31) becomes a steady-state form of

$$\nabla^2 p'(\mathbf{r}) + k^2 p'(\mathbf{r}) = -\mathrm{j}\rho\omega q'\delta(\mathbf{r}, \mathbf{r}_q), \quad \forall \mathbf{r} \in \Omega \tag{B.34}$$

with $\mathbf{r}$ the position vector, $\mathrm{j} = \sqrt{-1}$ the imaginary unit, ω the circular frequency, $k = \omega/c$ the wave number, q the strength amplitude of the acoustic volume velocity point source located at position $\mathbf{r}_q$, and δ the Dirac delta function. Equation (B.34) is also referred to as the Helmholtz equation. Rearranging the equation of motion (B.29a) by considering the steady-state acoustics yields the expression for the particle velocity, which is proportional to a gradient of the sound pressure

$$\mathbf{v}'(\mathbf{r}) = \frac{\mathrm{j}}{\rho\omega} \nabla p'(\mathbf{r}). \tag{B.35}$$

Note that the primes on the acoustic variables in (B.34) and (B.35) are usually omitted, when there is little possibility of confusing the ambient field variables with their acoustic perturbations.

B.3 Interior acoustic problems

An acoustic problem is referred to as an interior one if the fluid forming the solution domain Ω has a final size and is confined by its boundary $\partial\Omega$, see figure B.4(a). Since the Helmholtz equation (B.34) is a second-order partial differential equation, one boundary condition has to be specified at each point of the boundary in order for the problem to be well-posed. At the problem boundary $\partial\Omega = \Gamma$ three types of boundary condition forming a non-overlapping set $\Gamma = \Gamma_p \cup \Gamma_v \cup \Gamma_Z$ may be imposed:

- pressure boundary condition (Dirichlet/essential) $\forall \mathbf{r} \in \Gamma_p$:

$$p(\mathbf{r}) = \bar{p}(\mathbf{r}), \tag{B.36a}$$

- normal velocity boundary condition (Neumann/natural) $\forall \mathbf{r} \in \Gamma_v$:

$$\mathcal{L}_v(p(\mathbf{r})) = \frac{\mathrm{j}}{\rho\omega} \frac{\partial p(\mathbf{r})}{\partial n} = \bar{v}_n(\mathbf{r}), \tag{B.36b}$$

- normal impedance boundary condition (Robin/mixed) $\forall \mathbf{r} \in \Gamma_Z$:

$$\mathcal{L}_Z(p(\mathbf{r})) = \mathcal{L}_v(p(\mathbf{r})) - \frac{p(\mathbf{r})}{\bar{Z}_n(\mathbf{r})} = 0 \tag{B.36c}$$

with $\frac{\partial}{\partial n}$ the normal derivative and $\bar{p}(\mathbf{r})$, $\bar{v}_n(\mathbf{r})$ and $\bar{Z}_n(\mathbf{r})$ the prescribed values of the acoustic pressure, normal velocity and normal impedance, respectively.

(a)   (b)
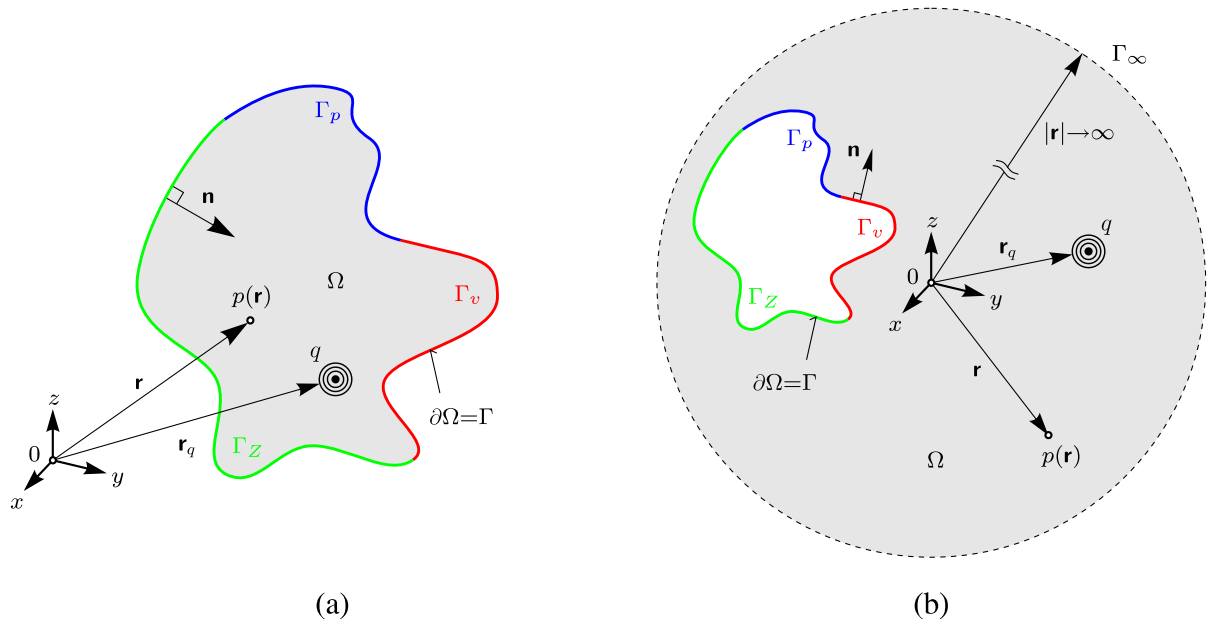
Figure B.4: A general uncoupled (a) interior and (b) unbounded acoustic problem

B.4 Unbounded acoustic problems

An unbounded acoustic problem involves domain Ω of an infinite extent, see figure B.4(b). Besides the boundary conditions (B.36) prescribed at the physical boundary Γ, an additional Sommerfeld radiation condition has to be imposed at Γ_∞ in order to ensure that no acoustic energy reflections occur at infinity $\forall \mathbf{r} \in \Gamma_\infty$:

$$\lim_{|\mathbf{r}| \to \infty} \left[|\mathbf{r}| \left(\frac{\partial p(\mathbf{r})}{\partial |\mathbf{r}|} + \mathrm{j}kp(\mathbf{r}) \right) \right] = 0. \tag{B.37}$$

Appendix C

Methodology and application of the Wave Based Technique for 2D problems

This appendix describes the methodology of the wave based technique for two-dimensional acoustic problems. First, section C.1 presents a general 2D acoustic problem considering both the interior and unbounded spatial domains.Section C.2 then reviews the mathematical formulation of WBT for the interior and unbounded 2D acoustic problems. Finally, section C.3 shows the application of the proposed approach to a 2D validation example considering a sound radiation analysis of a car-like cavity with an open boundary.

C.1 Problem definition

Consider an interior two-dimensional acoustic problem as shown in figure C.1. The problem consists of a closed boundary surrounded by fluid characterised by its speed of sound c and the density ρ. Assuming that the system is linear, the fluid is inviscid, and the process is adiabatic, the steady-state pressure response $p(\mathbf{r}, t) = p(\mathbf{r})\mathrm{e}^{\mathrm{j}\omega t}$ at an arbitrary position $\mathbf{r}$ within the solution domain Ω is governed by the inhomogeneous Helmholtz equation

$$\nabla^2 p(\mathbf{r}) + k^2 p(\mathbf{r}) = -\mathrm{j}\rho\omega q \delta(\mathbf{r}, \mathbf{r}_q), \ \forall \mathbf{r} \in \Omega, \tag{C.1}$$

where $\triangle \equiv \frac{\partial^2}{\partial x^2} + \frac{\partial^2}{\partial y^2}$ represents the Laplace operator in Cartesian coordinates, $\mathbf{r}$ the position vector, $\mathrm{j} = \sqrt{-1}$ the imaginary unit, ω the circular frequency, $k = \omega/c$ the wave number, q the strength of the acoustic volume velocity point source located at position $\mathbf{r}_q$, and δ the Dirac delta function.

C.1.1 Interior acoustic problems

Since the Helmholtz equation (C.1) is a second-order partial differential equation, one boundary condition has to be specified at each point of the boundary in order for the problem to be well-

posed. At the problem boundary $\partial\Omega = \Gamma$, three types of boundary condition forming a non-overlapping set $\Gamma = \Gamma_p \cup \Gamma_v \cup \Gamma_Z$ may be imposed:

- pressure boundary condition (Dirichlet/essential) $\forall \mathbf{r} \in \Gamma_p$:

$$p(\mathbf{r}) = \bar{p}(\mathbf{r}), \tag{C.2a}$$

- normal velocity boundary condition (Neumann/natural) $\forall \mathbf{r} \in \Gamma_v$:

$$\mathcal{L}_v(p(\mathbf{r})) = \bar{v}_n(\mathbf{r}), \tag{C.2b}$$

- normal impedance boundary condition (Robin/mixed) $\forall \mathbf{r} \in \Gamma_Z$:

$$\mathcal{L}_v(p(\mathbf{r})) = \frac{p(\mathbf{r})}{\bar{Z}_n(\mathbf{r})}, \tag{C.2c}$$

with the differential operator $\mathcal{L}_v(p(\mathbf{r}))$ as defined in (C.2b) and $\bar{p}(\mathbf{r})$, $\bar{v}_n(\mathbf{r})$ and $\bar{Z}_n(\mathbf{r})$ the prescribed values of the acoustic pressure, normal velocity and normal impedance, respectively. The particle velocity is proportional to a gradient of the sound pressure $p(\mathbf{r})$ and is defined as follows

$$\mathbf{v}(\mathbf{r}) = \frac{\mathrm{j}}{\rho\omega}\nabla p(\mathbf{r}). \tag{C.3}$$

As will be shown in section C.2, the velocity can be derived from the primary pressure results without any additional loss of accuracy, since the differentiation of the shape function used in the framework of the wave based approach can be performed in an analytical way.
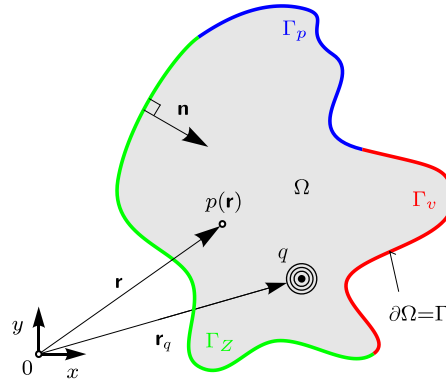
Figure C.1: A 2D interior acoustic problem (Rejlek et al., 2008a)

C.1.2 Unbounded acoustic problems

In addition to the boundary conditions (C.2) prescribed at the physical boundary Γ the Sommerfeld radiation condition has to be imposed at Γ_∞ in order to ensure, that no acoustic energy reflections occur at the infinity $\forall \mathbf{r} \in \Gamma_\infty$:

$$\lim_{r\to\infty}\left(\sqrt{r}\frac{\partial p}{\partial r} + \mathrm{j}kp\right) = 0. \tag{C.4}$$
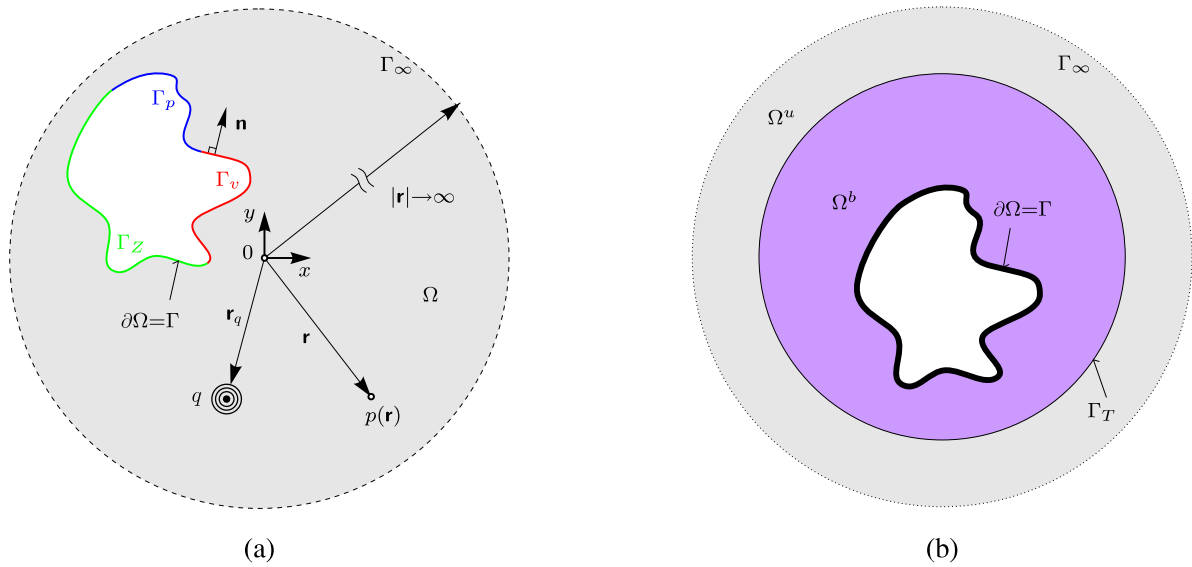
Figure C.2: (a) A 2D unbounded acoustic problem and (b) the concept of a truncation boundary Γ_T (Rejlek et al., 2007)

C.2 Basic concepts of the Wave Based Technique

This section describes the formulation of WBT for 2D acoustic problems. For a full derivation of the underlying theory, see section 5.2, which introduces the general concepts of WBT that are valid for 3D acoustic problems. This section only describes the specific distinctions that are relevant to 2D problems.

Similar to the formulation of WBT for three-dimensional unbounded acoustic problems, see chapter 5, the concept of an artificial truncation boundary Γ_T is adopted. The Γ_T divides the wave model into a bounded part and an unbounded part $\Omega = \Omega^b + \Omega^u$, see figure C.2(b). While the conventional interior formulation is used in the bounded part, some special-purpose functions, which also satisfy the Sommerfeld radiation condition (C.4), are adopted in the unbounded part.

C.2.1 Domain decomposition

To meet the converge requirements of WBT, the truncated solution domain Ω^b needs to be subdivided into a number of convex subdomains. At the coupling interface Γ_i between two subdomains, the following continuity conditions have to be imposed

$$\frac{\mathrm{j}}{\rho\omega}\frac{\partial p_1(\mathbf{r}_1)}{\partial n_1} - \frac{p_1(\mathbf{r}_1)}{\bar{Z}_{int}} = -\frac{\mathrm{j}}{\rho\omega}\frac{\partial p_2(\mathbf{r}_2)}{\partial n_2} - \frac{p_2(\mathbf{r}_2)}{\bar{Z}_{int}}, \qquad \mathbf{r}_{1,2} \in \Gamma_i \qquad (C.5a)$$

$$\frac{\mathrm{j}}{\rho\omega}\frac{\partial p_2(\mathbf{r}_2)}{\partial n_2} - \frac{p_2(\mathbf{r}_2)}{\bar{Z}_{int}} = -\frac{\mathrm{j}}{\rho\omega}\frac{\partial p_1(\mathbf{r}_1)}{\partial n_1} - \frac{p_1(\mathbf{r}_1)}{\bar{Z}_{int}}, \qquad \mathbf{r}_{1,2} \in \Gamma_i, \qquad (C.5b)$$

where n_1 and, n_2 are the outward-oriented normal vectors and $\bar{Z}_{int}$ is a non-zero complex number, which is set to ρc throughout this work.

C.2.2 Field variable expansion

Following the concept of a truncation boundary, different solution expansions are applied in the respective regions of the wave model. In the bounded part, a linear combination of basis functions extended by a particular solution function approximates the exact pressure solution. For the explicit modelling of the unbounded domain, the solution expansion must also satisfy the Sommerfeld radiation condition (C.4).

C.2.2.1 Bounded domain

Within the bounded part of the wave model, a linear combination of the shape functions approximates the exact pressure solution

$$p^b(\mathbf{r}) \approx \hat{p}^b(\mathbf{r}) = \sum_{i=1}^{M} p_i^b \Phi_i^b(\mathbf{r}) + \hat{p}_q(\mathbf{r}) = \mathbf{\Phi}^b(\mathbf{r})\, \mathbf{p}^b + \hat{p}_q(\mathbf{r}) \tag{C.6}$$

with the wave function set

$$\mathbf{\Phi}^b(\mathbf{r}) = \begin{cases} \Phi_r(x,y) = \cos(k_{rx}x)\, \mathrm{e}^{-\mathrm{j}k_{ry}y} \\[2mm] \Phi_s(x,y) = \mathrm{e}^{-\mathrm{j}k_{sx}x}\, \cos(k_{sy}y) \end{cases} \tag{C.7}$$

and p_i^b the M unknown contribution factors forming the interior degrees of freedom

$$M = \dim \mathbf{\Phi}^b = 2(n_r + 1) + 2(n_s + 1). \tag{C.8}$$

In equation (C.6), $\hat{p}_q(\mathbf{r})$ is the particular solution function representing the source term on the right hand side of the Helmholtz equation (C.1). The particular solution does not affect the size of the wave model.

Each function in the set (C.7) is an exact solution of the homogeneous Helmholtz equation (C.1). Since the only requirement for the wave number components in (C.7) is that

$$k_{rx}^2 + k_{ry}^2 = k_{sx}^2 + k_{sy}^2 = k^2, \tag{C.9}$$

an infinite number of wave functions (C.7) can be defined for the expansion (C.6). The wave number components are selected as follows (Desmet, 1998)

$$k_\bullet = \begin{cases} k_{rx} = \dfrac{r\pi}{L_x}, & r = 0, 1, 2, \ldots, n_r \qquad k_{ry} = \pm\sqrt{k^2 - k_{rx}^2} \\[3mm] k_{sy} = \dfrac{s\pi}{L_y}, & s = 0, 1, 2, \ldots, n_s \qquad k_{sx} = \pm\sqrt{k^2 - k_{sy}^2}. \end{cases} \tag{C.10}$$

The integer sets r and s determine the M degrees of freedom of the interior model, and L_x and L_y are the dimensions of the smallest rectangular domain enclosing the considered problem domain, the so-called bounding box.

C.2.2.2   Unbounded domain

Besides the Helmholtz equation (C.1) and the boundary conditions (C.2) prescribed at the physical boundary of the problem, the pressure approximation applied in the unbounded domain needs to satisfy the Sommerfeld radiation condition (C.4). The following pressure solution expansion complies with these requirements and converges for $N \to \infty$

$$p^u(\mathbf{r}) \approx \hat{p}^u(r, \varphi) = A_0 \mathrm{H}_0^{(2)}(kr) \sum_{n=1}^{N} \mathrm{H}_n^{(2)}(kr) \left(A_n \cos(n\varphi) + B_n \sin(n\varphi)\right) \tag{C.11}$$

with r and φ the polar radial and angular coordinates, $\mathrm{H}_n^{(2)}(kr)$ the nth order Hankel function of the second kind, and A_0, A_n and B_n the unknown contribution factors. Equation (C.11) may be rewritten in terms of two subsets

$$\hat{p}^u(r, \varphi) = \sum_{n_c=0}^{N} p_{n_c}^u \Phi_{n_c}^u(r, \varphi) + \sum_{n_s=1}^{N} p_{n_s}^u \Phi_{n_s}^u(r, \varphi) \tag{C.12}$$

with $\Phi_{n_c}^u$ and $\Phi_{n_s}^u$ being the radiation wave functions defined as

$$\boldsymbol{\Phi}_n^u(r, \varphi) = \begin{cases} \Phi_{n_c}^u(r, \varphi) = \mathrm{H}_{n_c}^{(2)}(kr) \cos(n_c\varphi) \\[2mm] \Phi_{n_s}^u(r, \varphi) = \mathrm{H}_{n_s}^{(2)}(kr) \sin(n_s\varphi) \end{cases} \tag{C.13}$$

and $p_{n_c}^u$ and $p_{n_s}^u$ the unknown contribution factors yielding the unbounded degrees of freedom

$$\dim \boldsymbol{\Phi}^u = 2N + 1. \tag{C.14}$$

C.2.3   Evaluation of boundary and interface conditions

The pressure approximations in the bounded (C.6) and unbounded (C.11) parts of the wave model satisfy the governing differential equation (C.1), but violate the boundary conditions (C.2) and the interface conditions (C.5a) and (C.5b). The unknown contribution functions p_i^b, $\Phi_{n_c}^u$ and $\Phi_{n_s}^u$ are determined by minimising the approximation errors of the boundary and interface conditions in an integral sense by applying the weighed residual formulation. The residual errors arising at the boundaries and interfaces of the corresponding subdomains are defined as follows

$$\mathbf{r} \in \Gamma_p : \quad R_p(\mathbf{r}) = \hat{p}(\mathbf{r}) - \bar{p}(\mathbf{r}), \tag{C.15a}$$

$$\mathbf{r} \in \Gamma_v : \quad R_v(\mathbf{r}) = \mathcal{L}_v(\hat{p}(\mathbf{r})) - \bar{v}_n, \tag{C.15b}$$

$$\mathbf{r} \in \Gamma_Z : \quad R_Z(\mathbf{r}) = \mathcal{L}_v(\hat{p}(\mathbf{r})) - \frac{\hat{p}(\mathbf{r})}{\bar{Z}_n(\mathbf{r})}, \tag{C.15c}$$

$$\mathbf{r} \in \Gamma_i : \quad R_i(\mathbf{r}) = \mathcal{L}_{1v}(\hat{p}_1(\mathbf{r})) - \frac{\hat{p}_1(\mathbf{r})}{\bar{Z}_i} + \mathcal{L}_{2v}(\hat{p}_2(\mathbf{r})) + \frac{\hat{p}_2(\mathbf{r})}{\bar{Z}_i}. \tag{C.15d}$$

For each subdomain Ω^e, the involved boundary residual error functions (C.15) are orthogonalised with respect to weighting function $\tilde{p}$ or its derivative

$$-\int_{\Gamma_p}\mathcal{L}_v(\tilde{p}(\mathbf{r}))R_p(\mathbf{r})\,\mathrm{d}\Gamma + \int_{\Gamma_v}\tilde{p}(\mathbf{r})R_v(\mathbf{r})\,\mathrm{d}\Gamma + \int_{\Gamma_Z}\tilde{p}(\mathbf{r})R_Z(\mathbf{r})\,\mathrm{d}\Gamma + \int_{\Gamma_i}\tilde{p}(\mathbf{r})R_i(\mathbf{r})\,\mathrm{d}\Gamma = 0. \quad \text{(C.16)}$$

Using the Galerkin approach, the weighting functions are expanded in terms of the same basis functions $\boldsymbol{\Phi}$ as those used for the pressure approximation $\hat{p}$ (C.6)

$$\tilde{p}(\mathbf{r}) = \sum_{i=1}^{M}\tilde{c}_i\Phi_i(\mathbf{r}) = \boldsymbol{\Phi}(\mathbf{r})\,\tilde{\mathbf{c}}, \quad \text{(C.17)}$$

where $\tilde{\mathbf{c}}$ represents an arbitrary weighting function contribution factor. Substituting the pressure approximation (C.6) and the weighting function (C.17) in the weighted residual formulation (C.16), together with the requirement that this relation should hold for any set of contribution factors $\tilde{\mathbf{c}}$, yields the following wave based model

$$\begin{bmatrix} (\mathbf{A}_1 + \mathbf{C}_{1b}) & \mathbf{C}_{12} \\ \mathbf{C}_{21} & (\mathbf{A}_2 + \mathbf{C}_{2b}) \end{bmatrix} \begin{Bmatrix} p_1 \\ p_2 \end{Bmatrix} = \begin{Bmatrix} \mathbf{b}_1 + \mathbf{c}_{1b} + \mathbf{c}_{12} \\ \mathbf{b}_2 + \mathbf{c}_{2b} + \mathbf{c}_{21} \end{Bmatrix} \quad \text{(C.18)}$$

with

$$\mathbf{A}_e = \mathbf{A}_p + \mathbf{A}_v + \mathbf{A}_Z \qquad \mathbf{b}_e = \mathbf{b}_p + \mathbf{b}_v + \mathbf{b}_Z, \quad \text{(C.19)}$$

where $e = 1, 2$ denotes the corresponding subdomain. The system matrices and vectors $\mathbf{A}_\bullet$ and $\mathbf{b}_\bullet$ together with the coupling $\mathbf{C}_{eg}$, $\mathbf{c}_{eg}$ ($g = 2, 1$) and back-coupling terms $\mathbf{C}_{eb}$, $\mathbf{c}_{eb}$ are defined as follows

$$\mathbf{A}_p = -\int_{\Gamma_p}\mathcal{L}_v(\boldsymbol{\Phi}^\mathsf{T})\boldsymbol{\Phi}\,\mathrm{d}\Gamma, \qquad\qquad \mathbf{b}_p = -\int_{\Gamma_p}\mathcal{L}_v(\boldsymbol{\Phi}^\mathsf{T})(\bar{p} - \hat{p}_q)\,\mathrm{d}\Gamma, \qquad \text{(C.20a)}$$

$$\mathbf{A}_v = \int_{\Gamma_v}\boldsymbol{\Phi}^\mathsf{T}\mathcal{L}_v(\boldsymbol{\Phi})\,\mathrm{d}\Gamma, \qquad\qquad \mathbf{b}_v = \int_{\Gamma_v}\mathcal{L}_v(\boldsymbol{\Phi}^\mathsf{T})(\bar{v}_n - \mathcal{L}_v(\hat{p}_q))\,\mathrm{d}\Gamma, \qquad \text{(C.20b)}$$

$$\mathbf{A}_Z = -\int_{\Gamma_Z}\boldsymbol{\Phi}^\mathsf{T}\mathcal{L}_Z(\boldsymbol{\Phi})\,\mathrm{d}\Gamma, \qquad\qquad \mathbf{b}_Z = -\int_{\Gamma_Z}\boldsymbol{\Phi}^\mathsf{T}\mathcal{L}_Z(\hat{p}_q)\,\mathrm{d}\Gamma, \qquad \text{(C.20c)}$$

$$\mathbf{C}_{1b} = \int_{\Gamma_i}\boldsymbol{\Phi}_1^\mathsf{T}\left[\mathcal{L}_{1v}(\boldsymbol{\Phi}_1) - \frac{\boldsymbol{\Phi}_1}{\bar{Z}_i}\right]\mathrm{d}\Gamma, \qquad \mathbf{c}_{1b} = -\int_{\Gamma_i}\boldsymbol{\Phi}_1^\mathsf{T}\left[\mathcal{L}_{1v}(\hat{p}_{q1}) - \frac{\hat{p}_{q1}}{\bar{Z}_i}\right]\mathrm{d}\Gamma, \qquad \text{(C.20d)}$$

$$\mathbf{C}_{12} = \int_{\Gamma_i}\boldsymbol{\Phi}_1^\mathsf{T}\left[\mathcal{L}_{2v}(\boldsymbol{\Phi}_2) + \frac{\boldsymbol{\Phi}_2}{\bar{Z}_i}\right]\mathrm{d}\Gamma, \qquad \mathbf{c}_{12} = -\int_{\Gamma_i}\boldsymbol{\Phi}_1^\mathsf{T}\left[\mathcal{L}_{2v}(\hat{p}_{q2}) + \frac{\hat{p}_{q2}}{\bar{Z}_i}\right]\mathrm{d}\Gamma, \qquad \text{(C.20e)}$$

$$\mathbf{C}_{2b} = \int_{\Gamma_i}\boldsymbol{\Phi}_2^\mathsf{T}\left[\mathcal{L}_{2v}(\boldsymbol{\Phi}_2) + \frac{\boldsymbol{\Phi}_2}{\bar{Z}_i}\right]\mathrm{d}\Gamma, \qquad \mathbf{c}_{2b} = -\int_{\Gamma_i}\boldsymbol{\Phi}_2^\mathsf{T}\left[\mathcal{L}_{2v}(\hat{p}_{q2}) + \frac{\hat{p}_{q2}}{\bar{Z}_i}\right]\mathrm{d}\Gamma, \qquad \text{(C.20f)}$$

$$\mathbf{C}_{21} = \int_{\Gamma_i}\boldsymbol{\Phi}_2^\mathsf{T}\left[\mathcal{L}_{1v}(\boldsymbol{\Phi}_1) - \frac{\boldsymbol{\Phi}_1}{\bar{Z}_i}\right]\mathrm{d}\Gamma, \qquad \mathbf{c}_{21} = -\int_{\Gamma_i}\boldsymbol{\Phi}_2^\mathsf{T}\left[\mathcal{L}_{1v}(\hat{p}_{q1}) - \frac{\hat{p}_{q1}}{\bar{Z}_i}\right]\mathrm{d}\Gamma. \qquad \text{(C.20g)}$$

In order to assemble the matrix system (C.18), the integrals (C.20) are evaluated in a numerical manner using the Gauss-Legendre quadrature rule.

C.3 Validation example: sound brick 2D

Consider a 2D car-like cavity of dimensions $3 \times 1, 4$ m with an open boundary, see figure C.3(a). At the inner side of a panel representing the firewall, a normal velocity boundary condition $v_n = 1$ m/s is imposed, whereas the remaining structure is assumed to be perfectly rigid, i.e. $v_n = 0$ m/s. The problem is surrounded by air with the speed of sound $c = 344.8$ m/s and the mass density $\rho = 1.2 \text{ kg/m}^3$.

(a)   (b)
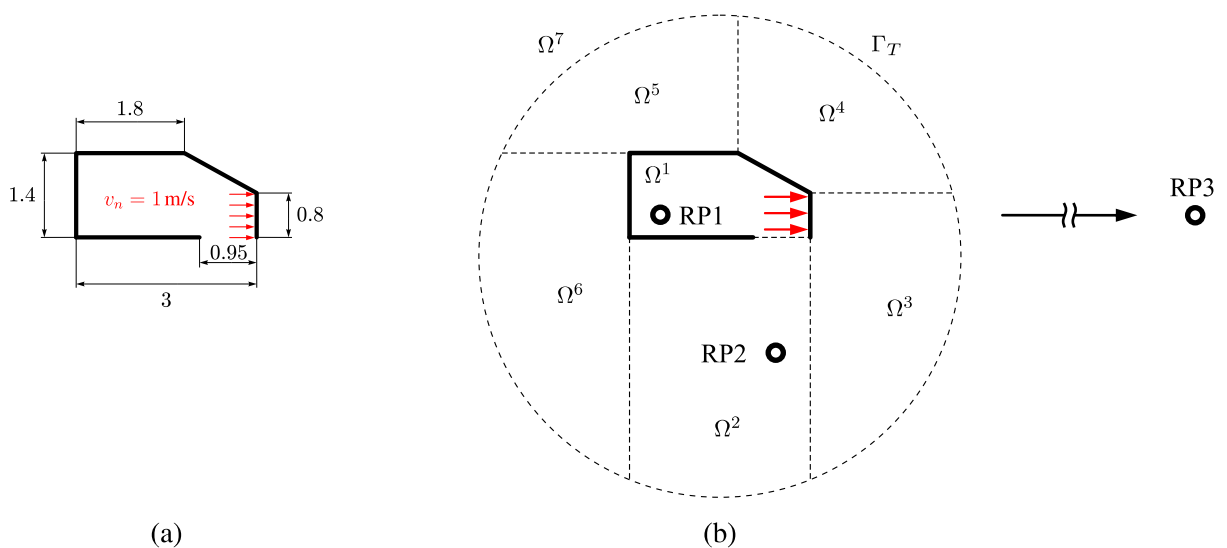
Figure C.3: Sound brick 2D: (a) problem definition with dimensions in [m] and (b) the corresponding WB model (Rejlek et al., 2007)

Figure C.3(b) shows the corresponding wave model consisting of 6 bounded and one unbounded domain (Rejlek et al., 2007). Within the bounded part, each of the 6 subdomains uses $n_r = n_s = 19$ to truncate the size of the wave function set. The model is subdivided into a bounded part and an unbounded part by introducing a truncation boundary Γ_T of radius $R = 4$ m. In addition, wave functions up to order $L = 10$ are applied in the unbounded region of the wave model, which yields a total number of 501 degrees of freedom. For the subsequent evaluation of the numerical results, three response points located in different regions of the model, namely inside the cavity (RP1), within the bounded region (RP2) and outside the truncation boundary (RP3), are selected, see figure C.3(b).

A BE model of the problem considered, which consists of 740 nodes and 739 linear elements with a maximum element length $h_{max} = 0.01$ m, is assembled. As the boundary of the problem is open, an indirect BEM formulation is used. The BE model is solved using *LMS/SYSNOISE* Rev. 5.6 (LMS International, 2010). The proposed BE model is considered a reference model in the frequency range of interest. Figure C.4 captures the pressure magnitude fields predicted at 80 Hz using the BEM and WBT. The contour plot proves the pressure continuity at the interfaces between the subdomains. Figure C.6 plots the pressure response spectra in the range 1–500 Hz

predicted in three different response points. The wave based results demonstrate the accuracy of the proposed approach in the whole frequency range of interest.

(a)   (b)
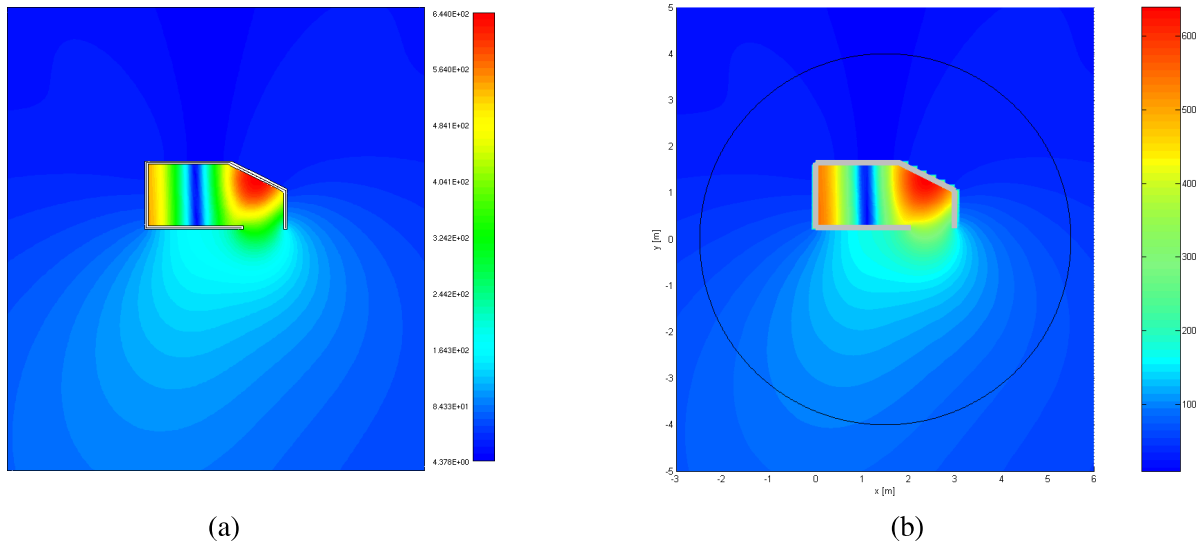
Figure C.4: Sound brick 2D: pressure magnitude predicted at 80 Hz by (a) BEM and (b) WBT

(a)   (b)
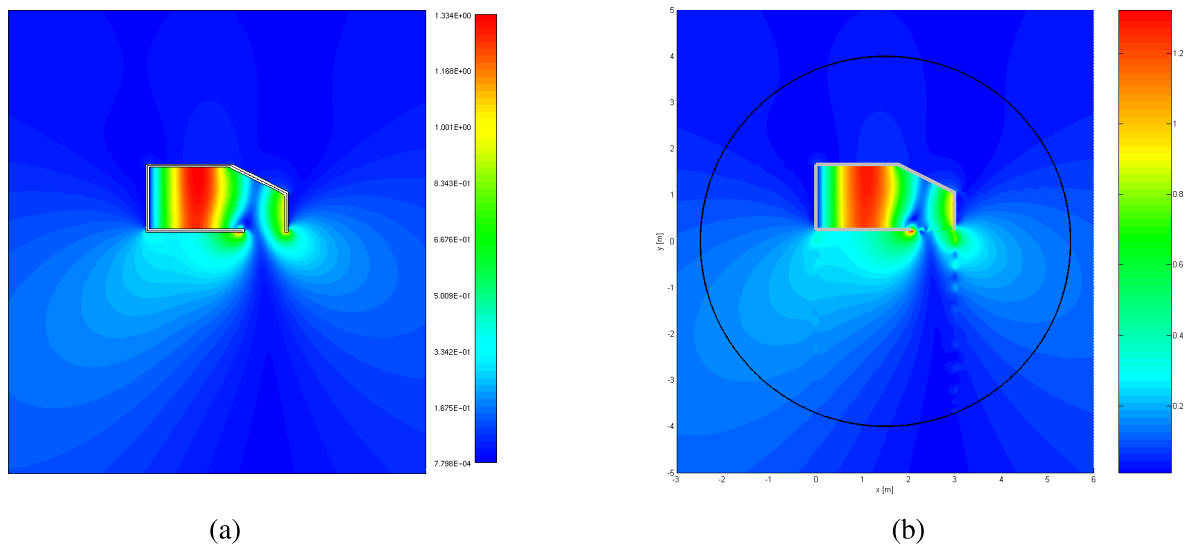
Figure C.5: Sound brick 2D: magnitude of the velocity x component field predicted at 80 Hz by (a) BEM and (b) WBT

Using equation (C.3) to relate the particle velocity to the sound pressure, the velocity field can be derived, as shown in figure C.5. However, a detailed investigation of the velocity distribution at the coupling interfaces reveals the violation of the continuity conditions – most distinctively between subdomains 2 and 3. In element 3, there is a common boundary edge with different types of prescribed boundary conditions. At the part adjacent to the cavity (element 1), a rigid boundary condition is imposed, while at the interface with element 2 the coupling condition is applied. This implies, that an arbitrary velocity may occur along this boundary segment.
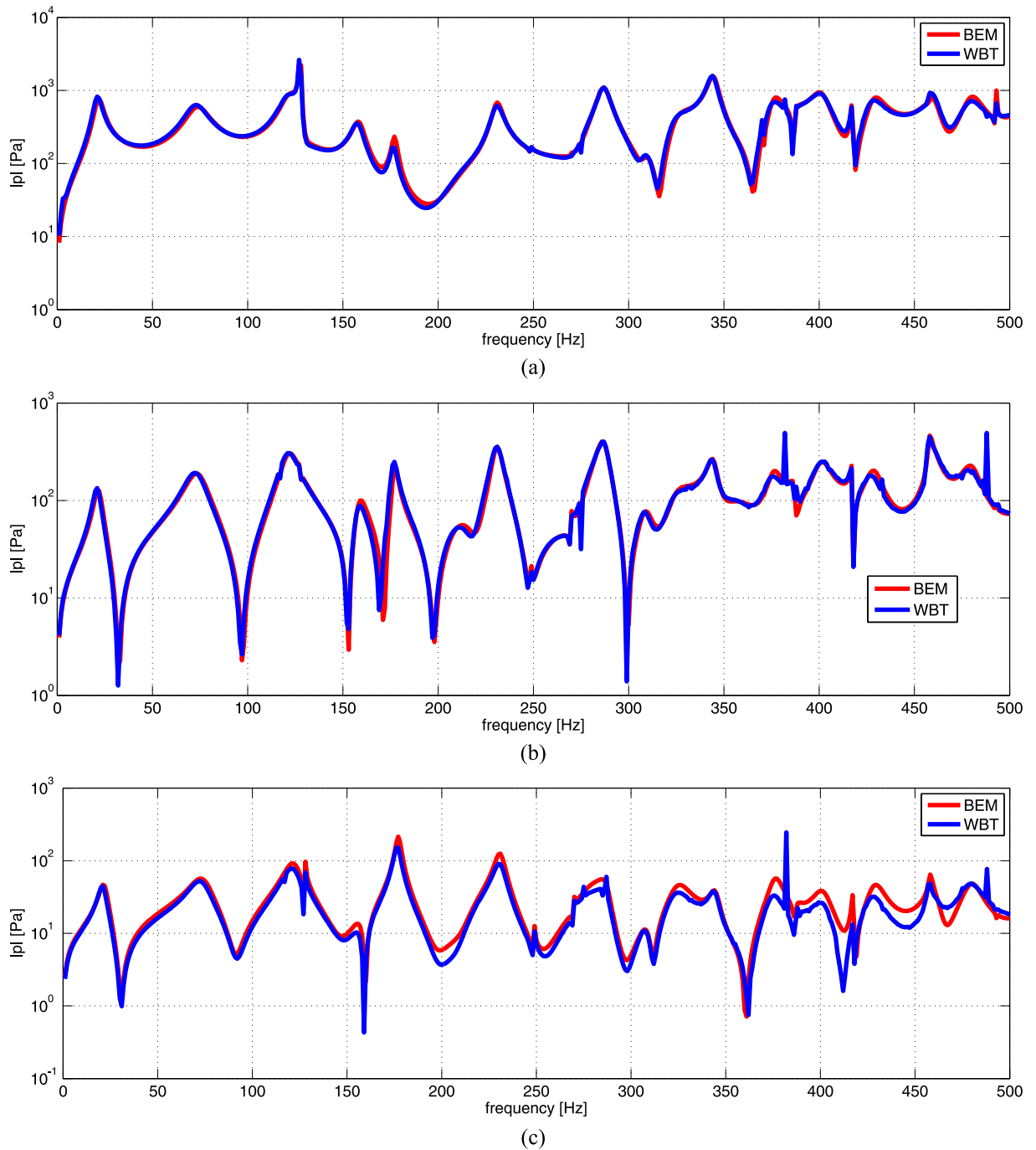
Figure C.6: Sound brick 2D: pressure response spectra predicted with BEM and WBT at point (a) RP1, (b) RP2 and (c) RP3 (Rejlek et al., 2007)

This problem is related to the existence of discontinuity in the boundary conditions. Appendix D describes the possible countermeasures for mitigating a deterioration of the WB prediction accuracy at the coupling interfaces between the subdomains.

Appendix D

Enrichment of the set of basis functions

Recent developments of the WBT for the analysis of unbounded acoustic problems have proven the efficiency of this novel approach for both two-dimensional (Pluymers et al., 2005) and three-dimensional problems (Diwoky et al., 2008). However, the preceding investigations (Rejlek et al., 2007; Mócsai et al., 2009) have also shown the importance of proper model discretisation. As demonstrated in appendix C, the prediction accuracy of WBT tends to deteriorate if a discontinuous boundary condition occurs in the wave model. In the WB formulation for interior problems the set of basis functions consists of globally defined wave-like functions which represent the evanescent and propagating plane waves. To avoid a decrease of the prediction accuracy in this particular case, either a sufficient number of shape functions (p-refinement) or a finer model discretisation with respect to those phenomena (h-refinement) has to be applied. Nevertheless, these refinement strategies imply, that the wave models become large and hence less economical.

This appendix reports on the investigations of modelling aspects, which consider the effects of a discontinuous boundary condition. It outlines the basic concepts of an enrichment strategy, which has been introduced in order to preserve the favourable computational efficiency of the wave based approach. The essential idea of the proposed approach is to enrich the original wave function set with some novel functions, which inherently satisfy the governing differential equation and a priori incorporate the discontinuous boundary condition. The achieved efficiency improvements are demonstrated by a two-dimensional validation example. First, a problem-specific enrichment scheme based on the numerical solution of an associated problem is discussed, while an outlook for the further development presents a more general enrichment strategy.

D.1 Discontinuous boundary condition

The essential property of the wave based technique is the selection of the shape functions. In contrast to finite or boundary element schemes, these wave-like functions satisfy the governing differential equation exactly. This inherent feature makes WBT extremely suitable for the analysis of steady-state acoustic problems. Since the Helmholtz equation (C.1) is a second order

partial differential equation, a classic formulation of the pressure has to be twice differentiable within the solution domain Ω, i.e. C^2-continuous. The velocity is C^1-continuous in Ω. At the boundary of the Neumann problem, however, it is sufficient for the pressure to be C^1. Normal velocity may exhibit discontinuities. Nevertheless, as the set of basis functions merely consists of evanescent and propagating plane waves, it is difficult to provide an adequate approximation of the boundary condition that exhibit discontinuities (Rejlek et al., 2008a)
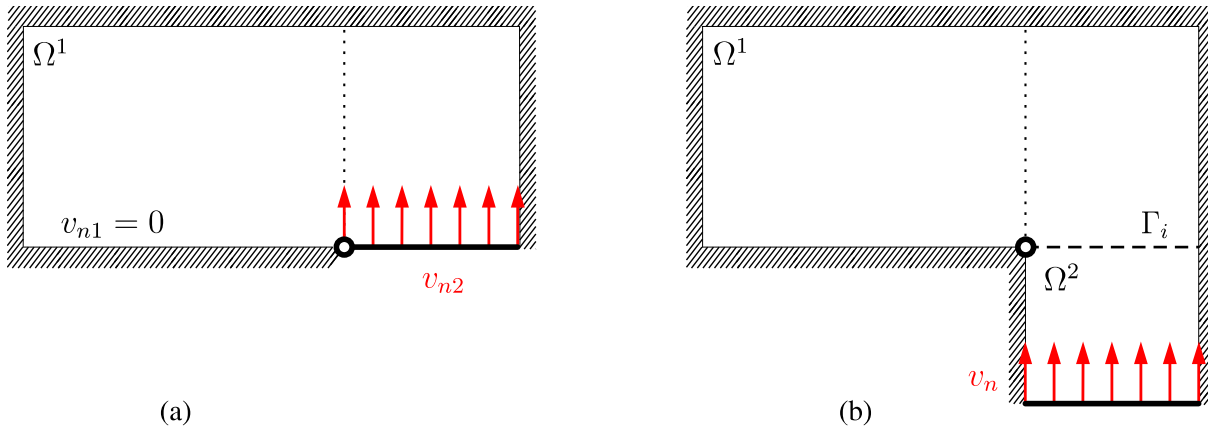
Figure D.1: (a) Discontinuous boundary condition and (b) the geometrical discontinuity (Rejlek et al., 2008a)

Figure D.1 illustrates the phenomenon. First, consider a single-domain problem as depicted on the left. The boundary of the problem is considered to be rigid except for the panel that have an imposed normal velocity boundary condition, see figure D.1(a). Obviously, a discontinuity in the normal velocity occurs at the bottom edge, and the problem is thus referred to as a discontinuous boundary condition. Figure D.1(b) illustrates a multi-domain problem consisting of two subdomains coupled via the interface Γ_i. Again, the boundary of the cavity consists of rigid walls, except for the vibrating panel located in subdomain Ω^2. As the bottom edge of the subdomain Ω^1 consists of one part with a prescribed rigid boundary condition and one part with an interface to subdomain Ω^2, in general, the velocity y component along this boundary may exhibit a discontinuity. This type of problem is referred to as a geometrical discontinuity. As a result, deterioration of the prediction accuracy for the particle velocity (C.3) can be expected in both cases. One countermeasure to maintain the prediction accuracy is to increase the number of wave functions. The second strategy is to employ a proper domain subdivision, which takes the existence of the discontinuity into account. The dotted lines indicate such a possible model refinement, which would prevent the decrease in accuracy.

D.1.1 Model refinement

Section C.3 reports on the application of the WBT for a two-dimensional unbounded problem. The achieved pressure results demonstrate the high prediction accuracy for both the response fields and the response spectra. However, by analysing the spatial distribution of the velocity, see figure C.5, reveals an insufficient accuracy. Although the global velocity pattern is captured fairly well, a detailed investigation of the velocity at the coupling interfaces reveals the violation of its continuity. For instance, in subdomain Ω^3, see figure D.2(a), the boundary adjoining subdomains Ω^1 and Ω^2 suffers from the existence of a discontinuous boundary condition. At the

part adjacent to subdomain Ω^1, a rigid boundary condition is imposed, whereas at the interface with subdomain Ω^2 arbitrary (non-zero) velocities occur.

A common measure to control the accuracy of the wave based approach is model refinement. Refinement of the original model is thus an adequate countermeasure to avoid deterioration of the prediction accuracy caused by the presence of a discontinuous boundary condition. As such, the wave model can be refined in two different manners, namely by employing either p- or h-refinement strategy. The p-refinement consists in increasing the number of wave functions per subdomain, while keeping the original model subdivision. In the framework of the wave based approach, this can be easily done by increasing the truncation parameters n_r and n_s. The h-refinement scheme, on the other hand, refers to refinement of the spatial discretisation, which is commonly used in element-based schemes. Figure D.2(b) illustrates the result of an h-refinement strategy applied to the considered validation example.

(a)　　　　　　　　　　　　　　(b)
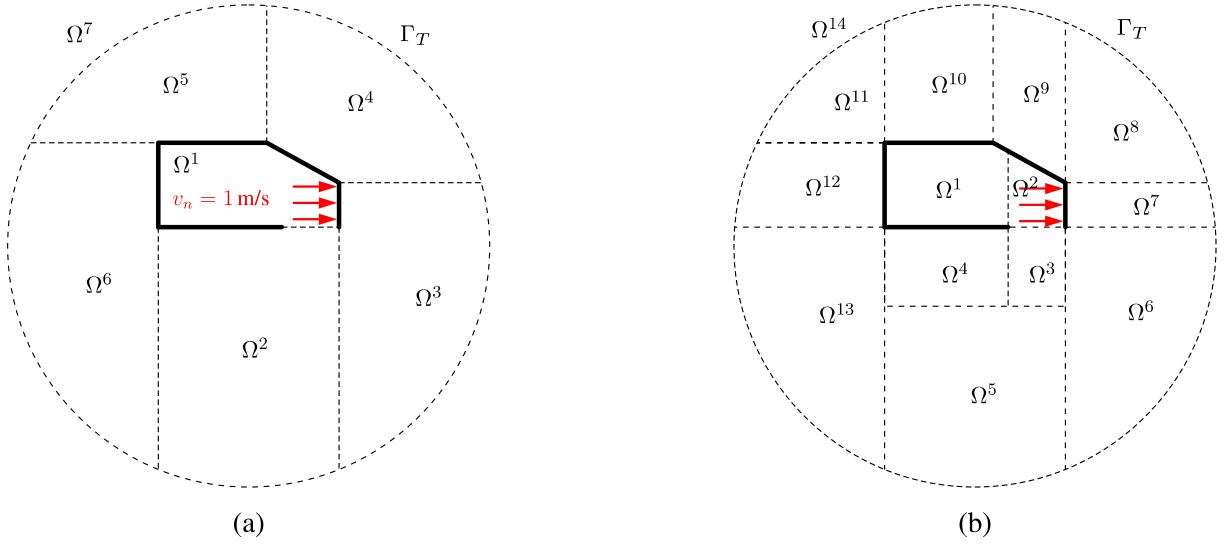
Figure D.2: The (a) original 6+1 and (b) h-refined 13+1 wave model

Figure D.3 illustrates the effect of model refinement. The contour plot on the left shows the spatial distribution of the magnitude of the velocity x component obtained at 80 Hz by the p-refined wave model, while the velocity pattern on the right captures the result predicted by a model employing the h-refinement strategy. Both results confirm that the WB solution converges towards the exact solution. Although the prediction accuracy has been recovered, both refined models are larger in terms of degrees of freedom than to the original one, see table D.1.

refinement scheme	$\#\Omega^b$	n_r, n_s	N	$\dim\boldsymbol{\Phi}^b$	$\dim\boldsymbol{\Phi}^u$	DOF
-	6	19		480		501
p	6	39	10	960	21	981
h	13	14		780		801

Table D.1: Attributes of the WB models

(a)   (b)
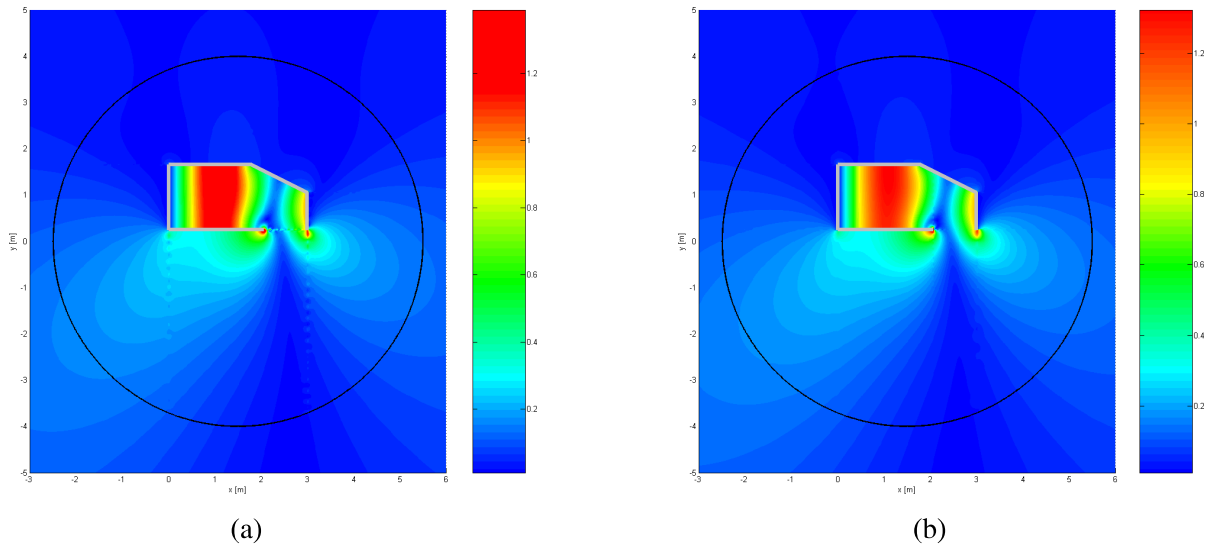
Figure D.3: Sound brick 2D: magnitude of the velocity x component field predicted at 80 Hz by the refined WB models: (a) p-refinement and (b) h-refinement

D.2   Concept of set enrichment

Section D.1 introduced the phenomenon of a discontinuous boundary condition and demonstrated its effect on the performance of the wave based approach. Model refinement is a commonly used measure for preventing the deterioration of the favourable prediction accuracy in this particular case. However, by employing the refinement the wave models become prohibitively large and less computationally efficient. In order to overcome this bottleneck, this section proposes a concept of set enrichment. The basic idea of this approach is to enrich the original wave function set with some special-purpose functions, which (i) inherently satisfy the governing differential equation, and (ii) incorporate the behaviour of a discontinuous boundary condition. These special-purpose functions, which are derived from the solution of an associated Neumann problem, exhibit the discontinuity in normal velocity boundary condition and are referred to as the auxiliary functions. For the wave based approach, analytical solutions are needed. However, for investigation purposes, a numerical evaluation of the associated problem is considered throughout this study. Analytical solutions must be derived for the properly chosen auxiliary functions at a later stage.

Two different enrichment strategies are considered. A conformal problem-specific enrichment scheme based on the numerical solution of an associated problem is discussed first, while the latter one presents a more general enrichment strategy.

D.2.1   Test case

As the existence of a discontinuous boundary condition concerns only the bounded part of a wave model, an interior acoustic problem is considered for the sake of simplicity. As a representative test case, the validation example introduced in section C.3 is reused. The simplified 2D car-like cavity problem consists of a closed boundary, see figure D.4(a). At the panel representing the footwell of the compartment, a normal velocity boundary condition $v_n = 1$ m/s is imposed, while the rest of the boundary is assumed to be perfectly rigid, i.e. $v_n = 0$ m/s. The

cavity is considered to be filled by air having the speed of sound $c = 344.8$ m/s and the mass density $\rho = 1.2$ kg/m^3.
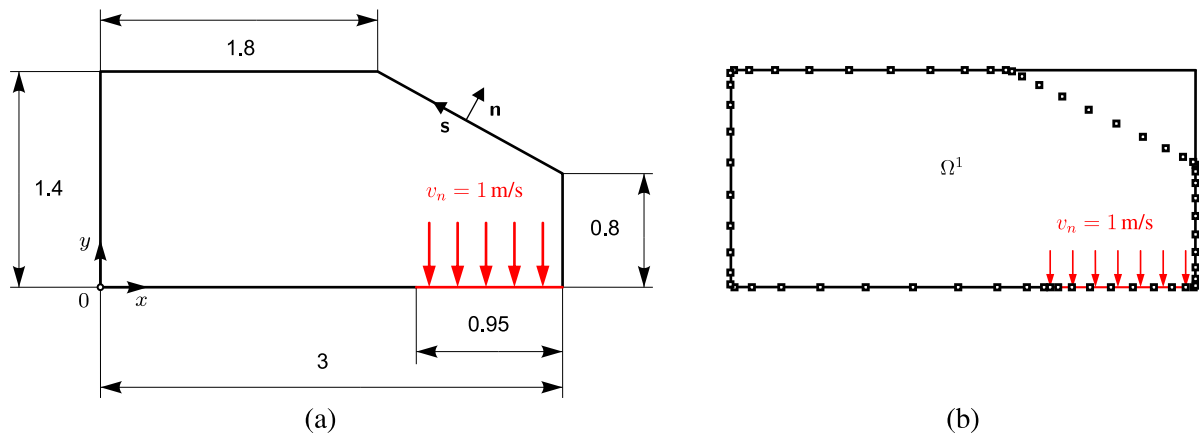
Figure D.4: (a) Dimensions of the validation example (in [m]) and (b) the problem-specific enrichment strategy (Rejlek et al., 2008a)

D.2.2 Problem-specific enrichment strategy

The wave functions (C.7) used for the pressure approximation are defined in terms of the smallest rectangular box enclosing the subdomain, namely the bounding box having dimensions L_x and L_y. Therefore, in the first enrichment approach, one considers a numerical solution of the associated problem, which has a rectangular domain of the same dimensions as the bounding box of the original problem. Figure D.4(b) shows the initial single-domain wave model of the problem being considered with the markers indicating the positions of the integration points and the solid black lines representing the geometry of an associated problem. The associated finite element model consists of 28 431 nodes forming 28 150 quadrilateral linear acoustic elements with the maximum element length of $h_{max} = 0.055$ m. Once the frequency response analysis has been carried out, the FE results are postprocessed at response points having congruent positions to the integration Gauss points of the wave model. The discrete pressure and normal velocity values obtained by FE calculation, see figure D.5, are then added into the wave function set (C.7) and further used during the set up and solution of the matrix system (C.18).

This section considers three wave models of different complexity, see table D.2. The first model, which utilises 16 wave functions, is valid up to approximately 250 Hz and represents an economical way of performing a frequency response analysis. However, an inadequate domain subdivision causes a deterioration of the prediction accuracy. In contrast, the next model employs 324 wave functions and stands for a brute-force calculation. The last wave model employs the enrichment strategy. It starts from the original economical model, which consists of 16 wave functions and its normal derivatives, while adding one auxiliary function $\boldsymbol{\Phi}^{aux}$ and its normal derivative $\frac{\partial}{\partial n}\boldsymbol{\Phi}^{aux}$. These correspond respectively to pressure and normal velocity evaluated using the associated finite element model, see figure D.5. Finally, a very fine finite element model consisting of 83 133 nodes forming 27 474 quadrilateral quadratic acoustic elements with the maximum element length of $h_{max} = 1.77 \cdot 10^{-2}$ m is considered as a reference.

Figure D.6 captures the imaginary part of the pressure calculated at 100 Hz. As the discontinuity occurs in the velocity boundary condition, the global pressure pattern predicted by the
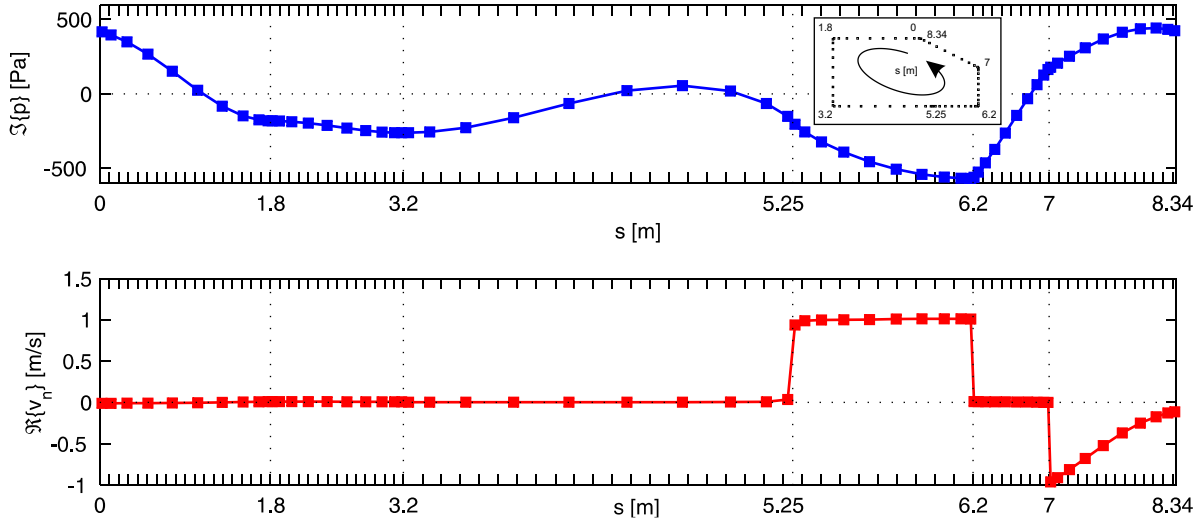
Figure D.5: Auxiliary functions: the pressure (top) and normal velocity (bottom) calculated at 100 Hz along the boundary (see insert) using an FEM-based associated problem (Rejlek et al., 2008a)

model	n_r, n_s	dim$\mathbf{\Phi}$	dim$\mathbf{\Phi}^{aux}$	DOF
economical	3	16	-	16
brute-force	80	324	-	324
enrichment	3	16	1	17

Table D.2: Attributes of the WB models

(a)

(b)

(c)

(d)
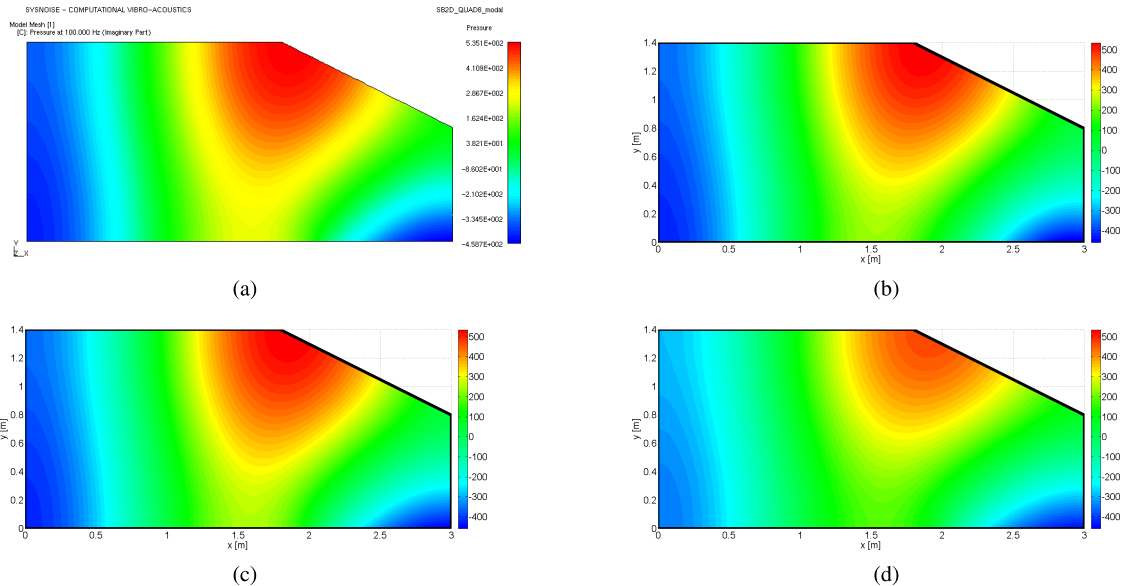
Figure D.6: $\Im\{p\}$ at 100 Hz: (a) FEM, (b) economical WBT, (c) brute-force WBT and (d) the WBT problem-specific enrichment approach (Rejlek et al., 2008a)

economical wave model remains almost unaffected by the existence of this phenomenon. Figure D.7, on the other hand, provides a detailed insight into the formation of the phenomenon
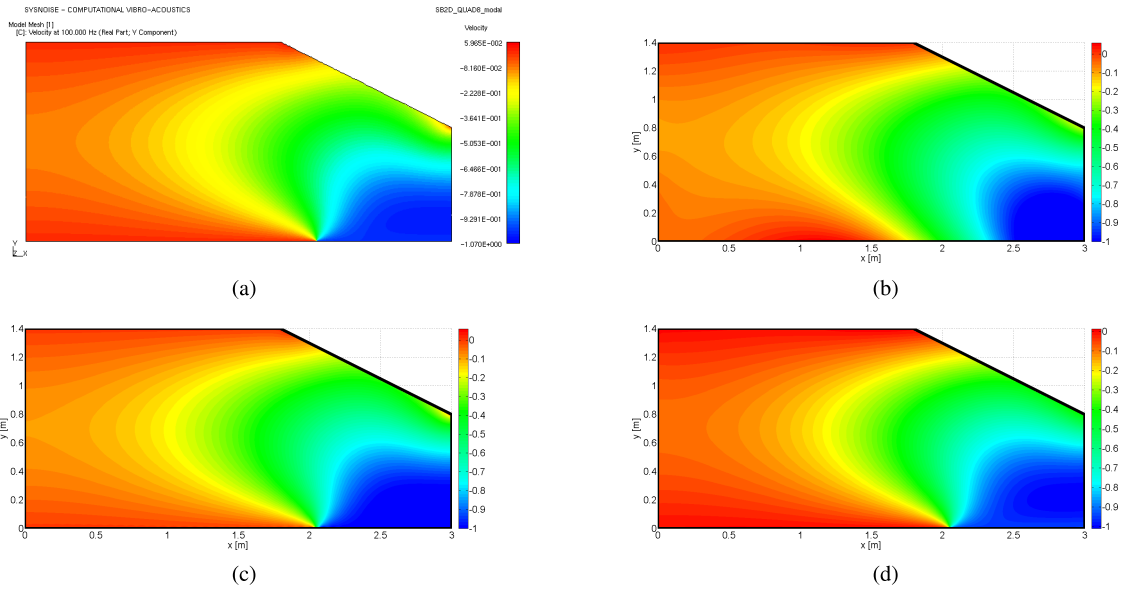
Figure D.7: $\Re\{v_y\}$ at 100 Hz: (a) FEM, (b) economical WBT, (c) brute-force WBT and (d) the WBT problem-specific enrichment approach (Rejlek et al., 2008a)

and its treatment by plotting the real part of the velocity y component. The economical model, which consists of only 16 wave functions, see figure D.7(b), can hardly approximate the discontinuous normal velocity boundary condition. Instead of an abruptly changing normal velocity, a smoothed solution is provided. Increasing the number of wave functions improves the prediction accuracy considerably, as illustrated by the result calculated using the brute-force model, see figure D.7(c). Nevertheless, the size of the model becomes prohibitively large. Finally, figure D.7(d) captures the solution obtained by employing the enrichment strategy. Although the quality of the result is fairly close to the brute-force solution, it is obtained in a substantially more efficient way.

Figure D.8 plots the imaginary part of pressure and the real part of the tangential and normal velocity evaluated at the boundary of the problem. The orientations of both the normal **n** and tangential **s** vector are in accordance with the notation defined in figure D.4(a). Moreover, the critical part of the boundary is scaled by a factor of two in order to represent the local phenomena in a more detailed way.

D.2.3   General enrichment scheme

Section D.2.2 discussed the application of enrichment strategy and demonstrated its potential in the case of a conformal associated problem. Although the velocity prediction accuracy was improved considerably, the proposed approach lacks a general applicability. In this section, the basic concept of set enrichment is further generalised by considering a problem-independent enrichment scheme. Finally, some preliminary results obtained by applying this approach to a problem depicted in figure D.4(a) are presented.

As the phenomenon discussed in section D.1 is solely affected by the adjacent part of a boundary which exhibits the discontinuity, the remaining boundary of the corresponding subdomain is omitted in the further assumptions. This yields a semi-infinite associated problem, see figure D.9, with a normal velocity boundary condition, which incorporates the discontinuity, im-
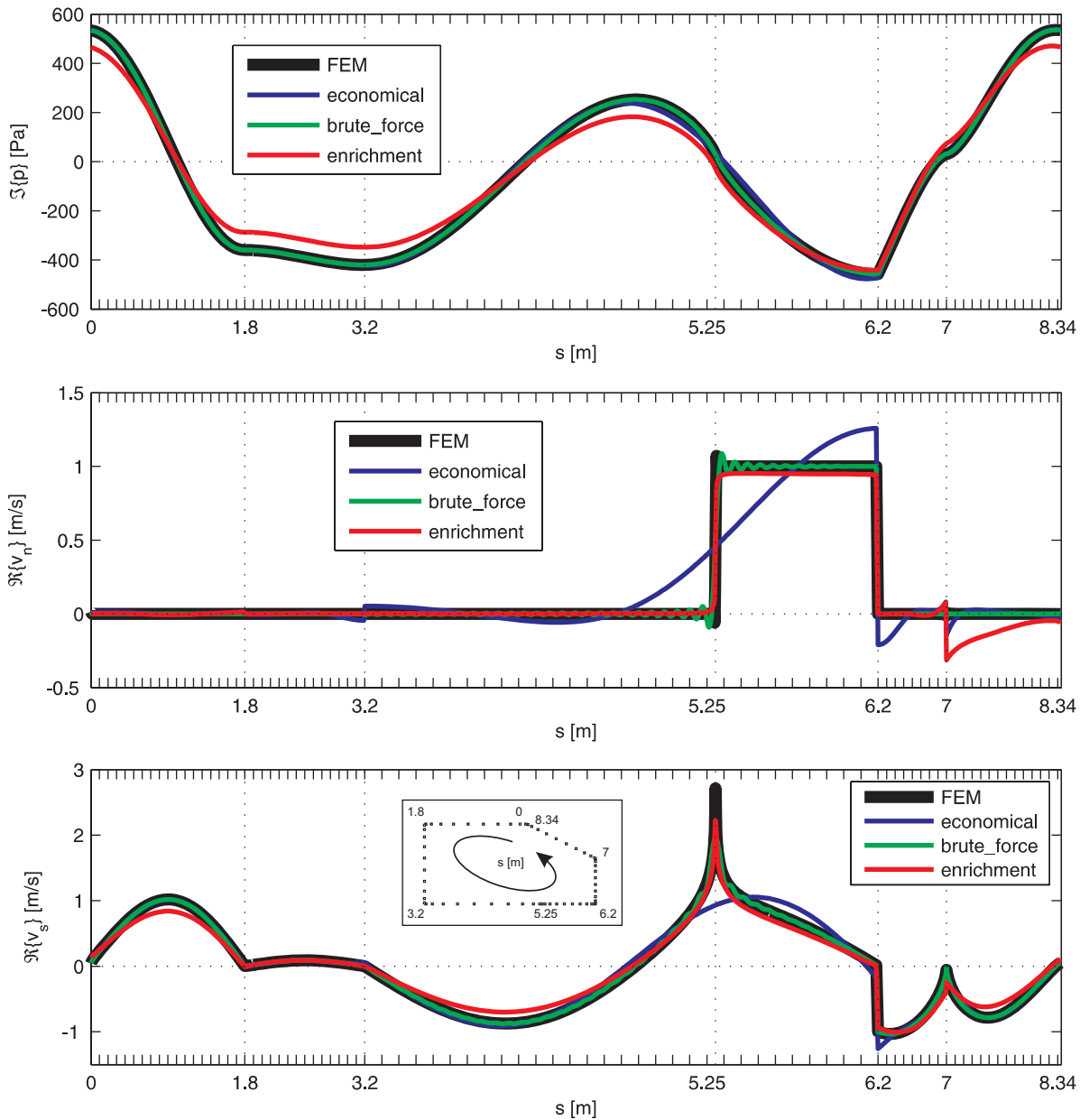
Figure D.8: p, v_n and v_s evaluated at 100 Hz at the boundary of the problem: FEM (black), economical WBT (blue), brute-force WBT (green) and the WBT problem-specific FEM-based enrichment approach (red solid line) (Rejlek et al., 2008a)

posed at a baffle plane. The infinite element method (I-FEM) (Astley et al., 1994; Astley, 2000; Gerdes, 1998b,a) is used to take into account the infinite part of the numerical model. For the imposed normal velocity boundary condition an appropriate decay function is applied, which ensures that the $v_n(s)$ converges to zero at a certain (finite) distance from the discontinuity. The effect of this measure is twofold: (i) it enables the solution of the associated problem in a numerical manner, since only the bounded part of the I-FE model is admissible for imposing a non-zero normal velocity boundary condition and (ii) it prevents the pollution of the solution by spurious contributions arising from a non-matched boundary condition termination. Moreover, the introduction of a decay function is based on the assumption that the overall radiation pattern of the associated problem is mainly affected by the local behaviour of the discontinuity.
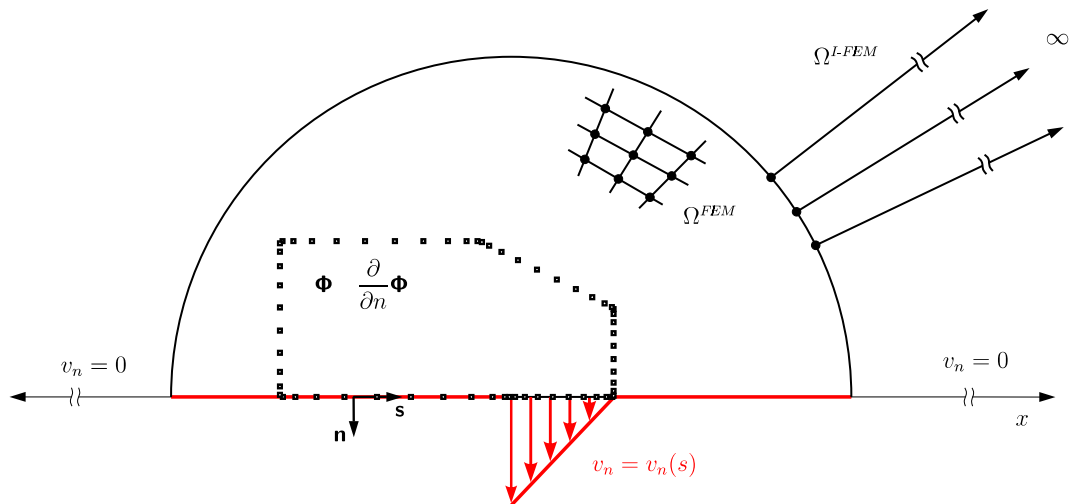
Figure D.9: The concept of a generalised enrichment strategy using I-FEM-based associated problem (Rejlek et al., 2008a)

A still unresolved task, however, is the selection of an appropriate decay function that provide a representative sample for any type of problem. Obviously, the amplitude of the velocity discontinuity and its spatial distribution are not a priori known in the case of geometrical discontinuity, which may arise at an interface between two subdomains, see figure D.1(b). Figure D.10 plots the auxiliary functions corresponding to an asymmetrical linear decay strategy, while figure D.11 shows the results calculated at the boundary of the problem using these auxiliary functions. The results demonstrate a significant improvement of the local behaviour in the vicinity of the discontinuity.
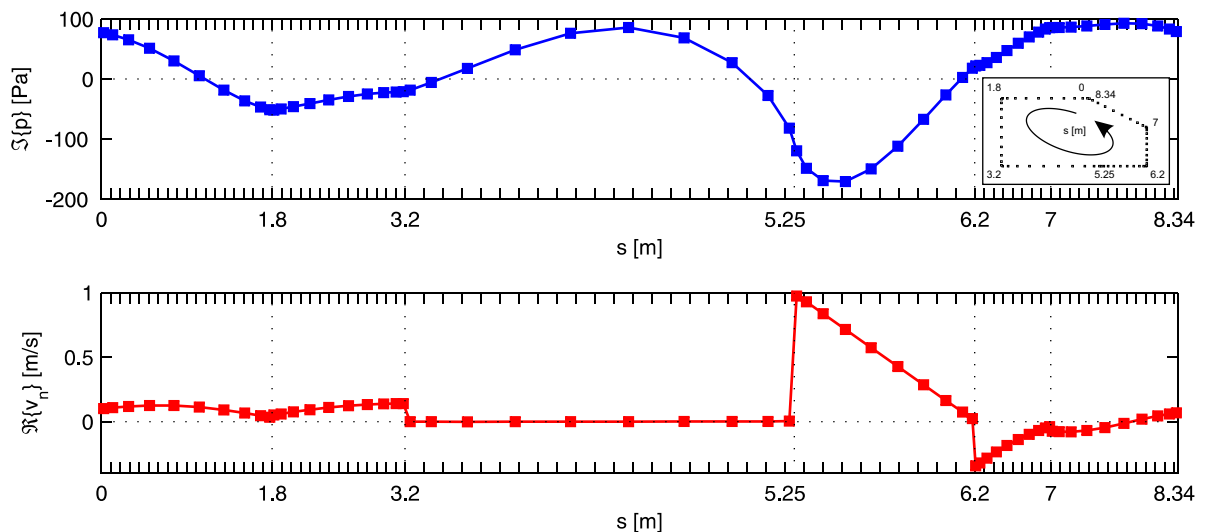
Figure D.10: Auxiliary functions: the pressure (top) and normal velocity (bottom) calculated at 100 Hz along the boundary (see insert) using an I-FEM-based associated problem (Rejlek et al., 2008a)
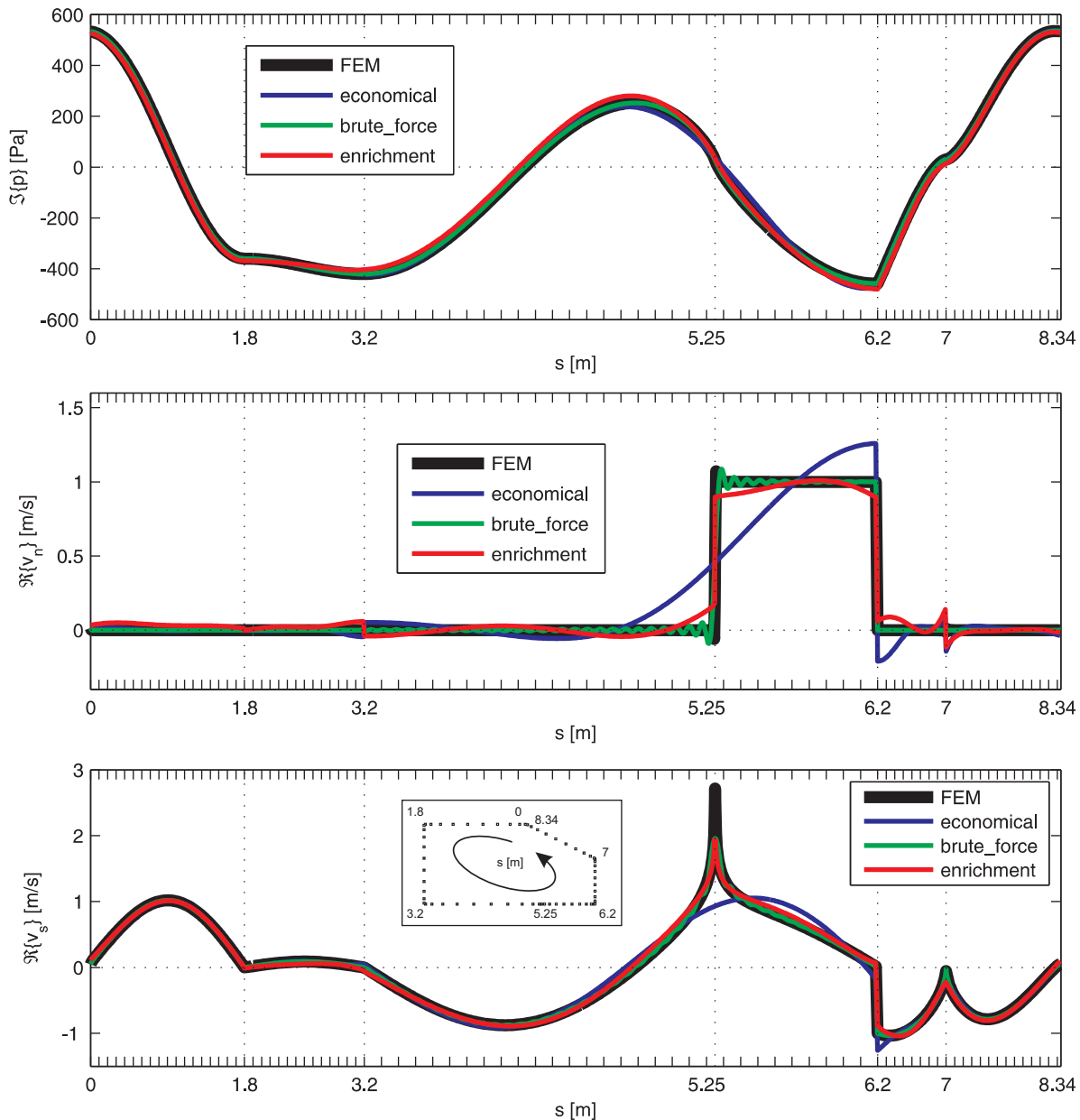
Figure D.11: p, v_n and v_s evaluated at 100 Hz at the boundary of the problem: FEM (black), economical WBT (blue), brute-force WBT (green) and the WBT general I-FEM-based enrichment approach (red solid line) (Rejlek et al., 2008a)

D.3 Practical implementation

For a practical implementation, *MATLAB* (MathWorks, Inc., 2007) in conjunction with the FEM/I-FEM module of the *LMS/SYSNOISE* commercial package (LMS International, 2010) are used. As a starting point, an already existing *MATLAB* WBT code for solving 2D unbounded acoustic problems is adopted. The *MATLAB* routines are further extended by the import/export interfaces. These interfaces provide the link to *LMS/SYSNOISE*, which is used for the solution of an associated problem.

To allow for a rapid modification of the parameters of the associated problem, the *SYSNOISE* jobs are run in the no-gui mode using the corresponding command files, see figures D.14 and

D.15. Figure D.12 displays a generic workflow used in the set enrichment strategy, which can be described as follows.

1. Set-up the *SYSNOISE* command file.

   - Link the file containing the mesh topology of the associated problem (nodal coordinates and the element connectivity matrix) – *MSC.Patran* neutral file format is used in this particular case.

   - If a spatially dependent boundary condition is imposed in the associated problem (concerns the general enrichment scheme), the *PATRAN* result file format is used to prescribe the decaying BC behaviour, see figure D.13. This type of boundary condition is then applied via the structural FE link in *LMS/SYSNOISE*. To generate a corresponding file containing the velocity BC profile, the `parse_patran_velo_BC` *MATLAB* function is used.

   - Import the coordinates of the integration Gauss points (= GP coords) used in the initial wave based model. By default, ten integration points per boundary edge are used in this example, which corresponds to a parameter setting `ngauss = 10` in the WBT code.

   - Repeat the previous step for the response points at the boundary of the initial problem (= RPb coords). This is used to plot the behaviour of pressure and velocity along the boundary of the problem.

   - Repeat this step again for the response points in the solution domain of the initial problem (= RPd coords), which are used for a later visualisation of results. A grid with an equidistant step size of 1 cm is used.

2. Run the *SYSNOISE* job in no-gui mode, i.e. by typing the command `sysnoise_nogui␣-if␣*.cmd␣-of␣*.log` on a *Windows* based system, with the asterisks denoting the corresponding command and log file.

3. Depending on the solution scheme (problem-specific versus general), either an FE- or I-FE-based associated problem is solved by the *SYSNOISE*. As a next step, the primary nodal results (denoted as potentials in terms of *SYSNOISE* terminology) are postprocessed at the positions corresponding to GP (p, vn@GP), RPb (p, vn@RPb) and/or RPd (p, vx, vy@RPd). These results are written into the ASCII files via the *SYSNOISE* free format interface, see figure D.16. From now on, the number and positions of the GP, RPb and RPd must not be altered in order to assure the consistency between the initial and associated problem.

4. Using the function `parse_sysnoise_free`, the raw results stored in the ASCII files are parsed, and the relevant data (pressures and the particle velocities) are stored in the *MATLAB* binary file.

5. Run a WBT job using the `runner.m` subroutine. As long as the global variable `av` is set to zero, the calculation runs in conventional WBT mode without employing the set enrichment strategy.

   - Once the variable `av` has been set to value unequal zero, the additional (enriching) information arising from the associated problem (referred to as auxiliary functions)

stored in the *MATLAB* binary file is fed back into the WBT code. In order to plot the auxiliary function(s) along the boundary of the problem, the function `plot_IFEM_at_boundary_multiple` and/or `plot_IFEM_at_boundary` can be used. Once the matrix system has been solved, the resulting solution vector along with other relevant variables are stored as a *MATLAB* binary file in the `\p_wbt` subfolder.

- In the final step, the solution vector is postprocessed at the response points located either at the boundary or inside the solution domain of the problem. The corresponding auxiliary functions stored in a *MATLAB* binary file (either p, vn@RPb or p, vx, vy@RPd) are loaded into a current workspace. Together with the wave function contribution factors, these are further used for back-substitution into the global pressure approximation, which yields the spatial description of the dynamic pressure/velocity field.
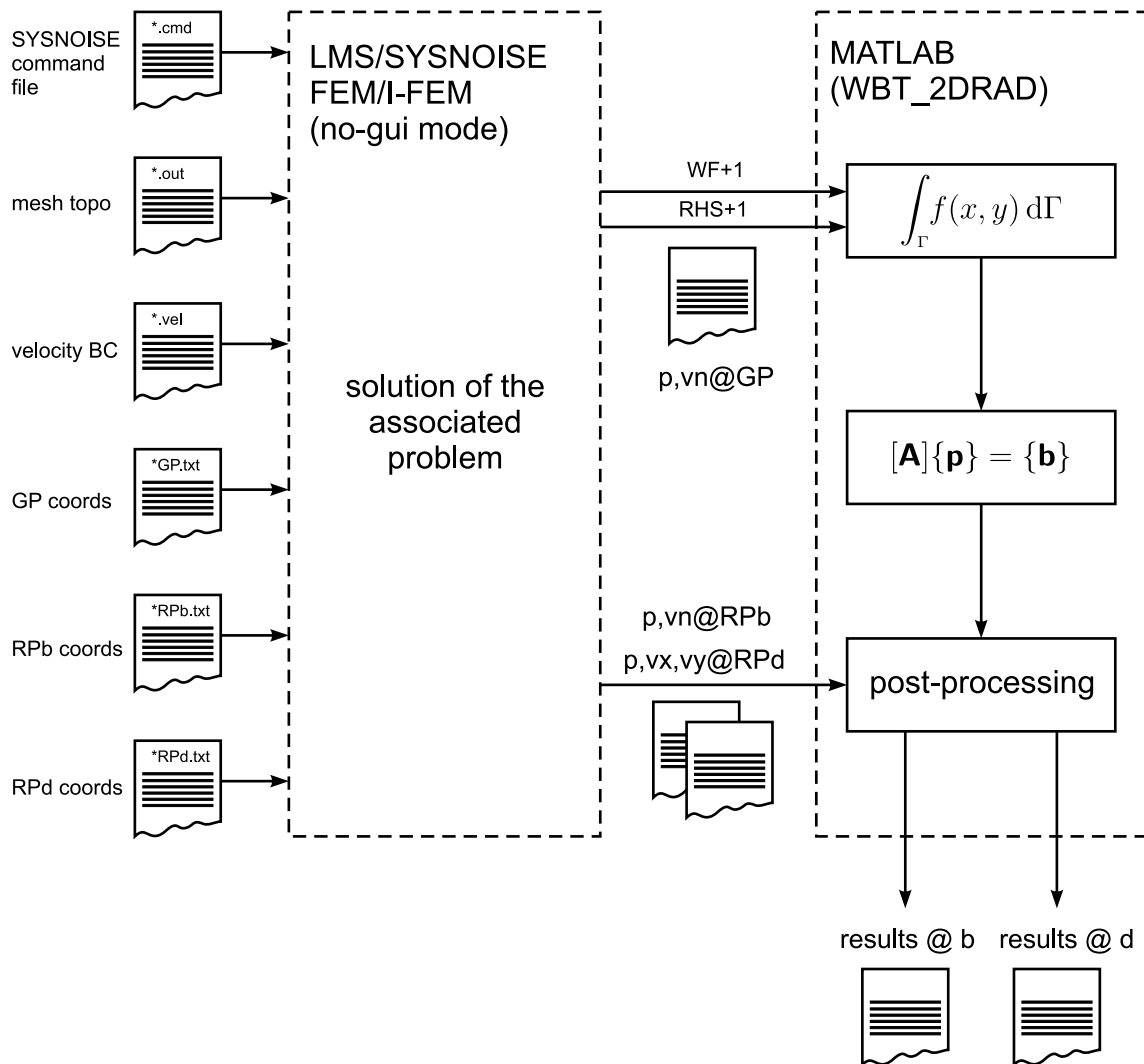
Figure D.12: The set enrichment strategy – a generic workflow

```
1s_linear.vel
     518    516  0.000000E+00        0        6
Frequency     1.000 Hz
NODAL VELOCITY
   42994.0000000E+000 0.000000000000.0000000E+000.0000000E+000.0000000E+000
.0000000E+000
   42995.0000000E+000 0.000000000000.0000000E+000.0000000E+000.0000000E+000
.0000000E+000
   43254.0000000E+000 -1.000000000000.0000000E+000.0000000E+000.0000000E+000
.0000000E+000
   43253.0000000E+000 -0.998947408933.0000000E+000.0000000E+000.0000000E+000
.0000000E+000
   43252.0000000E+000 -0.997894871784.0000000E+000.0000000E+000.0000000E+000
.0000000E+000
   43251.0000000E+000 -0.996841047449.0000000E+000.0000000E+000.0000000E+000
.0000000E+000
   43250.0000000E+000 -0.995789805329.0000000E+000.0000000E+000.0000000E+000
.0000000E+000
   43249.0000000E+000 -0.994737196616.0000000E+000.0000000E+000.0000000E+000
.0000000E+000
   43248.0000000E+000 -0.993683152685.0000000E+000.0000000E+000.0000000E+000
.0000000E+000
   43247.0000000E+000 -0.992632164473.0000000E+000.0000000E+000.0000000E+000
.0000000E+000
```

Figure D.13: An extract of a *SYSNOISE* velocity BC file (in *MSC.Patran* file format)

D.4 Recommendations for future developments

In addition to the extensions of WBT for three-dimensional vibro-acoustic problems discussed in this dissertation, investigations of some modelling aspects that consider the effects of a discontinuous boundary condition have been carried out for two-dimensional problems. In the course of this study, a computational performance of the wave based technique was analysed for the particular case, where a discontinuous boundary condition occurs in the model. In order to preserve the favourable computational efficiency of this method, the concept of enrichment strategy was introduced in this work. The original set of basis functions was enlarged by some additional functions derived from the solution of an associated problem, which implicitly incorporates the discontinuous boundary condition.

Two enrichment strategies have been discussed throughout this study. The first one represents an ad hoc problem-specific approach. A conformal associated problem is adopted in order to determine the auxiliary functions used for the enrichment of the initial wave function set. The results achieved by employing this strategy show an improvement in both the local and global behaviour related to the existence of the discontinuity. Despite the slight spatial distortion of the pressure and velocity fields at some frequencies, the local phenomena in the vicinity of the discontinuity are captured with a significantly higher accuracy. Moreover, the local behaviour is of high importance to assure an accurate approximation of the interface conditions imposed at the coupling between two subdomains. The second enrichment scheme is a generalisation of the previous strategy. Instead of utilising a conformal associated problem, only the adjacent part of the boundary affected by the discontinuous boundary condition is considered. Again, the results show a significant local improvement.

Future research will focus on further improvement of the set enrichment approach by adopting a problem-independent scheme. For this purpose, other classes of enrichment functions have to be investigated first. Once a multi-purpose enrichment strategy has been selected, an analytical solution of the associated problem will be derived. A long-term task is the extension of this concept towards three-dimensional formulation of the wave based technique, in which the phenomena related to the existence of the discontinuous boundary condition have a significant effect on the computational efficiency. The main task is the definition of appropriate basis functions, which form complete set of Trefftz functions assuring fast convergence of the method.

```
New Model 1 Original File rigid_const_via_cmd.sdb Return

Option  FEM Frequency Fluid Return

Import Mesh Format Patran File mesh\SB2D_box_enrichment_FEM.out Return

TwoDimensional Return

Check Mesh Return

Material Fluid
    Name 'air'
    Sound Real 343.799  Rho Real 1.19985
    Elements all
    Return

Set Name  "velo"
    Faces 1 3 5 7 9 11 13 15 17 19 21 23 25 27 29 31 33 35 37 39 41 43 45 47 49 51 53 55

    Faces  57 59 61 63 65 67 69 71 73 75 77 79 To 127
    Return
Save Return

Boundary Velocity  Real 1 Imag 0
    Faces Set 1
    Return

Solve
    Frequency 1 To 500 Linstep 1
    Return

Point  File  BC_sets\SB2D_IFEM_GP10.TXT Return

PostProcess
    Points all
    Frequency 1 To 500 Linstep 1
    Near 2
    Far 5
    Quadrature 2 2 1
    Save Results Step 1
    Return

Export Results Format Free
    Frequency  1 To 500 Linstep 1
    File rigid_const_GP.fre
    Return

Point Reset Return

Point  File  BC_sets\SB2D_IFEM_RPb.TXT Return

PostProcess
    Points all
    Frequency 1 To 500 Linstep 1
    Near 2
    Far 5
    Quadrature 2 2 1
    Save Results Step 1
    Return

Export Results Format Free
    Frequency 1 To 500 Linstep 1
    File rigid_const_RPb.fre
    Return

Point Reset Return

Point  File  BC_sets\SB2D_IFEM_RPd.TXT Return

PostProcess
    Points all
    Frequency 1 To 500 Linstep 1
    Near 2
    Far 5
    Quadrature 2 2 1
    Save Results Step 1
    Return

Export Results Format Free
    Frequency 1 To 500 Linstep 1
    File rigid_const_RPd.fre
    Return

save return
close return
```

Figure D.14: *SYSNOISE* command file as used in the problem-specific enrichment strategy

```
New Model 1 Original File 1s_linear_via_cmd.sdb Return

Option  FEM Frequency Fluid Return

Import Mesh Format Patran File mesh\SB2D_IFEM_hmax5cm_adapt.out Return

TwoDimensional Return

Check Mesh Return

Material Fluid
    Name 'air'
    Sound Real 343.799  Rho Real 1.19985
    Elements all
    Return

Set Name  "ifem"
    Faces 1 to 93 216 352 to 444 566
    Return

Set Name  "bottom"
    Faces 94 to 215 217 to 351 445 to 565 567 to 703 706
    Return

Infinite
    Order 6
    Type 1
    Conjugate
    Origin 0.000000 0 0.000000
    Sound 343.799
    Rho 1.19985
    Faces Set 1
    Return

Generate
    Face Set 2
    From Velocities File  BC_sets\1s_linear.vel Format Patran
    Frequency 15 100 206 353
    Return

Solve
    Frequency 15 100 206 353
    Return

Point  File  BC_sets\SB2D_IFEM_GP10.TXT Return

PostProcess
    Points all
    Frequency 15 100 206 353
    Near 2
    Far 5
    Quadrature 2 2 1
    Save Results Step 1
    Return

Export Results Format Free
    Frequency 15 100 206 353
    File 1s_linear_GP.fre
    Return

Point Reset Return

Point  File  BC_sets\SB2D_IFEM_RPb.TXT Return

PostProcess
    Points all
    Frequency 15 100 206 353
    Near 2
    Far 5
    Quadrature 2 2 1
    Save Results Step 1
    Return

Export Results Format Free
    Frequency 15 100 206 353
    File 1s_linear_RPb.fre
    Return

Point Reset Return

Point  File  BC_sets\SB2D_IFEM_RPd.TXT Return

PostProcess
    Points all
    Frequency 15 100 206 353
    Near 2
    Far 5
    Quadrature 2 2 1
    Save Results Step 1
    Return
Export Results Format Free
    Frequency 15 100 206 353
    File 1s_linear_RPd.fre
    Return

save return
close return
```

Figure D.15: *SYSNOISE* command file as used in the general enrichment strategy

```
SYSNOISE RESULTS FILE
Rev 5.5  Windows NT   30NOV2000
rigid_const_via_cmd
29-MAY-2008 19:37:21
FREQUENCY
     0.10000000E+01
PRESSURE VALUES
        1           1      0.00000000E+00      0.51076902E+04      0.51076902E+04
                           0.90000000E+02      0.16513359E+03      0.36116824E+04
        2           2      0.00000000E+00      0.51076736E+04      0.51076736E+04
                           0.90000000E+02      0.16513356E+03      0.36116706E+04
        3           3      0.00000000E+00      0.51075927E+04      0.51075927E+04
                           0.90000000E+02      0.16513343E+03      0.36116134E+04
...

VELOCITY VALUES
        1           1      0.64087165E-02      0.00000000E+00     -0.13322006E-03
                           0.00000000E+00      0.00000000E+00      0.00000000E+00
        2           2      0.33295234E-01      0.00000000E+00     -0.13162734E-03
                           0.00000000E+00      0.00000000E+00      0.00000000E+00
        3           3      0.79502838E-01      0.00000000E+00     -0.14300537E-03
                           0.00000000E+00      0.00000000E+00      0.00000000E+00
...


INTENSITY VALUES
        1           1      0.00000000E+00      0.16366869E+02      0.00000000E+00
                          -0.34022341E+00      0.00000000E+00      0.00000000E+00
        2           2      0.00000000E+00      0.85030594E+02      0.00000000E+00
                          -0.33615475E+00      0.00000000E+00      0.00000000E+00
        3           3      0.00000000E+00      0.20303406E+03      0.00000000E+00
                          -0.36520660E+00      0.00000000E+00      0.00000000E+00
...

SYSNOISE RESULTS FILE
Rev 5.5  Windows NT   30NOV2000
rigid_const_via_cmd
29-MAY-2008 19:37:21
FREQUENCY
     0.20000000E+01
PRESSURE VALUES
        1           1      0.00000000E+00      0.25572699E+04      0.25572699E+04
                           0.90000000E+02      0.15912463E+03      0.18082629E+04
        2           2      0.00000000E+00      0.25572366E+04      0.25572366E+04
                           0.90000000E+02      0.15912452E+03      0.18082393E+04
        3           3      0.00000000E+00      0.25570746E+04      0.25570746E+04
                           0.90000000E+02      0.15912397E+03      0.18081248E+04
...
```

Figure D.16: An extract of a *SYSNOISE* free format output file

```
FREQUENCY
     0.10000000E+01
PRESSURE VALUES
        1           1      Re{p}              Im{p}               |p|
                           phi{p}             SPL                 RMS
...
VELOCITY VALUES
        1           1      Re{vx}             Im{vx}              Re{vy}
                           Im{vy}             Re{vz}              Im{vz}
...
INTENSITY VALUES
        1           1      Re{ix}             Im{ix}              Re{iy}
                           Im{iy}             Re{iz}              Im{iz}
...
```

Figure D.17: Layout of a *SYSNOISE* free format output file

Appendix E

Spherical harmonics up to a degree of $l = 10$

$l = 0$ _____

$$\mathrm{Y}_0^0(\vartheta, \varphi) = \tfrac{1}{2}\sqrt{\tfrac{1}{\pi}}$$

$l = 1$ _____

$$\mathrm{Y}_1^{-1}(\vartheta, \varphi) = \tfrac{1}{2}\sqrt{\tfrac{3}{2\pi}}\, \mathrm{e}^{-\mathrm{j}\varphi}\, \sin\vartheta$$

$$\mathrm{Y}_1^0(\vartheta, \varphi) = \tfrac{1}{2}\sqrt{\tfrac{3}{\pi}}\, \cos\vartheta$$

$$\mathrm{Y}_1^1(\vartheta, \varphi) = \tfrac{-1}{2}\sqrt{\tfrac{3}{2\pi}}\, \mathrm{e}^{\mathrm{j}\varphi}\, \sin\vartheta$$

$l = 2$ _____

$$\mathrm{Y}_2^{-2}(\vartheta, \varphi) = \tfrac{1}{4}\sqrt{\tfrac{15}{2\pi}}\, \mathrm{e}^{-2\mathrm{j}\varphi}\, \sin^2\vartheta$$

$$\mathrm{Y}_2^{-1}(\vartheta, \varphi) = \tfrac{1}{2}\sqrt{\tfrac{15}{2\pi}}\, \mathrm{e}^{-\mathrm{j}\varphi}\, \sin\vartheta\, \cos\vartheta$$

$$\mathrm{Y}_2^0(\vartheta, \varphi) = \tfrac{1}{4}\sqrt{\tfrac{5}{\pi}}\, (3\cos^2\vartheta - 1)$$

$$\mathrm{Y}_2^1(\vartheta, \varphi) = \tfrac{-1}{2}\sqrt{\tfrac{15}{2\pi}}\, \mathrm{e}^{\mathrm{j}\varphi}\, \sin\vartheta\, \cos\vartheta$$

$$\mathrm{Y}_2^2(\vartheta, \varphi) = \tfrac{1}{4}\sqrt{\tfrac{15}{2\pi}}\, \mathrm{e}^{2\mathrm{j}\varphi}\, \sin^2\vartheta$$

$l = 3$

$$Y_3^{-3}(\vartheta, \varphi) = \tfrac{1}{8}\sqrt{\tfrac{35}{\pi}}\, e^{-3i\varphi}\, \sin^3 \vartheta$$

$$Y_3^{-2}(\vartheta, \varphi) = \tfrac{1}{4}\sqrt{\tfrac{105}{2\pi}}\, e^{-2j\varphi}\, \sin^2 \vartheta\, \cos \vartheta$$

$$Y_3^{-1}(\vartheta, \varphi) = \tfrac{1}{8}\sqrt{\tfrac{21}{\pi}}\, e^{-j\varphi}\, \sin \vartheta\, (5\cos^2 \vartheta - 1)$$

$$Y_3^{0}(\vartheta, \varphi) = \tfrac{1}{4}\sqrt{\tfrac{7}{\pi}}\, (5\cos^3 \vartheta - 3\cos \vartheta)$$

$$Y_3^{1}(\vartheta, \varphi) = \tfrac{-1}{8}\sqrt{\tfrac{21}{\pi}}\, e^{j\varphi}\, \sin \vartheta\, (5\cos^2 \vartheta - 1)$$

$$Y_3^{2}(\vartheta, \varphi) = \tfrac{1}{4}\sqrt{\tfrac{105}{2\pi}}\, e^{2j\varphi}\, \sin^2 \vartheta\, \cos \vartheta$$

$$Y_3^{3}(\vartheta, \varphi) = \tfrac{-1}{8}\sqrt{\tfrac{35}{\pi}}\, e^{3j\varphi}\, \sin^3 \vartheta$$

$l = 4$

$$Y_4^{-4}(\vartheta, \varphi) = \tfrac{3}{16}\sqrt{\tfrac{35}{2\pi}}\, e^{-4j\varphi}\, \sin^4 \vartheta$$

$$Y_4^{-3}(\vartheta, \varphi) = \tfrac{3}{8}\sqrt{\tfrac{35}{\pi}}\, e^{-3j\varphi}\, \sin^3 \vartheta\, \cos \vartheta$$

$$Y_4^{-2}(\vartheta, \varphi) = \tfrac{3}{8}\sqrt{\tfrac{5}{2\pi}}\, e^{-2j\varphi}\, \sin^2 \vartheta\, (7\cos^2 \vartheta - 1)$$

$$Y_4^{-1}(\vartheta, \varphi) = \tfrac{3}{8}\sqrt{\tfrac{5}{\pi}}\, e^{-j\varphi}\, \sin \vartheta\, (7\cos^3 \vartheta - 3\cos \vartheta)$$

$$Y_4^{0}(\vartheta, \varphi) = \tfrac{3}{16}\sqrt{\tfrac{1}{\pi}}\, (35\cos^4 \vartheta - 30\cos^2 \vartheta + 3)$$

$$Y_4^{1}(\vartheta, \varphi) = \tfrac{-3}{8}\sqrt{\tfrac{5}{\pi}}\, e^{j\varphi}\, \sin \vartheta\, (7\cos^3 \vartheta - 3\cos \vartheta)$$

$$Y_4^{2}(\vartheta, \varphi) = \tfrac{3}{8}\sqrt{\tfrac{5}{2\pi}}\, e^{2j\varphi}\, \sin^2 \vartheta\, (7\cos^2 \vartheta - 1)$$

$$Y_4^{3}(\vartheta, \varphi) = \tfrac{-3}{8}\sqrt{\tfrac{35}{\pi}}\, e^{3j\varphi}\, \sin^3 \vartheta\, \cos \vartheta$$

$$Y_4^{4}(\vartheta, \varphi) = \tfrac{3}{16}\sqrt{\tfrac{35}{2\pi}}\, e^{4j\varphi}\, \sin^4 \vartheta$$

$l = 5$

$$Y_5^{-5}(\vartheta, \varphi) = \tfrac{3}{32}\sqrt{\tfrac{77}{\pi}}\, e^{-5j\varphi}\, \sin^5 \vartheta$$

$$Y_5^{-4}(\vartheta, \varphi) = \tfrac{3}{16}\sqrt{\tfrac{385}{2\pi}}\, e^{-4j\varphi}\, \sin^4 \vartheta\, \cos \vartheta$$

$$Y_5^{-3}(\vartheta, \varphi) = \tfrac{1}{32}\sqrt{\tfrac{385}{\pi}}\, e^{-3j\varphi}\, \sin^3 \vartheta\, (9\cos^2 \vartheta - 1)$$

$$Y_5^{-2}(\vartheta, \varphi) = \tfrac{1}{8}\sqrt{\tfrac{1155}{2\pi}}\, e^{-2j\varphi}\, \sin^2 \vartheta\, (3\cos^3 \vartheta - 1\cos \vartheta)$$

$$Y_5^{-1}(\vartheta, \varphi) = \frac{1}{16} \sqrt{\frac{165}{2\pi}} \, e^{-j\varphi} \, \sin \vartheta \, (21 \cos^4 \vartheta - 14 \cos^2 \vartheta + 1)$$

$$Y_5^0(\vartheta, \varphi) = \frac{1}{16} \sqrt{\frac{11}{\pi}} \, (63 \cos^5 \vartheta - 70 \cos^3 \vartheta + 15 \cos \vartheta)$$

$$Y_5^1(\vartheta, \varphi) = \frac{-1}{16} \sqrt{\frac{165}{2\pi}} \, e^{j\varphi} \, \sin \vartheta \, (21 \cos^4 \vartheta - 14 \cos^2 \vartheta + 1)$$

$$Y_5^2(\vartheta, \varphi) = \frac{1}{8} \sqrt{\frac{1155}{2\pi}} \, e^{2j\varphi} \, \sin^2 \vartheta \, (3 \cos^3 \vartheta - 1 \cos \vartheta)$$

$$Y_5^3(\vartheta, \varphi) = \frac{-1}{32} \sqrt{\frac{385}{\pi}} \, e^{3j\varphi} \, \sin^3 \vartheta \, (9 \cos^2 \vartheta - 1)$$

$$Y_5^4(\vartheta, \varphi) = \frac{3}{16} \sqrt{\frac{385}{2\pi}} \, e^{4j\varphi} \, \sin^4 \vartheta \, \cos \vartheta$$

$$Y_5^5(\vartheta, \varphi) = \frac{-3}{32} \sqrt{\frac{77}{\pi}} \, e^{5j\varphi} \, \sin^5 \vartheta$$

$l = 6$

$$Y_6^{-6}(\vartheta, \varphi) = \frac{1}{64} \sqrt{\frac{3003}{\pi}} \, e^{-6j\varphi} \, \sin^6 \vartheta$$

$$Y_6^{-5}(\vartheta, \varphi) = \frac{3}{32} \sqrt{\frac{1001}{\pi}} \, e^{-5j\varphi} \, \sin^5 \vartheta \, \cos \vartheta$$

$$Y_6^{-4}(\vartheta, \varphi) = \frac{3}{32} \sqrt{\frac{91}{2\pi}} \, e^{-4j\varphi} \, \sin^4 \vartheta \, (11 \cos^2 \vartheta - 1)$$

$$Y_6^{-3}(\vartheta, \varphi) = \frac{1}{32} \sqrt{\frac{1365}{\pi}} \, e^{-3j\varphi} \, \sin^3 \vartheta \, (11 \cos^3 \vartheta - 3 \cos \vartheta)$$

$$Y_6^{-2}(\vartheta, \varphi) = \frac{1}{64} \sqrt{\frac{1365}{\pi}} \, e^{-2j\varphi} \, \sin^2 \vartheta \, (33 \cos^4 \vartheta - 18 \cos^2 \vartheta + 1)$$

$$Y_6^{-1}(\vartheta, \varphi) = \frac{1}{16} \sqrt{\frac{273}{2\pi}} \, e^{-j\varphi} \, \sin \vartheta \, (33 \cos^5 \vartheta - 30 \cos^3 \vartheta + 5 \cos \vartheta)$$

$$Y_6^0(\vartheta, \varphi) = \frac{1}{32} \sqrt{\frac{13}{\pi}} \, (231 \cos^6 \vartheta - 315 \cos^4 \vartheta + 105 \cos^2 \vartheta - 5)$$

$$Y_6^1(\vartheta, \varphi) = \frac{-1}{16} \sqrt{\frac{273}{2\pi}} \, e^{j\varphi} \, \sin \vartheta \, (33 \cos^5 \vartheta - 30 \cos^3 \vartheta + 5 \cos \vartheta)$$

$$Y_6^2(\vartheta, \varphi) = \frac{1}{64} \sqrt{\frac{1365}{\pi}} \, e^{2j\varphi} \, \sin^2 \vartheta \, (33 \cos^4 \vartheta - 18 \cos^2 \vartheta + 1)$$

$$Y_6^3(\vartheta, \varphi) = \frac{-1}{32} \sqrt{\frac{1365}{\pi}} \, e^{3j\varphi} \, \sin^3 \vartheta \, (11 \cos^3 \vartheta - 3 \cos \vartheta)$$

$$Y_6^4(\vartheta, \varphi) = \frac{3}{32} \sqrt{\frac{91}{2\pi}} \, e^{4j\varphi} \, \sin^4 \vartheta \, (11 \cos^2 \vartheta - 1)$$

$$Y_6^5(\vartheta, \varphi) = \frac{-3}{32} \sqrt{\frac{1001}{\pi}} \, e^{5j\varphi} \, \sin^5 \vartheta \, \cos \vartheta$$

$$Y_6^6(\vartheta, \varphi) = \frac{1}{64} \sqrt{\frac{3003}{\pi}} \, e^{6j\varphi} \, \sin^6 \vartheta$$

$l = 7$

$$Y_7^{-7}(\vartheta, \varphi) = \frac{3}{64} \sqrt{\frac{715}{2\pi}} \, e^{-7j\varphi} \, \sin^7 \vartheta$$

$$Y_7^{-6}(\vartheta, \varphi) = \frac{3}{64} \sqrt{\frac{5005}{\pi}} \, e^{-6j\varphi} \, \sin^6 \vartheta \, \cos \vartheta$$

$$Y_7^{-5}(\vartheta, \varphi) = \frac{3}{64} \sqrt{\frac{385}{2\pi}} \, e^{-5j\varphi} \, \sin^5 \vartheta \, (13 \cos^2 \vartheta - 1)$$

$$Y_7^{-4}(\vartheta, \varphi) = \frac{3}{32} \sqrt{\frac{385}{2\pi}} \, e^{-4j\varphi} \, \sin^4 \vartheta \, (13 \cos^3 \vartheta - 3 \cos \vartheta)$$

$$Y_7^{-3}(\vartheta, \varphi) = \frac{3}{64} \sqrt{\frac{35}{2\pi}} \, e^{-3j\varphi} \, \sin^3 \vartheta \, (143 \cos^4 \vartheta - 66 \cos^2 \vartheta + 3)$$

$$Y_7^{-2}(\vartheta, \varphi) = \frac{3}{64} \sqrt{\frac{35}{\pi}} \, e^{-2j\varphi} \, \sin^2 \vartheta \, (143 \cos^5 \vartheta - 110 \cos^3 \vartheta + 15 \cos \vartheta)$$

$$Y_7^{-1}(\vartheta, \varphi) = \frac{1}{64} \sqrt{\frac{105}{2\pi}} \, e^{-j\varphi} \, \sin \vartheta \, (429 \cos^6 \vartheta - 495 \cos^4 \vartheta + 135 \cos^2 \vartheta - 5)$$

$$Y_7^{0}(\vartheta, \varphi) = \frac{1}{32} \sqrt{\frac{15}{\pi}} \, (429 \cos^7 \vartheta - 693 \cos^5 \vartheta + 315 \cos^3 \vartheta - 35 \cos \vartheta)$$

$$Y_7^{1}(\vartheta, \varphi) = \frac{-1}{64} \sqrt{\frac{105}{2\pi}} \, e^{j\varphi} \, \sin \vartheta \, (429 \cos^6 \vartheta - 495 \cos^4 \vartheta + 135 \cos^2 \vartheta - 5)$$

$$Y_7^{2}(\vartheta, \varphi) = \frac{3}{64} \sqrt{\frac{35}{\pi}} \, e^{2j\varphi} \, \sin^2 \vartheta \, (143 \cos^5 \vartheta - 110 \cos^3 \vartheta + 15 \cos \vartheta)$$

$$Y_7^{3}(\vartheta, \varphi) = \frac{-3}{64} \sqrt{\frac{35}{2\pi}} \, e^{3j\varphi} \, \sin^3 \vartheta \, (143 \cos^4 \vartheta - 66 \cos^2 \vartheta + 3)$$

$$Y_7^{4}(\vartheta, \varphi) = \frac{3}{32} \sqrt{\frac{385}{2\pi}} \, e^{4j\varphi} \, \sin^4 \vartheta \, (13 \cos^3 \vartheta - 3 \cos \vartheta)$$

$$Y_7^{5}(\vartheta, \varphi) = \frac{-3}{64} \sqrt{\frac{385}{2\pi}} \, e^{5j\varphi} \, \sin^5 \vartheta \, (13 \cos^2 \vartheta - 1)$$

$$Y_7^{6}(\vartheta, \varphi) = \frac{3}{64} \sqrt{\frac{5005}{\pi}} \, e^{6j\varphi} \, \sin^6 \vartheta \, \cos \vartheta$$

$$Y_7^{7}(\vartheta, \varphi) = \frac{-3}{64} \sqrt{\frac{715}{2\pi}} \, e^{7j\varphi} \, \sin^7 \vartheta$$

$l = 8$

$$Y_8^{-8}(\vartheta, \varphi) = \frac{3}{256} \sqrt{\frac{12155}{2\pi}} \, e^{-8j\varphi} \, \sin^8 \vartheta$$

$$Y_8^{-7}(\vartheta, \varphi) = \frac{3}{64} \sqrt{\frac{12155}{2\pi}} \, e^{-7j\varphi} \, \sin^7 \vartheta \, \cos \vartheta$$

$$Y_8^{-6}(\vartheta, \varphi) = \frac{1}{128} \sqrt{\frac{7293}{\pi}} \, e^{-6j\varphi} \, \sin^6 \vartheta \, (15 \cos^2 \vartheta - 1)$$

$$Y_8^{-5}(\vartheta, \varphi) = \frac{3}{64} \sqrt{\frac{17017}{2\pi}} \, e^{-5j\varphi} \, \sin^5 \vartheta \, (5 \cos^3 \vartheta - 1 \cos \vartheta)$$

$$Y_8^{-4}(\vartheta, \varphi) = \frac{3}{128} \sqrt{\frac{1309}{2\pi}} \, e^{-4j\varphi} \, \sin^4 \vartheta \, (65 \cos^4 \vartheta - 26 \cos^2 \vartheta + 1)$$

$$Y_8^{-3}(\vartheta, \varphi) = \frac{1}{64} \sqrt{\frac{19635}{2\pi}} \, e^{-3j\varphi} \, \sin^3 \vartheta \, (39 \cos^5 \vartheta - 26 \cos^3 \vartheta + 3 \cos \vartheta)$$

$$Y_8^{-2}(\vartheta, \varphi) = \frac{3}{128} \sqrt{\frac{595}{\pi}} \, e^{-2j\varphi} \, \sin^2 \vartheta \, (143 \cos^6 \vartheta - 143 \cos^4 \vartheta + 33 \cos^2 \vartheta - 1)$$

$$Y_8^{-1}(\vartheta, \varphi) = \frac{3}{64} \sqrt{\frac{17}{2\pi}} \, e^{-j\varphi} \, \sin \vartheta \, (715 \cos^7 \vartheta - 1001 \cos^5 \vartheta + 385 \cos^3 \vartheta - 35 \cos \vartheta)$$

$$Y_8^{0}(\vartheta, \varphi) = \frac{1}{256} \sqrt{\frac{17}{\pi}} \, (6435 \cos^8 \vartheta - 12012 \cos^6 \vartheta + 6930 \cos^4 \vartheta - 1260 \cos^2 \vartheta + 35)$$

$$Y_8^1(\vartheta, \varphi) = \frac{-3}{64}\sqrt{\frac{17}{2\pi}}\, e^{j\varphi}\, \sin\vartheta\,(715\cos^7\vartheta - 1001\cos^5\vartheta + 385\cos^3\vartheta - 35\cos\vartheta)$$

$$Y_8^2(\vartheta, \varphi) = \frac{3}{128}\sqrt{\frac{595}{\pi}}\, e^{2j\varphi}\, \sin^2\vartheta\,(143\cos^6\vartheta - 143\cos^4\vartheta + 33\cos^2\vartheta - 1)$$

$$Y_8^3(\vartheta, \varphi) = \frac{-1}{64}\sqrt{\frac{19635}{2\pi}}\, e^{3j\varphi}\, \sin^3\vartheta\,(39\cos^5\vartheta - 26\cos^3\vartheta + 3\cos\vartheta)$$

$$Y_8^4(\vartheta, \varphi) = \frac{3}{128}\sqrt{\frac{1309}{2\pi}}\, e^{4j\varphi}\, \sin^4\vartheta\,(65\cos^4\vartheta - 26\cos^2\vartheta + 1)$$

$$Y_8^5(\vartheta, \varphi) = \frac{-3}{64}\sqrt{\frac{17017}{2\pi}}\, e^{5j\varphi}\, \sin^5\vartheta\,(5\cos^3\vartheta - 1\cos\vartheta)$$

$$Y_8^6(\vartheta, \varphi) = \frac{1}{128}\sqrt{\frac{7293}{\pi}}\, e^{6j\varphi}\, \sin^6\vartheta\,(15\cos^2\vartheta - 1)$$

$$Y_8^7(\vartheta, \varphi) = \frac{-3}{64}\sqrt{\frac{12155}{2\pi}}\, e^{7j\varphi}\, \sin^7\vartheta\, \cos\vartheta$$

$$Y_8^8(\vartheta, \varphi) = \frac{3}{256}\sqrt{\frac{12155}{2\pi}}\, e^{8j\varphi}\, \sin^8\vartheta$$

$l = 9$

$$Y_9^{-9}(\vartheta, \varphi) = \frac{1}{512}\sqrt{\frac{230945}{\pi}}\, e^{-9j\varphi}\, \sin^9\vartheta$$

$$Y_9^{-8}(\vartheta, \varphi) = \frac{3}{256}\sqrt{\frac{230945}{2\pi}}\, e^{-8j\varphi}\, \sin^8\vartheta\, \cos\vartheta$$

$$Y_9^{-7}(\vartheta, \varphi) = \frac{3}{512}\sqrt{\frac{13585}{\pi}}\, e^{-7j\varphi}\, \sin^7\vartheta\,(17\cos^2\vartheta - 1)$$

$$Y_9^{-6}(\vartheta, \varphi) = \frac{1}{128}\sqrt{\frac{40755}{\pi}}\, e^{-6j\varphi}\, \sin^6\vartheta\,(17\cos^3\vartheta - 3\cos\vartheta)$$

$$Y_9^{-5}(\vartheta, \varphi) = \frac{3}{256}\sqrt{\frac{2717}{\pi}}\, e^{-5j\varphi}\, \sin^5\vartheta\,(85\cos^4\vartheta - 30\cos^2\vartheta + 1)$$

$$Y_9^{-4}(\vartheta, \varphi) = \frac{3}{128}\sqrt{\frac{95095}{2\pi}}\, e^{-4j\varphi}\, \sin^4\vartheta\,(17\cos^5\vartheta - 10\cos^3\vartheta + 1\cos\vartheta)$$

$$Y_9^{-3}(\vartheta, \varphi) = \frac{1}{256}\sqrt{\frac{21945}{\pi}}\, e^{-3j\varphi}\, \sin^3\vartheta\,(221\cos^6\vartheta - 195\cos^4\vartheta + 39\cos^2\vartheta - 1)$$

$$Y_9^{-2}(\vartheta, \varphi) = \frac{3}{128}\sqrt{\frac{1045}{\pi}}\, e^{-2j\varphi}\, \sin^2\vartheta\,(221\cos^7\vartheta - 273\cos^5\vartheta + 91\cos^3\vartheta - 7\cos\vartheta)$$

$$Y_9^{-1}(\vartheta, \varphi) = \frac{3}{256}\sqrt{\frac{95}{2\pi}}\, e^{-j\varphi}\, \sin\vartheta\,(2431\cos^8\vartheta - 4004\cos^6\vartheta + 2002\cos^4\vartheta - 308\cos^2\vartheta + 7)$$

$$Y_9^0(\vartheta, \varphi) = \frac{1}{256}\sqrt{\frac{19}{\pi}}\,(12155\cos^9\vartheta - 25740\cos^7\vartheta + 18018\cos^5\vartheta - 4620\cos^3\vartheta + 315\cos\vartheta)$$

$$Y_9^1(\vartheta, \varphi) = \frac{-3}{256}\sqrt{\frac{95}{2\pi}}\, e^{j\varphi}\, \sin\vartheta\,(2431\cos^8\vartheta - 4004\cos^6\vartheta + 2002\cos^4\vartheta - 308\cos^2\vartheta + 7)$$

$$Y_9^2(\vartheta, \varphi) = \frac{3}{128}\sqrt{\frac{1045}{\pi}}\, e^{2j\varphi}\, \sin^2\vartheta\,(221\cos^7\vartheta - 273\cos^5\vartheta + 91\cos^3\vartheta - 7\cos\vartheta)$$

$$Y_9^3(\vartheta, \varphi) = \frac{-1}{256}\sqrt{\frac{21945}{\pi}}\, e^{3j\varphi}\, \sin^3\vartheta\,(221\cos^6\vartheta - 195\cos^4\vartheta + 39\cos^2\vartheta - 1)$$

$$Y_9^4(\vartheta, \varphi) = \frac{3}{128}\sqrt{\frac{95095}{2\pi}}\, e^{4j\varphi}\, \sin^4\vartheta\,(17\cos^5\vartheta - 10\cos^3\vartheta + 1\cos\vartheta)$$

$$Y_9^5(\vartheta, \varphi) = \frac{-3}{256}\sqrt{\frac{2717}{\pi}}\, e^{5j\varphi}\, \sin^5\vartheta\,(85\cos^4\vartheta - 30\cos^2\vartheta + 1)$$

$Y_9^6(\vartheta, \varphi) = \frac{1}{128} \sqrt{\frac{40755}{\pi}} \, e^{6j\varphi} \, \sin^6 \vartheta \, (17 \cos^3 \vartheta - 3 \cos \vartheta)$

$Y_9^7(\vartheta, \varphi) = \frac{-3}{512} \sqrt{\frac{13585}{\pi}} \, e^{7j\varphi} \, \sin^7 \vartheta \, (17 \cos^2 \vartheta - 1)$

$Y_9^8(\vartheta, \varphi) = \frac{3}{256} \sqrt{\frac{230945}{2\pi}} \, e^{8j\varphi} \, \sin^8 \vartheta \, \cos \vartheta$

$Y_9^9(\vartheta, \varphi) = \frac{-1}{512} \sqrt{\frac{230945}{\pi}} \, e^{9j\varphi} \, \sin^9 \vartheta$

$l = 10$ ─────────────────────────────

$Y_{10}^{-10}(\vartheta, \varphi) = \frac{1}{1024} \sqrt{\frac{969969}{\pi}} \, e^{-10j\varphi} \, \sin^{10} \vartheta$

$Y_{10}^{-9}(\vartheta, \varphi) = \frac{1}{512} \sqrt{\frac{4849845}{\pi}} \, e^{-9j\varphi} \, \sin^9 \vartheta \, \cos \vartheta$

$Y_{10}^{-8}(\vartheta, \varphi) = \frac{1}{512} \sqrt{\frac{255255}{2\pi}} \, e^{-8j\varphi} \, \sin^8 \vartheta \, (19 \cos^2 \vartheta - 1)$

$Y_{10}^{-7}(\vartheta, \varphi) = \frac{3}{512} \sqrt{\frac{85085}{\pi}} \, e^{-7j\varphi} \, \sin^7 \vartheta \, (19 \cos^3 \vartheta - 3 \cos \vartheta)$

$Y_{10}^{-6}(\vartheta, \varphi) = \frac{3}{1024} \sqrt{\frac{5005}{\pi}} \, e^{-6j\varphi} \, \sin^6 \vartheta \, (323 \cos^4 \vartheta - 102 \cos^2 \vartheta + 3)$

$Y_{10}^{-5}(\vartheta, \varphi) = \frac{3}{256} \sqrt{\frac{1001}{\pi}} \, e^{-5j\varphi} \, \sin^5 \vartheta \, (323 \cos^5 \vartheta - 170 \cos^3 \vartheta + 15 \cos \vartheta)$

$Y_{10}^{-4}(\vartheta, \varphi) = \frac{3}{256} \sqrt{\frac{5005}{2\pi}} \, e^{-4j\varphi} \, \sin^4 \vartheta \, (323 \cos^6 \vartheta - 255 \cos^4 \vartheta + 45 \cos^2 \vartheta - 1)$

$Y_{10}^{-3}(\vartheta, \varphi) = \frac{3}{256} \sqrt{\frac{5005}{\pi}} \, e^{-3j\varphi} \, \sin^3 \vartheta \, (323 \cos^7 \vartheta - 357 \cos^5 \vartheta + 105 \cos^3 \vartheta - 7 \cos \vartheta)$

$Y_{10}^{-2}(\vartheta, \varphi) = \frac{3}{512} \sqrt{\frac{385}{2\pi}} \, e^{-2j\varphi} \, \sin^2 \vartheta \, (4199 \cos^8 \vartheta - 6188 \cos^6 \vartheta + 2730 \cos^4 \vartheta - 364 \cos^2 \vartheta + 7)$

$Y_{10}^{-1}(\vartheta, \varphi) = \frac{1}{256} \sqrt{\frac{1155}{2\pi}} \, e^{-j\varphi}$
$$\sin \vartheta \, (4199 \cos^9 \vartheta - 7956 \cos^7 \vartheta + 4914 \cos^5 \vartheta - 1092 \cos^3 \vartheta + 63 \cos \vartheta)$$

$Y_{10}^0(\vartheta, \varphi) = \frac{1}{512} \sqrt{\frac{21}{\pi}}$
$$(46189 \cos^{10} \vartheta - 109395 \cos^8 \vartheta + 90090 \cos^6 \vartheta - 30030 \cos^4 \vartheta + 3465 \cos^2 \vartheta - 63)$$

$Y_{10}^1(\vartheta, \varphi) = \frac{-1}{256} \sqrt{\frac{1155}{2\pi}} \, e^{j\varphi}$
$$\sin \vartheta \, (4199 \cos^9 \vartheta - 7956 \cos^7 \vartheta + 4914 \cos^5 \vartheta - 1092 \cos^3 \vartheta + 63 \cos \vartheta)$$

$Y_{10}^2(\vartheta, \varphi) = \frac{3}{512} \sqrt{\frac{385}{2\pi}} \, e^{2j\varphi} \, \sin^2 \vartheta \, (4199 \cos^8 \vartheta - 6188 \cos^6 \vartheta + 2730 \cos^4 \vartheta - 364 \cos^2 \vartheta + 7)$

$Y_{10}^3(\vartheta, \varphi) = \frac{-3}{256} \sqrt{\frac{5005}{\pi}} \, e^{3j\varphi} \, \sin^3 \vartheta \, (323 \cos^7 \vartheta - 357 \cos^5 \vartheta + 105 \cos^3 \vartheta - 7 \cos \vartheta)$

$Y_{10}^4(\vartheta, \varphi) = \frac{3}{256} \sqrt{\frac{5005}{2\pi}} \, e^{4j\varphi} \, \sin^4 \vartheta \, (323 \cos^6 \vartheta - 255 \cos^4 \vartheta + 45 \cos^2 \vartheta - 1)$

$Y_{10}^5(\vartheta, \varphi) = \frac{-3}{256} \sqrt{\frac{1001}{\pi}} \, e^{5j\varphi} \, \sin^5 \vartheta \, (323 \cos^5 \vartheta - 170 \cos^3 \vartheta + 15 \cos \vartheta)$

$Y_{10}^6(\vartheta, \varphi) = \frac{3}{1024} \sqrt{\frac{5005}{\pi}} \, e^{6j\varphi} \, \sin^6 \vartheta \, (323 \cos^4 \vartheta - 102 \cos^2 \vartheta + 3)$

$$Y_{10}^7(\vartheta, \varphi) = \tfrac{-3}{512} \sqrt{\tfrac{85085}{\pi}} \, e^{7j\varphi} \, \sin^7 \vartheta \, (19 \cos^3 \vartheta - 3 \cos \vartheta)$$

$$Y_{10}^8(\vartheta, \varphi) = \tfrac{1}{512} \sqrt{\tfrac{255255}{2\pi}} \, e^{8j\varphi} \, \sin^8 \vartheta \, (19 \cos^2 \vartheta - 1)$$

$$Y_{10}^9(\vartheta, \varphi) = \tfrac{-1}{512} \sqrt{\tfrac{4849845}{\pi}} \, e^{9j\varphi} \, \sin^9 \vartheta \, \cos \vartheta$$

$$Y_{10}^{10}(\vartheta, \varphi) = \tfrac{1}{1024} \sqrt{\tfrac{969969}{\pi}} \, e^{10j\varphi} \, \sin^{10} \vartheta$$

Appendix F

Curriculum Vitae

Name	**Jan Rejlek**
Address	Neupauerweg 85
	8052 Graz
	Austria
E-mail	jan.rejlek@gmail.com
Place and date of birth	Tábor, March 11th 1979
Nationality	Czech

Jan Rejlek was born on March 11, 1979, in Tábor, Czech Republic. He began studying electrical engineering at the *Czech Technical University (CTU)* in Prague in 1997. In the course of the masters study program, he was granted a Socrates/Erasmus scholarship in 2002. This entitled him to study six months at the *Dresden University of Technology*, *Faculty of Electrical Engineering and Information Technology*, *Institute of Acoustics and Speech Communication*. In 2004, he graduated from *CTU* with his thesis focusing on the application of the boundary element method for the modelling of sound scattering problems.

After receiving his M.Sc., he joined the research institute *Acoustic Competence Centre Graz (ACC)* in early 2004. In *ACC*, he was involved in several research projects that addressed the development and application of alternative computational schemes for mid-frequency vibro-acoustic problems. Since October 2005, he has been a Ph.D. candidate in the field of mechanical engineering at the *Graz University of Technology*, *Faculty of Mechanical Engineering and Economic Sciences*.

In 2006, he became a fellow of the SIMVIA2 project, a Marie Curie (MC) Early Stage Research Training of the European Commission within the sixth framework program. In 2007, he was employed under this MC mobility scheme at the *Katholieke Universiteit Leuven*, *Department of Mechanical Engineering*, *Division PMA* as a research fellow for the period of six months. Since rejoining the *ACC Graz*, which subsequently became a part of the *Virtual Vehicle Competence Center (ViF)* in early 2008, he has mainly been involved in ongoing EU R&D Projects. Currently, he is a senior researcher at *ViF*.

Besides his research interests in computational vibro-acoustics, his professional career also includes three years of working experience in the field of environmental noise measurements

and noise control with an engineering and consulting company located in Prague. Besides Czech, his mother tongue, he has fluent command of German and English.

Appendix G

List of publications

International peer-reviewed journal articles

J. Rejlek, B. Pluymers, A. Hepberger, H.-H. Priebsch, and W. Desmet. Application of the Wave Based Technique for steady-state semi-infinite sound radiation analysis. *Computer Assisted Mechanics and Engineering Sciences (CAMES)*, 15(3-4):337–351, 2008. ISSN 1232-308X.

Full papers in proceedings of international conferences

J. Rejlek, B. Pluymers, F. Diwoky, A. Hepberger, H.-H. Priebsch, and W. Desmet. Validation of the wave based technique for the analysis of 2D steady-state acoustic radiation problems. In *proceedings of the International Conference on Engineering Dynamics (ICED2007), April 16–18, Carvoeiro, Algarve, Portugal*, 2007.

J. Rejlek, F. Diwoky, A. Hepberger, and B. Pluymers. Wave Based Technique: enrichment of the set of basis functions. In *proceedings of the International Conference on Noise and Vibration Engineering (ISMA2008), September 15–17, Leuven, Belgium*, pages 1595–1608, 2008. ISBN 978-90-7380-286-5.

J. Rejlek, T. Mócsai, P. Šilar, A. Hepberger, and H.-H. Priebsch. Wave Based Prediction Technique for Sound Radiation Analysis. In *proceedings of the International Conference on Acoustics (NAG/DAGA2009), March 23–26, Rotterdam, The Netherlands*, pages 206–209, 2009. ISBN 978-3-9808659-6-8.

J. Rejlek and H.-H. Priebsch. Wave based technique for the analysis of fully coupled structural-acoustic unbounded problems. In *proceedings of the International Conference on Noise and Vibration Engineering (ISMA2010), September 20–22, Leuven, Belgium*, pages 2407–2424, 2010. ISBN 978-90-7380-287-2.

J. Rejlek and H.-H. Priebsch. On the Use of the Wave Based Technique for a Three-Dimensional Noise Radiation Analysis of Coupled Vibro-Acoustic Problems. In *proceedings of the SAE 2011 Noise and Vibration Conference and Exhibition, May 16–19, Grand Rapids, Michigan, USA*, 2011. doi: 10.4271/2011-01-1713.

J. Rejlek, G. Ohenhen, P. Šilar, H.-H. Priebsch, A. Galezia, D. Hagen and S. Ruschmeyer. A weak-coupled finite element–wave based technique formulation: application for a noise radiation analysis of a truck exhaust muffler. *Paper submitted for the Noise and Vibration: Emerging Methods (NOVEM2012) conference, April 1–4, Sorrento, Italy*, 2012.

Abstracts in proceedings of international conferences

M. Danti, R. Raniolo, B. Van Genechten, M. Tournour, J. Rejlek, A. Galezia, S. Ruschmeyer. Recent advances in the simulation of exterior noise field propagation and its frequency extension. *Abstract submitted for the International Conference on Noise and Vibration Engineering (ISMA2012), September 17–19, Leuven, Belgium*, 2012.

Other publications

J. Rejlek. The mid-frequency gap – a real challenge in the numerical vibro-acoustic modelling. *Marie Curie Conference, Euroscience Open Forum 2008 (ESOF2008), July 17–22, Barcelona, Spain*, 2008, Poster.

J. Rejlek. SIMVIA2, seventh framework programme and beyond. *6th SIMVIA2 Workshop of Researchers, March 23, Graz, Austria*, 2010. Invited talk.

J. Rejlek, H.-H. Priebsch and F. M. Reich. Analysis of powertrain sound radiation behaviour by means of wave based technique. *6th International Styrian Noise, Vibration & Harshness Congress (ISNVH2010), June 9–11, Graz, Austria*, 2010. Presentation in the "Mid-frequency vibro-acoustic modelling tools (MID-MOD) session".

J. Rejlek. Wave based method for 3D unbounded problems. *Mid-frequency Analysis of Noise and Vibration, Professional Development Course and Industrial Workshop, April 5–8, St. Anne's College, Oxford, United Kingdom*, 2011. Presentation.

J. Rejlek, P. Šilar, G. Ohenhen. Numerical investigation on the noise radiation of a truck exhaust muffler. *Mid-frequency Analysis of Noise and Vibration, Professional Development Course and Industrial Workshop, April 5–8, St. Anne's College, Oxford, United Kingdom*, 2011. Presentation.

J. Rejlek. Wave based technique for a three-dimensional steady-state analysis of unbounded acoustic problems. *MIDEA Workshop, May 2–3, Schloss Thurnau, Germany*, 2011. Invited talk.